

# Microfluidic differentiation of subpopulations of cells based on their bioelectrical signature

Alireza Salmanzadeh-Dozdabi

Dissertation submitted to the faculty of the Virginia Polytechnic Institute and State University in partial fulfillment of the requirements for the degree of  
Doctor of Philosophy  
In  
Engineering Mechanics

Rafael V. Davalos  
Mark A. Stremler  
Eva M. Schmelz  
Ishwar K. Puri  
Chang Lu

March 26<sup>th</sup>, 2013

Blacksburg, Virginia

Keywords: Lab on a Chip, Microfluidics, Contactless Dielectrophoresis, Cell Subpopulations Differentiation, Rare Cell Enrichment, Cancer Early Diagnosis, Cancer Stem Cell, Tumor Initiating Cell

## Microfluidic differentiation of subpopulations of cells based on their bioelectrical signature

Alireza Salmanzadeh-Dozdabi

**Abstract:** Applications for lab-on-a-chip devices have been expanding rapidly in the last decade due to their lower required volume of sample, faster experiments, smaller tools, more control, and ease of parallelization compared to their macroscale counterparts. Moreover, lab-on-a-chip devices provide important capabilities, including isolating rare cells from body fluids, such as isolating circulating tumor cells from blood or peritoneal fluid, which are not feasible or at least extremely difficult with macroscale devices. Particles experience different forces (and/or torques) when they are suspended in a fluid in a microdevice. A dominant force is the drag force on the particle as it flows through the fluid. External forces such as dielectrophoresis, the motion of a particle due to its polarization in the presence of a non-uniform electric field, may also be applied. For instance, well-specified mixing or separation of particles can be achieved by using the combination of drag and dielectrophoretic forces. Two major mechanisms for manipulating particles in a microdevice include control of forces applied to the particles, such as those due to electric and velocity fields, and the geometry of the device that affects the nature of these fields. The coupling between the geometry of the microdevices and applied fields makes the prediction of associated forces inside the microdevice challenging and increasingly difficult when the applied field is time-dependent. Understanding the interaction of external forces and particles and fluid is critical for engineering novel microsystems. Determining this interaction is even more complicated when dealing with bioparticles, especially cells, due to their complex intrinsic biological properties which influence their electrical and mechanical properties. Particles with non-spherical geometries further increase the complexity, making drag and other shape-dependent forces, such as dielectrophoretic force, less predictable and more complicated. In order to introduce more complexity to the system and maintain precise control over particle movement and fluid flow, it is essential to have a comprehensive understanding about the mechanics of particles-fluid interaction and the dynamics of the particle movement. Although microfluidics has been investigated extensively, unanswered questions about the effect of forces on the particle remain. Answering these questions will facilitate designing novel and more practical microdevices for medical, biological, and chemical applications.

Microfluidics devices were engineered for differentiation of subpopulations of cells based on their bioelectrical properties. These microdevices were utilized for separating prostate, leukemia, and three different stages of breast cancer cells from hematologic cells with concentrations as low as  $1:10^6$  with efficiency of  $>95\%$ . The microfluidic platform was also utilized to isolate prostate cancer stem cells (CSCs) from normal cancer cells based on their electrical signature. Isolating these cells is the first step towards the development of cancer specific therapies. The signal parameters required to selectively isolate ovarian cancer cells at different cancer stages were also compared with peritoneal cells as the first step in developing an early diagnostic clinical system centered on cell biophysical properties. Moreover, the effect of non-toxic concentrations of two metabolites, with known anti-tumor and pro-tumor properties, on the intrinsic electrical properties of early and late stages of ovarian cancer cells was investigated. This work is the first to show that treatment with non-toxic doses of these metabolites correlate with changes in cells electrical properties.

# Acknowledgment

I would like to first thank my great advisers, Dr. Rafael V. Davalos and Dr. Mark A. Stremmer for their supervision, advice, support, and guidance through this interdisciplinary research from the very early stage. It is also a pleasure to thank all of the graduate and undergraduate students and faculties that assisted me in creating ideas, designing devices, analyzing them theoretically and computationally and conducting experiments during my stay at the Bioelectromechanical Systems (BEMS) laboratory in School of Biomedical Engineering and Sciences and also Engineering Science and Mechanics Department. I would like to thank my current and former labmates Hadi Shafiee, Mike Sano, Elizabeth Elvington, Mohammad Bonakdar, Roberto Gallo, Erin Henslee, Lisa Anders, Harsha Kitter, Caitlan Swafar, Karli Brittain, Paul Caron, and Nathan Roberson. I am grateful in any possible way and hope to keep up our collaboration in the future.

I would like to thank my family, and loved ones for their continuous support and encouragement. I certainly, owe my deepest gratitude to my dear parents for their never-ending love. It is not easy and possible to put the feelings about you in words and I can just say thank you for everything you have done. I will never forget the love and hard work of my parents which have been substantial to reach all of these achievements. To my sister and brother, Nasrin and Hamed, thank you for your love and support.

# Table of Contents

## Chapter One

Introduction	1
1.1 Isolating subpopulations of cells	2
1.2 Early cancer diagnosis	2
1.3 Cancer detection from peritoneal fluid	3
1.4 Cancer stem cells (CSCs)	4
1.5 Dielectrophoresis (DEP)	5
1.6 Contactless Dielectrophoresis (cDEP)	6
1.7 Overview	7

## Chapter Two

Theory	10
2.1 Introduction	10
2.2 Navier-Stokes equations	11
2.3 Electrical Reynolds number	13
2.4 Electrical forces	13
2.5 Dielectrophoresis	14
2.6 Other DEP-based techniques	37
2.7 Electro-rotation	38
2.8 Electrical double layer	41
2.9 Electrophoresis	42
2.10 Electroosmosis	43
2.11 AC-electroosmosis	44
2.12 Electrothermal effects in the fluid	45
2.13 Hydrodynamic force	48
2.15 Brownian motion	49

2.16 Summary	49
Chapter Three	
Materials and Methods	51
3.1 Introduction	51
3.2 Fabrication Process	51
3.3 Experimental Setup	52
3.4 Method of Analysis of Mixing	53
3.5 Electronics	54
3.6 Cell culturing	55
3.7 Cell preparation for flow cytometry	56
3.8 Cell Preparation for experiments	56
3.9 Immunofluorescence assay imaging	57
3.10 Protaspheres Culturing	57
3.11 Blood Sample Preparation	58
3.12 Computational Modeling	58
Chapter Four	
Investigating Dielectric Properties of Different Stages of Syngeneic Murine Ovarian Cancer Cells	60
4.1 Introduction	60
4.2 Device Layout	62
4.3 Data Analysis	64
4.4 Computational Results	66
4.5 Results and Discussion	67
4.6 Conclusions	73

Chapter Five	
Sphingolipid Metabolites Modulate Dielectric Characteristics of Cells in a Mouse	75
Ovarian Cancer Progression Model	
5.1 Introduction	75
5.2 Background	76
5.3 Device layout	79
5.4 Computational Results	80
5.5 Results and Discussion	81
5.6 Conclusions	87
Chapter Six	
Dielectrophoretic Differentiation of Ovarian Cancer Cells from Peritoneal Fluid	89
6.1 Introduction	89
6.2 Device Layout	90
6.3 Computational Results	91
6.4 Experimental Results	94
6.5 Discussion	97
6.6 Conclusions	101
Chapter Seven	
Isolation of Prostate Tumor Initiating Cells (TICs) through Their Dielectrophoretic Signature	102
7.1 Introduction	102
7.2 Device Layout	102
7.3 Data analysis	104
7.4 Flow cytometry	104
7.5 Computational Results	104
7.6 Results and Discussion	107
7.7 Conclusions	113

Chapter Eight	
Isolation of Rare Cancer Cells from Blood Cells Using Dielectrophoresis	114
8.1 Introduction	114
8.2 Device layout	116
8.3 Computational Results	116
8.4 Experimental Results	117
8.5 Conclusion	118
Chapter Nine	
Microfluidic mixing using contactless dielectrophoresis (cDEP)	120
9.1 Introduction	120
9.2 Device Layout	121
9.3 Computational Results	123
9.4 Experimental Results	124
9.5 Conclusions	133
Chapter Ten	
Investigating AC-electroosmotic flow in cDEP microdevices using particle tracking velocimetry	135
10.1 Introduction	135
10.2 Particle Tracking Velocimetry	135
10.3 Microdevice layout	136
10.4 Computational Results	137
10.5 Dimensionless number	137
10.6 Experimental Methodology for PTV	139
10.7 PTV Results	141
10.8 Temperature Measurement	141
10.9 Temperature dependence	142
10.10 Conclusions	143

Chapter Eleven	
Continuous Cell Sorting using Multilayer cDEP Microdevices	144
11.1 Introduction	144
11.2 Dominant forces	146
11.3 Theoretical consideration of traditional DEP interdigitated electrode array in 2D	148
11.4 Computational parametric study of 2D model with periodic BCs	154
11.5 3D computational modeling	169
11.6 Experimental results	174
11.7 Conclusion	176
Chapter Twelve	
Future Work	177
12.1 Advancing our understanding of the biophysical properties of cells	178
12.2 Enhancing selectivity	179
12.3 Increasing the throughput of cDEP microdevices	180
References	183

# List of Figures

<b>Fig. 1.1.</b> Relative 5-year survival rate of ovarian cancer [1].	4
<b>Fig. 2.1.</b> (a) Schematic of a dipole. (b) Schematic of a sphere in an electric field	16
<b>Fig. 2.2.</b> Real and Imaginary parts of Clausius-Mossotti factor of a particle.	20
<b>Fig. 2.3.</b> Schematic of (a) single- and (b) two-shell models. The real and imaginary parts of the Clausius-Mossotti factor as a function of frequency for (c) single- and (d) two-shell models.	23
<b>Fig. 2.4.</b> Polarity of mammalian cells changes by changing the frequency. (a) At low frequencies, cells behave as an electrically insulating particle. (b) At crossover frequency the induced dipole moment of cell is zero and cell behaves as being transparent to the electric field. (c) At high frequencies, cells are more polarizable than the suspending medium and the field penetrated inside the cell.	24
<b>Fig. 2.5.</b> A circuit model of a suspended cell in a fluid between two electrodes.	25
<b>Fig. 2.6.</b> Clausius-Mossotti factor for a typical mammalian cell at the sample conductivity of 100 $\mu\text{S}/\text{cm}$ . Arrows show how the Clausius-Mossotti factor of cells changes by changing the cells characteristics.	30
<b>Fig. 2.7.</b> Clausius-Mossotti factor changes by changing N/C ratio of cells.	35
<b>Fig. 2.8.</b> Schematic of the system used to derive EO relation.	43
<b>Fig. 3.1.</b> cDEP experimental system, including the syringe pump, microfluidic device on a portable microscope, laptop to control the portable electronics and view microscope videos.	55
<b>Fig. 4.1.</b> Top view schematic of the device. Flow is from left to right in the fluidic channel. Inset is a detailed view of a saw-tooth feature and the T-junction [2].	63
<b>Fig. 4.2.</b> (a) Due to negative DEP force, cells move towards the bottom of the channel at 10 kHz and 200 $V_{\text{RMS}}$ ; (b) normalized cell distribution from (a). (c) Due to positive DEP force, cells move towards the top of the channel at 60 kHz and 200 $V_{\text{RMS}}$ ; (d) normalized cells distribution from (b). The red solid line in (a) and (c) showed the location that cells distribution was studied. The red dashed line in (b) and (d) shows the center line of the cell distribution [2].	65
<b>Fig. 4.3.</b> Computational modeling of the microdevice. Surface plot of (a) the magnitude of the flow velocity ( $\mu\text{m s}^{-1}$ ), (b) shear rate ( $\text{s}^{-1}$ ), and (c) the magnitude of electric field, and (d) gradient of the electric field squared ( $\text{V}^2 \text{m}^{-3}$ ) at 200 $V_{\text{RMS}}$ and 30 kHz, in the fluidic channel. Flow is from left to right [2].	67
<b>Fig. 4.4.</b> (a) Crossover frequency and (b) area capacitance of the cell membrane for MOSE-E, -E/I, -I, and -L cells. *, **, and *** represent $p < 0.001$ , 0.01, and 0.05, respectively (n=3) [2].	68
<b>Fig. 4.5.</b> Organization of the cytoskeleton during MOSE neoplastic progression. Triple immunofluorescent staining of MOSE-E and MOSE-L cells to visualize actin filaments (phalloidin, green), tubulin filaments (red), and nucleus (DAPI, blue) [2].	71

- Fig. 4.6.** Clausius-Mossotti factor of MOSE-E and MOSE-L cells as a function of frequency using Equation (11.61). The previously reported values for cancer cells were used for both early and late stages: cell membrane relative permittivity,  $10^{-8}$  [3], membrane thickness, 5 nm [4], cytoplasm relative permittivity, 60 [5]. The cytoplasm conductivity of cells was approximated as  $0.5 \text{ S m}^{-1}$  [6]. Media permittivity and conductivity are  $\epsilon_m = \epsilon_{DEP} = 80$  and  $\sigma_m = \sigma_{DEP} = 0.01$ , respectively [2]. 73
- Fig. 5.1.** The overhead view schematic of the microfluidic device. The inset detail view shows a sawtooth feature and the thin insulating barrier separating sample channel and electrode channels [7]. 80
- Fig. 5.2.** Predicting the particles trajectories at (a) 5 kHz and (b) 20 kHz in red lines for 10 particles. Trajectories appear to diminish down the channel due to a simulation artifact that occurs when trajectories encounter a wall.  $\nabla(\vec{E}_{RMS} \cdot \vec{E}_{RMS})$  is also presented in the background. Darker areas indicate higher  $\nabla(\vec{E}_{RMS} \cdot \vec{E}_{RMS})$ . The scale bar represents 500  $\mu\text{m}$  [7]. 81
- Fig. 5.3.** Finding crossover frequency of cells based on their movement towards top or bottom half of the channel. MOSE-L cell movement in the sample channel (a) without applying any electric field, (b) due to applying 200  $V_{RMS}$  and negative DEP force at 5 kHz and (c) 200  $V_{RMS}$  and positive DEP force at 30 kHz. Normalized cell distributions corresponding to (d) no DEP force in the control (a), (e) negative DEP in (b), and (f) positive DEP in (c) [7]. 85
- Fig. 5.4.** So-treated late stage cells revert back to early stage based on their electrical signature. (a)  $f_{xo}/\sigma_m$  and (b) specific membrane capacitance of untreated, So-treated, and S1P-treated of MOSE-E and -L cells. \*, and \*\* represent  $p < 0.001$ , and  $0.01$ , respectively ( $n=3$  for treated cells and  $n=6$  for untreated cells experiments) [7]. 87
- Fig. 6.1.** (a) 2D top view schematic of the microdevices. (b) A section of the microdevice and pillars. Each pillar is 100  $\mu\text{m}$  in diameter. (c) Complete trapping of cells. Calcein AM, enzymatically converted to green fluorescent calcein, is added to the cell sample at 2 mL per mL of cell suspension [8]. 90
- Fig. 6.2.** (a) The gradient of the electric field squared ( $V^2 \text{ m}^{-3}$ ) at 300  $V_{rms}$  and 600 kHz. The line plot of  $\nabla(\vec{E}_{rms} \cdot \vec{E}_{rms})$  on a normalized diagonal line A-B is presented for (b) triangular and rectangular pillar arrangements, (c) circular pillars with 30, 60 and 120  $\mu\text{m}$  gap and diameter of 100  $\mu\text{m}$ , at 100  $V_{rms}$  and 500 kHz [8]. 93
- Fig. 6.3.** Ratio of drag force to dielectrophoretic force for microdevices with equal channel width and circular pillars with diameter of (a) 50  $\mu\text{m}$ , (b) 100  $\mu\text{m}$ , and (c) 200  $\mu\text{m}$ . In dark areas DEP force is dominant, and in light areas drag force prevails [8]. 94
- Fig. 6.4.** (a) Onset and (b) complete trapping voltages of early (MOSE-E), early-intermediate (MOSE-E/I), intermediate (MOSE-I), and late (MOSE-L) cells at 200, 300, 400, 500, and 600 kHz. Left and right columns present the onset of trapping and complete trapping, respectively. \*, \*\*, and \*\*\* indicate that data are significantly different with  $p < 0.0005$ ,  $p < 0.005$ , and  $p < 0.05$ , respectively ( $n=10$ ) [8]. 95

- Fig. 6.5.** (a) Onset and (b) complete trapping voltages of different stages of MOSE cells compared with macrophages (PC1) and fibroblasts (OP9) cells at 200, 300, 400, 500, and 600 kHz. Left and right columns present the onset of trapping and complete trapping, respectively. \*, \*\*, and \*\*\* indicate that data are significantly different with  $p < 0.0005$ ,  $p < 0.005$ , and  $p < 0.05$ , respectively (n=10) [8]. 96
- Fig. 6.6.** (a) Difference between complete trapping voltage of (a) fibroblasts (OP9) and (b) macrophages (PC1) and different stages of MOSE cells as a function of applied frequency (n=10) [8]. 97
- Fig. 7.1.** Top view schematic and dimensions of (a) a section of microchannels and pillars and (b) cDEP microdevice. (c) Trapped cells at 600 kHz and 129  $V_{rms}$  [9]. 103
- Fig. 7.2.** Identification of ALDH+ cells in a human prostate cancer cell line (PC3). 10,000 events were evaluated on a BD FACSaria cell sorter. Histograms show gated populations (a) without and (b) with Diethylaminobenzaldehyde (DEAB) inhibitor. Numbers in gated areas indicate the percent of the total population represented in the area [9]. 105
- Fig. 7.3.** Computational modeling was used to predict the performance of the 1 mm-wide device. Surface plot of (a) the gradient of the electric field squared ( $V^2/m^3$ ) at 300  $V_{rms}$  and 600 kHz, (b) flow velocity magnitude ( $\mu m/s$ ), and (c) shear rate (s) in the fluidic channel. (d) Dimensionless values of velocity and  $\nabla(\vec{E}_{rms} \cdot \vec{E}_{rms})$  on line A-B. Velocity,  $U$ , is dimensionalized by inlet velocity,  $U_o = 110 \mu m/s$ .  $\nabla(\vec{E}_{rms} \cdot \vec{E}_{rms})$  is dimensionalized by applied voltage,  $V_o$ , and the distance between electrode channels (= 1 mm), which is equal to channel width [9]. 106
- Fig. 7.4.** Voltage of trapping of ALDH positive and ALDH negative cells at (a) 200 kHz, (b) 300 kHz, (c) 400 kHz, (d) 500 kHz, and (e) 600 kHz (n=4). Light grey and dark grey bars present the onset of trapping and complete trapping, respectively. Complete trapping voltage of ALDH positive and negative cells at each frequency are significantly different ( $p < 0.005$ ), represented by \*. (f) Percentage of trapping of ALDH negative cells at 200-600 kHz at complete trapping voltage of ALDH positive cells [9]. 110
- Fig. 7.5.** Photos of spheroids generated by culturing (a) unsorted PC3 cells (control), (b) released cells at 280  $V_{rms}$  (ALDH negative), and (c) released cells after turning electric field off (ALDH positive). Images are taken after 3 weeks at 20X magnification. Bars are 50  $\mu m$  long [9]. 111
- Fig. 8.1.** (a - b) Schematic representation of the cDEP microdevice used in this study. The insulating barrier between the sample channel (grey) and the fluid electrode channels (blue) is 20- $\mu m$  thick. (c) Breast cancer cells (blue) are trapped due to DEP force. Blood cells are moving in the background flow. More cancer cells were used in to take this Fig. to make cells more visible [10]. 115
- Fig. 8.2.** Computational modeling is used to predict the performance of the device. Surface plot of drag force to DEP force ratio [10]. 117
- Fig. 8.3.** Percentage of trapping of MDA-MB-231 cells at 0-300  $V_{RMS}$  at 600 kHz [10]. 118

<b>Fig. 9.1.</b> 2D top view schematic of the microdevices. All dimensions are in $\mu\text{m}$ [11].	122
<b>Fig. 9.2.</b> $\log(\gamma)$ surface plot of (a) device 1, (b) device 2, (c) device 3, (d) device 4, at an applied frequency of 600 kHz. (e) Line plot of $\gamma$ for the four devices at 600 kHz [11].	125
<b>Fig. 9.3.</b> Flow in devices 1 (panels a and b) and 2 (panels c and d) before (panels a and c) and after (panels b and d) applying the electric field at 300 $V_{\text{rms}}$ and 600 kHz (flow is from left to right). The dotted rectangles ( $100\mu\text{m} \times 200\mu\text{m}$ ) show the areas used for calculating the mixing index before and after the mixing chambers. A small amount of Rhodamine B has been added to the PBS in the electrode channels to make them visible [11].	127
<b>Fig. 9.4.</b> (a) Variation of mixing index with respect to the applied voltage at a frequency of 600 kHz and a flow rate of 0.005 mL/hr for device 1 and 2, (b) variation of mixing index for device 2 versus the applied frequency at 250 $V_{\text{rms}}$ and a flow rate of 0.005 mL/hr, and (c) variation of mixing index for device 2 versus flow rate at a frequency of 600 kHz with two different voltages: 200 $V_{\text{rms}}$ and 300 $V_{\text{rms}}$ [11].	129
<b>Fig. 9.5.</b> Device 2 at frequency of 600 kHz and voltage of 300 $V_{\text{rms}}$ and flow rates of (a) 0.02 mL/hr, and (b) 0.2 mL/hr. Flow is from left to right [11].	131
<b>Fig. 9.6.</b> Mixing of two inlet streams using DEP at a frequency of 600 kHz and voltage of 300 $V_{\text{rms}}$ . The two streams are pure DI water and DI water containing blue dye and beads. Flow is from left to right [11].	132
<b>Fig. 9.7.</b> Flow in devices 3 (panels a and b) and 4 (panels c and d) before (panels a and c) and after (panels b and d) applying the electric field at 300 $V_{\text{rms}}$ and 600 kHz (flow is from left to right). A small amount of Rhodamine B has been added to the PBS in the electrode channels to make them visible [11].	133
<b>Fig. 10.1.</b> schematic of the device.	136
<b>Fig. 10.2.</b> Dimensionless number, $\gamma$ , for the flow inside the microchamber at different zeta potentials, 0.1, 1, and 10 mV, for applied voltages of 100 and 300 $V_{\text{rms}}$ , and for 1 and 10 $\mu\text{m}$ particles.	139
<b>Fig. 10.3.</b> Examples of regular and irregular trajectory patterns. Several examples of regular trajectory patterns were observed with varying numbers of swirling regions.	140
<b>Fig. 11.1.</b> (a) Schematic of the top view of the device. (b) Schematic of a periodic conventional interdigitated electrode array on a cross-section B-B. (b) Boundary condition at $z=0$	148
<b>Fig. 11.2.</b> Schematic of the 2D model with periodic boundary conditions.	155
<b>Fig. 11.3.</b> (a) $\nabla(\vec{E}_{\text{RMS}} \cdot \vec{E}_{\text{RMS}})$ and its contours for the geometry shown in Fig. 2 inside the sample channel with 5mm depth. (b) $\nabla(\vec{E}_{\text{RMS}} \cdot \vec{E}_{\text{RMS}})$ on line "A" in logarithmic scale (c) the vector plot of the direction of DEP force under the electrode channels	156
<b>Fig. 11.4.</b> (a) Voltage for the basic case. (b) Voltage at the surface of PDMS, (c) voltage under the electrode channels inside the PDMS.	157
<b>Fig. 11.5.</b> $\nabla(\vec{E}_{\text{RMS}} \cdot \vec{E}_{\text{RMS}})$ for conventional interdigitated electrode array (membrane	160

thickness = 0) when electrodes change sign (a) one by one or (b) two by two. Voltage at the surface of the electrodes (c) for case (a), and (d) for case (b). (e) and (f) show two approximation of (d).

**Fig. 11.6.** (a)  $\nabla(\vec{E}_{RMS} \cdot \vec{E}_{RMS})$  for circular electrode channels. (b)  $\nabla(\vec{E}_{RMS} \cdot \vec{E}_{RMS})$  on a line in the same location as line “A” in Fig. 2. 161

**Fig. 11.7.**  $\nabla(\vec{E}_{RMS} \cdot \vec{E}_{RMS})$  as a function of (a) applied frequency (1, 10, 100, 200, and 500 kHz) at a constant applied voltage of 100 V, (b) membrane thickness (0, 10, 20, 50, and 100  $\mu\text{m}$ ) (c) the distance between positive and negative electrode channels (0, 10, 20, 50, 100, and 200  $\mu\text{m}$ ), (d) the distance between positive-positive and negative-negative electrode channels (10, 50, 100, 500, and 1000  $\mu\text{m}$ ), (e) electrode channel width (10, 20, 50, 100, 200, 500, and 1000  $\mu\text{m}$ ), and (f) sample channel heights (20, 30, 40, 50, 100, 500, and 1000  $\mu\text{m}$ ). 162

**Fig. 11.8.**  $\vec{E}_{RMS} \cdot \vec{E}_{RMS}$  at heights of 10, 20, 30, 40, 50, 100, and 200 $\mu\text{m}$  under the PDMS surface. 163

**Fig. 11.9.** Trajectories of particles and  $\nabla(\vec{E}_{RMS} \cdot \vec{E}_{RMS})$  at a sample channel 500  $\mu\text{m}$  in depth. 166

**Fig. 11.10.**  $\nabla(\vec{E}_{RMS} \cdot \vec{E}_{RMS})$  in sample channel for (a) electrode channel with opposite charge (b) with the same charge as electrode channels on the other side. 167

**Fig. 11.11.** (a) The top view of a conventional interdigitated electrode array (sink-source pattern). (b) The equivalent multilayer cDEP device (sink-sink-source-source pattern). (c) and (d) show  $\nabla(\vec{E}_{RMS} \cdot \vec{E}_{RMS})$  for two cases presented in (a) and (b), respectively. (e)  $\nabla(\vec{E}_{RMS} \cdot \vec{E}_{RMS})$  on lines 10, 20, 30, 40, 50, and 100  $\mu\text{m}$  under the membrane for two cases shown in (c) and (d). Blue dashed line represents sink-source pattern (case (a)) and black solid line represents sink-sink-source-source pattern (case (b)). (f)  $\nabla(\vec{E}_{RMS} \cdot \vec{E}_{RMS})$  on a line parallel to the membrane, 10  $\mu\text{m}$  under the membrane, when the gap between similar charge electrode channels changes as 0, 10, 20, 30, 40, 50, and 100  $\mu\text{m}$ . The sample channel width is normalized since it changes by changing the gap between electrode channels. 168

**Fig. 11.12.** (a) the schematic of the cross-section of the sample channel. The velocity profiles on a center line on. 170

**Fig. 11.13.** (a) DEP force on a 15  $\mu\text{m}$  diameter particle with  $Re\{f_{CM}\} = 0.5$  on line “B”. (b) The net force (DEP and drag forces) in devices with  $\theta = 45$  degree. The surface plots of DEP are shown on a plane 5  $\mu\text{m}$  under the PDMS surface and force vectors are shown on the center line of the plane in x-direction. 172

**Fig. 11.14.** (a) 3D view of the device with fluidic electrode channel on one side. 2D model of  $\nabla(\vec{E}_{RMS} \cdot \vec{E}_{RMS})$  and particle trajectory at 100 V and 500 kHz for a 15  $\mu\text{m}$  diameter particle when particles experience (b) positive (c) negative DEP. 173

**Fig. 11.15.** (a) Schematic of the device at  $\theta=30$ ,  $V=100$ , and frequency=500 kHz. The 175

particles trajectory are shown in red. (b)  $\nabla(\vec{E}_{RMS} \cdot \vec{E}_{RMS})$  on x-y plane at  $z=0$ .

**Fig. 11.16.** Experimental results. Cancer cells are shown in green and WBCs are shown in red. The fluid flow is from left to right. 175

**Fig. 12.1.** A high-throughput cDEP microdevice with parallel sample channels in blue and fluid electrode channels in gray. The throughput of this device is 1 mL/hr. 182

# List of Tables

**Table 2.1.** The important phenomena in electrohydrodynamics and their equations.

50

# Chapter One

## Introduction

There are numerous situations in which it is highly desirable to separate very similar yet distinct cells and/or small organisms with minor differences. Applications include separating stem cells from adipose tissue, removing circulating tumor cells and/or bacteria from blood, and isolating cancer cells based on stage for individualized medicine. Additionally, separating bioparticles allows us to unlock some of the mysteries behind the smallest system level – the cell. In this research, I focused on the isolation of subpopulations of mammalian cells from cell mixtures or body fluids.

Existing cell sorting approaches, such as fluorescence activated cell sorting (FACS) [12], magnetic activated cell sorting [13], and chemically functionalized pillar-based microchips [14], perform based on known receptors expressed on the surface of the membrane. Although a powerful technique, biomarker-based methods rely upon surface marker expression labeling, which is time-consuming and requires special training to implement. The use of biomarkers also requires a priori knowledge, which is not yet available for all cell types. Moreover, irreversible binding of particles to the cells' membrane can permanently disturb the functionality of the cell during isolation, making it difficult to do post-studies [1].

*It is hypothesized that different coupled electrical and mechanical phenomena that occur in cDEP microdevices (such as dielectrophoresis) enable particle-specific manipulation, making it possible to sort subpopulations of cells.*

## **1.1 Isolating subpopulations of cells**

Isolating subpopulations of cells is challenging mostly due to low number of target cells as well as similarity in their size comparing to background cells. For example, cancer stem cells (CSCs) are a subpopulation of cancer cells that have the ability to transplant a new tumor from an existing one. CSCs are thought to be responsible for the metastatic properties of tumors. In the case of pancreatic cancer, less than 1% of cancer cells expressed positive to specific biomarkers and showed significantly high tumorigenic potential, indicating they are CSCs [15]. Moreover, in some applications, cells' subpopulations are similar in size which makes their isolation difficult. For instance, different stages of cancer cells are very similar in size; however they have different phenotype and biophysical properties which enable us to sort them. Sorting different stages of cancer cells in a patient sample and body fluid can play a critical role in cancer early detection and personalized medicine.

## **1.2 Early cancer diagnosis**

Early cancer detection is a critical event for the successful treatment of cancer [16]. Majority of tumors originate from epithelial cells that disseminate from the primary tumor into bodily fluids even at the earliest stages [16]. The key to using circulating tumor cells (CTCs) as predictive clinical biomarkers is their separation and enrichment due to their low concentration in these fluids. For example, in screening for circulating tumor cells (CTCs) to detect cancer, there are only a few CTCs per mL of blood, which includes approximately a billion red blood cells and a million white blood cells. Specifically, it has been reported that there are less than 5 CTCs per 7.5 mL blood detectable using immunomagnetic labeling in patients diagnosed with metastatic breast cancer [17].

Specific tumor cell surface markers required by some approaches may not be known for some cancers, or the individual pattern of genetic or epigenetic alterations in multigenic cancers does

not allow for the use of a single or even multiple-gene product(s) with a sufficient rate of identification. In addition, the expression levels of the involved gene products may not be comparable in all stages, all of which may cause cancer cells with a different genotype to remain undetected, greatly impacting the detection of the disease and individual treatment decisions for various forms of cancers.

### **1.3 Cancer detection from peritoneal fluid**

Ovarian cancer is one of the cancers with high rate of mortality, the leading cause of death from gynecological malignancies in women, which is diagnosed usually in late stages. Ovarian cancer cells exfoliate from the primary tumor and disseminate throughout the peritoneal cavity. The changing peritoneal microenvironment, characterized by increasing numbers of immune cells, mostly monocytes/macrophages [18], and increased protein and bioactive lipid levels in the ascites fluid [19, 20] promotes tumor cell survival, proliferation and metastasis. Ascites fluid can also contain benign cell populations of macrophages and fibroblasts [18, 21]. The percentage of tumor cells versus non-tumor cells can vary greatly in women from 1 to >60% [22]. Because of the different physical characteristics of these cells, it is theorized that resident and recruited peritoneal cells can be separated from ovarian cancer cells. Unlike cancers of other sites, ovarian cancer cells rarely enter systemic distribution. Thus, the peritoneal fluid is the appropriate source for detection of disseminating ovarian cancer cells.

The primary challenge is the detection of the ovarian cancer at an early stage since this increases drastically the survival rate. Fig. 1.1. presents the relative 5-year survival rate of ovarian cancer. Traditionally, specific biomarkers expressed mainly by the target tumor cell population are used to isolate cells from each other. CA-125, the most popular biochemical marker for ovarian cancer, is found in 50% of early stage patients and 80% of late stage patients [23]. Other markers can vary greatly. Detection techniques include, ultrasound and color-flow Doppler imaging,

using morphological and vascular markers respectively [23]. Recently, proteomics has become a promising means by which new potential biomarkers are identified.

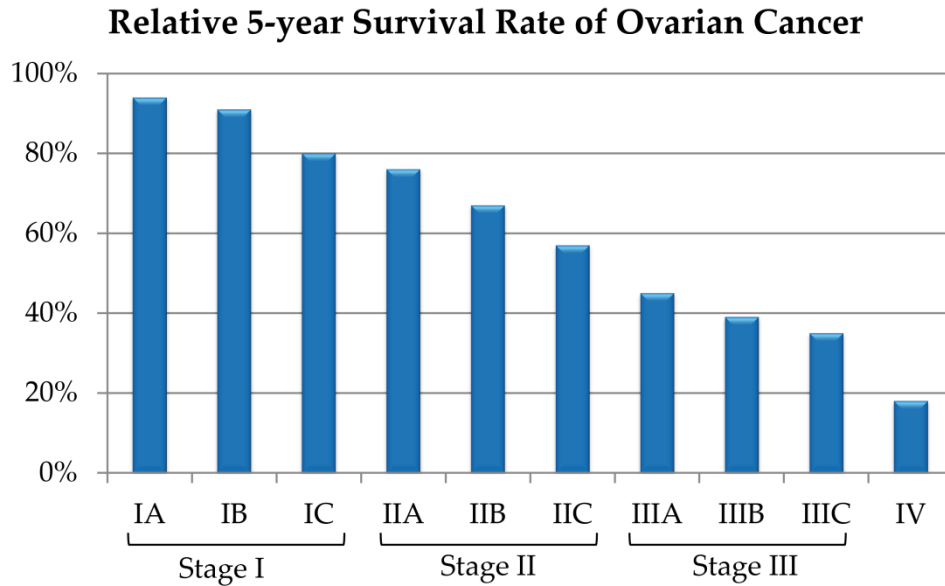


**Fig. 1.1.** Relative 5-year survival rate of ovarian cancer. Adapted from [1].

#### 1.4 Cancer Stem Cells (CSCs)

Cancer stem cells (CSCs), also known as tumor initiating cells (TICs), are cells within a tumor possessing the ability to generate a new tumor from an existing one and are generally present in very low concentrations compared to normal cancerous cells [24]. Normal stem cells and cancer stem cells possess similar attributes that suggest a common origin (reviewed in [24]). Like normal stem cells, cancer stem cells possess self-renewal capabilities. Additionally, some data suggest that the bulk of a tumor is generated from a finite number of cells that possess extended replicative capacity. Some of the crucial biological applications of CSCs include development of animal models of carcinogenesis and understanding metastasis and other key biological processes [25]. A major critical issue in current cancer treatment methods is that a fraction of

malignant cells survive chemotherapy and radiation. There is evidence suggesting that these surviving cells possess tumor initiating capabilities responsible for their therapeutic resistance [25]. Isolation and identification of this rare cell subpopulation is the first step towards development of targeted strategies to ablate this cell population.

The use of non-invasive methods to detect and enrich CSCs independent of their genotype is critical for diagnostic and treatment purposes. Current efforts in this direction are hampered by the lack of a suitable high throughput and rapid method to isolate these cells [26-28]. Specifically about the prostate cancer, which is the focus of this study at Chapter Seven, previous works with human prostate cancer cell lines and with primary human prostate samples have identified several markers for CSCs. These markers include increased expression of cell surface proteins such as CD133, CD44, and  $\alpha 2\beta 1$  integrin. Data from other tissue types also support the use of aldehyde dehydrogenase (ALDH), which can be measured by a fluorescent substrate, as a marker for CSCs. It has been shown that the number of ALDH positive cells increases in tumor derived samples, consistent with its expression being associated with CSCs [29, 30]. In addition to the tumor epithelium in adenocarcinoma of the prostate, there are also infiltrating activated stromal cells, as well as vascular endothelium and other stromal components that make up the bulk of the tumor. This complexity is typically increased with a mixture of benign glands intermixed with the carcinoma.

## **1.5 Dielectrophoresis (DEP)**

Dielectrophoresis (DEP), the motion of a particle due to its polarization in the presence of a non-uniform electric field, can be used to differentiate between cells based on their intrinsic properties [31]. The important advantage of this technique is that no assumptions regarding the cells' genetic make-up are necessary. Instead, DEP relies upon the cells' biophysical properties, which are closely aligned with the propensity of the abnormal cell to migrate from its natural environment, an early step in metastatic disease [32].

Several DEP applications to selectively concentrate specific cell populations have been effectively demonstrated based on their size, shape, internal structure, and electrical properties such as conductivity and polarizability. A few pertinent examples include the separation of human leukemia cells from red blood cells in an isotonic solution [33], entrapment of human breast cancer cells from blood [34], separation of human monocytic cells from peripheral blood mononuclear cells (PMBC) [6], separation of bacteria from blood [35], and separation of cancer cells from CD34+ hematopoietic stem cells [36]. This technique has also been used to separate neuroblastoma cells from HTB glioma cells [6], isolate cervical carcinoma cells [37], isolate K562 human CML cells [38], separate live yeast cells from dead [39], and isolate mammalian cells based on their cell-cycle phase [40, 41].

## **1.6 Contactless Dielectrophoresis (cDEP)**

Although DEP has been a very successful technique, its drawbacks include electrolysis, electrode delamination, and expensive fabrication [42, 43]. In this research a relatively new technique, known as contactless dielectrophoresis (cDEP), is used which capitalizes on the sensitivity of dielectrophoresis while eliminating many of its challenges.

In cDEP, an electric field is created in the sample microchannel using electrodes inserted into two electrode channels (filled with conductive solution), which are separated from the sample microchannel by thin insulating barriers. These insulating barriers exhibit a capacitive behavior and therefore an electric field can be produced in the sample channel by applying an AC field across the barriers. The absence of contact between electrodes and the sample fluid inside the channel prevents bubble formation and avoids any contaminating effects the electrodes may have on the sample. Moreover, through the use of cDEP, the search strategy isolates and enriches rare cells while maintaining cell viability. The absence of electrochemical contamination makes cDEP an ideal “isolate-and-culture” platform to investigate the biological processes of sorted cells.

## 1.7 Overview

In the remainder of this dissertation, the details of the different electrokinetics phenomena as well as the governing equations of the movement of suspended particle in an electric field will be presented in Chapter Two. In Chapter Three, the fabrication process, experimental setup, electronics utilized in this study, methods of analysis of data, cell culturing, cell and blood preparation, and immunofluorescence assay imaging are explained. Also the computational modeling and the applied boundary conditions are explained in this chapter. I believe that multiphysics modeling that couples dielectrophoretic effects with the motion of cells through a fluid will allow prediction of system behavior leading to more efficient device.

The electrical properties of four different stages of mouse ovarian surface epithelial (MOSE) cells are investigated using cDEP, in Chapter Four. I found that the specific membrane capacitance increased as the stage of malignancy advanced from a non-malignant benign stage to the most aggressive stage. This study is the first to report the crossover frequency and cell specific membrane capacitance of different stages of cancer cells that are derived from the same cell line. In Chapter Five, I use DEP to investigate the effect of non-toxic concentrations of two bioactive sphingolipid metabolites, sphingosine (So), with potential anti-tumor properties, and sphingosine-1-phosphate (S1P), a tumor-promoting metabolite, on the intrinsic electrical properties of early and late stages of MOSE cancer cells. I present an association between So treatment and a shift in the bioelectrical characteristics of late stage MOSE (MOSE-L) cells towards a profile similar to that of benign MOSE-E cells. This work is the first to indicate that treatment with non-toxic doses of So correlates with changes in the electrical properties and surface roughness of cells. It also demonstrates the potential of cDEP to be used as a new, rapid technique for drug efficacy studies, and eventually designing more personalized treatment regimens.

In Chapter Six, I investigate the dielectrophoretic responses of progressive stages of MOSE cells, as well as mouse fibroblast, and macrophages cell lines, representing normal and inflammatory cells found in the peritoneal fluid, utilizing cDEP. I compared the signal parameters required to selectively capture and isolate MOSE cells at different cancer stages from normal fibroblast and macrophages. These results demonstrate the potential of cDEP as a method of early detection and diagnosis of ovarian cancer.

In Chapter seven, I showed that CSCs and non-CSCs have different dielectrophoretic properties [9]. Aldehyde dehydrogenase (ALDH) marker was used to isolate prostate cancer cell line (PC3) CSCs and non-CSCs through FACS. Then, the dielectrophoretic responses of ALDH+ (CSCs) and ALDH- (non-CSCs) were investigated by cDEP microdevices. I showed that complete trapping of prostate CSCs occurs at a lower voltage than that needed for complete trapping of non-CSCs. Then, I enriched ALDH+ cells (CSCs) by selectively trapping ALDH+ cells while letting all ALDH- cells flow due to the difference in their dielectrophoretic properties. The collected samples of ALDH+ and ALDH- cells as well as non-sorted cells were cultured separately to study their capabilities to form spheroids. Based on the spheroid culturing results, the average size of the cDEP enriched ALDH+ spheroids was larger than cDEP enriched ALDH- cells spheroids, indicating that isolated cells were indeed initiating cells.

Chapter Eight presents the separation and enrichment of circulating tumor cells from blood. The results of Chapters Five to Eight are consistent with the hypothesis that different cell types have different electrical properties and target cells can be isolated from a cells mixture or background flow based on the their unique dielectric properties.

In Chapters Nine and Ten particles manipulation, instead of cells', has been described. In Chapter Eight, the first experimental evidence of mixing enhancement in a microfluidic system using cDEP is presented. When the time scales of the bulk fluid motion and the dielectrophoretic motion were commensurate, rapid mixing was observed. Four system designs with rectangular

and circular mixing chambers were tested and it was found that the rectangular mixing chambers were found to be more efficient than the circular chambers. This approach shows potential for mixing low diffusivity biological samples, which is a very challenging problem in laminar flows at small scales. In Chapter Ten, AC field was applied in a microfluidic device to manipulate particles and to study different AC electrokinetic phenomena. Particle tracking velocimetry (PTV) was used to measure the velocity of particles and their trajectories. I studied experimentally and computationally the effects of AC-electroosmosis, dielectrophoresis, and electrothermal and their relative importance. I showed that dielectrophoresis and electrothermal effects are negligible in our study while AC-EO is the dominant phenomena.

Chapter Eleven presents multilayer cDEP devices which provide continuous sorting, in contrast to all previous Chapters which presented batch sorting. This chapter demonstrates some analytical simulation to predict electric field and DEP force inside the sample channels. Then, computational modeling is used for parametric study of various electrical and geometrical parameters to optimize the design. At the end the multilayer devices are used to separate cancer cells from white blood cells.

Chapter Twelve covers the proposed future work and is mostly focused on advancing our understanding of the biophysical properties of cells and improving the selectivity and throughput of cDEP microdevices. I propose to use the improved devices for important applications such as isolating CSCs for animal studies and investigating the electrical properties of cancer cells after treating with drugs.

# Chapter Two

## Theory

### 2.1 Introduction

Electrohydrodynamics is a branch of fluid mechanics that focuses on the effects of an electrical force on a fluid. It can also be thought of as a part of electrodynamics involving the influence of fluid flow on an electric field. Electrohydrodynamics can be considered as a combination of both of these areas as electrohydrodynamics involves both the effect fluid motion on an electric field and the influence of an electric field on fluid flow [44].

Manipulating particles in a fluid suspension has many biological applications (such as manipulation of blood cells in a blood sample [45, 46]), chemical systems [47], medicine (such as drug delivery) [48, 49], and electronics (such as single-electron transistors and nanoparticle memory and antenna array manipulation [50]). It is also important that particle manipulation be precisely controllable, fast, and affordable. In this regard, manipulation of both organic and nonorganic particles, including viruses, bacteria, and cells have been reported. Different techniques including chemical [51, 52], electrothermal [53, 54], mechanical [46, 55, 56], acoustic [57, 58], optical [59-61], magnetic [62, 63], and electrical [64-67], as well as their combinations [62, 68-70] have been used to accurately manipulate particles.

Development in integrated circuit microfabrication techniques have played an important role in improving the MEMS fabrication techniques and making the use of electrokinetic techniques more prevalent. Understanding the different electrokinetic techniques and their advantages and limitations enables us to use them more efficiently. These electrical techniques can be divided into subcategories including electrowetting [70], electroosmotic [68], electrostatic [64, 66], electrophoresis [71-73], and dielectrophoresis (DEP) [74]. Each of these electrokinetic

techniques has its own advantages and limitations. For instance electrothermal (ET) techniques affect the bulk of the fluid while electroosmosis only affects the fluid near electrodes and boundaries. Different phenomena can exist simultaneously, for example DEP, AC-EO, and AC-ET. Which one is dominant depends on the applied voltage and frequency, geometry of the microdevice, conductivity and permittivity of the sample, and the size of the suspended particles. These techniques and their differences will be explained in greater detail later in this chapter

Electrical techniques can be divided into two categories based on whether AC or DC electric fields are applied. AC electrokinetics is a well-established technique for particle manipulation [75, 76]. One of the advantages compared to DC electrokinetics is that in a DC field the magnitude of the flow induced by EO depends on the applied voltage and the charge density. However in AC field, it depends on many parameters including applied frequency, permittivity and conductivity [76]. As another advantage is that AC-EO micropumps work at a lower applied voltage than DC-EO micropumps [76]. We focused mostly on AC electric field in this research.

In this chapter, first the Navier-Stokes equations in a microscale system are presented. Then, it is shown that electrical, mechanical, and thermal equations can be decoupled. Lastly, different electrokinetic phenomena will be presented with an overview of the applied equations on each phenomenon. Other forces that can be applied on a suspended particle will also be presented.

## **2.2 Navier-Stokes equations**

In almost all of the electrokinetics applications it is required to have the particles suspended in a fluid. This makes studying fluid mechanics essential to understand and utilize electrokinetics in a better way. We need to study fluid flow in microsystems to understand the effect of the flow on particles movements and also to move fluid for specific applications, such as micropumping [76].

It has been shown by others that the order of magnitude of the relative pressure is proportional to the square of the ratio of the velocity of the flow to the velocity of sound in the fluid [77]. The velocity of flow in microfluidic systems is usually less than 1 mm/s and the speed of sound in water at 30 C is about 1500 m/s, thus the pressure change is ignorable in microfluidic systems and the flow can be assumed incompressible. The Navier-Stokes equations for an incompressible fluid can be written as:

$$\vec{\nabla} \cdot \vec{v} = 0 \quad (1.1)$$

$$\rho_m \left( \frac{\partial v}{\partial t} + (\vec{v} \cdot \vec{\nabla}) \vec{v} \right) = -\vec{\nabla} p + \eta \nabla^2 \vec{v} + \vec{F}_{ext} + \rho_m \vec{g} \quad (1.2)$$

In this study  $\vec{F}_{ext}$  is given by electrokinetic forces. Reynolds number, defined as the ratio of convection (inertia term) to viscous effects, is usually very low in microfluidics applications

$$Re \equiv \frac{\rho_m v l}{\eta} \quad (1.3)$$

where  $\rho_m$  and  $\eta$  are the density and viscosity of the medium, respectively,  $v$  is the velocity, and  $l$  is the length scale. Considering  $v$  in the order of 100  $\mu\text{m/s}$  and  $l$  in the order of 100  $\mu\text{m}$ , Re number will be in the order of  $10^{-2}$ , which is very small and the flow is very laminar. Thus, the convective term in the Navier-Stokes equation is ignorable.

Also, comparing the time dependent and viscous terms, the required time to reach steady state condition can be estimated as

$$t = \frac{\rho_m l^2}{\eta} \quad (1.4)$$

which is in the order of  $10^{-2}$ . Thus, the time dependent term in the Navier-Stokes equation is also negligible.

### 2.3 Electrical Reynolds number

Studying the Maxwell's electromagnetic equations is out of the scope of this research. However, very briefly we show that the electrical equations are decoupled from the mechanical equation. Electrical Reynolds number is defined as the ratio of a charge-relaxation time to a time for the fluid to move a characteristic length  $l$  at the characteristic velocity  $v$  [44].

$$Re_{electrical} = \frac{|\nabla \cdot (\epsilon \vec{E}) \vec{v}|}{|\sigma \vec{E}|} \approx \frac{\epsilon / \sigma}{l / v} \quad (1.5)$$

Electrical Reynolds number can also be interpreted as the ratio of conduction current to convection current [44, 75].

For a typical microfluidic problem  $v$  is in the order of 100  $\mu\text{m/s}$ ,  $l$  is in the order of 100  $\mu\text{m}$ , and  $\sigma$  is about 0.01 S/m, thus the electrical Reynolds number is in the order of  $10^{-7}$ . This means that the velocity of the charge in response to electric field is much larger than the fluid velocity [76], which means that the electrical equations are decouples from mechanical equations [44].

### 2.4 Electrical forces

It has been shown by [53] and [76] that the time-averaged electrical body force can be written as:

$$f_E = \frac{1}{2} Re \left[ \left( \frac{(\sigma \nabla \epsilon - \epsilon \nabla \sigma) \cdot \vec{E}}{\sigma + i\omega \epsilon} \right) \vec{E} - \frac{1}{2} |\vec{E}|^2 \nabla \epsilon \right] \quad (1.6)$$

where  $\vec{E}$  is the applied electric field voltage, and  $\omega$  is the applied frequency. In this equation  $f_E$  is defined as the permittivity and conductivity gradients, which can also be written in terms of temperature gradients as  $\nabla \epsilon = (\partial \epsilon / \partial T) \nabla T$  and  $\nabla \sigma = (\partial \sigma / \partial T) \nabla T$ . Then, the electrical body force can be written as:

$$f_E = \frac{1}{2} Re \left[ \frac{\varepsilon(\alpha - \beta)}{1 + (\omega\tau)^2} (\nabla T \cdot \vec{E}) \vec{E} - \frac{1}{4} \varepsilon \alpha |\vec{E}|^2 \nabla T \right] \quad (1.7)$$

where  $\tau$  is the charge relaxation time,  $\varepsilon/\sigma$ ,  $\alpha = (\partial\varepsilon/\partial T)/\varepsilon$  1/K, and  $\beta = (\partial\sigma/\partial T)/\sigma$  1/K. The first term on right hand side of this equation is the Coulomb force and the other term is the dielectric force. At low frequencies Coulomb force is dominant and at high frequencies the dielectric force [76]. For an aqueous electrolyte solution variations in conductivity are usually much greater than the variations in permittivity;  $\alpha \approx -0.004$  1/K and  $\beta \approx 0.02$  1/K [78].

## 2.5 Dielectrophoresis

Dielectrophoresis (DEP), the motion of particles due to polarization in a non-uniform electric field, is a nondestructive noninvasive particle manipulation technique. One of the advantages of DEP is that it does not rely only upon particle size, but it also depends upon the intrinsic electrical properties of the particle which makes it possible to separately manipulate similarly sized particles that have different intrinsic electrical properties. The magnitude and direction of the DEP force depends upon the size, conductivity, and permittivity of the particle, the conductivity and permittivity of the media, and the applied voltage and frequency. It is also a popular technique due to the ease of integration with other microfluidic systems and the ability to generate both positive and negative forces. DEP has been shown to be a successful particle manipulation technique that can be used for mixing [11], separation [79-81], enrichment [36, 82], detection [83], and characterization [84, 85].

When a neutral particle is placed in a non-uniform electric field, the positive and negative charges move to form the interfacial charge layer [86]. The movement of the charges creates the electrical double layer around the cell and gives the cell the properties of a dipole which is explained in more details below.

To study the physics of a polarized particle in an electric field, first we should study the physics of a dipole. A dipole consists of two opposite charges,  $q$ , separated by a distance  $\vec{d}$ . Within a uniform electric field a dipole will rotate while a non-uniform electric field will induce a force that can cause movement. The dipole moment,  $\vec{p}$ , can be defined as a vector pointing from the negative to the positive charge:

$$\vec{p} = q\vec{d} \quad (1.8)$$

The dipole moment has units of Coulomb-meter or Debye. The dipole moment of a 5  $\mu\text{m}$  cell is in the order of  $2.5 \times 10^5$  Debye [86]. The force a dipole experiences in an electric field,  $\vec{E}$ , can be approximated by applying the Taylor series approximation

$$\begin{aligned} \vec{F} &= q\vec{E}(\vec{r} + \vec{d}) - q\vec{E}(\vec{r}), \\ \vec{E}(\vec{r} + \vec{d}) &\cong \vec{E}(\vec{r}) + (\vec{d} \cdot \nabla)\vec{E}(\vec{r}) \\ \vec{F} &= q\vec{E}(\vec{r}) + q(\vec{d} \cdot \nabla)\vec{E}(\vec{r}) - q\vec{E}(\vec{r}) = (q\vec{d} \cdot \nabla)\vec{E}(\vec{r}) = (\vec{p} \cdot \nabla)\vec{E}(\vec{r}) \end{aligned} \quad (1.9)$$

and the torque which works to align the dipole with the electric field is

$$\vec{\Gamma} = \frac{\vec{d}}{2} \times q\vec{E} + \frac{-\vec{d}}{2} \times (-q\vec{E}) = \vec{p} \times \vec{E}. \quad (1.10)$$

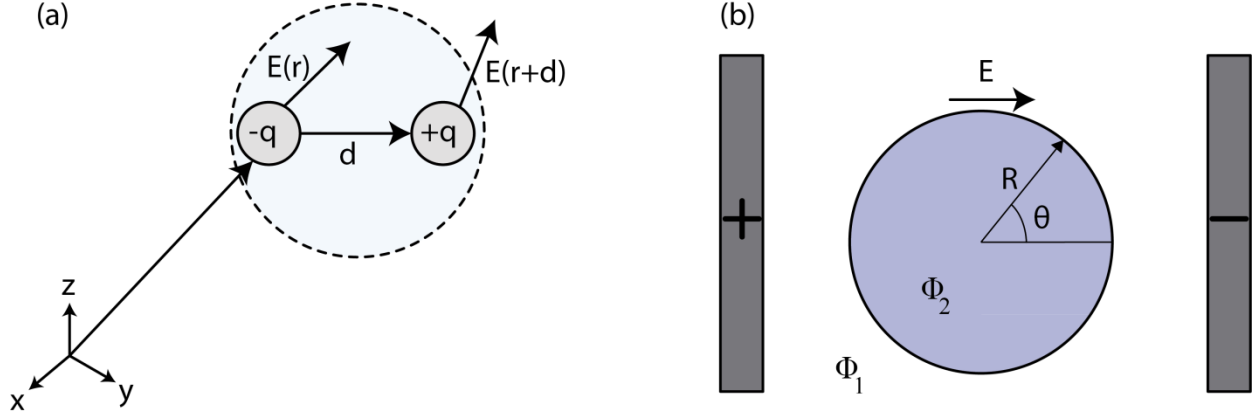


**Fig. 2.1.** (a) Schematic of a dipole. (b) Schematic of a sphere in an electric field

**Effective Dipole Moments of Lossless Dielectric Particles:** When a neutral spherical particle is suspended in a medium and a uniform electric field is applied,  $\vec{E}$ , the Laplace equation must be satisfied. By assuming the particle is a dielectric, meaning that it is polarizable in an electric field, and that it is lossless, that there is no lag between the electric field and the induced dipole, the solution inside and outside of the particle can be written as [87]

Outside 
$$\Phi_1(r, \theta) = -Er \cos \theta + \frac{A \cos \theta}{r^2}, r > R \quad (1.11a)$$

Inside 
$$\Phi_2(r, \theta) = -Br \cos \theta, r < R \quad (1.11b)$$

where  $E$  is the magnitude of the electric field,  $R$  is the particle's radius, and  $r$  and  $\theta$  are the spherical coordinates as is shown in Fig. 2. 1. The boundary conditions (BC) can be written as follows.

The radial component of the displacement flux vector,  $\epsilon E_{\text{radial}}$ , should be continuous, meaning

BC1 
$$\epsilon_1 \left( -\frac{\partial \Phi_1}{\partial r} \right) = \epsilon_2 \left( -\frac{\partial \Phi_2}{\partial r} \right)$$

The electrostatic potential is continuous across the boundary, resulting in

$$\text{BC2} \quad \Phi_1 = \Phi_2$$

where  $\epsilon_1$  and  $\epsilon_2$  are the permittivity of medium and particle respectively. The constants A and B can be found as

$$A = \frac{\epsilon_2 - \epsilon_1}{\epsilon_2 + 2\epsilon_1} R^3 E$$

$$B = \frac{3\epsilon_1}{\epsilon_2 + 2\epsilon_1} E$$

On the other hand, the electrostatic potential around a dipole moment of magnitude  $p$  in a dielectric medium of permittivity  $\epsilon_1$  can be written as [87]

$$\Phi = \frac{p_{eff} \cos \theta}{4\pi\epsilon_1 r^2} \quad (1.12)$$

Combining equations (1.11a) and (1.12), the effective dipole moment on a circular particle becomes[76]

$$p_{eff} = 4\pi\epsilon_1 A = 4\pi\epsilon_1 \left( \frac{\epsilon_2 - \epsilon_1}{\epsilon_2 + 2\epsilon_1} \right) r^3 E \quad (1.13)$$

$\frac{\epsilon_2 - \epsilon_1}{\epsilon_2 + 2\epsilon_1}$  is defined as the Clausius-Mossotti (CM) factor,  $f_{CM}$

$$f_{CM} = \frac{\epsilon_2 - \epsilon_1}{\epsilon_2 + 2\epsilon_1} \quad (1.14)$$

In the case of AC field with an applied frequency of  $\omega$ , harmonic potential can be defined as

$$\varphi(\vec{x}, t) = \text{Re}\{\varphi(x)e^{i\omega t}\} \quad (1.15)$$

And consequently

$$\vec{E}(\vec{x}, t) = \text{Re}\{E(x)e^{i\omega t}\} \quad (1.16)$$

Then, the time average DEP force can be written as

$$\vec{F}_{DEP} = \frac{1}{2} \text{Re}\{(\vec{p} \cdot \nabla)E^*\} \quad (1.17)$$

Where

$$\vec{p} = 4\pi\epsilon_1 r^3 f_{CM} \vec{E} e^{i\omega t} \quad (1.18)$$

The time average DEP force can be written as

$$\vec{F}_{DEP} = 4\pi\epsilon_m r^3 \text{Re}\{f_{CM}(\omega)\} \vec{E} \cdot \nabla \vec{E} = 2\pi\epsilon_m r^3 \text{Re}\{f_{CM}(\omega)\} \nabla(\vec{E} \cdot \vec{E}) \quad (1.19)$$

**Lossy Dielectric Particle in an AC Electric Field:** Particles that are not perfectly insulating in an AC electric field have a different behavior. The permittivity of these particles is a function of the applied frequency and is defined as a complex function [87]

$$\epsilon^* = \epsilon - j \frac{\sigma}{\omega} \quad (1.20)$$

And the Clausius-Mossotti function is rewritten as a complex function as well

$$f_{CM}(\epsilon_1^*, \epsilon_2^*) = \left( \frac{\epsilon_2^* - \epsilon_1^*}{\epsilon_2^* + 2\epsilon_1^*} \right) \quad (1.21)$$

**Lossy Dielectric Sphere in an AC Electric Field, Charge Relaxation:** There is a delay for dipole moment of an imperfect insulating particle in an instantaneous field. On the other hand, the dipole moment exhibits a phase lag in an AC field. The ratio between polarizability and

depolarization ability are two important factors affect the delay lag which is defined as follows (adopted from Holmes' thesis [87]):

$$\text{charge relaxation time } \tau = \frac{\epsilon}{\sigma}$$

Thus the complex form of the Clausius-Mossotti factor can be rewritten as

$$f_{CM}(\epsilon_1^*, \epsilon_2^*) = \left( \frac{\sigma_2 - \sigma_1}{\sigma_2 + 2\sigma_1} \right) \left[ \frac{j\omega\tau_0 + 1}{j\omega\tau_{MW} + 1} \right] \quad (1.22)$$

Where  $\tau_{MW}$  is the Maxwell-Wagner relaxation time corresponding to the free charge at the particle-medium interface and  $\tau_0$  is a constant [88].

$$\tau_{MW} = \left( \frac{\epsilon_2 + 2\epsilon_1}{\sigma_2 + 2\sigma_1} \right) \quad (1.23a)$$

$$\tau_0 = \left( \frac{\epsilon_2 - \epsilon_1}{\sigma_2 - \sigma_1} \right) \quad (1.23b)$$

When two dielectric materials with different conductivities and/or permittivities are in contact with each other, for instance a particle suspended in a fluid, charges will gather at the interface. If an electric field is applied the positive and negative charges will separate, this process is known as polarization. This polarization acts as an effective dipole moment which is dependent upon the applied electric field frequency and the properties of the particle and the suspending fluid. In frequencies in the order of a few Hz, particles move due to electrophoresis. The direction of movements changes due to using AC electric field. However, by increasing the frequency over around 1 kHz, cells reversed movement vanishes and no electrophoresis effect will be observed [86].

**DEP force:** Depending on the sign of  $f_{CM}$ , given by equation (1.21), the DEP force can either be positive, in which case it is directed towards the strongest part of the electric-field region, or

negative, in which case it is directed towards the weakest part of the field. This dependence is related to the polarizability of the particle with respect to the surrounding medium which is explained in more depth below.

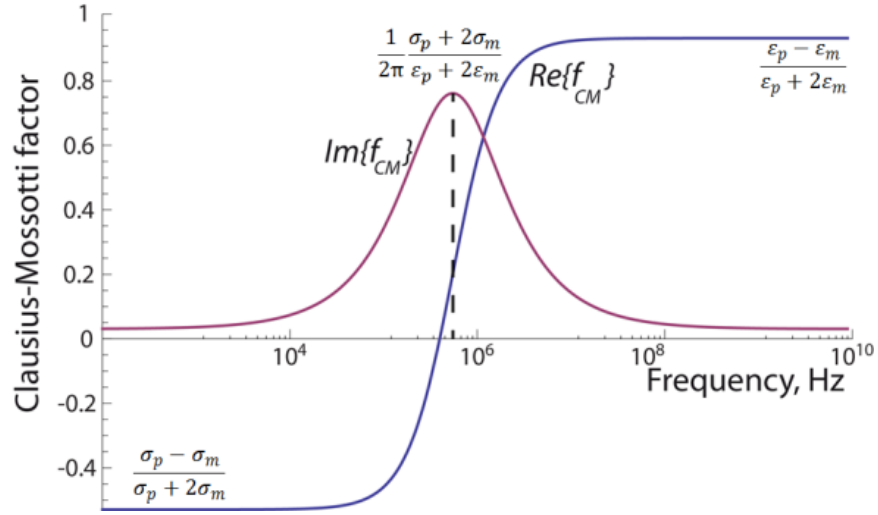


**Fig. 2.2.** Real and Imaginary parts of Clausius-Mossotti factor of a particle.

**Multi-Shell Models:** Because biological particles have a complicated internal structure, there are some models that can predict their dielectric properties more accurately than others, however each model type has its own set of limitations. One of these models is the multi-shell model [89]. In this model the membrane of the bioparticles, the nucleus, and even the nucleus membrane can be considered. The single shell model is mathematically simpler allowing for greater ease of calculation however it achieves that by neglecting the complicated internal structure of a biological particle.

**Single Shell Model:** In the single shell model only the bioparticles' thin lipid membrane and the internal cytoplasm are considered. Thus,  $f_{CM}$  can be written as

$$\varepsilon_p^* = \varepsilon_2^* \frac{\gamma_{12}^3 + 2 \left( \frac{\varepsilon_3^* - \varepsilon_2^*}{\varepsilon_3^* + 2\varepsilon_2^*} \right)}{\gamma_{12}^3 - \left( \frac{\varepsilon_3^* - \varepsilon_2^*}{\varepsilon_3^* + 2\varepsilon_2^*} \right)} \quad (1.24)$$

where  $\gamma_{12}^3 = r_1/r_2$  and  $r_1 = r_2 + d$ ,  $d$  is the thickness of the membrane,  $r_1 \gg d$ . The conductivity of the membrane is much lower than the surrounding medium. For frequencies well below dispersion ( $\sim 1$  MHz [90]), we can write [91]

$$\frac{\varepsilon_3^* - \varepsilon_2^*}{\varepsilon_3^* + 2\varepsilon_2^*} \cong 1 \quad (1.25)$$

Then,  $\varepsilon_p^*$  can be written as

$$\varepsilon_p^* = \varepsilon_2^* \frac{\left( \frac{1}{1-d/r_1} \right)^3 + 2}{\left( \frac{1}{1-d/r_1} \right)^3 - 1} \cong \varepsilon_2^* \frac{r_1 + d}{d} \cong \varepsilon_2^* \frac{r_1}{d} \quad (1.26)$$

The effective permittivity of a cell can be also written as a function of the relaxation times of the membrane,  $\tau_2 = \frac{C_{mem}r}{\sigma_3}$  and cytoplasm,  $\tau_3 = \frac{\varepsilon_3}{\sigma_3}$  by taking the assumption that the membrane is very thin [87, 92]

$$\varepsilon_p^* \cong C_{mem}r \frac{j\omega r \tau_3 + 1}{j\omega(\tau_2 + \tau_3) + 1} \quad (1.27)$$

where  $\sigma_3$  and  $\varepsilon_3$  are the conductivity and permittivity of the cytoplasm, respectively. The Clausius-Mossotti factor can be written as

$$f_{CM}(\omega) = - \frac{\omega^2(\tau_1\tau_2 - \tau_3\tau_2') + j\omega(\tau_2' - \tau_1 - \tau_2) - 1}{\omega^2(\tau_3\tau_2' + 2\tau_1\tau_2) - j\omega(\tau_2' + 2\tau_1 + \tau_2) - 2} \quad (1.28)$$

where  $\tau_1 = \frac{\varepsilon_1}{\sigma_1}$  and  $\tau_2' = \frac{C_{mem}r}{\sigma_1}$ .

The single shell model assumes a simpler cellular structure than is actually present and while successful and simple for predicting a cell line's biophysical properties, will deviate from experimental results at times [93]. To be explicit, the single shell model assumes a thin and spherical surrounding membrane and a spherical and homogenous interior. Thus it does not take into account the membrane inhomogeneity, cytoplasm, and nuclear structural features which limits its ability such that it cannot correlate the membrane morphological complexity with the specific membrane capacitance  $C_{mem}$ , [94].

In the two-shell model the nucleus is added as an additional layer. However, it is worth noting that the membrane of the nucleus is considered as a thin membrane, not always a realistic assumption.  $\epsilon_3^*$  in equation (1.21) will be replaced by

$$\epsilon_{34}^* = \epsilon_3^* \frac{\gamma_{23}^3 + 2 \left( \frac{\epsilon_4^* - \epsilon_3^*}{\epsilon_4^* + 2\epsilon_3^*} \right)}{\gamma_{23}^3 - \left( \frac{\epsilon_4^* - \epsilon_3^*}{\epsilon_4^* + 2\epsilon_3^*} \right)} \quad (1.29)$$

where  $\gamma_{23}^3 = r_2/r_3$ . Using a multi-layer model, the changes in the physical properties of the cells due to malignancy or invasion by pathogens [76] can be studied as the internal structure is being considered.

One of the limitations of this multi-shell model is that it deviates from experimental results since membrane inhomogeneity, cytoplasm, and nuclear structural features are neglected [94]. It also assumes the cell membrane is thin and spherical. Last, the surface charge effects cannot be captured. There are many groups working to further develop the cell model so that it will better reflect actual cell geometry and predict experimental results.

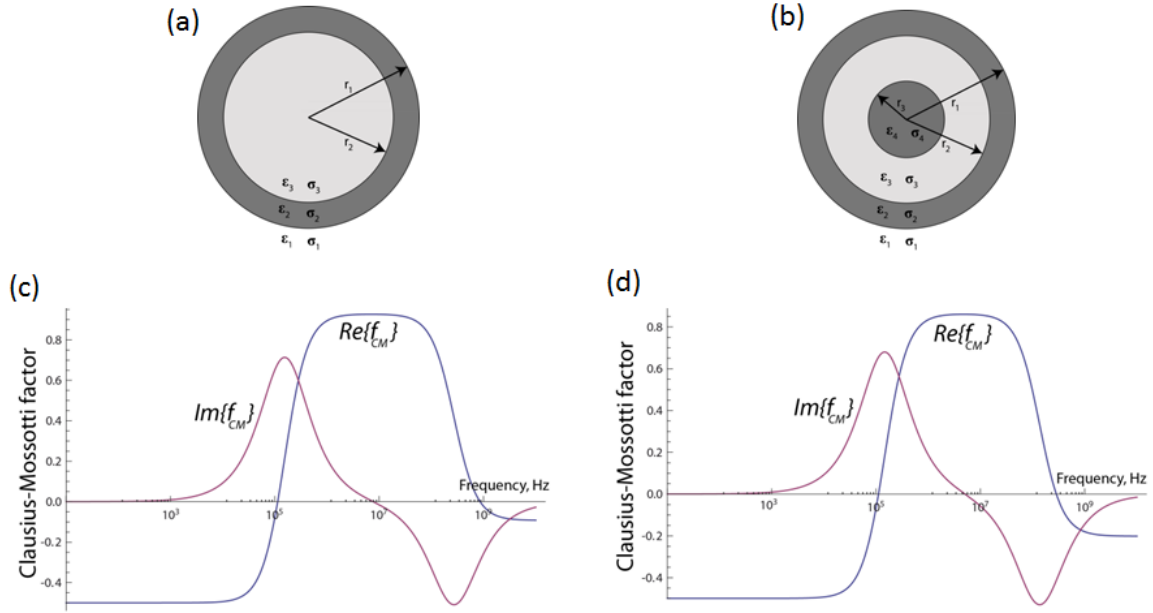


**Fig. 2.3.** Schematic of (a) single- and (b) two-shell models. The real and imaginary parts of the Clausius-Mossotti factor as a function of frequency for (c) single- and (d) two-shell models.

Then, for a spherical particle  $Re\{f_{CM}(\omega)\}$  can be written as [6]

$$Re\{f_{CM}(\omega)\} = \frac{\omega^2 \tau_{MW}^2}{1 + \omega^2 \tau_{MW}^2} \left( \frac{\epsilon_p - \epsilon_m}{\epsilon_p + 2\epsilon_m} \right) + \frac{1}{1 + \omega^2 \tau_{MW}^2} \left( \frac{\sigma_p - \sigma_m}{\sigma_p + 2\sigma_m} \right) \quad (1.30)$$

In low frequencies,  $\omega \tau_{MW} \ll 1$ , it can be reduced to

$$Re\{f_{CM}(\omega)\} = \frac{\sigma_p - \sigma_m}{\sigma_p + 2\sigma_m} \quad (1.31)$$

For cells the low frequency condition is applicable for frequencies less than about 10 kHz in a low conductivity medium ( $\sim 100 \mu\text{S/cm}$ ) in which the plasma membrane of the cell acts as an electrical insulator. Thus, cells behave as an insulator suspended in a conducting media [95] meaning that the conductivity of the cell is less than the medium and cell polarizes in opposite

direction to the electric field (see Fig. 2.4(a)). From equation (1.21), DEP force is negative for low frequencies.

At high frequencies,  $\omega\tau_{MW} \gg 1$ ,  $Re\{f_{CM}(\omega)\}$  can be estimated as

$$Re\{f_{CM}(\omega)\} = \frac{\epsilon_p - \epsilon_m}{\epsilon_p + 2\epsilon_m} \quad (1.32)$$

For cells the high frequency condition is applicable for frequencies greater than about 100 kHz. Above that frequency the permittivity of the cell becomes larger than the permittivity of the medium due to interfacial polarization of the membrane surfaces, for instance the endoplasmic reticulum, nucleus, and mitochondria [95]. From equation (1.21), the DEP force on a cell becomes positive at high frequencies. Also the conductivity of the cell will be greater than the medium due to the presence of insulating bodies and structures such as the cytoskeleton and the lipid membrane [95]. This means that the electric field penetrated into the cell and the cell polarizes in the same direction as the field [95] (see Fig. 2.4(a)).

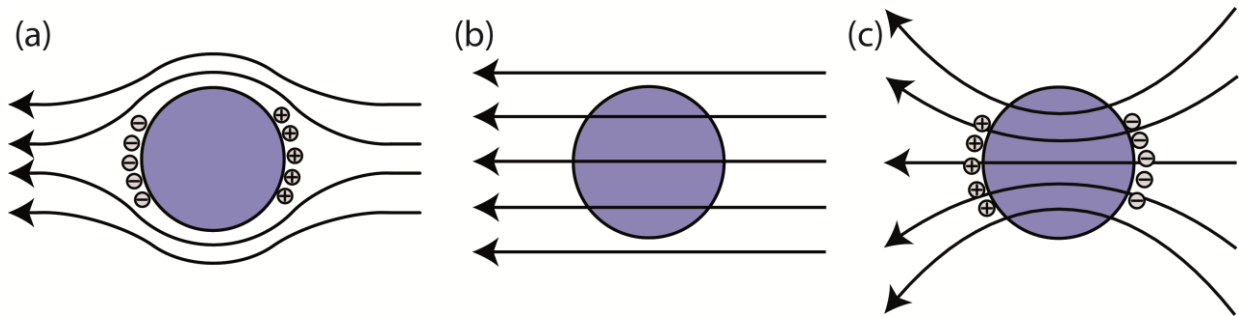


**Fig. 2.4.** Polarity of mammalian cells changes by changing the frequency. (a) At low frequencies cells behave as an electrically insulating particle. (b) At the crossover frequency the induced dipole moment of the cell is zero and the cell behaves as being transparent to the electric field. (c) At high frequencies cells are more polarizable than the suspending medium and the field penetrates inside the cell. Adapted from [95].

Fig. 2.5 demonstrates modeling a suspended cell in a flow between two electrodes. In this model the cell's cytoplasm is represented as a resistor, the cell's membrane as a resistor and capacitor in parallel, which are in parallel with the medium, modeled as a capacitor and resistor in parallel. At low frequencies the thin cell membrane has a high capacitance and the polarization of the membrane is dominant. At high frequencies, however, the membrane is short-circuited, the membrane capacitance tends to zero and the internal resistance of the cell dominates. The membrane is assumed to have a very high capacitance and the internal capacitance of the cell is ignored. The double layer which is modeled as a resistor and a capacitor in series is only important to model at low frequencies.

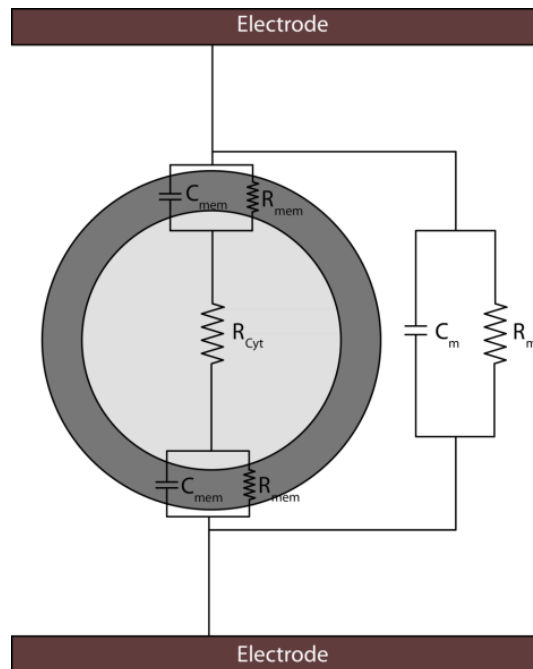


**Fig. 2.5.** A circuit model of a suspended cell in a fluid between two electrodes. Mem refers to the cell membrane, cyt refers to the cell cytoplasm, and m refers to the media.

**Crossover Frequency:** For each cell type, within a specific media, there exists a unique frequency at which the cells and the media have an equivalent complex permittivity, known as

the crossover frequency,  $f_{xo}$ . At this frequency the real part of the  $f_{CM}$  equals zero,  $Re\{K(\varepsilon_p^*, \varepsilon_m^*)\} = 0$ , thus there is no net DEP force acting on the cell. At this frequency the cell is invisible to the electric field (see Fig. 2.4(b)). A very small change in the biophysical properties of the cell will change the membrane properties of the cell and consequently the crossover frequency of the cell. Thus, the crossover frequency can be used as a tool to monitor changes in cells such as changes after treating cell with drugs or toxicants.

Crossover frequency can be found from (1.12) by putting  $Re\{f_{CM}(\omega)\}$  equal to zero and solving for frequency.  $f_{xo}$  can then be found as

$$f_{xo} = \frac{1}{2\pi} \sqrt{\frac{(\sigma_p - \sigma_m)(\sigma_p + 2\sigma_m)}{(\varepsilon_p - \varepsilon_m)(\varepsilon_p + 2\varepsilon_m)}}, \quad (1.33)$$

The material properties of cells and biological tissues change with the applied frequency. This disparity in properties is known as dispersion. At frequencies less than 10 kHz, counterion polarization happens along the cell membrane ( $\alpha$  dispersion). In the higher frequency range, interfacial polarization of the cell membrane occurs, which develops due to the polarization of proteins and other macromolecules ( $\beta$  dispersion) [96]. For frequencies well below  $\beta$  dispersion (<1 MHz), the cells dielectric properties are related to membrane properties [97]. Then, the specific capacitance of the cell membrane,  $C_{mem}$ , and the conductance associated with the transport of ions across the membrane  $G_{mem}$ , can be defined as

$$C_{mem} = \frac{\varepsilon_{mem}}{d} \quad (1.34)$$

$$G_{mem} = \frac{\sigma_{mem}}{d} \quad (1.35)$$

The crossover frequency can be written then as [98]

$$f_{xo} = \frac{\sqrt{2}\sigma_m}{8\pi r_1 C_{mem}} \sqrt{(4\sigma_m - r_1 G_{mem}^*)^2 - 9r_1^2 G_{mem}^{*2}}, \quad (1.36)$$

and the total effective conductance per unit area of the cell membrane,  $G_{mem}^*$  as [99]

$$G_{mem}^* = \frac{2K_{ms}}{r_1^2} + G_{mem} \quad (1.37)$$

$K_{ms}$  is the surface conductance of the membrane related to the electrical double layer around the cell, and  $G_{mem}$  is the conductance associated with the transport of ions across the membrane [99, 100]. For viable mammalian cells,  $K_{ms}$  and  $G_{mem}$  are in the range of 2–3 ns and 10–100 S/m<sup>2</sup>, respectively [101]. Equation (1.36) is mostly valid for frequencies below 100 kHz. The difference between  $G_{mem}^*$  and  $G_{mem}$  is that  $G_{mem}^*$  represents the contribution of all effects that influence the medium conductivity around the cell. However,  $G_{mem}$  represents the conductivity only through the cell's membrane. The additional term,  $\frac{2K_{ms}}{r_1^2}$ , represent the effects tangential to the cell membrane surface and shows that the conductivity around the cell also affects  $G_{mem}^*$  [102].

At low frequencies, < 100 kHz, the low value of  $G_{mem}$ , representing the membrane bulk conductivity, prevents the penetration of the applied electric field inside the cells. As the frequency increases over 100 kHz, membrane resistance begins to short-circuit and the electric field penetrates inside the cell, as discussed before and shown in Fig. 2.4.

Equation (1.36) can be simplified to the form of [99]

$$f_{xo} = \frac{\sqrt{2}\sigma_m}{2\pi r_1 C_{mem}} - \frac{\sqrt{2}G_{mem}^*}{8\pi C_{mem}}, \quad (1.38)$$

The second term on the right hand side can be neglected for  $G_{mem}^* \ll 4\sigma_m/r_1$ . This inequality is valid for low conductivity media, which is valid in this study since the conductivity of the

sample was about 100 mS/m, and considering the reported cell radii in this work. Thus, the second term is negligible and the crossover frequency can be calculated as

$$f_{xo} = \frac{\sqrt{2}\sigma_m}{2\pi r_1 C_{mem}} \quad (1.39)$$

The first crossover frequency of mammalian cells typically happens between 10-100 kHz, and the second crossover frequency is typically on the order of 10 MHz for a sample with a conductivity of 100  $\mu$ S/cm [99]. Cell size, shape, cytoskeleton, and membrane morphology affect the first crossover frequency and cytoplasm conductivity, nuclear envelope permittivity, nucleus-cytoplasm (N/C) volume ratio, and endoplasmic reticulum affect the second crossover frequency [5]. For instance, larger cells need a longer time (equivalent to a smaller frequency) to charge the surface membrane using ions in the electrolyte. Changes in the shape of the cells, for instance from spherical to elliptical, can cause a significant change in their dielectric properties. However, cells usually become round and spherical when suspended in the solution. The biophysical cell parameters affecting the two crossover frequencies and the Clausius-Mossotti factor are shown in Fig. 2.6 for a mammalian cell using two-shell model and will be discussed further in this chapter.

The other method to achieve equation (1.39) is that for frequencies well below the interfacial dispersion frequency ( $\sim 1$  MHz) the permittivity of the particle dominates the permittivity of the surrounding media but the conductivity of the medium is much higher than particle. Thus, we can write equation (1.33) as

$$f_{xo} \approx \frac{\sqrt{2}\sigma_m}{2\pi\epsilon_p} \quad (1.40)$$

From equation (1.40), and by referring to the definition of the specific membrane capacitance from equation (1.34),  $C_{mem}$  can be written as

$$C_{mem} = \frac{\epsilon_{mem}}{d} = \frac{\epsilon_p}{r_1} \quad (1.41)$$

which makes equations (1.39) and (1.40) the same. The total membrane capacitance is defined as

$$C_{tot} = 4\pi r^2 C_{mem} \quad (1.42)$$

The system consists of the cell membrane, which acts like a dielectric, and two electrodes consisting of conductive media, making the entire system similar to a capacitor. The dielectric nature of the membrane is further established due to the fact that its conductivity is  $10^{16}$  times less than copper and its permittivity is only about 10 times higher than air [86]. The magnitude of induced charge in a capacitor is proportional to its surface area. Similarly way, the capacitance of a cell depends on the cell's membrane surface. Smooth cells have a lower membrane capacitance in contrast to cells with blebs, protrusions, foldings, and microvilli.  $C_{mem}$  can also be reduced due to increase in the membrane thickness, and changes in intramembrane components which changes polarizability of the membrane.

Gascoyne et al [102] defined a membrane-specific area parameter,  $\phi$ , which shows the ratio of the actual membrane area to the membrane area that would be required to cover a smooth cell with the same radius.  $\phi$  quantify the amount of surface foldings and protrusions and shows the morphological feature such as microvilli, villi, ruffles, ridges, and blebs [102]. These complications on the membrane increase the surface area and consequently the membrane capacitance. It has been shown before that a smooth cell has a membrane capacitance of  $9 \text{ mF/m}^2$  [103, 104]. Base on this fact,  $\phi$  can be as also defined as the membrane capacitance of a cell to the membrane capacitance of a very smooth cell,  $9 \text{ mF/m}^2$ . Thus,  $\phi$  will be one for a perfectly smooth cell and higher values for cells with uneven surfaces.

The specific membrane capacitance can also be written as [94]

$$C_{mem} = \alpha C_{sl} + (1 - \alpha) C_{sn} \quad (1.43)$$

where  $C_{sl}$  and  $C_{sn}$  are the specific capacitance of lipid and other components (membrane proteins, cholesterol, and other elements between cytoplasm and the cellular space), respectively, and  $\alpha$  is the proposition of lipid in the membrane measured by area. For instance for murine erythroleukaemia cells, considering the reasonable value for lipid specific capacitance is  $7.8 \text{ mF/m}^2$  the specific capacitance of the protein region can be up to  $1.04 \text{ mF/m}^2$ , and assuming that the protein membrane area is accounted for %40 of the plasma membrane area ( $\alpha=0.6$ ), then  $C_{mem}=9.4 \text{ mF/m}^2$  [94]. However, [94] showed that the real value of  $C_{mem}$  was 1.5-2 times higher this value ( $\phi=1.5-2$ ) due to the microvilli and other structures observed by SEM on the cells surface.

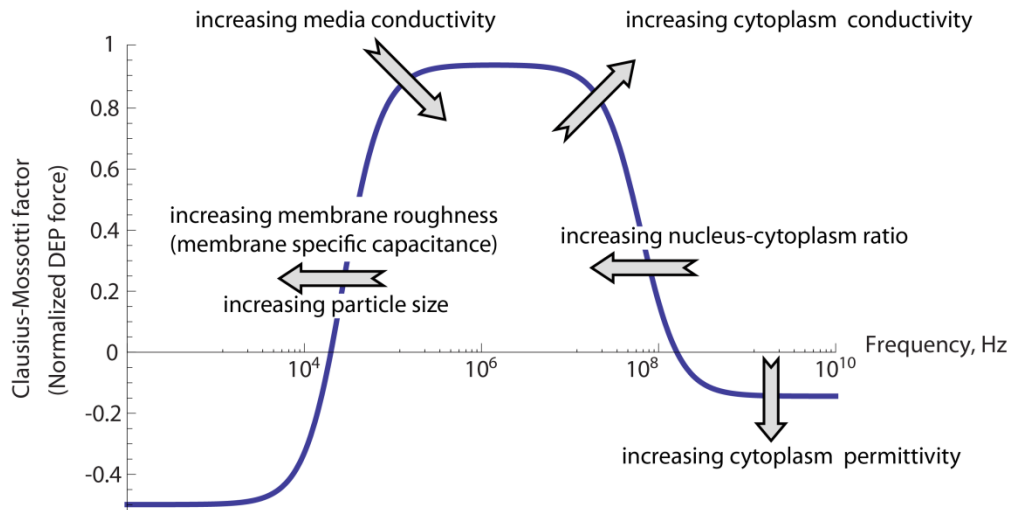


**Fig. 2.6.** Clausius-Mossotti factor for a typical mammalian cell at the sample conductivity of  $100 \mu\text{S/cm}$ . Arrows show how the Clausius-Mossotti factor of cells changes by changing the cells characteristics. Adapted from [95].

Differences in cells viability, morphology, and structural architecture can also affect polarizability of the cells which consequently changes cells dielectric properties. For instance when a cell is dead, its membrane becomes permeable and the ion can pass through it. This increases the conductivity of a cell from about  $10^{-7}$  to around  $10^{-3}$  which changes the

polarizability of the cell. Also different cell types and cells at different stages of differentiation have different morphological and cytoskeleton structure which makes their polarizability different and consequently, the DEP force they experience in the same condition different. Different DEP works have shown that exposing cells to DEP force does not influence cells viability [36, 105-109].

It has also been shown that cancerous and normal cells have different electrical properties. Oral squamous cell carcinomas have distinctly different electrical properties than more normal keratinocyte populations [110], and non-cancer-derived oral epithelial cells [111]. Additionally, transformed and non-transformed rat kidney cells [112], malignant human breast cancer epithelial cells and benign breast epithelial cells [113, 114], and healthy and infected erythrocytes have been shown to have different electrical properties [115].

Similarly, normal, pre-cancerous and, cancerous oral keratinocytes have distinct electrical properties [116]. By progression of the disease to more malignant stages,  $C_{mem}$  increases from  $6.9 \pm 0.6$  to  $10.9 \pm 2$ ,  $15.1 \pm 2.6$ , and  $14.3 \pm 4.5$   $\text{mF m}^{-2}$ , and the cytoplasm conductivity decreases from  $0.71 \pm 0.08$  to  $0.42 \pm 0.26$ ,  $0.26 \pm 0.06$ , and  $0.25 \pm 0.10$   $\text{S m}^{-1}$  for primary normal oral keratinocytes, dysplastic, and malignant oral keratinocyte cell lines, respectively [116]. Treating cells can also change their membrane capacitance. For instance, treating murine erythroleukaemia by hexamethylene bisacetamine (HMBA) decreases their membrane capacitance from 17.4 to 15.3  $\text{mF/m}^2$  [94]. Change in the membrane capacitance is associated with the complexity in the surface morphology, specifically microvilli and the density of complex features. Also, the mechanical rigidity of treated cells enhances after treating with HMBA, compatible with the initial stages of development of their membrane skeleton during differentiation [94]. Thus, the membrane capacitance reflects membrane morphology.

The membrane capacitance also increases by increasing the osmolality of the buffer which is again due to the development of the membrane cytoskeleton of cells from early stage to more

mature erythrocyte [94]. Although the surface morphology and the membrane capacitance of the cells strongly depend on the osmolality of the buffer, the total membrane capacitance of cells was almost independent from the osmolality of the buffer, except for small osmolalities [94]. This happens due to the decrease in the cells radius by increasing the osmolality of the suspending buffer. SEM images from untreated cells at different osmolality as well as untreated cells showed that treated cells have smoother less villus surface, the size of the blebs is about 0.5-1 um, and in high osmolalities long and more interdigitated microvilli can be observed and cells have more granular surface and shorter protrusions. Also, in both treated and non-treated cells the microvilli and blebs are in continuity with the cytoplasm thus the plasma membrane is a continuous surface [94].

There are always variations in measuring the cells membrane capacitance which root in the fact that cancer cells have typically heterogeneous cell morphology and ploidy. In experiments the cells are mixed in cell cycle phase, and therefore not all cells undergo differentiation spontaneously and response in the same way to treatment [94].

From the morphological view, the differentiation of the erythroleukaemia cells changes the characteristics of the surface from having numerous microvilli and filopodia that protrude from cells body to mature cells which are smooth and discoid surface. These changes happen simultaneously with the development of the cytoskeleton which causes loss of microvilli and a smoother surface texture. Also the conductivity of the membrane decreases 5 times which is due to the increase in the integrity of the spectrin in cytoskeleton and increase in structural protein content of the membrane that causes decrease in the membrane leakage and membrane fluidity [117].

To study the surface charges effect on DEP properties of cells, the net cells surface charge decreased by treating cell by a chemical by 60% [117]. However, the DEP responses of cells did not change at frequencies higher than 2 kHz, thus, the influence of net surface charge is

ignorable in frequencies higher than 2 kHz. However, it has been shown that the DEP force at frequencies less than 100 Hz is affected by surface charges [118].

Based on these discussions DEP can be used to investigate the bioelectrical properties of cells during treatment and differentiation and changes in the cells membrane morphology due to cells physiological activities and induction of pathologic state is related to the dielectric properties of cells [97, 118-125]. For instance, DEP can be used to distinguish cell membrane properties, such as membrane protrusions [94] and membrane conductivity [118], as well as the membrane skeleton [94, 117]. Cell differentiation changes the characteristics of the cytoskeleton linkage to integrins and the lipid and protein composition of the membrane [117].

It has been also shown that DEP can be used to study the cells biophysical properties under apoptosis [99, 126, 127]. Since apoptosis causes loss of structural features such as microvilli and formation of blebs [127] it changes the dielectric properties of cells. [99] measured the specific membrane capacitance of Jurkat T-cells under etoposide-induced apoptosis. At the beginning, the specific membrane capacitance of cells was  $13.34 \pm 2.88$  mF/m<sup>2</sup>, however, after exposing to etoposide for 2, 4, and 6 hours, it reduced to  $12.51 \pm 2.45$ ,  $12.08 \pm 3.35$ , and  $10.49 \pm 4.00$  mF/m<sup>2</sup>, respectively. This is equivalent to the reduction in the surface density of pseudopods and microvilli, and appearance of plasma membrane blebs which are consistent with the expected morphological changes due to apoptosis [99]. However, the results of [126] about apoptosis of K562 is in contradiction with [99] and [127]. In this study the membrane capacitance of cells increased from 9.7 to 14.9 mF/m<sup>2</sup>, although the cells average radius decreased and the conductivity of cytoplasm increased from 0.28 to 0.45 S/m [126]. This suggests that apoptosis may cause different morphological changes in different cell types. It is also suggested that DEP might be able to distinguish between apoptosis and necrosis of cells and to sort apoptotic and necrotic cells from normal cell [127].

One of the important applications of DEP can be studying and selectively isolating stem cells and cancer stem cells. There are several certain and possible differences in biophysical properties of stem cells and non-stem cells as well as cancer stem cells (CSCs), also known as tumor initiating cells (TICs), and non-CSCs including protein expression, size, morphology, nucleus/cytoplasm (N/C) ratio, nucleic acid content, presence and conductivity of internal membrane-bound vesicles, surface charge, and charged cytoplasmic molecules, which make their dielectric properties different. For instance, Fig. 2.7 demonstrates how Clausius-Mossotti factor changes by changing N/C ratio of cells. This Figure is consistent with presented results that CSCs (assuming they have higher N/C ratio than non-CSCs) need lower DEP force to be trapped than non-CSCs at the same frequency in the range of 200-600 kHz [9].

The progenitor cells can be isolated from the stromal vascular fraction which includes cell debris, erythrocytes, and nucleated cells. Progenitor cells have been separated based on their differences between the density, morphology, and size of putative stem cells and other cells [105]. CD34<sup>+</sup> stem cells can also be isolated from peripheral blood stem cell harvests using differences in cells dielectrophoretic properties [36]. Moreover, DEP isolate human breast cancer cells from hematopoietic CD34<sup>+</sup> stem cells due to differences in cell polarization, morphological characteristic, and the density [128]. The specific membrane capacitance of breast cancer cells and hematopoietic CD34<sup>+</sup> stem cells are reported as  $23.0 \pm 7.1$  and  $10.2 \pm 1.5$  mF/m<sup>2</sup>, respectively [128]. These studies showed that differences in cells density can play a role isolations of some cells, but in some important applications, such as isolating TICs from non-TICs the density of both cells are almost the same.

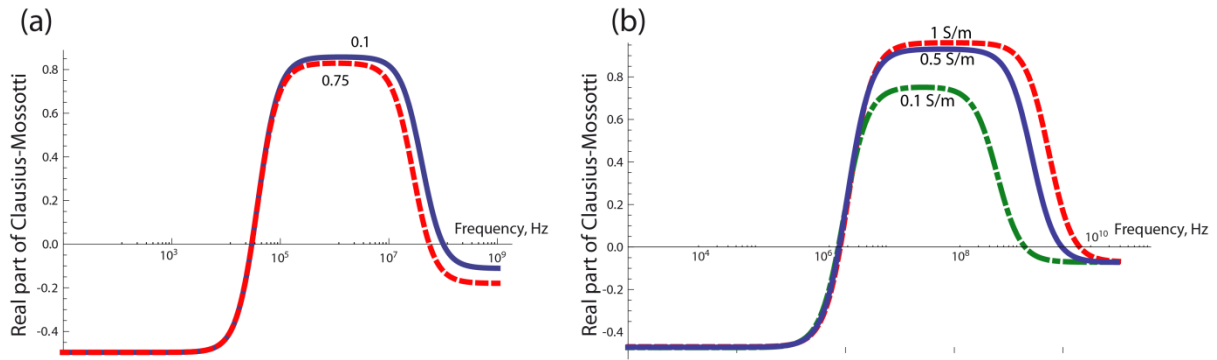


**Fig. 2.7.** Clausius-Mossotti factor changes by changing (a) N/C ratio of cells and (b) cytoplasm conductivity.

Populations of mouse neural stem/precursor cells (NSPCs) can be isolated from differentiated neurons and differentiated astrocytes using DEP [109]. There is a shift in dielectric properties of cells reflecting their fate and makes these cells have distinct DEP properties. Cells' dielectric properties can reveal the developmental progression of progenitor cell populations. By comparing these results with results of [6] for glioma and neuroblastoma, they showed that the differences in cell dielectric properties remains in cancerous states of these cells [109]. Thus, DEP can solve the challenge of isolating stem cells from more differentiated progeny.

The polarization of endoplasmic reticulum, nucleus, and mitochondria affects cells dielectric properties in frequencies less than 1 MHz and increase the relative permittivity of the cells due to interfacial polarizations of these organelles [95]. On the other hand, cells' organelles change during differentiation of cells. For instance, mitochondrial membrane potential heterogeneity is different in CSCs and normal cancer cells and can be used as a tool for isolating CSCs [129]. Mitochondrial membrane potential is related to the differentiation of cells and their tumorigenicity and malignancy. Differentiation, transformation, and tumorigenicity of cells make a significant change in mitochondrial membrane potential [129]. Also, carcinoma cells have higher mitochondrial membrane potential than normal cells [130-132]. There is a minimum of 60 mV differences in mitochondrial membrane potential of normal can cancer cells [130]. There is

also a relation between tumorigenicity of stem cells and their mitochondrial membrane potential; stem cells with higher mitochondrial membrane potential have higher tendency to form tumors [133]. Based on cells mitochondrial membrane potential [129] sorted them as CSC > cancer cells > normal epithelial cells. Moreover, mitochondria have an important role in the metabolism in the cells; the difference in the metabolism of CSCs and non-CSCs [129] can be related to the reported differences in the Mitochondria of these cells.

There is a distinct difference in the morphology of human pancreatic cancer stem cells and non-CSCs [134], which can be used to distinguish CSCs and non-CSCs. CSCs are more spindle-shape and have greater metastatic and ascites formation capability. These cells also can grow without anchorage which is the property of very malignant cells [134]. This results are in agreement with [135] reporting that a CSCs-enriched population of pancreatic cancer cells have more mesenchymal-like shape and with less adhesion proteins which enables them to migrate.

CSCs and non-CSCs have different surface proteins, including CD24, CD44, CD133, which play a significant role as a marker to identify CSCs as well as in tumor progression, metastases, and as possible targets for therapy [136]. The differences in surface proteins between CSCs and non-CSCs is another possible reason making their dielectric properties different.

N/C ratio decreases by cell differentiation and maturity [1] and changes the effective conductivity and permittivity of cells. For instance, limbal epithelial stem cells have a higher N/C ratio ( $=0.82$  [137]) than peripheral corneal epithelial cell ( $=0.17$  [138]), [1]. Also, N/C ratio is one of the morphological characteristics relevant to consider for the grading of cervical dysplasia [139]. In areas of dysplasia, the metaplastic squamous epithelium exhibited mild to marked nuclear atypia (hyperchromasia, irregularity, clumping of chromatin) and an increased N/C ratio [140]. Also, human embryonic stem (hES) cells have much higher N/C ratio than ordinary somatic cells. Thus, the cells with different N/C ratio will have different dielectric properties and can be sorted based on that. Specifically, differences in N/C ratio changes the

second crossover frequency of cells (Fig. 2.7). There is also a network of cytoskeleton structures between around the nucleus in somatic cells. Possible lack of this network due to smaller cytoplasmic volume in hES cells can be another reason for difference in their dielectric properties than somatic cells [141].

At frequencies higher than 10 MHz, the permittivity of cell internal organelles has dominant effects on the permittivity of the cell. Changing the Clausius-Mossotti factor from positive to negative at the second crossover frequency shows that the permittivity of the cells decreases to less than the buffer permittivity,  $\sim 80$ . This change is mostly due to changes in nucleus of the cells. Due to the counter-ion fluctuations the DNA shows a dielectric dispersion and the proteins show relaxations of polar groups [1].

## 2.6 Other DEP-based techniques

***Insulator based dielectrophoresis (iDEP):*** Although DEP has been a very successful technique for manipulating microparticles [142, 143], it does have drawbacks such as electrolysis (bubble formation), electrode delamination, and sample contamination [144, 145]. Traditionally, the non-uniform electric fields necessary to induce dielectrophoresis are generated by patterning metal electrodes onto the bottom of a microfluidic channel or by using insulating structures to distort a uniform electric field [146]. The alternative of using insulators to create the non-uniformity of the electric field is known as insulator-based dielectrophoresis (iDEP), which arose to overcome drawbacks of electrode-based dielectrophoresis (eDEP) such as complex and expensive fabrication, and loss of functionality due to fouling [147, 148].

iDEP is one of the practical methods used to overcome traditional DEP difficulties. The patterned electrodes required by traditional DEP are complex and expensive to fabricate. In contrast, iDEP uses insulating obstacles rather than the geometry of the electrodes to generate nonuniformities in the electric field. iDEP microdevices can thus be fabricated using simple etching techniques and from a single master, allowing for more economical

large-scale systems and mass production [149-152]. iDEP microdevices have been successfully tested for different applications, ranging from macromolecules such as DNA [153, 154], to cells such as bacteria [79, 155], yeast [156], and microalgae [157]. However, it is still difficult to use iDEP with highly conductive biological samples because joule heating and bubble formation still occur.

***Contactless dielectrophoresis (cDEP):*** Contactless dielectrophoresis (cDEP) is an extension of these techniques in which metal electrodes are exchanged for conductive fluid electrode channels. In cDEP, an electric field is created in a microchannel by electrodes that are inserted into two side channels filled with conductive solution. These side channels are separated from the main channel by thin insulating barriers that exhibit a capacitive behavior. The application of a high-frequency electric field to the electrode reservoirs causes their capacitive coupling to the main channel and an electric field is induced across the sample fluid. Not having direct contact between the sample and the metallic electrodes eliminates many of the challenges with conventional DEP such as electrolysis in the sample channel and electrode delamination. Furthermore, the fabrication process is relatively simple because it is not necessary to pattern micro-electrodes in the main channels. This method is well suited to traditional mass fabrication techniques such as hot embossing and injection molding.

cDEP has recently been used to enrich a population of tumor initiating cells (TICs) from non-tumor initiating cells [9], to isolate THP-1 human leukemia monocytes from a heterogeneous mixture of live and dead cells [158], to segregate cancer cells from erythrocytes [159], and to separate breast cancer cells from different cell lines based on their metastatic potential [160].

## **2.7 Electro-rotation**

Electrorotation is the rotation of polarized particles suspended in a liquid due to an induced torque in a rotating electric field [161]. Electrorotation happens in any electric field with a spatially dependent phase. The time averaged torque on a particle can be written as:

$$\vec{\Gamma}_{DEP} = \frac{1}{2} \text{Re}\{\vec{p} \times \vec{E}^*\} \quad (1.44)$$

Then by substituting Equations (1.16) and (1.18) for electric field and dipole moment, respectively, we can write

$$\vec{\Gamma}_{DEP} = 4\pi\epsilon_m r^3 \text{Re}\{f_{CM}(\omega)(\vec{E} \times \vec{E}^*)\} = -4\pi\epsilon_m r^3 \text{Im}\{f_{CM}(\omega)\}(\text{Re}\{\vec{E}\} \times \text{Im}\{\vec{E}^*\}) \quad (1.45)$$

Knowing that

$$\text{Re}\{\vec{E}\} \times \text{Im}\{\vec{E}^*\} = |\vec{E}|^2 = \vec{E} \cdot \vec{E} \quad (1.46)$$

Then, the time-averaged first order torque on a particle is given by

$$\vec{\Gamma}_{DEP} = -4\pi\epsilon_m r^3 \text{Im}\{f_{CM}(\omega)\}(\vec{E}_{RMS} \cdot \vec{E}_{RMS}) \quad (1.47)$$

where  $\text{Im}\{f_{CM}(\omega)\}$  is the imaginary part of the Clausius-Mossotti factor.

If the induced dipole moment lags behind the field, the direction of rotation of particle is the same as the field. Otherwise, if the induced dipole moment leads the field, the direction of rotation of particle is opposite to the field.

For a particle more polarizable than the medium, spin direction is the same as the field, called co-field electrorotation. However if the particle is less polarizable, the direction of rotation is opposite to the field, known as anti-field electrorotation [86].

The imaginary part of Clausius-Mossotti factor is zero at high and low frequencies and peaks at the Maxwell-Wagner relaxation frequency

$$\tau_{MW} = \frac{\epsilon_p + 2\epsilon_m}{\sigma_p + 2\sigma_m} \quad (1.48)$$

in which  $Im\{f_{CM}(\omega)\}$  has the value of

$$\frac{1}{2} \left( \frac{\varepsilon_p - \varepsilon_m}{\varepsilon_p + 2\varepsilon_m} - \frac{\sigma_p - \sigma_m}{\sigma_p + 2\sigma_m} \right) \quad (1.49)$$

This makes  $Im\{f_{CM}(\omega)\}$  bounded between  $-3/4$  and  $+3/4$ . When a particle rotates in a fluid, it experiences a drag torque. Assuming the cells are spherical particles in the medium and the rotation rate is slow (a few  $\text{rad.s}^{-1}$ ), the hydrodynamic frictional torque,  $R$ , due to rotation is given by

$$R = 8\eta\pi r^3 \Omega \quad (1.50)$$

where  $r$  is the particle radius,  $\eta$  is the medium viscosity,  $R$  is induced torque, and  $\Omega$  is electrorotation rate ( $\text{rad.s}^{-1}$ ). The steady state rotational velocity of the particle is given by

$$\Omega = \frac{\varepsilon_m}{2\eta} Im\{f_{CM}(\omega)\} (\vec{E}_{RMS} \cdot \vec{E}_{RMS}) \quad (1.51)$$

where  $\Omega$  is the angular velocity of the particle and is independent from the particle size, unlike the DEP force. The electrorotation (ROT) rate can also be written in terms of the applied voltage as

$$\Omega = \frac{\varepsilon_m}{2\eta} Im\{f_{CM}(\omega)\} (V_{RMS}^2 k^2) \quad (1.52)$$

where  $k = \vec{E}_{RMS}/V_{RMS}$  is a constant relating the electrodes geometry and the position of the particle in the electrode chamber [94].  $\Omega$  is a function of the viscosity of the media, permittivity and conductivity of the media and particle, the geometry of the device, the position of the particle in the device, and the applied voltage and frequency.

ROT spectrum of cells over a large range of frequencies (100 Hz-10 MHz) can be used as a fingerprint of the cell to find cell's viability as well as conductivity and permittivity of different compartments in its structure [90].

$\text{Im}\{f_{CM}(\omega)\}$  can be written as a function of

$$\text{Im}\{f_{CM}(\omega)\} = \frac{3\omega\tau_{MW}(\varepsilon_p\sigma_m - \varepsilon_m\sigma_p)}{(1 + \omega^2\tau_{MW}^2)(\varepsilon_p + 2\varepsilon_m)(\sigma_p + 2\sigma_m)} \quad (1.53)$$

The frequency spectra of DEP and ROT can reveal significant information about the electrical properties of cells [86, 90, 91, 100, 104, 119, 122, 125, 161].

## 2.8 Electrical double layer

In most of microfluidic problems, bioparticles are suspended in an aqueous solution of ions, known as electrolyte. These suspensions also usually have some sugar to adjust the osmolality, otherwise bioparticles, especially cells, will burst. Ions number and type in a solution changes the conductivity and even permittivity of the solution [76]. Ions also gather in interfaces between particle or electrodes and the electrolyte to maintain electroneutrality. This is known as the electrical double layer. Studying the double layer is very important because it changes the forces applies on the particle or the fluid, such as AC-electroosmosis.

When an ion is suspended in an electrolyte, polarized water molecules gather around the ion to maintain electroneutrality of the solution. The length scale of this layer of polarized molecules is defined as the Debye length

$$\kappa \equiv \sqrt{\frac{\sigma}{D\varepsilon}} \quad (1.54)$$

where D is diffusion constant. The time required for an ion to move a distance in the order of Debye length is known as charge relaxation time and is defined as

$$\tau \equiv \frac{1}{D\kappa^2} = \frac{\varepsilon}{\sigma} \quad (1.55)$$

When an electric field is applied to an electrode which is in contact with an electrolyte, a couple of layers of opposite charge ions attach to the electrode and form a plane known as electrical double layer. The potential at this slip plane is defined as the zeta potential,  $\zeta$  [76].

## 2.9 Electrophoresis

Electrophoresis is the movement of charged particles in an electric field. The electrophoretic mobility of a charged particle moving in an electric field is defined as the ratio of its velocity to the electric field

$$\mu_{EP} \equiv \frac{u}{E} \quad (1.56)$$

The double layer forms around a charged particle to maintain electroneutrality. Thus, this double layer, specially its thickness, has an important role in  $\mu_{EP}$  of particles. The ratio of the radius of the particle to thickness of the double layer, Debye length  $\kappa^{-1}$ , is shown as  $\kappa r$ . Then, the mobility can be written as a general form

$$\mu_{EP} = \frac{\varepsilon\zeta}{\eta} f(\kappa r) \quad (1.57)$$

where  $\varepsilon$  and  $\eta$  are the permittivity and viscosity of the medium, respectively, and  $\zeta$  is the zeta potential of the particle. The oscillatory displacement of a particle due to EO is equal to  $\vec{u}_{EO}/\omega$  [75]. If the electric field is about  $10^5$  V/m, and the frequency in the order of kHz, and zeta potential about 10 mV, then the velocity will be in the order of 1 mm/s and the oscillatory displacement of the will be in the order of 1  $\mu$ m. The oscillatory displacement can be negligible comparing to the displacement of the particles due to DEP.

For a thin double layer,  $f(\kappa r) = 1$ , known as Helmholtz-Smolunchowski limit, and for thick double layer  $f(\kappa r) = 2/3$ , known as Huckel-Onsager limit (very dilute electrolyte or very small particles) [76].

Electrophoresis has a very wide application for manipulation, mostly separation, of small molecules [162, 163], DNA [164, 165], and proteins [166]. Electrophoresis separation has been used in food industry, anti-terrorism, and environment safety through using portable microdevices [167]. For particle separation using electrophoresis see Ref. [167, 168].

## 2.10 Electroosmosis

The electrical double layer potential depends on the applied frequency in AC fields since the double layer needs a certain time to form. At low frequencies, when the electric field time scale is larger than the time required to form double layer, at each half of the cycle, double layer has enough time to form, thus the potential drops completely inside the double layer. However, at high frequencies there is not enough time for double layer to form, thus the potential at electrodes is the same in the electrolyte. At intermediate frequencies, the potential of the electrolyte decreases by decreasing the applied frequency [76].

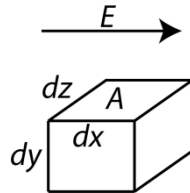


**Fig. 2.8.** Schematic of the system used to derive EO relation.

The 2D electroosmotic velocity in a channel can be calculated as follow. It is assumed that the channel depth is infinite. By considering the balance between the electrical force (Coulomb force) and the friction force, we can write

$$E_x \rho_e dx dy dz = \eta dx dz \left[ \left( \frac{du_x}{dy} \right)_y - \left( \frac{du_x}{dy} \right)_{y+dy} \right] \quad (1.58)$$

which can be written as

$$E_x \rho_e dy = \eta \left( \frac{d^2 u_x}{dy^2} \right) dy \quad (1.59)$$

Charge density,  $\rho_e$ , can be substituted from the Poisson's equation by

$$E_x \varepsilon \left( \frac{d^2 \varphi}{dy^2} \right) dy = \eta \left( \frac{d^2 u_x}{dy^2} \right) dy \quad (1.60)$$

Then, by integrating both side of the equation (1.60) from the electrode surface (no slip boundary condition) where potential is equal to zeta potential, to infinity gives

$$\vec{u}_{EO} = \frac{\varepsilon \zeta}{\eta} \vec{E} = \mu_{EO} \vec{E} \quad (1.61)$$

The velocity of the fluid is proportional to the zeta potential of the surface,  $\zeta$ , permittivity,  $\varepsilon$ , and viscosity,  $\eta$ , of the fluid, and the applied electric field,  $E$ .  $\mu_{EO}$  is defined as the electroosmosis mobility.

## 2.11 AC-electroosmosis

AC-electroosmosis (AC-EO) is another particle manipulation as well as flow generation technique which has been used in several microfluidic applications recently. AC-EO has the advantage over DC-electroosmosis that it requires less voltage for operation. Two of the most frequent applications of AC-EO are fluid micropumping [169, 170] and micromixing [171, 172].

Electroosmosis happens when a tangential electric field is applied to a surface which is in contact with electrolytes. The tangential electric field applies a force to the double layer charges on the

surface and consequently pulls the fluid and creates a flow. The fluid flow rate in AC-EO pumping depends on the applied voltage and frequency, electrodes shape and arrangement, the properties of the fluid, and the zeta potential.

It is important to mention that in AC-electroosmosis, the electric field should be non-uniform to have a non-zero time-averaged flow. Flow will be zero in a uniform AC field [76]. This is similar to dielectrophoresis which is zero in uniform electric field.

One of the differences between AC-EO and pressure-driven flow pumping is that in AC-EO flow, velocity decreases by increasing the distance from the electrodes, while in pressure driven flow, velocity is zero close to walls and has its maximum value at the center.

The magnitude of AC-EO depends on the charge density and charge density depends on the applied frequency. Thus, AC-EO depends on the frequency. At low frequencies (<10 kHz) AC-EO is almost zero since there is not any field in the bulk of the fluid. At high frequencies (>100 kHz) AC-EO is again zero since there is not enough time to induce charges to form double layer. At frequencies higher than 100 kHz usually electrothermal effects are dominant, depending on the conductivity of the sample.

## **2.12 Electrothermal effects in the fluid**

Due to applying a nonuniform AC field, a nonuniformity in the temperature of the fluid happens which changes the conductivity, permittivity, density, and viscosity of the fluid locally. This imbalance in the properties of the fluid creates electrothermal forces in the fluid which leads to the movement of the fluid [171].

To understand the electrothermal effects, we should consider the energy balance equation [173]

$$\rho_m c_p \vec{v} \cdot \nabla T + \rho_m c_p \frac{\partial T}{\partial t} = k \nabla^2 T + \sigma E^2 \quad (1.62)$$

where  $\rho_m$  is the density,  $k$  thermal conductivity,  $\sigma$  electrical conductivity, and  $c_p$  the specific heat at constant pressure of the fluid,  $\vec{v}$  velocity of the fluid, and  $T$  the temperature. We consider the effect of each term here. The diffusion time can be estimated from the Fourier equation:

$$\rho_m c_p \frac{\partial T}{\partial t} = k \nabla^2 T \quad (1.63)$$

By analyzing the order of magnitude, the diffusion time can be estimated as [53]

$$t \approx \frac{\rho_m c_p l^2}{k} \quad (1.64)$$

In our study the length scale of the microdevice,  $l$ , is in the order of 100  $\mu\text{m}$ ,  $k=0.6 \text{ J/m.s.K}$  and the heat capacitance at constant temperature,  $c_p= 4200 \text{ J/kg.K}$ . Thus, the diffusion time is estimated as 0.07 s, which shows that the thermal equilibrium forms very fast. This calculations are in agreement with [53].

The ratio of convection term to thermal conductivity (heat diffusion) term, known also as Peclet number, can also be approximated as [53]

$$\frac{\rho c_p \vec{v} \cdot \nabla T}{k \nabla^2 T} \approx \frac{\rho c_p v l}{k} \equiv Pe \quad (1.65)$$

In our study velocity is in the order of  $10^{-5}$ - $10^{-4}$  m/s, thus the above term will be in the order of  $10^{-3}$ - $10^{-2}$ , showing that the convection term is negligible comparing to thermal conductivity term. This means heat transfer is not affected by fluid flow thus the temperature and velocity equations are decoupled in microsystems. Also the electric field is decoupled from velocity field and thermal problem, thus they can be solved separately [76]. After

neglecting the transient and convection terms, the temperature can be reduced to Poisson's equation:

$$k\nabla^2 T = -\sigma E^2 \quad (1.66)$$

The temperature increase can be estimated from the balance between Joule heating and thermal conductivity:

$$\Delta T \approx \frac{\sigma E^2 l^2}{k} \quad (1.67)$$

In our experiments  $E$  is in the order of  $10^5$  and thermal conductivity of the sample, in case of beads suspended in DI water, was measured as  $7 \mu\text{S}/\text{cm}$ , thus the temperature increase is about  $0.12 \text{ C}$ . These calculations showed that the electrothermal effects are negligible in our study.

There are some differences between AC-EO and ET. AC-EO usually happens at frequencies less than  $100 \text{ kHz}$ , but the frequency to observe ET is usually more than  $100 \text{ kHz}$ . The conductivity of sample in AC-EO is usually very low ( $<0.01 \text{ mS}/\text{m}$ ), most of the time DI water is used, but the conductivity of the sample in ET pumping is usually high ( $>0.01 \text{ S}/\text{m}$ ) [78, 174]. AC-EO happens because of the charges on the surface of electrodes or walls due to Faradaic or capacitive charging [78]. However, ET is a volume force.

To make a directional movement in a fluid, such a pumping, we should make asymmetry in the flow. This can happen by making asymmetry in the geometry and/or making unbalance in one of the properties, such as temperature. In most of the AC-EO (as well as AC-ET) applications, traveling wave has been used on an array of electrodes to create unbalance, and consequently flow [175-178]. One of the disadvantages of this system is that each of the electrodes should be connected individually to a phase which makes the fabrication process difficult [78]. In some other cases a planar electrode has been used, which has electrodes

with different width [179, 180] or other type of generating asymmetry [181, 182].

### 2.13 Hydrodynamic force

As particles move under the influence of the DEP force, they interact with the surrounding fluid and experience a hydrodynamic force. Assuming the steady state fluid flow, medium viscosity,  $\eta$ , is relatively high (such as with water), and that the particles are small, spherical, and are moving with a relatively low velocity, the hydrodynamic force can be approximated as Stokes' drag, which is given by

$$\vec{F}_{Drag} = 6\eta r\pi(\vec{u}_p - \vec{u}_f) \quad (1.68)$$

where  $r$  is the particle radius,  $\vec{u}_p$  is the velocity of the particle, and  $\vec{u}_f$  is the medium velocity. To study the movement of a particle in a fluid, we can write

$$m_p \frac{d\vec{u}_p}{dt} = -6\eta r\pi(\vec{u}_p - \vec{u}_f) + \vec{F}_{ext} \quad (1.69)$$

By solving this equation,  $\vec{u}_p$  can be found as

$$\vec{u}_p = \left( u_p - \vec{u}_f - \frac{\vec{F}_{ext}}{6\eta r\pi} \right) e^{-\left(\frac{6\eta r\pi}{m}\right)t} + \vec{u}_f + \frac{\vec{F}_{ext}}{6\eta r\pi} \quad (1.70)$$

For a spherical particle, the characteristic time of acceleration can be defined as

$$\tau_a = \frac{m}{6\eta r\pi} = \frac{\rho 4/3\pi r^3}{6\eta r\pi} = \frac{2}{9} \frac{\rho r^2}{\eta} \quad (1.71)$$

For instance, for a 10  $\mu\text{m}$  diameter cell, and assuming that the density of the cells are close to density of water, and the viscosity of suspending medium is equal to water,  $\tau_a$  will be in the

order of  $10^{-5}$ . This time is much less than typical observation time,  $\sim 1$  s, thus it can be assumed that the particle is moving in terminal velocity:

$$\vec{u}_p = \vec{u}_f + \frac{\vec{F}_{ext}}{6\eta r\pi} \quad (1.72)$$

This means that the terminal velocity of a particle is the velocity of the fluid plus the velocity induced by an external force acting on the particle, such as DEP force. For considering the acceleration of fluid, see [183]. If the fluid is at rest, quiescent fluid, then the velocity of the particle will be proportional to the applied external force. Also if the particle is moving and the force is stopped, the particle stops moving almost immediately because the deceleration time is so short that cannot be observable.

## 2.15 Brownian motion

The random motion of particles due to thermal effects is known as Brownian motion, which has zero average displacement. The deterministic force movement of a particle should be greater than the Brownian motion movement to see a net movement of a particle [75]. The root-mean-square of the displacement in one dimension can be found as

$$\Delta x = \sqrt{2Dt} = \sqrt{\frac{k_B T}{3\pi r\eta}} t \quad (1.73)$$

where  $D$  is the diffusion constant,  $k_B$  is Boltzman's constant,  $T$  is the temperature, and  $t$  is the period of observation.

## 2.17 Summary

In this chapter, the governing equation of the movement of a particle in a microfluidic device was investigated. Electrical, mechanical, and thermal equations were presented and it was shown

that they are decoupled from each other. In the rest of the chapter different electrokinetic phenomena were presented with a special focus on dielectrophoresis. Important phenomena in electrohydrodynamics and their equations are summarized in Table 1.

**Table 1.** The important phenomena in electrohydrodynamics and their equations.

Phenomena	Equations	Scaling of the force to the particle size
Dielectrophoresis	$\vec{F}_{DEP} = \pi \varepsilon_m r^3 \text{Re} \left\{ \frac{\varepsilon_p^* - \varepsilon_m^*}{\varepsilon_p^* + 2\varepsilon_m^*} \right\} \nabla (\vec{E} \cdot \vec{E})$	$r^3$
Electrorotation	$\vec{\Gamma}_{DEP} = -4\pi \varepsilon_m r^3 \text{Im} \left\{ \frac{\varepsilon_p^* - \varepsilon_m^*}{\varepsilon_p^* + 2\varepsilon_m^*} \right\} (\vec{E}_{rms} \cdot \vec{E}_{rms})$	$r^3$
Electrothermal	$f_E = \frac{1}{2} \text{Re} \left[ \frac{\varepsilon(\alpha - \beta)}{1 + (\omega\tau)^2} (\nabla T \cdot \vec{E}) \vec{E} - \frac{1}{4} \varepsilon \alpha  \vec{E} ^2 \nabla T \right]$	$r^0$
Electrophoresis	$\vec{u}_{EP} = \frac{\varepsilon \zeta}{\eta} f(\kappa r) \vec{E}$	
Electroosmosis	$\vec{u}_{EO} = \frac{\varepsilon \zeta}{\eta} \vec{E}$	$r^0$
Viscous drag	$\vec{F}_{Drag} = 6\eta r \pi (\vec{u}_p - \vec{u}_f)$	$r^1$
Buoyancy	$\vec{F}_B = \frac{\partial \rho_m}{\partial T} \Delta T \vec{g}$	$r^0$
Brownian motion	$\Delta x = \sqrt{2Dt} = \sqrt{\frac{k_B T}{3\pi r \eta} t}$	$r^{-1/2}$
Gravity	$\vec{u}_p = \frac{2r^2(\rho_p - \rho_m)\vec{g}}{9\eta}$	$r^3$

# Chapter Three

## Materials and Methods

### 3.1 Introduction

In this chapter we cover fabrication process, experimental setups, and material and methods used for the experiments such as methods for analyzing the experimental results. We also report the electronics and the cells have been used during experiments. At the end of the chapter computational methods, including boundary conditions, electrical properties of materials, and modeling modules are explained.

### 3.2 Fabrication Process

#### *Deep Reactive Ion Etching (DRIE)*

Experimental devices were fabricated using standard soft lithography techniques [184]. First, AZ 9260 (AZ Electronic Materials, Somerville, NJ, USA) photoresist was spun onto a clean <100> silicon substrate. The wafer was exposed to UV light for 60 s through a mask patterned with the design. Then the exposed photoresist was removed using Potassium-based buffered developer AZ 400K (AZ Electronic Materials, Somerville, NJ, USA). Deep Reactive Ion Etching (DRIE) was used to etch the silicon master stamp to a depth of 50 microns.

The scalloping effect, which is unfavorable to the stamping process [185], was removed by 5 minutes of wet etching using TMAH 25% at 70°C. A thin layer of Teflon was then deposited on the silicon master using a DRIE system to facilitate the stamping process.

## ***PDMS***

The liquid phase PDMS was made by mixing PDMS monomers and a curing agent in a 10:1 ratio (Sylgard 184, Dow Corning, Midland, MI, USA). Bubbles in the liquid PDMS were removed by exposing the mixture to a vacuum for one hour. PDMS liquid was poured onto the silicon master, cured for 45 min at 100°C and then removed from the silicon mold. Finally, fluidic connections to the channels were punched with 1.5 mm puncher (Howard Electronic Instruments, USA). The PDMS replica was bonded with clean glass slides after treating with air plasma for 2 minutes.

### **3.3 Experimental Setup**

Prior to experimentation, the microfluidic devices were placed in a vacuum jar for 30 minutes to reduce issues with bubble formation within the channels. The fluid electrode channels were filled with phosphate buffered saline (PBS) (GIBCO PBS pH7.4, Invitrogen Corp., Carlsbad, CA, USA). These pipette tips were kept in place to serve as PBS reservoirs, and 20 gauge copper wire electrodes were placed in these reservoirs. The metal electrodes inserted in one of the electrode channels were used for excitation, while the electrodes inserted in the other electrode channel were grounded. Thin walled 20 gauge Teflon tubes (Cole-Palmer Instrument Co., Vernon Hills, IL, USA), with inner and outer diameters of 0.76 mm and 1.4 mm respectively, were inserted into the inlets and outlet of the main channel. 1 mL syringe was fastened to a microsyringe pump (Harvard Apparatus Syringe Pumps, Plymouth Meeting, PA, USA) and connected to the inlet tubes.

An inverted light microscope (Leica DMI 6000B, Leica Microsystems, Bannockburn, IL, USA) equipped with a color camera (Leica DFC420, Leica Microsystems, Bannockburn, IL, USA) was used to monitor the particles flowing through the main channel. A 10x objective was used for most of the experiments.

For TIC experiments, Chapter Eleven, a portable inverted epifluorescence video microscope for microfluidics model SVM340 (LabSmith, Livermore, CA, USA), shown in Fig. 3.1, was used to monitor the cells flowing through the main channel, and the dielectrophoretic behavior of the cells were recorded as pictures and videos by using the software uScope (LabSmith, Livermore, CA, USA). A 4x objective was used for all TIC experiments. The microscope requires the use of a personal computer for its operation.

### 3.4 Method of Analysis of Mixing

In mixing experiments, in order to visualize mixing, we have used 0.5  $\mu\text{m}$  diameter carboxylate-modified polystyrene microspheres (Invitrogen Molecular Probes, Eugene, OR, USA), which emit red light at a wavelength of 605 nm when excited at wavelength of 580 nm in a solution of deionized water. In each experiment, images of the flow are recorded in “target windows” before and after the mixing chambers. In each of the resulting images, the red intensity of each pixel,  $c_i$ , was used to define a local concentration. We use a mixing index,

$$MI = \left(1 - \frac{S}{S_0}\right) \quad (3.1)$$

to quantify the sample homogeneity, where

$$S = \sqrt{\frac{1}{N} \sum_{i=1}^N |c_i - c_{ref}|} \quad (3.2)$$

is the standard deviation of the concentration after mixing and  $S_0$  is the standard deviation of the concentration before mixing [186]. The average concentration in each image was used as  $c_{ref}$  for determining  $S$  in that image. We confirmed that the value of  $c_{ref}$  is nearly identical for the images before and after mixing. The mixing index is theoretically 1 in the case of

complete mixing and zero in the case of no mixing.

### **3.5 Electronics**

#### *Low frequency (5-100 kHz) experiments*

A custom electronics system, based around a LM4780 audio power amplifier (National Semiconductor, Santa Clara, CA), was used to conduct experiments. Two high power audio amplifiers were wired in a parallel push-pull configuration with a gain of 15 yielding a -3 dB bandwidth of 120 kHz. Output voltages, up to 200 V<sub>RMS</sub>, were produced by driving the output of the amplification stage into a custom wound transformer (AL-T75-V25/300-F20K/120K, Amp-Line Corp., West Nyack, NY) with a linear output response between 10 and 120 kHz. The system was powered by an unregulated DC power supply with positive and negative output voltage rails at 32 V<sub>DC</sub> and ripple rejection provided by 10,000  $\mu$ F capacitors on each rail. The amplitude and frequency of the output signal were controlled using a function generator (GFG-3015, GW Instek, Taipei, Taiwan) and output voltages and frequencies were measured using a high voltage probe (Enhancer 3000, Harvard Apparatus, Inc., Holliston, MA) and oscilloscope (TDS-1002B, Tektronics Inc. Beaverton, OR). For the experiments the applied voltage was held constant at 200 V<sub>RMS</sub>. Based on preliminary experiments, frequencies were selected in the range of 5 to 35 kHz in 2.5 kHz intervals, and in the range of 40 to 70 kHz in 10 kHz intervals. For each experiment, the frequency was selected at random and experiments were repeated three times with different cell samples.

#### *High frequency (100-600 kHz) experiments*

AC electric fields are applied to the microfluidic devices using a combination of waveform generation and amplification equipment. Waveform generation was performed by a function generator (GFG-3015, GW Instek, Taipei, Taiwan) where the output was then fed to a wideband power amplifier (AL-50HF-A, Amp-Line Corp., Oakland Gardens, NY). A high-voltage

transformer was then used to step-up the voltage of the signal before it was applied to the microfluidic device. The capacitive nature of the dielectric barriers that separate the electrodes from the sample fluid in the main microfluidic channel indicates that the magnitude of the electric field in the main channel was frequency dependent. It should be noted that voltages and frequencies higher than 300 V<sub>rms</sub> and 600 kHz, respectively, were not tested due to the PDMS breakdown voltage [187] and limitations in the power supply.



**Fig. 3.1.** cDEP experimental system, including the syringe pump, microfluidic device on a portable microscope, laptop to control the portable electronics and view microscope videos.

### 3.6 Cell culturing

**MOSE cells:** MOSE cells were cultured in Dulbecco's Modified Eagle's Medium (DMEM)-high glucose medium supplemented with 4% fetal bovine serum (FBS, Atlanta Biological, Atlanta, GA) and 100 µg/mL each of penicillin and streptomycin, at 37°C in a humidified atmosphere as described previously [188, 189].

**Macrophages:** PC1 macrophages were grown in DMEM–low Glucose (Sigma-Aldrich, St. Louis MO), containing 5 mL of penicillin and streptomycin (Invitrogen, Carlsbad CA), and 10% FBS (Atlanta Biological).

**Fibroblast:** OP9 fibroblast were maintained in  $\alpha$ -MEM (Invitrogen, Carlsbad CA), containing 5 mL of penicillin and streptomycin (Invitrogen, Carlsbad CA), and 20% FBS (Atlanta Biological).

**Prostate cancer cell line:** Human prostate cancer cell line, PC3 cells, were grown on 10 cm dishes, using Roswell Park Memorial Institute (RPMI) medium (Invitrogen cat. 11875-093), 10% fetal bovine serum (FBS) (Gemini Bio-products cat. 900-108), and 1% Penicillin/Streptomycin (P/S).

### 3.7 Cell preparation for flow cytometry

In order to prepare the cells for flow cytometry, cells were trypsinized, spun to collect, and the pellet was resuspended in Aldefluor assay buffer (filter sterilized). After counting the cells, the cell dilution was prepared to achieve  $1 \times 10^6$  cells/ml and transferred to an eppendorf tube. Then, cells were incubated with Aldefluor substrate for 45 minutes at 37 °C, with or without Diethylaminobenzaldehyde (DEAB) inhibitor. Following incubation all samples were centrifuged for 5 minutes at  $250 \times g$  and the supernatant was removed. The cell pellet was resuspended in 500  $\mu$ l Aldefluor assay buffer and placed at 4 °C before flow cytometry process.

### 3.8 Cell Preparation for experiments

A sugar solution with low electrical conductivity, consisting of 8.5% sucrose [wt vol<sup>-1</sup>], 0.3% glucose [wt vol<sup>-1</sup>], and 0.725% [vol vol<sup>-1</sup>] RPMI [109] was used for the experiments. Cells were harvested by trypsination, washed twice in the sugar solution and then individually resuspended to a concentration of  $3 \times 10^6$  cells per mL for low frequency experiments and  $1 \times 10^6$  cells per mL for high frequency experiments. The final electrical conductivity of the samples, measured prior to each experiment using a conductivity meter (Horiba B-173 Twin Conductivity/Salinity Pocket Testers, Cole-Parmer), which was usually about  $100 \text{ S m}^{-1}$  for experiments with cells. The radius and viability of cells were measured using the Cell Viability Analyzer (Vi-Cell, Beckman

Coulter). Calcein AM, enzymatically converted to green fluorescent calcein, was added to the cell sample at 2  $\mu\text{L}$  per mL of cell suspension to increase the contrast between cells and background for improved data analysis.

### **3.9 Immunofluorescence assay imaging**

MOSE cells were seeded on sterile coverslips in a 24-well plate and incubated for 48 hours. The cells were fixed with 3% paraformaldehyde in 250 mM HEPES for 10 minutes, permeabilized with 0.25% triton X100 in 6% paraformaldehyde, and quenched with 50 mM glycine for 10 minutes. After blocking with 2% BSA in PBS for 1 hour, the coverslips were kept in sterile PBS at 4°C until staining.

The cells were then immunostained to visualize actin filaments and tubulin. Cells were incubated with phalloidin conjugated to Alexa Fluor488 (MolecularProbes, Eugene OR) for 1 hour at room temperature, and washed three times with PBS. They were then incubated with anti-tubulin antibody overnight at 4°C, followed by incubation with Alexa Fluor 594-conjugated secondary antibody (Molecular Probes) for 1 hour at room temperature. After washing three times with PBS, the cells were mounted with Prolong Gold containing DAPI (Invitrogen, Carlsbad, CA) to visualize the nuclei. The images were taken using a Nikon 80i epifluorescence microscope, utilizing UV, FITC, and TRITC filters and a DS-U2 monochromatic camera. NIS Elements BR 3.0 software (Nikon Instruments, Inc., Melville, NY) was used to capture images and Adobe Photoshop® to process images.

### **3.10 Protaspheres Culturing**

Sorted cells by cDEP were cultured with concentration of  $1 \times 10^3$  cells/mL in 10 cm low attach dish (Fisher Scientific Co. 05-539-101) by adding 10 mL of Endothelial Cell Basal Medium (EBM) media with the following supplements: 100 mL of EBM (Lonza CC-3121) supplemented with 2 mL of B27 (Gibco 17504044) with a concentration of 50X (final concentration of 2%),

100  $\mu\text{l}$  of Insulin (5mg/mL, Invitrogen, Core Lab) with a concentration of 4 mg/mL (final concentration of 4  $\mu\text{g/mL}$ ), 20  $\mu\text{l}$  of EGF (Fisher CB 40001) with a concentration of 100  $\mu\text{g/mL}$  (final concentration of 20 ng/mL), and 100  $\mu\text{l}$  of FGF (Invitrogen PH60024) with a concentration of 20  $\mu\text{g/mL}$  (final concentration of 20 ng/mL). Spheroids should be collected after 2 to 3 weeks and can be analyzed morphologically by quantifying the number of colonies formed.

### 3.11 Blood Sample Preparation

Whole blood was collected from a healthy donor and stored in Vacutainer tubes (BD Vacutainer  $\text{\textcircled{R}}$  Sodium Heparin, BD, Franklin Lakes, NJ). The blood was centrifuged for 10 minutes at 3100 RPM (IEC Medilite, Thermo Scientific, Vernon Hills, IL). The high conductivity plasma was aspirated and replaced with the same volume of low conductivity buffer [109]. This process was repeated until the suspension had a conductivity of  $120 \pm 5$   $\mu\text{S/cm}$  as measured with a conductivity meter (Horiba B-173 Twin Conductivity/Salinity Pocket Testers, Cole-Parmer). All experiments were completed within 6 hours after the blood was collected. Individual samples of human breast cancer cell lines were used. The cancer cells and blood sample were then mixed together in one conical tube with a final conductivity of  $120 \pm 5$   $\mu\text{S/cm}$ .

### 3.12 Computational Modeling

Computational modeling of the electric field was used to estimate the performance of microdevices and to improve the device performance, specifically to reach a strong dielectrophoretic force, resulting in efficient trapping of cells or mixing. To do so, COMSOL Multiphysics 4.3 (Comsol Inc., Burlington, MA, USA) was used.

Spatial variations in  $\nabla(\vec{E}_{rms} \cdot \vec{E}_{rms})$  modeled to estimate DEP force. This was done by solving for the potential distribution,  $\phi$ , using the governing equation  $\nabla \cdot (\sigma^* \nabla \phi) = 0$ , , where  $\sigma^*$  is the complex conductivity ( $\sigma^* = \sigma + j\omega\epsilon$ ) of the sub-domains in the microfluidic devices. The

boundary conditions used are prescribed uniform potentials at the inlet or outlet of the side channels. The boundary conditions used were prescribed uniform potentials at the inlet and outlet of the electrode channels. The computational modeling was used to determine the range of frequency and voltage necessary to provide sufficiently large gradients of the electric field. The considered range of voltage and frequency were limited by the breakdown voltage of the PDMS barrier, which is about 300 V for a 20  $\mu\text{m}$  barrier.

The electrical properties of PDMS, PBS, DEP buffer, and DI water are shown in Table 1. The electrical properties of PBS were used for electrode channels and the properties of deionized water or DEP buffer (depending on the experiments) was used for the main microfluidic channels.

<b>Electrical Properties</b> <b>Materials</b>	<b>Electrical Conductivity (S/m)</b>	<b>Relative Electrical Permittivity</b>
<b>PDMS</b>	$0.83 \times 10^{-12}$	2.65
<b>PBS</b>	1.4	80
<b>DEP Buffer</b>	0.01	80
<b>DI Water</b>	$5.5 \times 10^{-6}$	80

The fluid flow in the sample channel was modeled to find the maximum shear rate. A condition of constant fluid velocity was defined at the inlet boundary to match the experimental volumetric flow rate in the experiments. The sample channel outlets were defined as zero pressure boundaries. The viscosity and density of water, 0.001 Pa.s and 1000  $\text{kg m}^{-3}$ , respectively, were used in the main fluidic channel.

# Chapter Four

## Investigating Dielectric Properties of Different Stages of Syngeneic Murine Ovarian Cancer Cells

### 4.1 Introduction

Ovarian cancer is the most common cause of death arising from gynecological malignancies and is one of the top causes of cancer-related deaths of women in United States and Europe [190, 191]. This high rate of mortality is largely a result of the lack of sufficient early cancer detection and efficient treatment techniques. The relative 5-year survival rate for invasive epithelial ovarian cancer patients diagnosed at early stages is more than 90%, while for the late stages is less than 30% [192].

Diagnosis and treatment of ovarian cancer in early stages has been hindered by the lack of syngeneic cell models to study this form of cancer at different stages and the inability to isolate early cancer cells from peritoneal fluid. Addressing the lack of adequate cell models, Roberts *et al.* established a progressive mouse ovarian surface epithelial (MOSE) cell model by isolating and culturing ovarian surface epithelial cells; the cells spontaneously transform and progress from a premalignant nontumorigenic to a highly aggressive malignant phenotype [188, 189].

This MOSE model enables the study of cellular and molecular changes in different stages of syngeneic ovarian cancer to determine regulatory mechanisms that may drive cancer progression and as such potential targets for cancer diagnosis and treatment [189]. Four stages of the disease were established based on their geno- and phenotype: early (MOSE-E), early-intermediate (MOSE-E/I), intermediate (MOSE-I) and late (MOSE-L) cells [188, 189].

Typically, ovarian cancers originate from surface epithelial cells of the ovary or fallopian tubes [193, 194]. Exfoliated cancer cells can disseminate throughout the peritoneal cavity where they will either form ascites or adhere to the organs or peritoneal lining and begin forming secondary tumors [189]. Addressing the challenge of isolating ovarian cancer cells from peritoneal fluid, we previously demonstrated that a microfluidic approach based on exploitation of cell electrical properties could be useful [8]. In this study, we further investigate the differences in the electrical properties of each cell stage of the MOSE model. Studying the electrical properties of MOSE cells provides important information as a first step to developing cancer-treatment techniques that could partially reverse the cytoskeleton disorganization of malignant cells to a morphology more similar to that of benign cells.

It has been shown that benign and cancerous cells are different in many aspects including proliferation, metabolism, cytoskeleton, and other functional categories [188, 195]. Some of these differences can lead to distinctions in these cells' electrical properties. It has been reported previously that oral squamous cell carcinomas have distinctly different electrical properties than more normal keratinocyte populations [110], primary normal keratinocytes, and pre-cancerous,

dysplastic cells [116], and non-cancer-derived oral epithelial cells [111]. Additionally, transformed and non-transformed rat kidney cells [112], malignant human breast cancer epithelial cells and benign breast epithelial cells [113, 114], and healthy and infected erythrocytes have been shown to have different electrical properties [115].

The challenges to ovarian cancer treatment indicate a need for further characterization of individual stages of ovarian cancer cells by their biophysical properties, independent of their heterogeneous genotype. In this study, the crossover frequency of different stages of cancer cells which are derived from the same cell line are found for the first time using a recently developed method by Sano et al [196]. We investigated the specific membrane capacitance of MOSE cells as they progress from benign to highly malignant stage. We also showed that the electrical properties of a cell are also affected by changes in morphology. This suggests that cytoskeleton structure could be correlated with bioelectrical characteristics of ovarian cancer cells to provide a transformative approach for characterizing cell progression and phenotypic response to treatment. Since the electrical properties changes during progression are associated with the disease phenotype, the outcome of a treatment regimen that affects cytoskeleton and membrane topography can be predicted by studying these changes.

## **4.2 Device Layout**

A top view schematic of the device is shown in Fig. 4.1. This device includes one sample channel (blue) and three fluid electrode channels (gray) which are separated from the sample

channel by 20  $\mu\text{m}$  barriers. Two symmetric electrode channels work as a source and the other electrode channel as a sink. These source and sink electrode channels are 1 cm apart and are filled with phosphate buffered saline (PBS,  $\sigma = 1.4 \text{ S m}^{-1}$ ). The six rounded saw-tooth obstructions in the flow channel create the non-uniform electric field necessary to induce a DEP force. Cells in this region will experience positive or negative DEP force depending on their intrinsic electrical properties and the applied frequency. Positive DEP will force cells to the top of the channel, while negative DEP will push the cells to the bottom boundary of the sample channel. At the end of the sample channel, there is a T-junction which allows for the collection of cells from one of two outlets. All channels are 50  $\mu\text{m}$  deep.

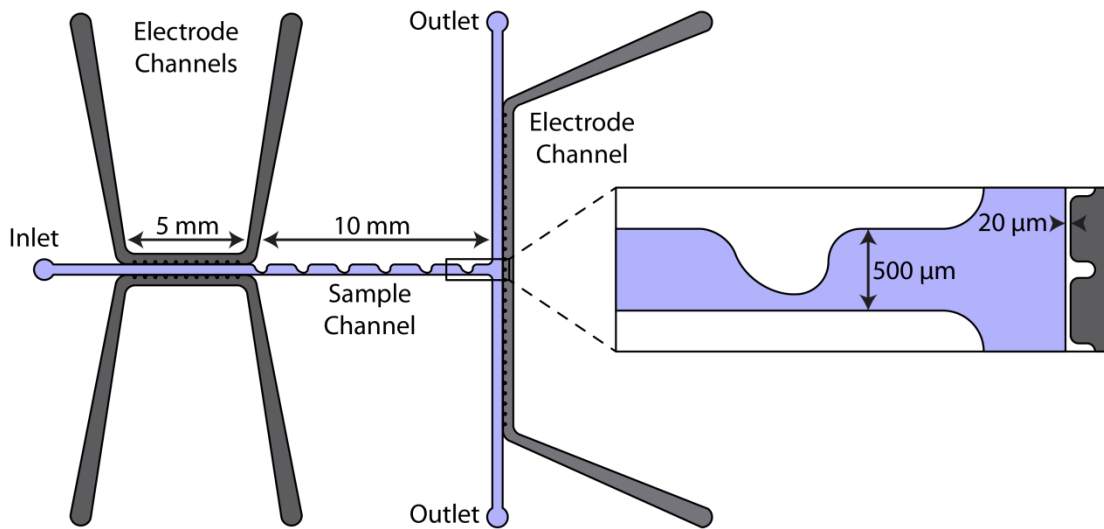


**Fig. 4.1.** Top view schematic of the device. Flow is from left to right in the fluidic channel. Inset is a detailed view of a saw-tooth feature and the T-junction [2].

### 4.3 Data Analysis

200 V<sub>RMS</sub> was applied at each frequency for five minutes prior to evaluation to ensure that cells being evaluated traveled the full length of the sample channel. Then, a two-minute video was recorded at the T-junction in the sample channel as shown in the inset of Fig. 4.1. MATLAB (Version R2010b, The MathWorks Inc., Natick, MA, USA) was used to determine the cell distribution across the width of the channel. At each frequency, the average location of the cells was determined by finding a distribution centerline that resulted in half of the cells being located on each side of the line (the red dashed line in Fig. 4.2.b. and d). The centerline of the cell distribution was compared to the geometrical centerline of the device to determine if the DEP force was positive or negative. Control experiments were also recorded without an applied voltage to verify that the cells were randomly distributed in the absence of an electric field. Moreover, electrorotation was not observed during the experiments suggesting that the applied electric field was not sufficient to overcome the friction of the medium to rotate.

The CM factor is theoretically bound between -0.5 and 1. This is visible experimentally in the distribution of cells as they experience positive and negative DEP force (Fig. 4.2.a. and c). Because the maximum value of negative DEP force is half of the value of the maximum value of positive DEP force, the cells occupy a relatively wide region on the bottom half of the channel (experiencing negative DEP force) comparing to the top half of the channel (experiencing positive DEP force). For each cell type, there is a frequency at which the cells are distributed

equally in the top and bottom of the channel. At this frequency, the geometrical center of the channel matches the line that divides the cells distribution into two equal parts, and this was considered as the crossover frequency.

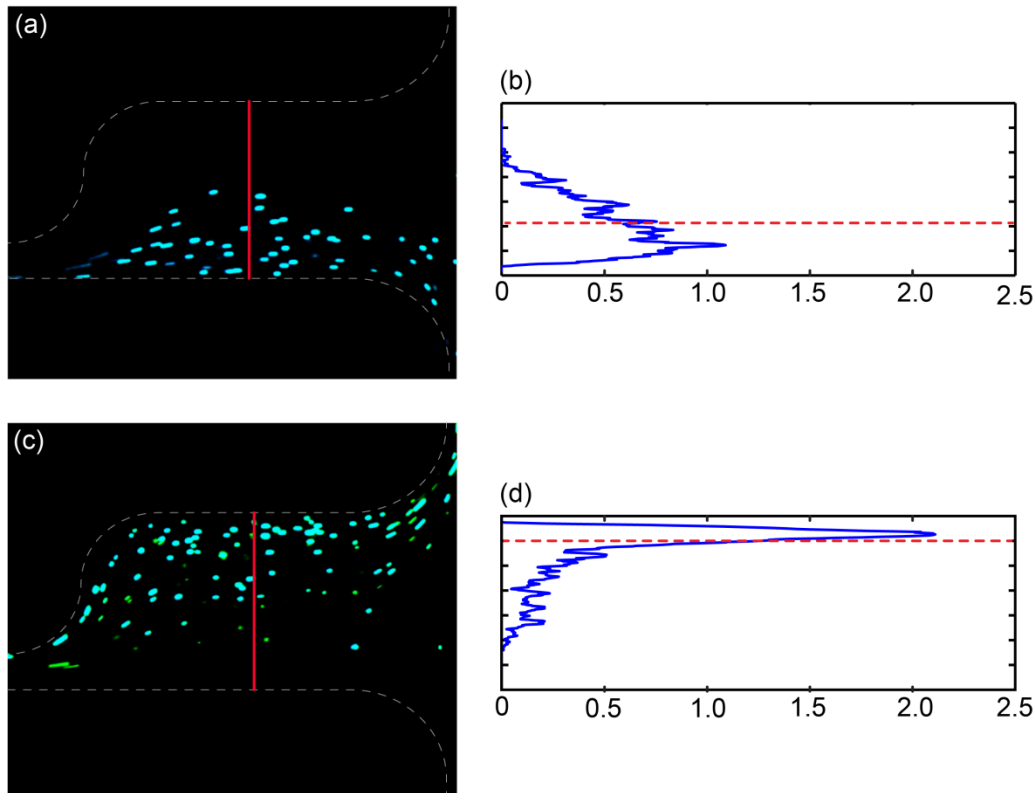


**Fig. 4.2.** (a) Due to negative DEP force, cells move towards the bottom of the channel at 10 kHz and 200 V<sub>RMS</sub>; (b) normalized cell distribution from (a). (c) Due to positive DEP force, cells move towards the top of the channel at 60 kHz and 200 V<sub>RMS</sub>; (d) normalized cells distribution from (b). The red solid line in (a) and (c) showed the location that cells distribution was studied. The red dashed line in (b) and (d) shows the center line of the cell distribution [2].

Since the conductivity of the sample was slightly different in each, the crossover frequency was normalized by the experimental sample conductivity,  $f_{xo}/\sigma_M$ , to facilitate comparison between different stages and experimental runs. The specific membrane capacitance was then calculated using Equation (1.39), the normalized crossover frequencies, and the average cell radii. These values were compared using the Student's t-test.

#### 4.4 Computational Results

Fig. 4.2.a. and b show the fluid flow and shear rate in the fluidic channel, respectively. The maximum shear rate in the sample channel was found to be approximately  $60 \text{ s}^{-1}$ . This is two orders of magnitude less than the reported threshold for shear induced cell lysis of approximately  $5000 \text{ s}^{-1}$  [197, 198].

Fig. 4.3.c and d show the surface plot of the magnitude of electric field and  $\nabla(\vec{E}_{RMS} \cdot \vec{E}_{RMS})$ , respectively, at 30 kHz. The highest spatial non-uniformity in the electric field is found in the regions at the bottom of the round saw-tooth bumps. It is in this region where cells experience the greatest DEP forces.

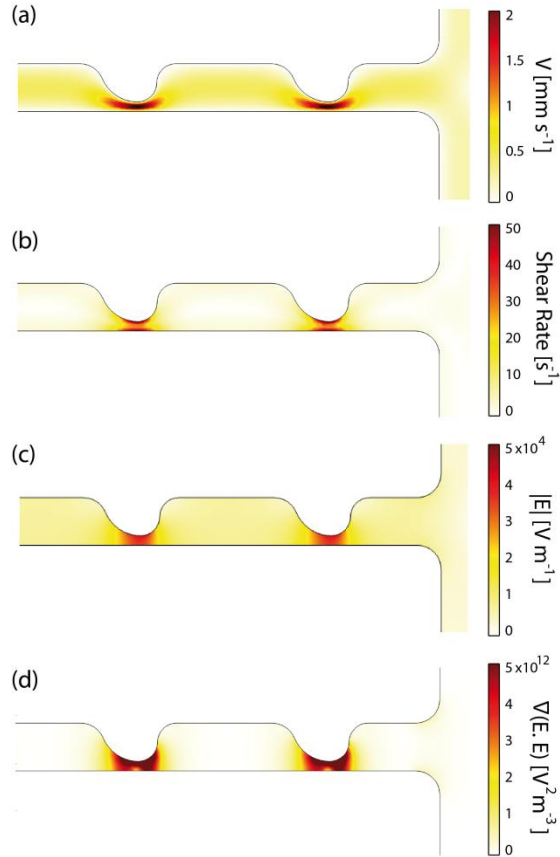


**Fig. 4.3.** Computational modeling of the microdevice. Surface plot of (a) the magnitude of the flow velocity ( $\mu\text{m s}^{-1}$ ), (b) shear rate ( $\text{s}^{-1}$ ), and (c) the magnitude of electric field, and (d) gradient of the electric field squared ( $\text{V}^2 \text{m}^{-3}$ ) at  $200 \text{ V}_{\text{RMS}}$  and  $30 \text{ kHz}$ , in the fluidic channel. Flow is from left to right [2].

## 4.5 Results and Discussion

At low frequencies, between 5 and 10 kHz, it was observed that most of the cells were forced into the bottom half of the sample channel, as shown in Fig. 4.2.a. This indicates that a strong

negative DEP force was exerted on the cells. At higher frequencies, above 30 kHz, the cells were forced towards the top wall of the device as they experienced a strong positive DEP force (Fig. 4.2.c). Fig. 4.2.b and d present the cells distribution across the red line shown on Fig. 4.2.a and c. Since the number of cells crossing the line is not exactly equal in all of the experiments, cells distributions are normalized by the total number of cells crossing the red line in Fig. 4.2.a and c to make comparing different experiments cells distributions possible.

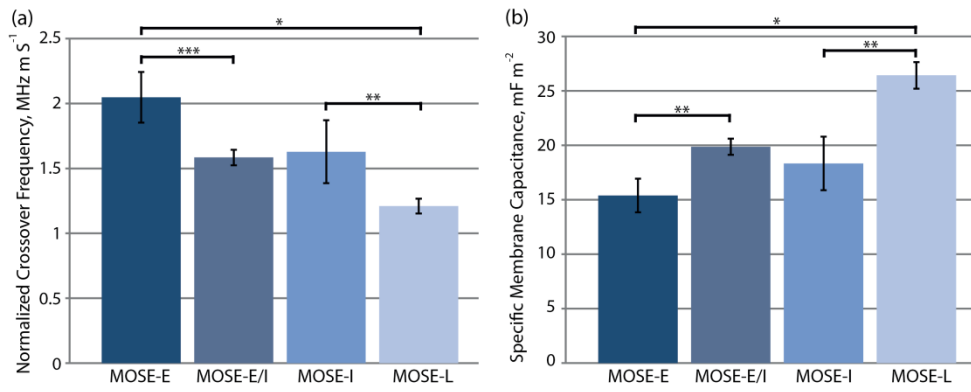


**Fig. 4.4.** (a) Crossover frequency and (b) area capacitance of the cell membrane for MOSE-E, -E/I, -I, and -L cells. \*, \*\*, and \*\*\* represent  $p < 0.001$ , 0.01, and 0.05, respectively ( $n=3$ ) [2].

The average crossover frequencies,  $f_{xo}$ , were  $20.14 \pm 1.73$  kHz,  $16.73 \pm 0.64$  kHz,  $16.28 \pm 1.07$  kHz,  $11.90 \pm 0.63$  kHz for MOSE-E, -E/I, -I, and -L cells, respectively. The crossover frequencies was then normalized by the sample conductivity in each experiment, shown in Fig. 4.4(a), as was explained before. The normalized crossover frequencies,  $f_{xo}/\sigma_M$ , for the four stages of MOSE

cells are in the same range of values reported previously for different breast cancer cell lines and normal cells [102, 199].

Then, using Equation (1.39), area specific membrane capacitances for different stages were calculated as  $15.39 \pm 1.54$ ,  $19.87 \pm 0.74$ ,  $18.33 \pm 2.46$ , and  $26.42 \pm 1.22$  mF m<sup>-2</sup> for MOSE-E, E/I, I, and L cells, respectively (Fig. 4.4.b).  $C_{mem}$  increases with progression of the cells from benign early stage to a tumorigenic, malignant state, which is similar to the previously reported behavior of cell lines [112, 116, 200-202].

The Student's t-test method was used to determine if the differences in crossover frequency and cell specific membrane capacitance of different cell lines were statistically significant. The crossover frequency and cell specific membrane capacitance of MOSE-E and -L were significantly different ( $p < 0.001$ ). The crossover frequency and cell specific membrane capacitance for MOSE-E and -E/I ( $p < 0.05$  and  $p < 0.01$ , respectively) and for MOSE-I and -L ( $p < 0.005$  for both, the crossover frequency and cell specific membrane capacitance) were also statistically different. However, the crossover frequency and specific membrane capacitance for MOSE-E/I and -I are not statistically different ( $p = 0.27$  and  $p = 0.18$ , respectively).

A smooth spherical shape cell has been estimated to have a membrane capacitance,  $C_{mem}$ , of approximately 6 mF m<sup>-2</sup> [4]. It has been demonstrated previously that the membrane ruffling of cancer cells is related to increased invasiveness and metastatic potential [203]. This increase in  $C_{mem}$  with increased aggressiveness shows that  $C_{mem}$  is related to the increase in surface

protrusions, folds, and ruffling. This is compatible with the observation that MOSE-L cells have more surface protrusions compared to MOSE-E cells. MOSE cells progress from the cobblestone-like phenotype seen in MOSE-E cells to the more heterogeneous appearance of MOSE-E/I cells, and finally develop a more spindle-shaped phenotype in the more aggressive stages (MOSE-I, MOSE-L) [188, 189]. Additionally, membrane protrusions increase as MOSE cells progress to a more aggressive phenotype, which could account for the increase in  $C_{mem}$  and consequent decrease in crossover frequency. The gene products that are determinants for the observed bioelectrical properties are subject of further investigation in our laboratories.

The crossover frequency is affected by cell size and shape, membrane integrity and morphology, and cytoskeleton architecture [1, 99]. Since there is no statistical difference in cell size, the changes in crossover frequency at different stages of MOSE cells are due to other factors, specifically membrane morphology and cytoskeleton. This is supported by previous studies on MOSE cell pheno-and genotypical changes during progression [188, 189]. It has been shown that the gene expression in MOSE cells changes in a stepwise manner from MOSE-E to MOSE-I to MOSE-L [188]. The gene expression profiles from transformed stages of MOSE cells have shown significant changes in cell cycle, proliferation, metabolism, and other functional categories which are related to morphological changes and biological behavior of the progressive MOSE cell model [188]. These changes in gene expression levels can directly affect cells' electrical properties by changing membrane morphology and properties of the cytoskeleton and

cytoplasm, which can lead to differences in the crossover frequency and specific area capacitance for these cells.

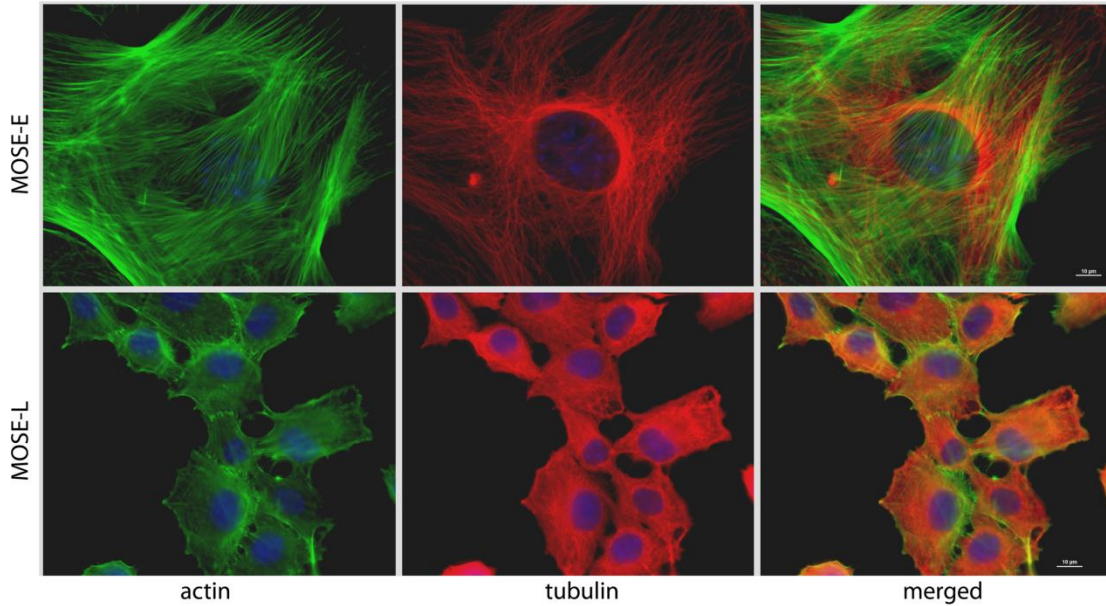


**Fig. 4.5.** Organization of the cytoskeleton during MOSE neoplastic progression. Triple immunofluorescent staining of MOSE-E and MOSE-L cells to visualize actin filaments (phalloidin, green), tubulin filaments (red), and nucleus (DAPI, blue) [2].

The cytoskeleton organization changes drastically during MOSE progression (Fig. 4.5.). While MOSE-E cells exhibit well-organized actin and tubulin networks, MOSE-L cells have lost the long actin cables and the tubulin organization. This loss of actin stress fibers and tubulin organization may affect the cellular architecture of cancer cells, cellular properties, functions, growth, and signaling events [188].

Immunofluorescence microscopy was used to determine differences in cells subcellular organization. Fig. 4.5., shows changes in the actin (green) and tubulin (red) organization during MOSE progression and demonstrates the loss of actin stress fibers and tubulin organization that affect the cellular architecture of cancer cells, cellular properties, functions, growth, and signaling events [188]. This figure shows that there is a decrease in the actin protein levels during the progression of MOSE cells. MOSE-E cells have more long cable-like fibers compared to MOSE-L cells which have actin structure ranging from small fibers to ruffled short actin filaments [188]. The concentration of actin fibers is also higher in MOSE-E cells in thickness and fibers' organization. Moreover, a significant decrease in tubulin was observed. In MOSE-E cells the  $\alpha$ - and  $\beta$ -tubulin are long filaments which are a normal structure in epithelial cells. However, MOSE-L cells have a random disorganized filaments structure [188]. These results are in agreement with the changes in morphology and surface protrusion of the cells which will consequently change the cells membrane capacitance.

By substituting measured cell radius and crossover frequency, using the calculated values for specific membrane capacitance and previously reported values for cancer cell membrane relative permittivity,  $10^{-8}$  [3], membrane thickness, 5 nm [4], cytoplasm relative permittivity, 60 [5], and knowing the media permittivity and conductivity,  $\epsilon_m = \epsilon_{DEP} = 80$  and  $\sigma_m = \sigma_{DEP} = 0.01 \text{ S m}^{-1}$ , respectively, the Clausius-Mossotti factor for different stages of MOSE cells can be predicted as a function of frequency. The cytoplasmic conductivities of MOSE cells was approximated as  $0.5 \text{ S m}^{-1}$  [6]. The Clausius-Mossotti factors for early and late stages of MOSE cells are shown in

Fig. 4.6. The average radius of MOSE-E, -E/I, -I, and -L cells were  $7.19 \pm 1.00$ ,  $7.16 \pm 1.25$ ,  $7.29 \pm 1.49$ , and  $7.05 \pm 1.20$   $\mu\text{m}$ , respectively ( $n=250$ ).

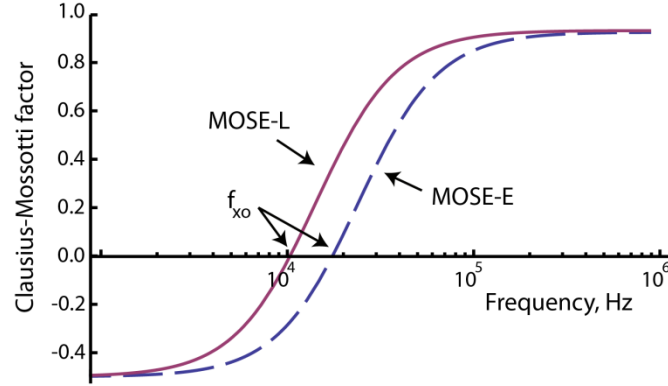


**Fig. 4.6.** Clausius-Mossotti factor of MOSE-E and MOSE-L cells as a function of frequency using single-shell model. The previously reported values for cancer cells were used for both early and late stages: cell membrane relative permittivity,  $10^{-8}$  [3], membrane thickness, 5 nm [4], cytoplasm relative permittivity, 60 [5]. The cytoplasm conductivity of cells was approximated as  $0.5 \text{ S m}^{-1}$  [6]. Media permittivity and conductivity are  $\epsilon_m = \epsilon_{DEP} = 80$  and  $\sigma_m = \sigma_{DEP} = 0.01$ , respectively [2].

## 4.6 Conclusions

In this study, the crossover frequency and specific membrane capacitance of different stages of MOSE cells were calculated using cDEP. We found that the specific membrane capacitance of MOSE cells increases as the cells progress from a benign stage to more malignant stages. These differences are due to morphological differences and changes in the cytoskeleton of these cells as

they transition to a more aggressive phenotype. These results indicate that cDEP can be used to study cell membrane properties and the differences between membranes of different cell lines, specifically between individual stages of cancer cells or differentiated cells. This study also advanced our knowledge of ovarian cancer progression by characterizing the electrical properties of MOSE cells. This transformative research provided previously unknown information as to the electrical properties of a syngeneic ovarian cancer cell model, which may lead to more effective early detection and cancer-treatment techniques.

# Chapter Five

## Sphingolipid Metabolites Modulate Dielectric Characteristics of Cells in a Mouse Ovarian Cancer Progression Model

### 5.1 Introduction

Currently, conventional cancer treatment regimens often rely upon highly toxic chemotherapeutics or target oncogenes that are variably expressed within the heterogeneous cell population of tumors. These challenges highlight the need for novel treatment strategies that 1) are non-toxic yet able to at least partially reverse the aggressive phenotype of the disease to a benign or very slow-growing state, and 2) act on the cells independently of variably expressed biomarkers. Using cDEP, we investigated the effect of non-toxic concentrations of two bioactive sphingolipid metabolites, sphingosine (So), with potential anti-tumor properties, and sphingosine-1-phosphate (S1P), a tumor-promoting metabolite, on the intrinsic electrical properties of early and late stages of mouse ovarian surface epithelial (MOSE) cancer cells. In the previous chapter, we demonstrated that electrical properties change as cells progress from a benign early stage to late malignant stages. Here, we demonstrate an association between So treatment and a shift in the bioelectrical characteristics of late stage MOSE (MOSE-L) cells

towards a profile similar to that of benign MOSE-E cells. Particularly, the specific membrane capacitance of MOSE-L cells shifted toward that of MOSE-E cells, decreasing from  $23.94 \pm 2.75$  to  $16.46 \pm 0.62$  mF/m<sup>2</sup> after So treatment, associated with a decrease in membrane protrusions. In contrast, SIP did not reverse the electrical properties of MOSE-L cells. This work is the first to indicate that treatment with non-toxic doses of So correlates with changes in the electrical properties and surface roughness of cells. It also demonstrates the potential of cDEP to be used as a new, rapid technique for drug efficacy studies, and eventually designing more personalized treatment regimens.

## **5.2 Background**

Ovarian cancer, the most frequent cause of death from gynecological malignancies in women and the fifth leading cause of death from cancer in women [190, 191], is a genetically and histologically heterogeneous disease. The lack of common genetic markers hinders both cancer detection at earlier stages and the development of successful treatment options. Development of treatment regimens and detection techniques that do not rely upon the expression of specific genes or surface markers could ameliorate these challenges.

Moreover, we have previously utilized cDEP to quantify dielectric properties of a syngeneic mouse cell model for progressive ovarian cancer [2]. In this model, isolated primary mouse ovarian surface epithelial (MOSE) cells undergo transformation in vitro and progress to malignant stages [189]. Since human cell lines providing different stages of ovarian cancer

derived from one genetic source are not available for study, the MOSE model represents a useful alternative that avoids the potential confounding variable of inter-subject genetic differences. Based on phenotype, MOSE cells were categorized into early, intermediate, and late stages of malignancy. An increasingly dysregulated cytoskeleton organization and changes in the expression of cytoskeleton genes and their regulators were observed during neoplastic progression, accompanied by an increase in membrane ruffles and protrusions [189, 204]. Cytoskeletal changes were associated with stage-specific changes in cellular biomechanical properties [205]. Also, we have recently shown for the first time that the dielectric responses of cells are different in different stages of progression [2]. We compared the crossover frequency and membrane capacitance of different stages of MOSE cells, finding that the membrane capacitance was greater in malignant cells compared to benign cells [2]. Aggressive MOSE cells also showed different dielectric responses from peritoneal cells, specifically macrophages and fibroblasts [8], indicating that cDEP may be an option for isolating ovarian cells from peritoneal fluid for cancer detection.

Current cancer treatments rely upon highly toxic doses of chemotherapeutics and can cause severe adverse side effects. In addition to achieving early detection, the development of less aggressive treatment options that at least partially reverse the aggressive phenotype of the disease to an earlier, more benign state and therefore may turn a deadly cancer into a chronic disease could be highly beneficial for patients. In this regard, we have used orally administered complex sphingolipids to successfully suppress colon and breast cancer.[206-210] Sphingolipid

metabolites influence membrane biology and as lipid second messengers modulate cellular homeostasis, functions and responses to extracellular stimuli. Sphingolipids are involved in the regulation of cell growth, cell death, migration, angiogenesis, and metabolism, among many other cell functions.[211, 212] Dysregulation in metabolic pathways of sphingolipids can cause progression of some diseases, including cancer.[213, 214] The sphingolipid metabolites ceramide (Cer), sphingosine (So), and sphingosine-1-phosphate (S1P), can stimulate opposing cellular responses depending upon their relative levels in a cell, forming the so-called sphingolipid rheostat [215, 216]. In general, So and Cer are known as a death-promoting factors leading to apoptosis, inhibition of cell growth, differentiation, migration, and angiogenesis and thus could be considered tumor suppressors. However, Cer has also been associated with inflammation [217], suggesting a tumor promoting effect. In contrast, S1P acts to support growth and survival of numerous cell types. As such, it has tumor-promoting effects, including inhibition of apoptosis and stimulation of angiogenesis, cell proliferation, differentiation, and migration. Elevated levels of S1P have been reported in human ascites fluid of patients with ovarian cancer [218] and may promote the survival, adherence, and outgrowth of peritoneal metastases. Interestingly, therapies targeting S1P generation and signaling have led to a decreased tumor formation in mice [219].

In this chapter, we used cDEP to characterize MOSE cells' electrical properties after So and S1P treatment to compare the effects of exogenous sphingolipid metabolites associated with anti- and pro-cancer effects, respectively. We demonstrate that sphingolipid modulation therapy induced

distinct changes in the bioelectrical properties of cancer cells. Importantly, the treatments were non-toxic, allowing us to use cDEP to discriminate among viable MOSE-derived cancer cells. We report that So treatment correlated with a shift in electrical properties of the aggressive MOSE cells towards a profile reminiscent of more benign stages, whereas S1P did not significantly impact the electrical properties of either early or late stage MOSE cells. The association of the altered electrical phenotype of the So treated cells with cancer suppression and the potential for use of electrical phenotype as a marker for treatment efficacy will be explored in future studies. The underlying molecular or structural alterations responsible for the changes in dielectric properties and the response to treatment may be critical for the design of devices for cancer detection and treatment control.

### **5.3 Device layout**

Our microdevice, shown in Fig. 5.1, consists of a straight main channel and parallel fluid electrode channels, each 50  $\mu\text{m}$  in depth. The main channel has an inlet and outlet with a series of rounded 'sawtooth' features that constrict the main channel from 500  $\mu\text{m}$  width to 100  $\mu\text{m}$ . These sawtooth features create high electric field gradients in the region where the sample channel is constricted, and the series of features increases the length of time that the cells are exposed to the DEP force. Fluidic electrode channels are separated from the sample channel by 20  $\mu\text{m}$  thick insulating barriers. Throughout this article, the side of the channel which has

sawtooth features will be referred to as top side of the channel and the opposite side of the channel which is a straight wall will be referred to as bottom side of the channel.

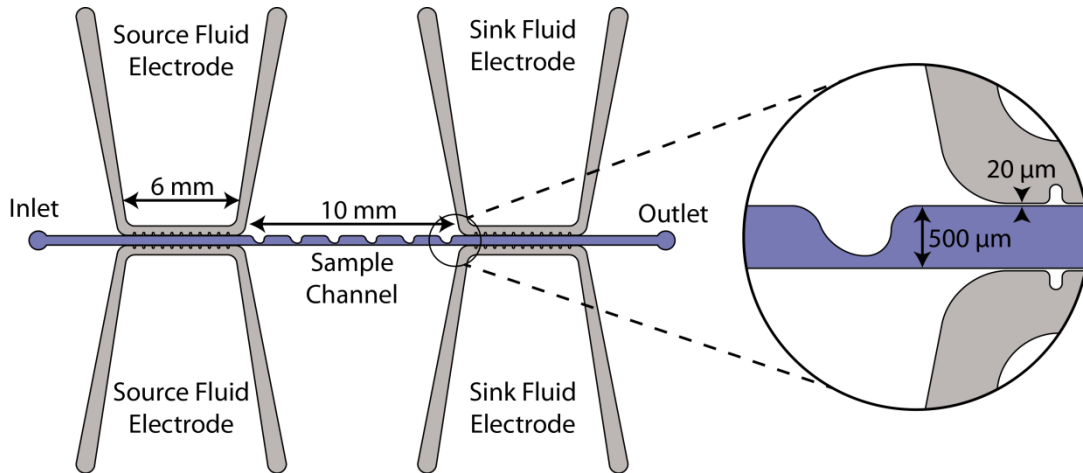


**Fig. 5.1.** The overhead view schematic of the microfluidic device. The inset detail view shows a sawtooth feature and the thin insulating barrier separating sample channel and electrode channels [7].

## 5.4 Computational Results

The Particle Tracing for Fluid Flow module was used to predict the trajectories of particles at different frequencies. Trajectories of 10 particles with uniform initial position distribution were simulated (Fig. 5.3). Drag and DEP forces were added to the model using velocity and electric fields computed from Laminar Flow and Electric Currents modules. The simulations were based on untreated MOSE-L cell properties. Since DEP and drag forces are both proportional to the size of the cells, the smallest cell radius, 5.85 μm, reported previously,[8] was used in the simulations. Also,  $Re[K(\omega)]$  at 5 and 20 kHz were estimated as -0.37 and 0.36, respectively, from the  $Re[K(\omega)]$  graph reported previously.[2] Fig. 5.3.a and b demonstrate cells trajectories

at 5 and 20 kHz, respectively. At frequencies less than the crossover frequency, cells experience nDEP, thus they are repelled from higher  $\nabla(\vec{E}_{RMS} \cdot \vec{E}_{RMS})$  and move towards the bottom half of the sample channel (Fig. 5.2.a). At frequencies higher than the crossover frequency cells experience pDEP, thus they are attracted towards higher  $\nabla(\vec{E}_{RMS} \cdot \vec{E}_{RMS})$  and the top half of the sample channel (Fig. 5.3.b). In Fig. 5.2.b, some particle trajectories meet the top wall of the sample channel. The plot does not continue to display these trajectories, leading to the appearance of fewer trajectories down the channel.

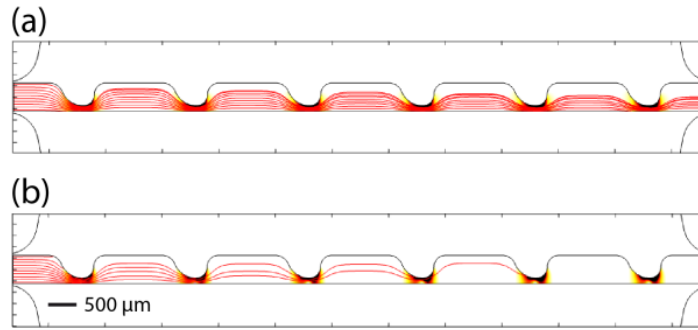


**Fig. 5.2.** Predicting the particles trajectories at (a) 5 kHz and (b) 20 kHz in red lines for 10 particles. Trajectories appear to diminish down the channel due to a simulation artifact that occurs when trajectories encounter a wall.  $\nabla(\vec{E}_{RMS} \cdot \vec{E}_{RMS})$  is also presented in the background. Darker areas indicate higher  $\nabla(\vec{E}_{RMS} \cdot \vec{E}_{RMS})$ . The scale bar represents 500  $\mu\text{m}$  [7].

## 5.5 Results and Discussion

Fig. 5.3.a, b, and c demonstrate cell movement in the sample channel without any applied electric field, and due to applying 200  $V_{RMS}$  and at frequencies lower and higher than the crossover frequency, respectively. As was shown in the computational results,  $\nabla(\vec{E}_{RMS} \cdot \vec{E}_{RMS})$  is much greater at the top side of the channel due to the sawtooth features, which induce non-

uniformities into the electric field. When applying a frequency less than the first crossover frequency of cells, cells will experience a negative DEP force and will be repelled from the sawtooth features. Then, they will move towards the bottom half of the channel. However, when applying a frequency higher than the first crossover frequency, cells will experience pDEP force and will be attracted towards sawtooth features and the top side of the channel. Fig. 5.3.d, e, and f demonstrate the normalized cells distribution corresponding to no DEP force from Fig. 5.3.a, nDEP from Fig. 5.3.b, and pDEP from Fig. 5.3.c, respectively. Fig. 5.3.d shows the distribution of cells without an applied voltage to verify that the cells were randomly distributed in the absence of an electric field. Cell distributions were normalized by the total number of cells crossing the red line in Fig. 5.3. to make comparing cells distributions in different experiments possible since the number of cells crossing the line is not exactly equal in all of the experiments. The results presented in Fig. 5.3.b and c are in agreement with the computational modeling of the trajectories of particles at 5 and 20 kHz.

As shown in Fig. 5.3., cells experience a stronger pDEP force than nDEP and they are focused in a narrower stream at the top side of the channel while experiencing pDEP force than when they experience nDEP force, due to two reasons. First, since  $K(\omega)$  is constrained between -0.5 and 1, the maximum possible value of pDEP force, regardless of the applied frequency, is twice stronger than the nDEP force. Also,  $\nabla(\vec{E}_{RMS} \cdot \vec{E}_{RMS})$  increases as the applied frequency is increased, and because, pDEP for cells occurs at higher frequencies than nDEP, cells experience a stronger DEP force during pDEP than nDEP.

The average crossover frequency for the benign MOSE-E and malignant MOSE-L cells under each treatment condition was calculated. Since the sample conductivity of each cell sample was slightly different, the crossover frequency from each experiment was divided by the sample conductivity in that experiment, based on the linear relationship between conductivity of the sample and crossover frequency (Equation (1.39)). These values,  $f_{xo}/\sigma_m$ , were compared by a student t-test (Fig. 5.4.a). The ratio of crossover frequencies to sample conductivity,  $f_{xo}/\sigma_m$ , for

untreated, So-treated, and S1P-treated MOSE-E cells were  $1.96\pm 0.16$ ,  $2.06\pm 0.18$ , and  $2.00\pm 0.39$  MHz·m/S, respectively, which were not statistically different, indicating that exogenous sphingolipids do not affect the crossover frequencies of MOSE-E. Under identical treatment conditions,  $f_{xo}/\sigma_m$  of MOSE-L cells were  $1.35\pm 0.07$ ,  $1.94\pm 0.07$ , and  $1.21\pm 0.14$  MHz·m/S, respectively.  $f_{xo}/\sigma_m$  for So-treated MOSE-L cells was significantly higher than the control or S1P treated MOSE-L cells ( $p<0.001$ ). Importantly, there was no statistically significant difference between  $f_{xo}/\sigma_m$  of So-treated MOSE-L cells and control MOSE-E cells ( $p=0.29$ ), indicating that So treatment effectively reversed the crossover frequency of MOSE-L cells to that observed in MOSE-E cells. The crossover frequency of MOSE-L cells did not change after the treatment with S1P, indicating that the change in electrical properties was due to the So or its metabolites rather than the conversion to S1P or a generic reaction to sphingolipid treatment.

Given the conductivity of the media and the known crossover frequency and radius of the cells, the specific membrane capacitance,  $C_{mem}$ , can be calculated using Equation (1.39). For MOSE-E control, So or S1P-treated cells,  $C_{mem}$  was  $16.05\pm 1.28$ ,  $15.26\pm 1.38$ , and  $16.15\pm 3.55$  mF/m<sup>2</sup>, and for MOSE-L cells with identical treatments,  $C_{mem}$  was found to be  $23.94\pm 2.75$ ,  $16.46\pm 0.62$ , and  $26.89\pm 3.91$  mF/m<sup>2</sup>, respectively. Neither So nor S1P treatment caused a significant change in  $C_{mem}$  of MOSE-E cells. The specific membrane capacitance of MOSE-L cells was significantly higher ( $p<0.01$ ) than MOSE-E cells; treatment with So, however, significantly decreased  $C_{mem}$  to the levels of MOSE-E cells while S1P treatment was not associated with a change in  $C_{mem}$  of MOSE-L cells (Fig. 5.4.b). The results indicate that the decrease in  $C_{mem}$  is specific for So treatment of aggressive cancer cells and benign cells are not affected. The measured radius of  $7.185\pm 1.004$  and  $7.050\pm 1.195$   $\mu\text{m}$  of MOSE-E and MOSE-L cells, respectively, were used to calculate  $C_{mem}$ .

Given the results for dielectric properties obtained in this study, the following discussion explores possible physiological sources for the observed properties. The specific membrane capacitance of cells can be elevated by an increase in surface protrusions, roughness, and

membrane ruffling, traits known to manifest with progressing malignancy, invasiveness, and metastatic potential.[203] This has been shown for leukemia, breast cancer lines, transformed rat kidney, murine erythroleukemia, and oral cancer cells.[220, 221],[222],[223] Consistent with these studies, we observed an the elevated specific membrane capacitance with progressing malignancy of MOSE cells (Fig. 5.4.b).

Along these lines, Gascoyne et al[102, 224] defined a membrane-specific area parameter,  $\varphi$ , the ratio of the actual membrane area to the membrane area that would be required to cover a smooth cell with the same radius. Thus,  $\varphi$  can be defined as  $\varphi = C_{mem}/C_0$ , where  $C_0$  is the membrane capacitance of a smooth cell, approximately  $C_0 = 9 \text{ mF/m}^2$ . [104] The amount of surface folding and protrusions, and morphological features such as microvilli, villi, ruffles, ridges, and blebs are quantified by  $\varphi$ . [102] These complexities increase the membrane surface area and consequently the membrane capacitance. Cells with irregular surfaces will have  $\varphi$  greater than unity, while a perfectly smooth cell will have  $\varphi=1$ . In the current study,  $\varphi$  increases from  $1.78\pm 0.14$  for MOSE-E cells to  $2.66\pm 0.31$  for untreated MOSE-L cells ( $p<0.001$ ), based on the results presented in Fig. 5.4.b, demonstrating that malignant cells have more surface irregularities than early cells. In our previous study we also showed that  $\varphi$  for MOSE-I cells is  $2.01\pm 1.61$ , which is in between  $\varphi$  values of MOSE-E and MOSE-L cells [2]. After treating MOSE-L cells with So,  $\varphi$  decreased to  $1.83\pm 0.07$ , which is statistically significantly different ( $p<0.01$ ) from untreated MOSE-L cells. However, treatment of MOSE-L cells with S1P increased  $\varphi$  to  $2.99\pm 0.43$  ( $p=0.06$ ) which is an indicator of an increased surface roughness associated with S1P treatment.

To relate the membrane properties of suspended cells to cells in an attached state, Gascoyne recently measured  $C_{mem}$  and  $\varphi$  of the cell lines in the NCI-60 panel,[225] and also examined the exterior morphology of these cell lines by defining a membrane area morphological score,  $M$ .  $M$  includes three characteristics of cells when are attached in cell culture flask: flattening on the culture flask surface, cell elongation and the long dendritic projections, and small features, such as ruffles, folds and microvilli on cell surface.[225] They also showed that there is a correlation

between  $\phi$  and  $M$  which means that the cells DEP characteristics depend not only on cells size and morphology when suspended, but also on the exterior morphology of cell before releasing from the site of origin or cell culture flask[225] It was shown previously that MOSE-E cells exhibit a more cobble-stone like appearance, whereas the cells take on a more spindle-like morphology as they subsequently progress to more aggressive phenotypes.[189] This observation indicates that  $M$ , membrane area morphological score, increases during cancer progression and results, consequently, in increasing  $\phi$  and changes in dielectric properties of cells, which is consistent with our experimental results.

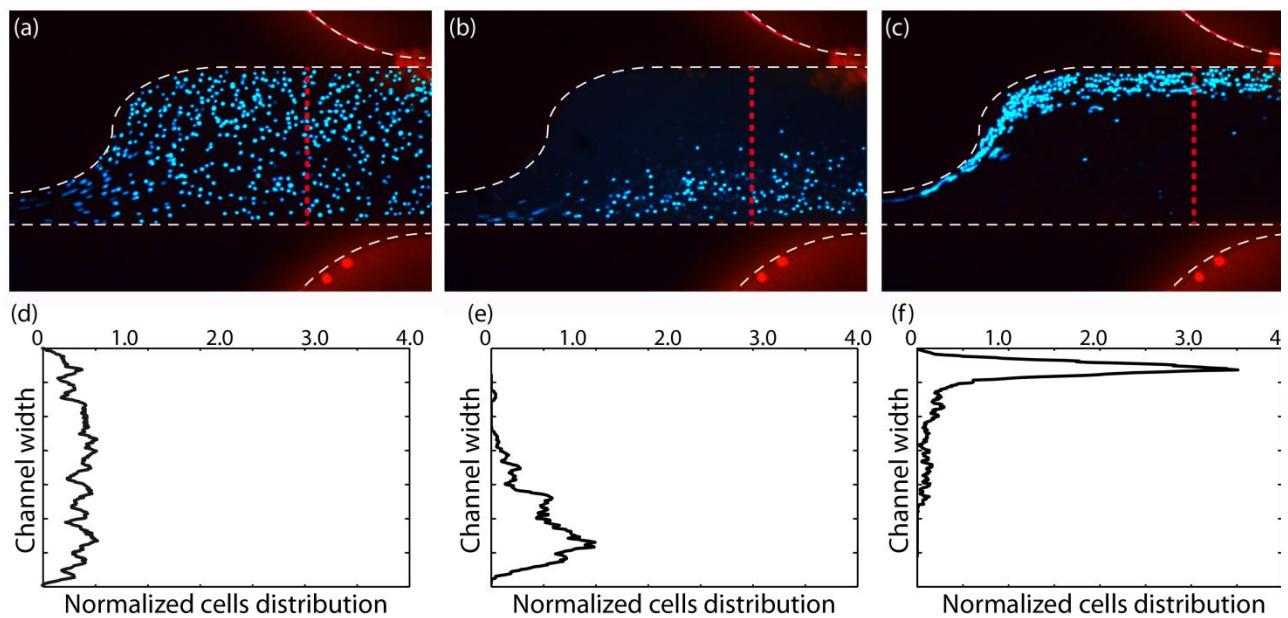


**Fig. 5.3.** Finding crossover frequency of cells based on their movement towards top or bottom half of the channel. MOSE-L cell movement in the sample channel (a) without applying any electric field, (b) due to applying  $200 V_{\text{RMS}}$  and negative DEP force at 5 kHz and (c)  $200 V_{\text{RMS}}$  and positive DEP force at 30 kHz. Normalized cell distributions corresponding to (d) no DEP force in the control (a), (e) negative DEP in (b), and (f) positive DEP in (c) [7].

Changes in dielectric properties of MOSE cells during cancer progression might also result from dysregulation of the cytoskeleton.[2] This dysregulation is common in cancer progression and alters the cellular architecture of cancer cells, affecting cellular functions, growth, and signaling events. The MOSE cell model recapitulates these changes in cellular architecture: MOSE-E cells have well-organized, long, cable-like bundles of actin fibers while MOSE-L cells have a highly disorganized actin and microtubule cytoskeleton,[189] [204] critical for the viscoelasticity of the cells.[205] Stage-dependent, step-wise changes in gene expression levels during MOSE neoplastic progression have been reported previously by using mouse whole genome microarray and gene ontology analyses.[189, 204] Specifically, progression was associated with a significant change in the expression or subcellular distribution of key cytoskeletal regulatory proteins, including focal adhesion kinase,  $\alpha$ -actinin, and vinculin.[204] Moreover, after treating MOSE-L cells with So, a significant change in the expression levels of these proteins was observed (unpublished observations). These observations are in agreement with the noted changes in dielectric properties of MOSE-derived cancer cells and suggest that the dielectric properties of cells could be correlated to a cell gene expression profile, [225]

Sphingolipid metabolites have been shown to be involved in the regulation of the cytoskeleton architecture,[226, 227] and this phenomenon has recently been confirmed in MOSE-derived cancer cells: treatment with So, but not S1P, was associated with an increased organization of the actin stress fibers,[204] and increased mechanical stiffness of MOSE-L cells. In contrast, S1P treated cells demonstrated more microvilli-like protrusions on the cell surface (unpublished observations) which may have contributed to the calculated  $\varphi$  increase in MOSE-L cells following S1P treatment ( $\varphi = 2.66 \pm 0.31$  for untreated MOSE-L). Overall, the observed shift in dielectric properties of So-treated MOSE-L cells towards a more benign-like MOSE-E profile appears consistent with our previous findings indicating direct associations between changes in cytoskeleton architecture[189, 204] elasticity,[205] and dielectric properties[2, 8] throughout progression, and the effects of sphingolipids on MOSE cell morphology.

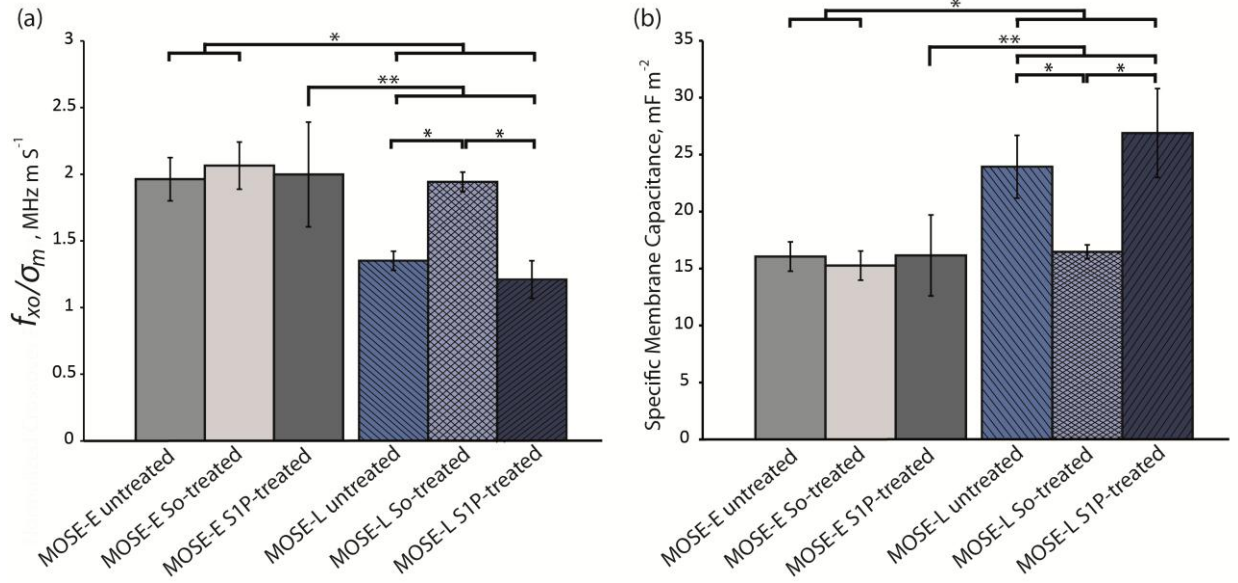


**Fig. 5.4.** So-treated late stage cells revert back to early stage based on their electrical signature.

(a)  $f_{xo}/\sigma_m$  and (b) specific membrane capacitance of untreated, So-treated, and S1P-treated of MOSE-E and -L cells. \*, and \*\* represent  $p < 0.001$ , and  $0.01$ , respectively ( $n=3$  for treated cells and  $n=6$  for untreated cells experiments) [7].

## 5.6 Conclusions

In this study, we investigated the effect of non-toxic concentrations of the sphingolipid metabolites, So, a potential anti-cancer agent, and S1P, which is regarded as tumor promoting, on the intrinsic electrical properties of benign and aggressive stages of ovarian cancer. Our results show that in contrast to S1P treatment, So treatment correlates with a partial reversal of the aggressive phenotype of late-stage ovarian cancer cells defined by a shift (decrease) in the membrane specific capacitance of MOSE-L cells towards that observed for less aggressive cells. In addition, S1P increased surface membrane protrusions whereas So-treated cells overall exhibited a smoother surface. The basis of these results is in agreement with our previous study

showing that the specific membrane capacitance of cells increases during ovarian cancer progression in a synergic model of ovarian cancer cells.[2] These studies suggest that the electrical properties of cancer cells can be targets of cancer preventive and promoting efforts. Future studies need to correlate these changes with the tumorigenicity of the cells and structural and molecular events for the design of effective prevention and treatment strategies. It is foreseeable that in the future, we may use cDEP to not only detect cancer cells of different stages but also determine the effectiveness and predict the success of chemopreventive drugs. For instance, the effectiveness of So or conventional chemotherapeutic drugs that impact the cells' surface topography and the actin cytoskeleton may be ascertained by monitoring changes in the cells' electrical signature. This would be an advantage over methods that rely solely upon expressed surface receptors, not only for applications such as cell identification and enrichment but also for targeted treatments. Utilizing cDEP for mapping electrical properties of treated cancer cells to specific disease stages of non-treated cells may allow a new, rapid method for determining drug efficacy and for performing dosage studies.

# Chapter Six

## Dielectrophoretic Differentiation of Ovarian Cancer Cells from Peritoneal Fluid

### 6.1 Introduction

Epithelial ovarian cancer is the leading cause of death from gynecological malignancies and the fourth leading cause of death in women in the United States among all cancers [190, 191]. The World Health Organization estimates that approximately 225,500 women worldwide are diagnosed with ovarian cancer [228] and 140,200 women die from it annually. In the U.S., it was estimated that 21,990 new cases of ovarian cancer would be diagnosed in 2011, and 15,460 women would die from this disease [229]. Much of this lethality is attributable to its late detection due to the lack of symptoms of earlier stages and routine screening methods are not established. However, early detection improves the survival rates of women to more than 90% [192], highlighting the importance of early detection and treatment of ovarian cancer. Ideally, screening tests should be non-invasive and highly specific to reduce false-positive results, the associated risks, and costs for the affected women [191].

In this chapter we compared the signal parameters (voltage and frequency) required to selectively capture and isolate MOSE cells at different cancer stages from normal fibroblast and macrophages that can be found in the peritoneal fluid. These results demonstrate the potential of cDEP as a method of early detection and diagnosis of ovarian cancer.

## 6.2 Device Layout

Fig. 6.1. shows the top view schematic of the microdevice. Electrode channels, which are approximately 1 cm long, are separated from the sample channel by 20  $\mu\text{m}$  barriers. Insulating pillars, 100  $\mu\text{m}$  in diameter, in the sample channel increase the non-uniformity of the electric field and enhance the DEP force.

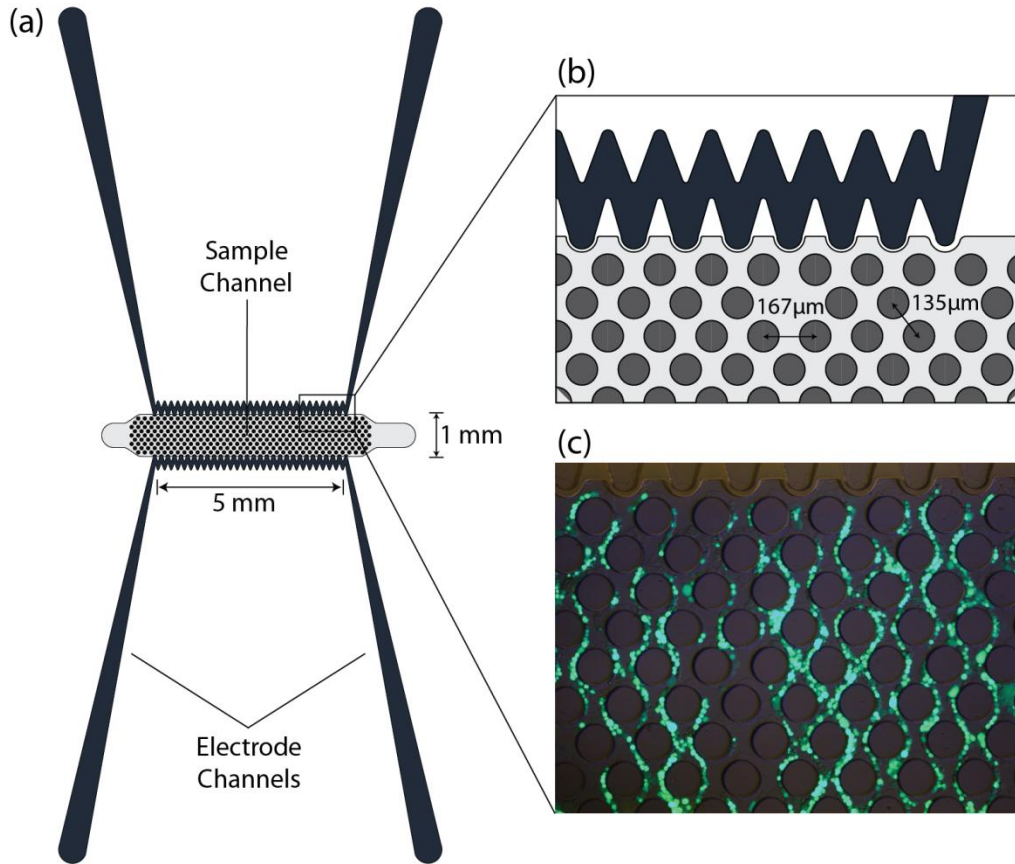


**Fig. 6.1.** (a) 2D top view schematic of the microdevices. (b) A section of the microdevice and pillars. Each pillar is 100  $\mu\text{m}$  in diameter. (c) Complete trapping of cells. Calcein AM, enzymatically converted to green fluorescent calcein, is added to the cell sample at 2 mL per mL of cell suspension [8].

The dielectrophoretic responses of early (MOSE-E), early-intermediate (MOSE-E/I), intermediate (MOSE-I), and late stage ovarian cells (MOSE-L), as well as macrophages (PC1) and fibroblasts (OP9), were studied separately using the device shown in Fig. 6.1. The frequency of the AC signal was set as indicated in each experiment for five selected frequencies: 200, 300, 400, 500, and 600 kHz. These frequencies were selected at random, and the associated voltages required to observe trapping of the first two cells (onset of trapping) and trapping of all cells (complete trapping) were recorded (Fig 6.1.b-c). Each experiment was repeated 10 times using cells from biological replicates. The student t-test method was used to determine if data from different cell lines were statistically significant different. The purpose of these experiments was to investigate if there is a difference in onset of and complete trapping between these cells types.

### 6.3 Computational Results

The fluid dynamics within the sample channel were also modeled to find the velocity field and the shear rate. Based on past experiments, the inlet velocity was set to 110  $\mu\text{m/s}$ , approximately corresponding to 0.02 mL/hr [9]. The insulating structures inside the main channel are essential tools to enhance the dielectrophoretic force by increasing the electrical resistance of the sample channel, as well as increasing the non-uniformity of the electric field. Without these structures, gradients in the electric field would be limited to areas close to the side walls of the sample channel, and most cells would not experience a strong enough dielectrophoretic force to be trapped. Adding the insulating structures allows for wider channels with uniform  $\nabla(\vec{E} \cdot \vec{E})$ , which consequently increases the throughput and selectivity of the devices.

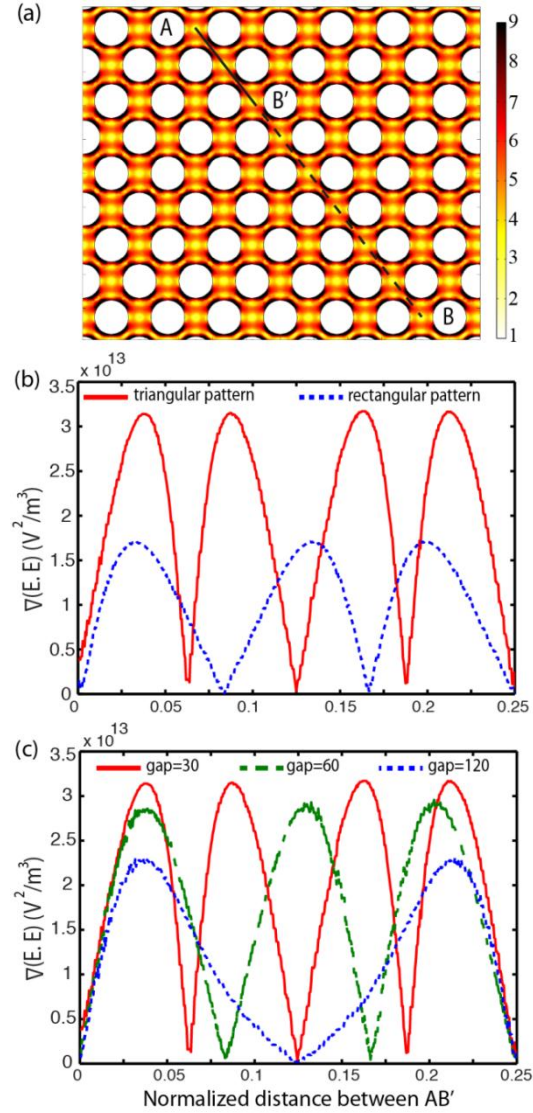
To compare microdevices with different circular pillar geometries, a diagonal line located on the center of the device has been drawn (line A-B on Fig. 6.2.a). Only the values on A-B' are shown in Fig. 6.2.b-d because these values are repeated periodically on other parts of line A-B. Fig.

6.2.a shows the contour plot of  $\nabla(\vec{E}_{RMS} \cdot \vec{E}_{RMS})$ . For the designs presented here, frequencies from 100-600 kHz and voltages from 0-300 V<sub>RMS</sub> were studied.

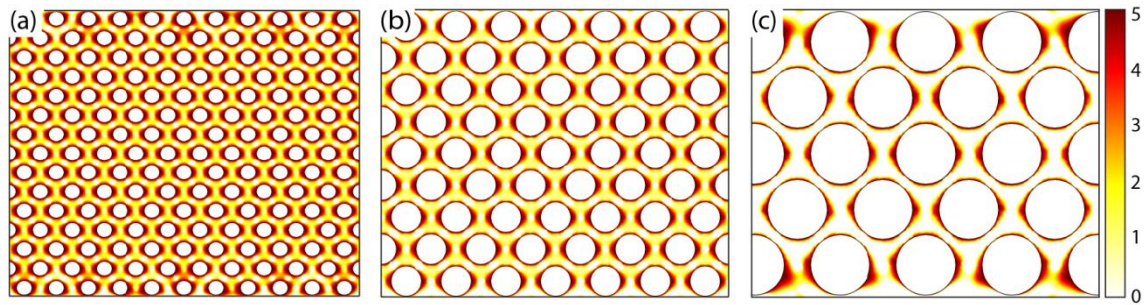
Line plots of  $\nabla(\vec{E}_{RMS} \cdot \vec{E}_{RMS})$  inside the sample channel for two different pillar arrangements, triangular (staggered, similar to Fig. 6.2.a) and rectangular arrangements are shown in Fig. 6.2.b. These demonstrate that the triangular arrangement creates higher  $\nabla(\vec{E}_{RMS} \cdot \vec{E}_{RMS})$  compared to the rectangular arrangement. This arrangement has the added benefit that the calculated hydrodynamic efficiency for capturing cells is better in triangular than in rectangular arrangements [230]. Additionally, the triangular arrangement increases the probability of cell trapping, since there is a higher frequency of cell collisions with the pillars. Based on these results, a triangular arrangement was selected.

Fig. 6.2.c shows the line plot of  $\nabla(\vec{E}_{RMS} \cdot \vec{E}_{RMS})$  for three devices with 100  $\mu\text{m}$  diameter and different gaps between the circular pillars, 30  $\mu\text{m}$ , 60  $\mu\text{m}$ , and 120  $\mu\text{m}$ . This shows that  $\nabla(\vec{E}_{RMS} \cdot \vec{E}_{RMS})$  has an inverse relation with the distance between the pillars, *i.e.*, the DEP force increases by decreasing the gap between the pillars, although this increase is not significant. To avoid mechanically filtering the cells, the distance between pillars were not reduced to less than 30  $\mu\text{m}$ . A spacing of 30  $\mu\text{m}$  was used for the remainder of this study because decreasing the gap between pillars increases the number of pillars per unit area, which increases the probability of cell trapping.

Computational results predict that the maximum shear rate in the device has a maximum value of 52 s<sup>-1</sup> which is two orders of magnitude less than the cell lysis limit of approximately 5000 s<sup>-1</sup> [231, 232]. In order to trap a cell in a moving fluid, the dielectrophoretic force should overcome the drag force. Fig. 6.3. presents drag force to dielectrophoretic force ratios for pillars with diameter of 50  $\mu\text{m}$ , 100  $\mu\text{m}$ , and 200  $\mu\text{m}$ . It was found that 50  $\mu\text{m}$  pillars have 2.25 times smaller DEP dominant area than devices with 200  $\mu\text{m}$  pillars.



**Fig. 6.2.** (a) The gradient of the electric field squared ( $\text{V}^2 \text{m}^{-3}$ ) at  $300 \text{ V}_{\text{rms}}$  and  $600 \text{ kHz}$ . The line plot of  $\nabla(\vec{E}_{\text{rms}} \cdot \vec{E}_{\text{rms}})$  on a normalized diagonal line A-B is presented for (b) triangular and rectangular pillar arrangements, (c) circular pillars with 30, 60 and  $120 \mu\text{m}$  gap and diameter of  $100 \mu\text{m}$ , at  $100 \text{ V}_{\text{rms}}$  and  $500 \text{ kHz}$  [8].



**Fig. 6.3.** Ratio of drag force to dielectrophoretic force for microdevices with equal channel width and circular pillars with diameter of (a) 50  $\mu\text{m}$ , (b) 100  $\mu\text{m}$ , and (c) 200  $\mu\text{m}$ . In dark areas DEP force is dominant, and in light areas drag force prevails [8].

In contrast, increasing the size of pillars reduces the total number of pillars per unit area, which decreases the probability of a cell entering a DEP dominant area. As a compromise between these two results, a diameter of 100  $\mu\text{m}$  was chosen. It is also important to note that the size of the trapping area should be sufficiently large to encompass several particles and avoid saturation; otherwise, the captured cells may be released by small fluctuations in the fluid flow, and thus decrease our trapping efficiency

## 6.4 Experimental Results

To determine the individual voltages for trapping the MOSE cells, we used the device shown in Fig. 6.1. Fig. 6.4. shows the onset and complete trapping voltages for four different stages of MOSE cells. The voltages required to trap different stages were statistically significant different among most stages. The largest variation in trapping between cell types was seen when comparing the voltage required for complete trapping. Between 200 and 500 kHz, the voltage required for complete trapping of MOSE cells increased as the cell type became more tumorigenic. For all cell types, the complete trapping voltages were significantly different with p-values of 0.005 or less.

At 500 kHz, MOSE-L cells were trapped at a higher voltage than MOSE-I cells, while at 600 kHz the reverse occurred. This phenomenon did not occur for complete trapping at any other frequencies or for the other cell types, and we predict that the Clausius-Mossotti factors for MOSE-L and MOSE-I cells overlapped at a frequency between 500-600 kHz.

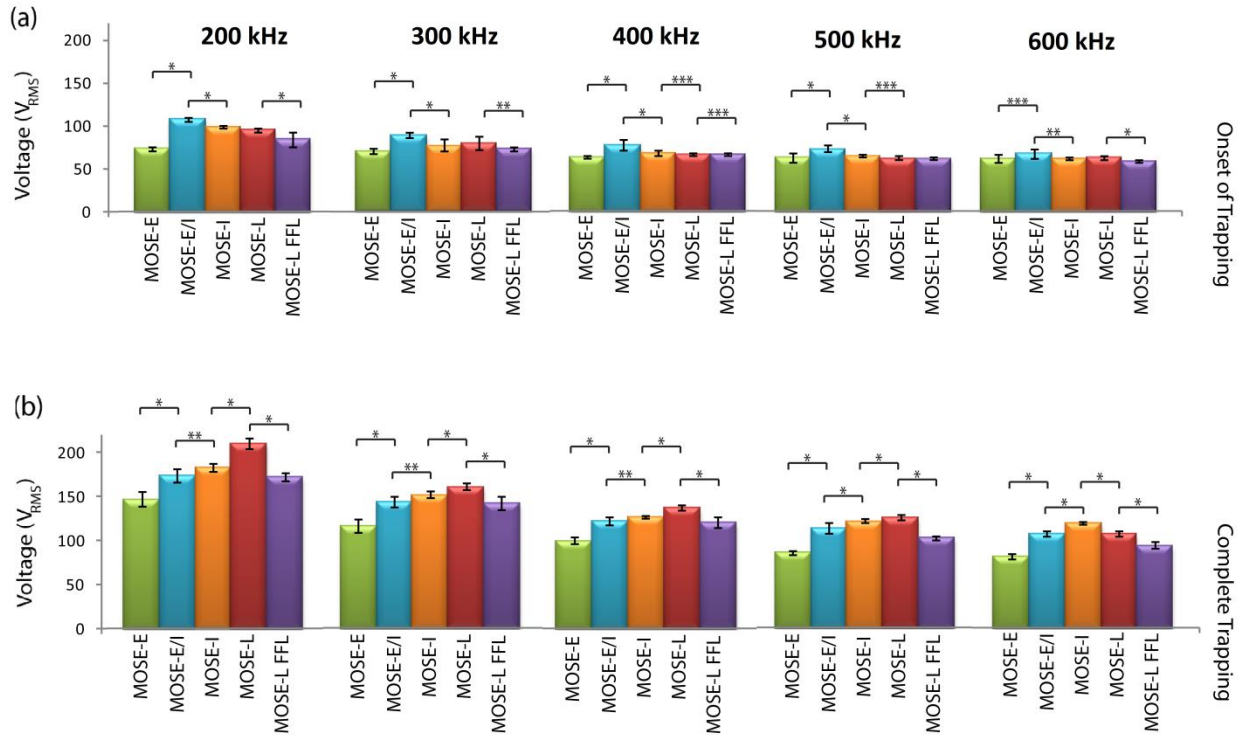


**Fig. 6.4.** (a) Onset and (b) complete trapping voltages of early (MOSE-E), early-intermediate (MOSE-E/I), intermediate (MOSE-I), late (MOSE-L), and FFL (MOSE-FFL) cells at 200, 300, 400, 500, and 600 kHz. Left and right columns present the onset of trapping and complete trapping, respectively. \*, \*\*, and \*\*\* indicate that data are significantly different with  $p < 0.0005$ ,  $p < 0.005$ , and  $p < 0.05$ , respectively ( $n=10$ ).

The onset and complete trapping of macrophages (PC1) and fibroblasts (OP9) are compared with different stages of MOSE cells in Fig. 6.5. Voltages for complete trapping of PC1 and OP9 cells

are statistically different from the various stages of MOSE cells at almost all applied frequencies in the range of 200-600 kHz. Similarly to Fig. 6.4., the voltages for onset of trapping are statistically different.

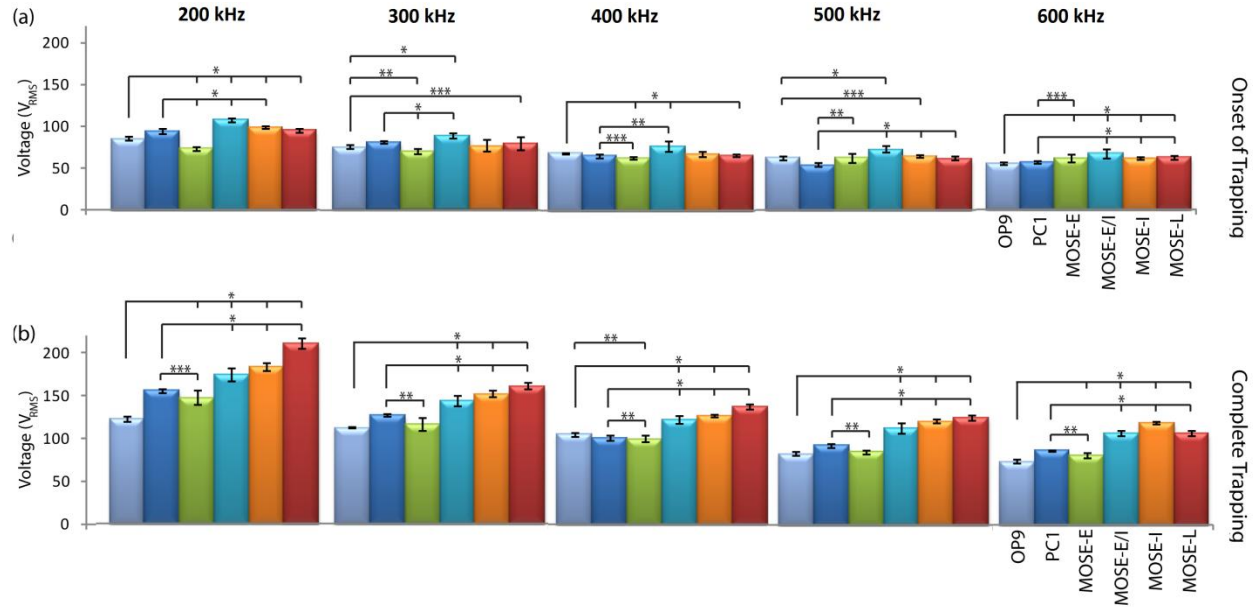


**Fig. 6.5.** (a) Onset and (b) complete trapping voltages of different stages of MOSE cells compared with macrophages (PC1) and fibroblasts (OP9) cells at 200, 300, 400, 500, and 600 kHz. Left and right columns present the onset of trapping and complete trapping, respectively. \*, \*\*, and \*\*\* indicate that data are significantly different with  $p < 0.0005$ ,  $p < 0.005$ , and  $p < 0.05$ , respectively (n=10) [8].

Fig. 6.6.a and b present the difference between the complete trapping voltage of fibroblasts (OP9) and macrophages (PC1), respectively, with different stages of MOSE cells as a function of applied frequency. These results show that the difference between the complete trapping voltage of PC1 and OP9 and different stages of MOSE cells increases with increases in malignancy and stage of the MOSE cells.

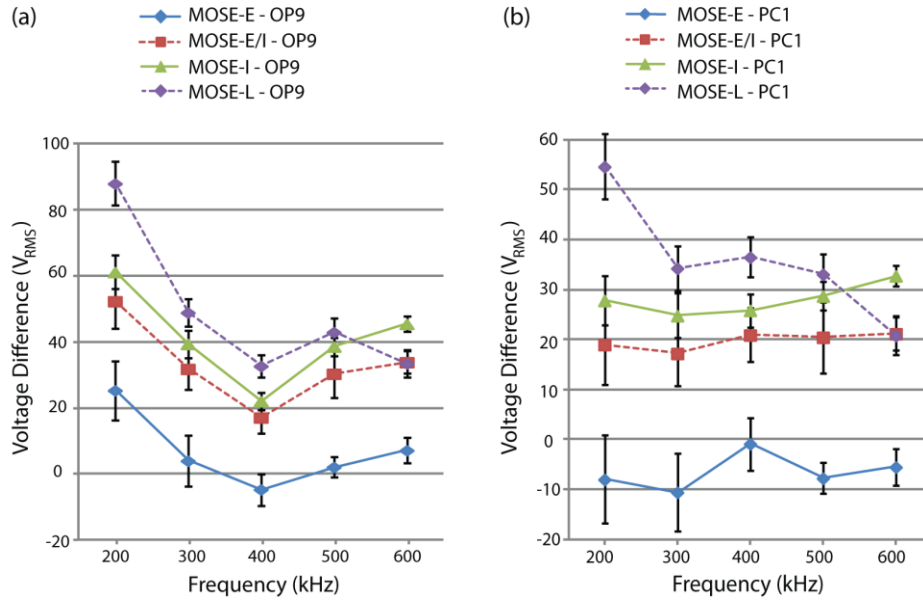


**Fig. 6.6.** (a) Difference between complete trapping voltage of (a) fibroblasts (OP9) and (b) macrophages (PC1) and different stages of MOSE cells as a function of applied frequency (n=10) [8].

## 6.5 Discussion

The dielectrophoretic properties of cells are influenced by cell membrane morphologies, membrane surface permeability, cytoplasm conductivity, and cell size [94, 233]. In this study, the cell size did not play an important role because the radii of different stages of MOSE cells were in a similar range. Radius and viability of cells were measured using Cell Viability Analyzer (Vi-Cell, Beckman Coulter). The average radius of MOSE-E, -E/I, -I, and -L cells were  $7.185 \pm 1.004$ ,  $7.163 \pm 1.245$ ,  $7.292 \pm 1.493$ , and  $7.050 \pm 1.195$   $\mu\text{m}$ , respectively. The radii of PC1 macrophages and OP9 fibroblasts were  $6.451 \pm 1.530$  and  $6.673 \pm 1.211$   $\mu\text{m}$ , respectively. Thus, we believe that the observed differences in the electrical properties of different stages of MOSE cells, Fig. 6.4., are due to the intrinsic difference between the cells not their size, as will be discussed below.

The complex dielectric properties of living cells may result from the expression levels of various surface proteins and interfacial polarization of ions at cell membrane surfaces [234]. Since different cells have dissimilar properties, they can be selectively manipulated using DEP. Cell size, shape, and membrane morphology affect the first crossover frequency and cytoplasm conductivity and nucleus-cytoplasm volume ratio affect the second crossover frequency [235]. The first crossover frequency of mammalian cells is typically less than 100 kHz [99] and the second crossover frequency is normally in the order of 10 MHz for the sample with conductivity of 100  $\mu\text{S}/\text{cm}$  [99]. The frequency range used in this study was limited between 200-600 kHz; thus, all of the aforementioned biophysical properties, especially membrane morphology, could play a role as to why different stages of MOSE cells exhibit different DEP properties.

The electrical capacitance of the cell membrane is a function of structural features, such as membrane folding, microvilli, and blebs [5]. It has been reported that there are more protrusions on the surface of transformed cells than normal cells, which results in transformed cells having a higher effective membrane capacitance than normal cells [97, 220, 221, 236]. For instance, leukemia and breast cancer cells lines have higher effective membrane capacitance than normal T lymphocytes and erythrocytes [220, 221]. This was also reported for rat kidney cells [97], murine erythroleukemia cells [236] and oral cancer cells [116].

It has been reported that there is an increase in membrane ruffles in MOSE cells as they progress to a more aggressive phenotype [188]. MOSE-E cells show a more typical cobblestone-like phenotype. MOSE-E/I cells change to more spindle-shape morphology and are smaller than MOSE-E cells. In general, MOSE cells become more spindle-shape and smaller as they progress into MOSE-I and then MOSE-L [188]. Among other functional categories, the cytoskeleton and its regulators are significantly altered during MOSE progression, which affects both cell morphology [188] and viscoelasticity [237]. Based on the presented results (Fig 6.4-6.6), *we hypothesize that these morphological changes, including the increase in surface ruffling in later*

*stages, could be the main reasons of dielectrophoretic changes between different stages of cancer cells.* This will be investigated in more detail.

In addition, membrane proteins can be related to cells' dielectrophoretic properties. For instance the dielectrophoretic properties of erythrocytes from different blood types are determined by the diverse ABO-Rh antigens on the red blood cell membrane surface; thus blood cell membranes from donors with different blood types polarize differently [229]. In yeast cells, DEP properties are modulated by the binding of lectin which can change the permittivity of the cell [238]. These observed differences in DEP response could be due to the expression levels of different, perhaps specific surface proteins or to a change in the total electrical charge and the conductivity of the cell membrane. Clearly, more in depth investigations are needed to identify changes in the MOSE cell membranes that are causal for the changes in their dielectrophoretic properties.

Most studies compare non-transformed cells with highly aggressive cancer cells, often derived from different patients [113, 116, 220, 221]. In two other studies, a normal and a malignant cell, derived from the same cell line, have been compared [97, 236]. The MOSE model allows for detection of step-wise changes during progression of syngeneic cancer cells, avoiding inter-individual differences that may affect the membrane organization, and thereby influence the dielectrophoretic properties. Thus, this model is more applicable to identify differences between progressive stages of transformed cells derived from the same cell line as would occur in the clinical setting. The current study is the first study that compares the dielectrophoretic responses of different stages of cancer cells, which are extracted from one cell line.

Furthermore, MOSE cells display unique behavior in comparison to fibroblasts and macrophages, representing normal and inflammatory cells found in the peritoneal fluid. These varying physical properties between MOSE cells, OP9 fibroblasts, and PC1 macrophages can be used to explain the distinct trapping regions among these cells, as shown in Fig. 6.5. From these data, it would seem possible to selectively screen for ovarian cells in the midst of background

peritoneal cells, which is a likely scenario in true patient samples. Thus, these preliminary results suggest that cDEP technique has the potential to be used as a tool for early detection of ovarian cancer.

MOSE-L firefly luciferase-expressing (FFL) cells are highly aggressive, metastatic tumor-initiating cells that can rapidly disseminate disease with as few as 100 implantable cells [239]. Fig. 6.4. shows that trapping voltage of MOSE-FFL cells does not follow the trend of progression from MOSE-E to MOSE-L cells. Although MOSE-FFL cells are more aggressive, the trapping voltage of MOSE-FFL cells is less than MOSE-L cells. The results presented in Chapter 7 for enriching prostate cancer stem cells suggests that cDEP microdevices (shown in Fig. 6.1) are sensitive enough to separate aggressive cancer stem cells from cancer stem cells. However, these microdevices may not be able to separate CSCs from intermediate stages of the disease, since CSCs trapping voltage decreases towards the voltages for trapping intermediate stages of cancer cells. We think that the difference in the trapping voltage of MOSE-E and MOSE-FFL cells is still significant enough to enable cDEP to enrich MOSE-FFL cells from a mixture of benign cells based on their dielectrophoretic properties; however, a step by step sorting can be used as is explained below.

There is a heterogeneous mixture of different stages of ovarian cancer cells as well as peritoneal cells in a patient peritoneal sample. The results presented in Fig. 6.4 show that it is not possible to sort the cells as a one stage cDEP device. Instead devices with different stages of separation (probably at different voltages and/or frequencies, or different geometrical parametric designs) should be used. This separation strategy is suggested: first cancer cells at late stage can be separated from other cells, since MOSE-L cells require higher voltage to be trapped comparing to all other studied cells. Then, since cancer stem cells are the next having highest trapping voltage, they can be separated from the remained mixture which includes intermediate stage and benign and normal cells. After isolating late stage cells and cancer stem cells, the remaining sample includes intermediate and benign cancer cells as well as normal peritoneal cells.

## **6.6 Conclusions**

The results presented here demonstrate that aggressive ovarian cancer cells display a significantly different voltage that allows them to be dielectrophoretically distinguished and trapped from their non-transformed progenitor cells as well as from other cell types that may be found in peritoneal serous exudate fluid. Studying the dielectrophoretic responses of these cells is the first step in developing a clinical diagnostics system centered on contactless dielectrophoresis to separate ovarian epithelial cells from peritoneal fluid to potentially detect even early and intermediate stages of the disease. Early diagnosis will result in early treatment and will increase the survival rates of the affected women. Future work will focus on optimizing device performance and building towards a clinically applicable method for early detection of ovarian cancer.

# Chapter Seven

## Isolation of Prostate Tumor Initiating Cells (TICs) through Their Dielectrophoretic Signature

### 7.1 Introduction

In this chapter, we have investigated the dielectric response of prostate tumor initiating cells (TICs) utilizing contactless dielectrophoresis. A 1 mm wide cDEP device was used to characterize the dielectrophoretic response of prostate TICs. Two higher throughput devices, each 5 mm wide, were used in parallel to separate TICs from non-TICs and analyze the sample off-chip. Our results show that TICs have distinctively different dielectric properties than non-TICs and demonstrate that the voltage required to completely trap the cells in the collection array is different for the two cell types. Our results with the two wider devices verified cell viability and enabled us to culture the sorted cells. Unsorted samples of prostate cancer cells were separated using our cDEP device based on their dielectrophoretic response and subsequently cultured. Only the cells with a DEP response indicating they were TICs generated spheroids once cultured, which is indicative of tumor initiating cells.

### 7.2 Device Layout

Fig. 7.1. shows the top view schematic of the 1 mm wide microdevice. Electrode channels, which are approximately 1 cm long, are separated from the fluidic channel by 20  $\mu\text{m}$  PDMS barriers. Insulating pillars of 100  $\mu\text{m}$  in diameter have been used in the fluidic channel to create

the nonuniformity of the electric field and enhance the dielectrophoretic force. The distance between the pillars has been optimized using computational modeling. Since the throughput of this device is low (0.02 mL/hr), it does not allow isolation of enough number of cells to test cell viability and culturing. Thus, two microdevices with 5 mm wide, 10 mm long, and 50  $\mu\text{m}$  deep were used in parallel (0.2 mL/hr in total) which allowed collection of cells.

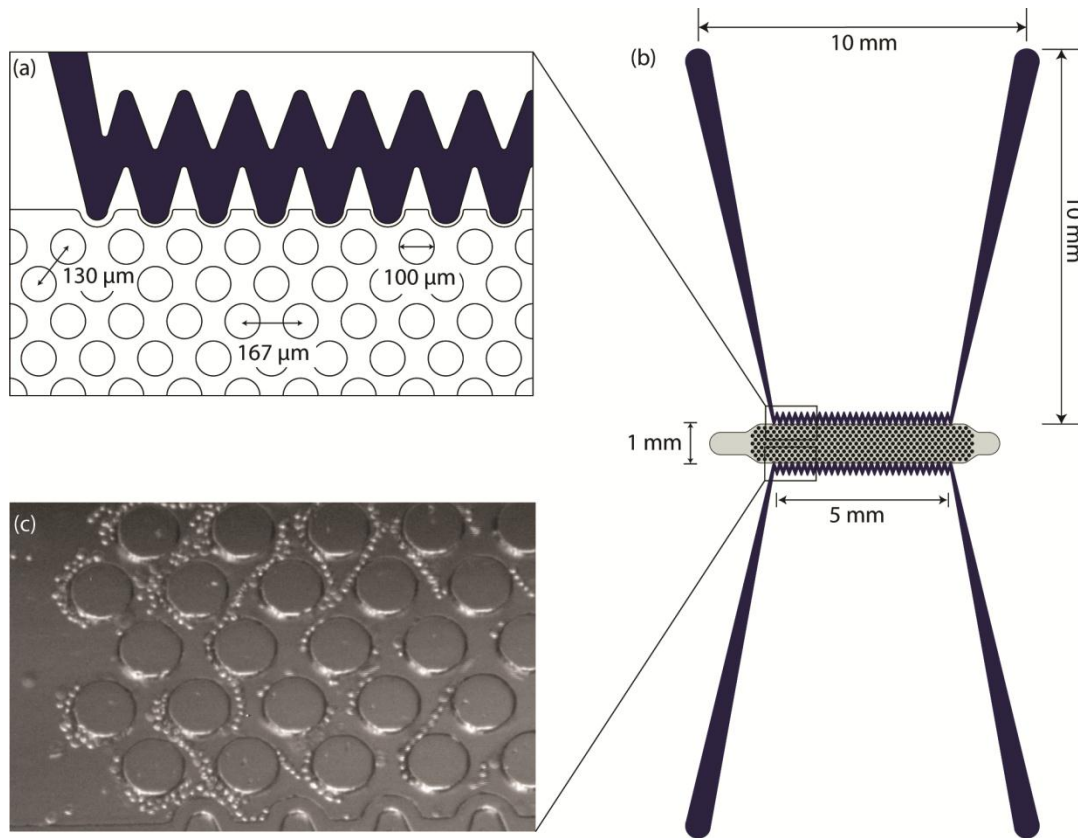


**Fig. 7.1.** Top view schematic and dimensions of (a) a section of microchannels and pillars and (b) cDEP microdevice. (c) Trapped cells at 600 kHz and 129  $V_{\text{rms}}$  [9].

### 7.3 Data analysis

Percentage of trapping of the cells was calculated by recording the outlet before and after turning on the electric field, and the number of cells leaving the pillar arrangement was counted manually in each case. To determine whether or not some cells are trapped due to fouling, several control experiments were run without applying an electric field and the number of cells entering the channel were counted and compared to the number of cells leaving the channel per unit of time. It was found that cell fouling is negligible in these experiments and trapping is a result only of the dielectrophoretic force acting on the cells.

### 7.4 Flow cytometry

Flow cytometry was used to isolate cells with putative markers of TIC to use them for the characterization of the cells dielectric properties. Single-cell suspensions of the PC3 cells were labeled with BODIPY®-aminoacetaldehyde (Aldefluor, for ALDH) as explained above. DEAB (ALDH inhibitor) was used for ALDH control in separate incubations to validate specificity. The labeled cells and their controls were sorted in an Aria cell sorter in the flow cytometry core facility of the Wake Forest University Comprehensive Cancer Center. Fig. 7.2. shows representative data from PC3 cells for ALDH expression. Data indicates that approximately 15.4% of cells specifically express ALDH.

### 7.5 Computational Results

Fig. 7.3.a denotes  $\nabla(\vec{E}_{rms} \cdot \vec{E}_{rms})$ , at 300 V<sub>rms</sub> and 600 kHz in the 1 mm wide device. Insulating pillars located in the fluidic channel induce a large dielectrophoretic force by generating non-uniformities in the electric field.

The effect of the distance between the circular pillars on creating a strong and uniform gradient of the electric field intensity across the main channel was studied. It was observed that the

gradient of the electric field has an inverse relation with the distance between the pillars (results not shown). However, this gap cannot be less than 30  $\mu\text{m}$  as such devices will mechanically filter the prostate cancer cells due to their size. Thus, the device with 30  $\mu\text{m}$  gap between the pillars is optimum for our experiments.

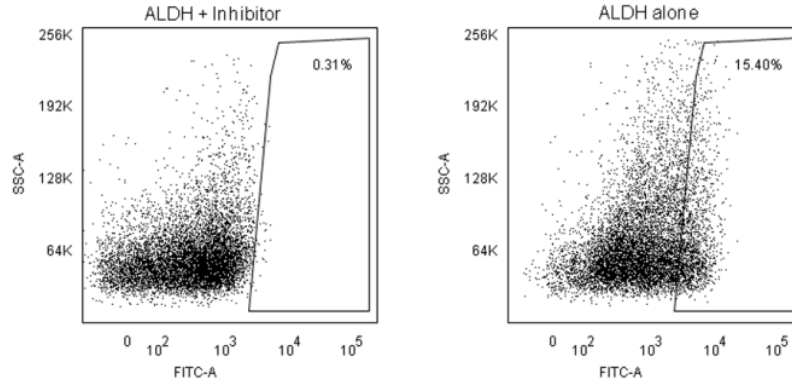


**Fig. 7.2.** Identification of ALDH+ cells in a human prostate cancer cell line (PC3). 10,000 events were evaluated on a BD FACS Aria cell sorter. Histograms show gated populations (a) without and (b) with Diethylaminobenzaldehyde (DEAB) inhibitor. Numbers in gated areas indicate the percent of the total population represented in the area [9].

$\nabla(\vec{E}_{rms} \cdot \vec{E}_{rms})$  was calculated for both, the 1 mm and the 5 mm wide devices. A comparison between  $\nabla(\vec{E}_{rms} \cdot \vec{E}_{rms})$  on line A-B demonstrated in Fig. 7.3.c showed that  $\nabla(\vec{E}_{rms} \cdot \vec{E}_{rms})$  generated by the 1 mm device is approximately 2.4 times higher than the 5 mm device. On the other hand,  $\nabla(\vec{E}_{rms} \cdot \vec{E}_{rms})$  is proportional to applied voltage squared,  $V_{rms}^2$ ; thus, by applying  $\sqrt{2.4}$  times higher voltage in 5 mm device, equal  $\nabla(\vec{E}_{rms} \cdot \vec{E}_{rms})$  as 1 mm device can be generated. Results for the magnitude of  $\nabla(\vec{E}_{rms} \cdot \vec{E}_{rms})$  for the 1 mm device is shown on Fig. 7.3.a.

Fluid dynamics was also modeled to find the velocity field and shear rate in the main fluidic channel (Fig. 7.3.b-c). The inlet velocity was set to  $110 \mu\text{m/s}$  based on the flow rate in the experiments. It can be seen in Fig. 7.3.c that the computational result predicts the maximum shear rate in the device to be approximately two orders of magnitude less than the cell lysis limit.

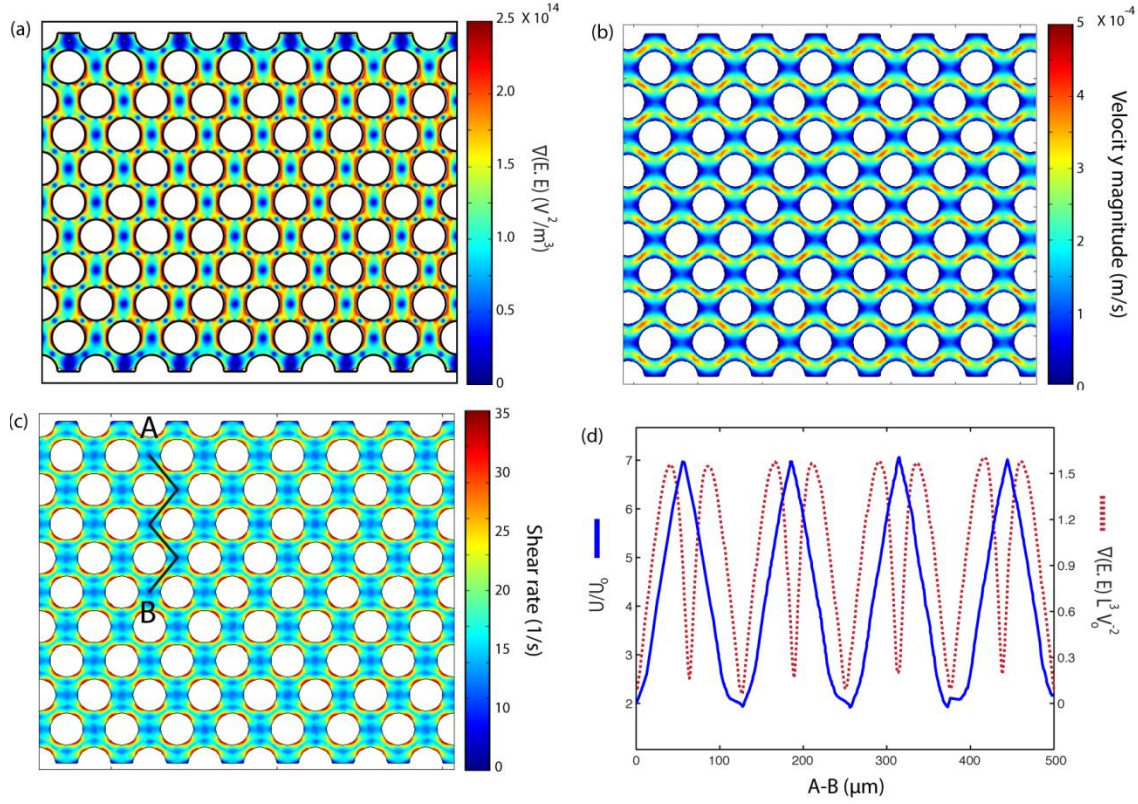


**Fig. 7.3.** Computational modeling was used to predict the performance of the 1 mm-wide device. Surface plot of (a) the gradient of the electric field squared ( $\text{V}^2/\text{m}^3$ ) at  $300 \text{ V}_{\text{rms}}$  and  $600 \text{ kHz}$ , (b) flow velocity magnitude ( $\mu\text{m/s}$ ), and (c) shear rate (s) in the fluidic channel. (d) Dimensionless values of velocity and  $\nabla(\vec{E}_{\text{rms}} \cdot \vec{E}_{\text{rms}})$  on line A-B. Velocity,  $U$ , is dimensionalized by inlet velocity,  $U_o = 110 \mu\text{m/s}$ .  $\nabla(\vec{E}_{\text{rms}} \cdot \vec{E}_{\text{rms}})$  is dimensionalized by applied voltage,  $V_o$ , and the distance between electrode channels ( $= 1 \text{ mm}$ ), which is equal to channel width [9].

Fig. 7.3.d presents the dimensionless values of  $\nabla(\vec{E}_{rms} \cdot \vec{E}_{rms})$  and velocity on line A-B, which are proportional to the values of the dielectrophoretic and drag forces, respectively. Dimensionless velocity profile shows that by travelling between rows of pillars, the velocity increases and reaches its maximum value in the diagonal gap between the pillars.  $\nabla(\vec{E}_{rms} \cdot \vec{E}_{rms})$  has two maximum between each two row of pillars which are located approximately in the narrow gap between the insulators, and there is also a local minimum between these maximums. Minimum values of both velocity and  $\nabla(\vec{E}_{rms} \cdot \vec{E}_{rms})$  on line A-B are located in the horizontal gap between two columns of pillars.

## 7.6 Results and Discussion

The DEP response of prostate cancer cells expressing ALDH positive (TICs) and ALDH negative (non-TICs) was investigated separately to evaluate their dielectrophoretic response. Cells used were isolated and enriched by FACS and their signal parameters for DEP trapping was measured and recorded for the microfluidic platform described. It was observed that there was a great tendency for cells to move towards the high DEP regions in the main channel around the pillars and in the narrow region between them (Fig. 7.1.c). Comparing with our numerical modelling, these results indicate that TICs were experienced positive DEP force in the frequency range we applied in our microfluidic devices.

The voltages and frequencies of the applied signal for trapping of ALDH positive and negative prostate cancer cells are reported in Fig. 7.4.a-e. The frequency of the signal was set as indicated in each experiment, and the associated voltages required to observe i) trapping of the first cell (onset of trapping) and ii) trapping of all cells (complete trapping) were recorded. These results indicate that complete trapping of prostate TICs occurs at a lower voltage than that needed for complete trapping of non-TICs. Fig. 7.4.a-e also shows that by increasing the frequency, the voltage required for trapping decreases. This decrease occurs because the magnitude of the

electric field gradient increases by increasing the frequency due to the capacitive behavior of the barriers, so that the same DEP force can be achieved by applying a lower voltage.

Ideally, the proposed device will selectively trap all ALDH positive cells while letting all ALDH negative cells flow towards the outlet due to the difference in their dielectric properties. To evaluate the selectivity of the design, experiments with ALDH negative cells were performed at voltages and frequencies for complete trapping of ALDH positive cells. Results show that only 60-70% of ALDH negative cells were trapped at the complete trapping voltages and frequencies of ALDH positive cells (Fig. 7.4.f).

It was observed, Fig. 7.4.a-e, that the difference between onset of trapping and complete trapping voltage required for ALDH positive cells is less than negative cells. This difference also decreases with frequency when it is increased from 200 kHz to 600 kHz, specifically for ALDH positive cells, thus enhancing the separation of the cells. Therefore, separation of ALDH positive from negative cells was performed only at a frequency of 600 kHz in the following experiments.

A 1 mm wide device (see Fig. 7.1.) was used to compare the electrical properties of ALDH positive (TICs) and negative cells (non-TICs). However, since the 1 mm wide device has a very low throughput (0.02 mL/hr) it is not practical for taking cells off the chip in the quantities necessary for evaluation of cell viability and for culturing cells after the DEP experiments. On the other hand, due to microscopy limitations, the onset and complete trapping of cells can be accurately observed only in the 1 mm wide design since the narrower device allows simultaneous visualization of the entire width. Two devices that were 5 mm wide were used in parallel (0.2 mL/hr in total) which allows collection of cells. The flow rate used in the wider devices produced the same average flow velocity as in the 1 mm wide device (110  $\mu\text{m/s}$ ). Moreover, the applied voltage has been adjusted using computational modelling for the 5 mm device to produce the same DEP force as the 1 mm device at a specific frequency. Thus, the cells will exhibit the

same behavior in both devices, while increasing the throughput of the system by using 5 mm wide devices.

Generation of spheroids from cells derived from a number of tissues grown in a low-binding environment has been used to selectively propagate and enrich cells with enhanced stem cell properties. Furthermore, data suggests that spheroids from tumor cell populations are enriched with TIC properties. Therefore, a prostasphere assay was performed to evaluate sphere-forming abilities of the cDEP separated cells. Non-sorted PC3 cells were continuously injected into the cDEP microdevice at the flow rate of 0.2 mL/hr using a microsyringe pump and an electric field at 600 kHz and 300  $V_{\text{rms}}$  was generated to trap the cells by means of DEP. After 30 minutes, the voltage was decreased to 280  $V_{\text{rms}}$  ( $\approx \sqrt{2.4} \times 179 V_{\text{rms}}$ , where 179  $V_{\text{rms}}$  is the complete trapping voltage of ALDH positive cells at 600 kHz, see Fig. 7.4.e) to release some cells while the rest were still immobilized in the areas of high DEP force around the pillars of the device. Cells that could have escaped the trapping area when the potential of 300  $V_{\text{rms}}$  was applied as well as those that were released when the voltage was decreased to 280  $V_{\text{rms}}$  were collected and cultured. Then, by decreasing the voltage to 150  $V_{\text{rms}}$  (complete trapping voltage for TICs) some other cells were released. It can be inferred from the results presented in Fig. 7.4. that most of the non-trapped and released cells are non-TICs, since the voltage for their complete trapping is higher than that for the TICs. Afterwards, the inlet fed was switched to DEP buffer for 15 minutes while the electric field was maintained at TIC trapping conditions to ensure all released cells exited the microdevice. Collection of the rest of the cells, which were expected to be enriched in TICs, was achieved by removing the electric field using DEP buffer as suspending medium.

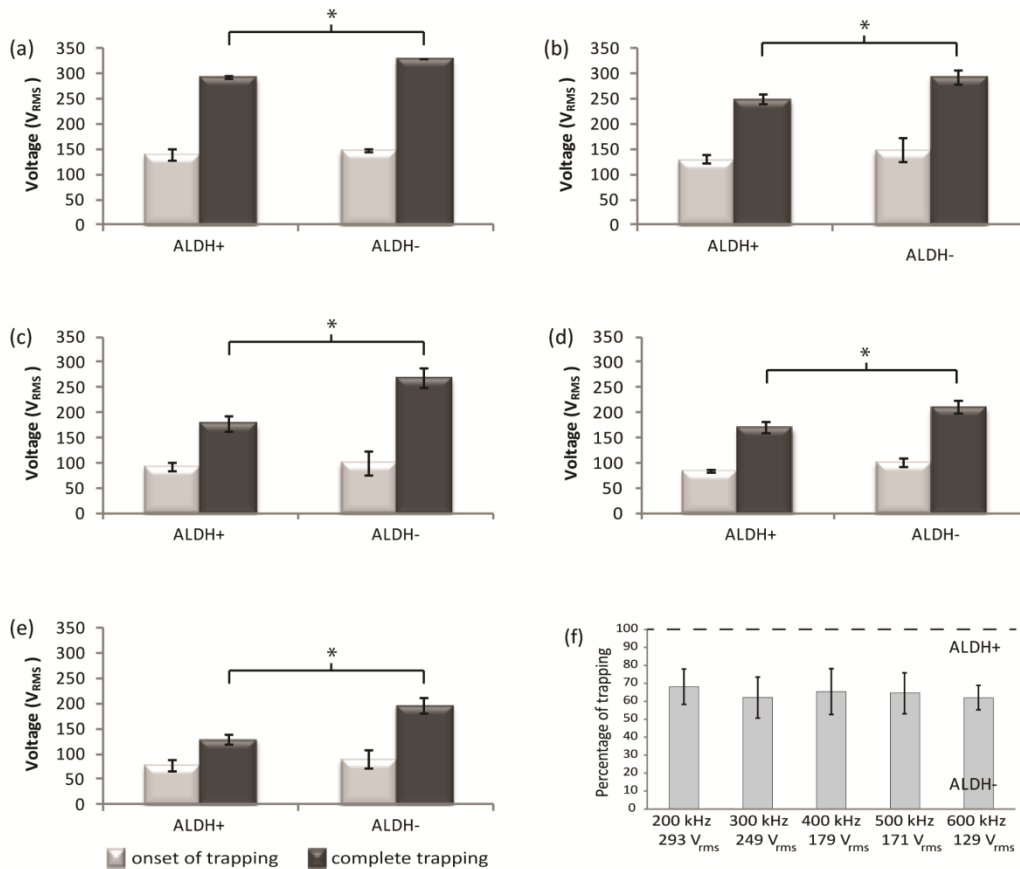


**Fig. 7.4.** Voltage of trapping of ALDH positive and ALDH negative cells at (a) 200 kHz, (b) 300 kHz, (c) 400 kHz, (d) 500 kHz, and (e) 600 kHz (n=4). Light grey and dark grey bars present the onset of trapping and complete trapping, respectively. Complete trapping voltage of ALDH positive and negative cells at each frequency are significantly different ( $p < 0.005$ ), represented by \*. (f) Percentage of trapping of ALDH negative cells at 200-600 kHz at complete trapping voltage of ALDH positive cells [9].

The collected samples as well as non-sorted PC3 cells were cultured, used as the control experiment. Fig. 7.5. shows the formation of spheroids of the three groups of cells after 3 weeks. It can be seen that no large spheroid was observed in the dish containing cells which were released before or at 280 V<sub>rms</sub> (Fig. 7.5.b), evidence that the majority of these cells were non-

TICs. On the other hand, there were several large spheroids in the dish cultured with the cells that were released after turning off the electric field (Fig. 7.5.c), which validates the presence of TICs. Viability of the cells was also determined by trypan blue exclusion before and after the experiments and no significant change in the cells viability was observed. These results are in agreement with the results presented in Fig. 7.4, demonstrating that TICs exhibit stronger DEP force than non-TICs at a specific frequency and voltage since their dielectric properties differ, and therefore lower voltages are needed to trap them.

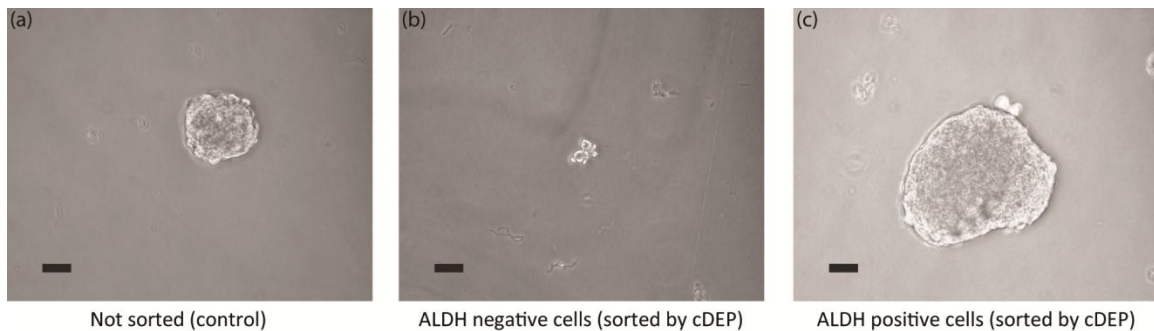


**Fig. 7.5.** Photos of spheroids generated by culturing (a) unsorted PC3 cells (control), (b) released cells at  $280 V_{\text{rms}}$  (ALDH negative), and (c) released cells after turning electric field off (ALDH positive). Images are taken after 3 weeks at 20X magnification. Bars are 50  $\mu\text{m}$  long [9].

Comparing the results presented in Fig. 7.4 for prostate ALDH+ cells (CSCs) and ALDH- cells (normal cancer cells) with the results presented in Fig. 6.4 for MOSE-L cells and MOSE-FFL cells (which have cancer stem cells properties), we can conclude that the trapping voltage of cells with cancer stemness properties is lower than late stages of cancer cells. Thus, cDEP has the potential to isolate cancer stem cells from the late stages of the disease. It can be seen that the trapping voltage of MOSE-FFL cells is closer to intermediate stage of MOSE cells. Based on the presented results we predict that cDEP microdevices (shown in Fig. 6.1) can be used to isolate CSCs from a mixture of late stages and benign cancer cells as well as normal background cells. However as was discussed in Chapter Six, first late stage of cells should be isolated since they

have the highest trapping voltage, and then cancer stem cells can be isolated from benign cells and normal peritoneal cells. After isolating late aggressive and cancer stem cells, the remaining sample contains benign and normal cells.

Up until recently, no one has studied whether there are bioelectrical differences between CSCs and their counterpart. Current CSCs enrichment techniques rely on cell membrane surface biomarkers. This becomes more significant knowing that in some cancer types, CSCs are very rare. For instance in the case of pancreatic cancer, less than 1% of cancer cells expressed positive to specific biomarkers and showed significantly high tumorigenic potential, indicating they are CSCs [15].

In this study we tried to further investigate the biophysical reasons that make CSCs different from normal cancer cells. Stage of differentiation changes the cells protein cytoskeleton which consequently changes the mechanical and electrical properties of cells at different stages of differentiation [95]. As an example, the differentiation of the erythroleukaemia cells changes the characteristics of the surface from having numerous microvilli and filopodia that protrude from cells body to mature cells which are smooth and have a discoid surface [117]. Differentiation also increases the integrity of the spectrin in cytoskeleton and increases structural protein content of the membrane causing a decrease in the membrane leakage and membrane fluidity [117].

Cells' organelles, e.g. endoplasmic reticulum, nucleus, and mitochondria, change during differentiation of cells and can affect their DEP properties. As an example, differentiation, transformation, and tumorigenicity of cells make a significant change in mitochondrial membrane potential [129]. Carcinoma cells have higher mitochondrial membrane potential than normal cells [130-132]. Based on their mitochondrial membrane potential, cells can be sorted as CSC > cancer cells (aggressive stages) > normal epithelial (or benign) cells [129]. Moreover, N/C ratio decreases by cell differentiation and maturity [1] and changes the effective conductivity and permittivity of cells. For instance, limbal epithelial stem cells have a higher

N/C ratio ( $=0.82$  [137]) than peripheral corneal epithelial cells ( $=0.17$  [138]), [1]. Human embryonic stem (hES) cells have typically higher N/C ratio than ordinary somatic cells which affects their dielectric properties and consequently can be used to separate these cells.

## **7.7 Conclusions**

The enrichment achieved by the presented device demonstrates the difference in the dielectric properties of prostate TICs and non-TICs. This difference can be used to isolate them by means of positive DEP, eliminating the necessity of extensive sample preparation (no antibody labeling) which is the other advantage of cDEP over other cell sorting techniques. Another advantage of cDEP when compared to flow cytometry techniques, such as FACS, is that cDEP can be utilized to isolate probable subpopulations of cells by sorting populations at different voltages. Since current techniques cannot entirely isolate TICs from background, cDEP may offer an opportunity to identify the rare subpopulation(s) of ALDH positive cells that are the tumor initiating cell.

# Chapter Eight

## Isolation of Rare Cancer Cells from Blood Cells Using Dielectrophoresis

### 8.1 Introduction

Circulating tumor cells (CTCs) are rare cells which are shed from tumors during the progression of cancer [16]. There exists a strong potential that investigation of these rare cells will lead to novel cancer treatments and patient specific medicines. However, isolation and characterization of these cells is arduous due to their low concentration in whole blood [16], thought to be fewer than 100 cells per mL [14]. The current state of the art CTC detection methods include fluorescence activated cell sorting (FACS) [12], magnetic bead assisted cells sorting (MACS) [13], and functionalized pillar microchips [14] which use surface or intracellular antibody probes to identify rare cells.

In addition to identification via surface proteins, rare cells can be distinguished and sorted using their intrinsic biophysical and electrical properties [240]. In this study, we demonstrate the ability to trap a low concentration of cancer cells from a blood cells sample. MDA-MB-231 breast cancer cells were individually added to a physiologically comparable suspension of hematologic cells in a low conductivity buffer. Non-simultaneous visualizations of the inlet and outlet regions of the device ascertained maximum cancer cell trapping percentage of 96% at a flow rate of 0.2 mL/hr.

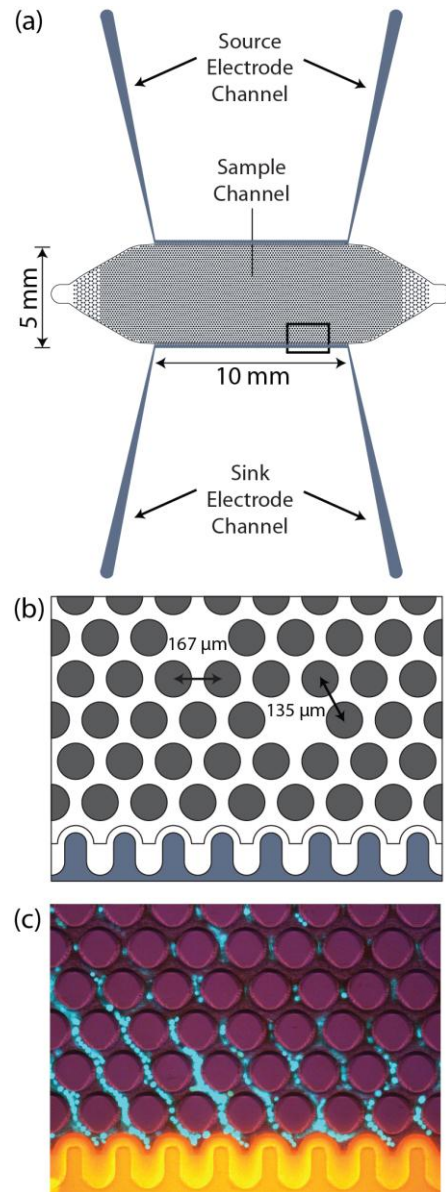


**Fig. 8.1.** (a - b) Schematic representation of the cDEP microdevice used in this study. The insulating barrier between the sample channel (grey) and the fluid electrode channels (blue) is 20- $\mu\text{m}$  thick. (c) Breast cancer cells (blue) are trapped due to DEP force. Blood cells are moving in the background flow. More cancer cells were used in to take this figure to make cells more visible [10].

## 8.2 Device layout

Two cDEP devices, shown in Fig. 8.1.a-b, each with a 5-mm wide, 10-mm long, and 50- $\mu\text{m}$  deep sample channel were used in parallel. There are 4000 pillars in each sample channel that produce regions of highly non-uniform electric field in their periphery. The geometry and size of these insulating pillars have been designed to optimize the fluid drag and DEP forces ratio resulting in efficient trapping of cancer cells [9].

After a steady fluid velocity was achieved, a 600 kHz sine wave was applied at voltages between 0 and 300  $V_{\text{RMS}}$ . The inlet section of the device was observed for 15 minutes and the number of cells observed was counted. Then the outlet section of the device was observed for 15 minutes and the number of cells was again counted. The estimated trapping percentage was then calculated based on the differences in these observations. This process was repeated 3 times for each signal parameter.

Several control experiments were run without applying an electric field, and the number of cells entering the channel were counted and compared to the number of cells leaving the channel per unit of time. In the absence of an applied electric field, fouling of both cancer cells and blood cells was found to be negligible.

## 8.3 Computational Results

Computational modeling of the electric field and fluid dynamics were used to estimate device performance (Fig. 8.2). Our numerical results indicate that  $\nabla|\vec{E}_{\text{RMS}} \cdot \vec{E}_{\text{RMS}}|$  is on the order of  $10^{14} \text{ V}^2\text{m}^{-3}$  when 300  $V_{\text{RMS}}$  is applied. This level is sufficiently above the required threshold of  $10^{12} \text{ V}^2\text{m}^{-3}$  established in previous cDEP studies [196]. Previous investigations on the edge-to-edge separation of pillars found that  $\nabla|\vec{E}_{\text{rms}} \cdot \vec{E}_{\text{rms}}|$  has an inverse relation with the distance between the pillars [9]. An edge-to-edge spacing of 25  $\mu\text{m}$  was chosen for the

experimental device to maximize DEP forces and minimize fouling. The maximum shear rate in this configuration was  $52 \text{ s}^{-1}$  [9], well below the established threshold to cause cell lysis of  $5000 \text{ s}^{-1}$  [231].

The ratio of drag force to DEP force was calculated assuming an average cell radius of approximately  $9 \text{ }\mu\text{m}$  [196] and  $f_{\text{CM}} = 1$  [114]. The spatial variation of this ratio is shown in Fig. 8.2. There are regions on the front and back of each pillar where DEP force is significantly stronger than drag force. We observed that most of the cells were indeed trapped in these DEP-dominant areas, consistent with the computational results.

## 8.4 Experimental Results

When a 600 kHz signal was applied, cancer cells began to move toward the pillars. As the voltage was increased cancer cells began to be trapped near the front and back surfaces of the pillars. These regions correspond to the simulated regions of highest  $\nabla|\vec{E}_{\text{RMS}} \cdot \vec{E}_{\text{RMS}}|$ . In contrast, the red blood cells were mostly unaffected by the DEP force, since that force is proportional to the cubed radius of the particles. However, a small (comparing to cancer cells), un-quantified number of these blood cells were trapped, which is under further investigation.

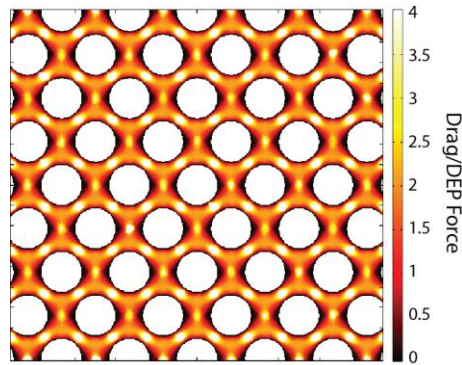


**Fig. 8.2.** Computational modeling is used to predict the performance of the device. Surface plot of drag force to DEP force ratio [10].

Samples with cancer cell concentrations of  $10^3$  cancer cells per mL ( $10^7$ :1 ratio of hematologic to cancer cells) were evaluated. Fig. 8.3. presents the percentage of MDA-MB-231 cells that were trapped at a constant frequency of 600 kHz and voltages ranging from 0-300  $V_{RMS}$  for concentration of  $10^3$  cancer cell per 1 mL of suspended blood cells. On average, 96% of MDA-MB-231 cells were trapped at 300  $V_{RMS}$  and 600 kHz. Our preliminary results showed that similar trapping percentages can be achieved for lower concentrations of cancer cells, including 100 cancer cells per mL of blood cells sample as well as other cancer cell lines using this parameter (data not shown), indicating that this method will potentially work for the detection of many types of cancer cells and in lower concentrations.

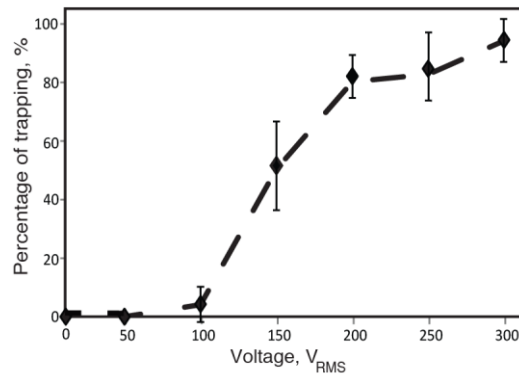


**Fig. 8.3.** Percentage of trapping of MDA-MB-231 cells at 0-300  $V_{RMS}$  at 600 kHz [10].

## 8.5 Conclusion

In this study, we used a cDEP device that has a high selectivity towards cancer cells, a low selectivity towards red blood cells, high flow rate, and low shear rate. The first two objectives ensure that a majority of cancer cells, which are typically present in low concentrations, can be trapped while preventing clogging due to over-enrichment of red blood cells. A high flow rate is necessary to seek out the hypothesized 10-100 CTCs in each milliliter of patient blood. Finally, a low shear rate is essential for preventing cell damage

due to the velocity of the sample fluid. This work shows the potential of cDEP for early diagnosis applications and is the first study using this technique to selectively trap cells present in samples with blood cell concentrations similar to that in whole blood. We will further investigate the selectivity of our technique for isolation of cancer cells versus white and red blood cells in our future studies.

# Chapter Nine

## Microfluidic mixing using contactless dielectrophoresis (cDEP)

### 9.1 Introduction

Mixing in microfluidic devices has an important role in numerous biological and chemical applications. Rapid mixing is necessary in many lab-on-a-chip (LOC) and Micro Total Analysis Systems ( $\mu$ TAS) devices for chemical processes [241], including specific applications such as chemical reactions [242, 243], and for biological processes [244, 245], such as enzyme reactions [246-248], DNA or RNA analysis [249-251], and protein folding [252].

Despite the small length scale of microdevices, rapid and efficient mixing is difficult to achieve. Due to this small length scale the Reynolds number is small. Thus, mixing without any intentional stretching and folding of interfaces is dominated by molecular diffusion, which takes a long time relative to the typical operating timescale of these microdevices. To address this limitation, various techniques for enhancing mixing in microdevices have been proposed, including both active and passive techniques [245] that are based on phenomena such as chaotic advection [253]. There are many active mixing techniques, including those that use pressure, magnetohydrodynamic, acoustic, or thermal disturbances to enhance mixing [244]. Electrokinetic mixing has proven to be an efficient method for actively mixing solutions or microparticles [254]. Approaches of this type include use of electrohydrodynamics [255], electroosmosis [256, 257], electrowetting-on-dielectric [258, 259], and dielectrophoresis [260, 261]. In these electrokinetic mixing studies, both DC [241,

255, 262] and AC [255, 261, 263] electric fields have been used.

DEP has shown great potential for micro- and nano-scale particle separation, manipulation, and identification [264-271]. However, studies in the literature using DEP for mixing enhancement are fairly limited. Lee *et al.* [260] and Deval *et al.* [261] presented devices that use time-dependent DEP forces on particles in a fluid to generate mixing. Their DEP-based microdevices induced chaotic trajectories of embedded particles by periodically changing the frequency of the electric field, which caused periodic changes in the direction of the DEP force. It has also been shown that DEP forces that are generated by asymmetrical microelectrode geometries can be used to increase mixing of biological particles such as living cells with a solution [272].

We consider mixing in four devices that are inspired by the DEP-based devices in [260, 261]. A pressure drop is used to drive the flow of two parallel fluid streams through the devices. The stream from inlet 2 contains beads and the stream from inlet 1 does not. We focus primarily on distributing the beads across the outlet channel due to the DEP force generated by gradients in the magnitude of the imposed electric field. We also show that the secondary flow generated by the bead motions can be used to mix the two fluid streams. In contrast to the approach of [260, 261], in which mixing is induced through time-periodic variations in frequency of the imposed electric field, we find that this system is able to mix relatively well even when the frequency of the electric field is held constant in time.

## 9.2 Device Layout

We consider four variations of a device that consists of two “mixing chambers” located on opposite sides of a 50  $\mu\text{m}$  or 100  $\mu\text{m}$  rectangular microchannel. Schematics of the four devices are shown in Fig. 9.1. The chambers are either rectangular or semi-circular, and they are either placed symmetrically on opposite sides of the channel or are staggered with an

axial spacing of 300  $\mu\text{m}$ . In all cases, the depth of the chambers is 50  $\mu\text{m}$  to match the channel depth.

The design of our cDEP device is similar to the DEP-based device in [20], which uses a mixing chamber design like that of device 2 in Fig. 9.2. The DEP forces in [20] are driven by three electrodes, located on the edges of the mixing chambers, that are in direct contact with the working fluid solution. In our cDEP device, in contrast, the electrodes are only in direct contact with the electrode channels, which are separated from the mixing chamber by insulating PDMS barriers. The electrode channels are filled with a conductive solution, and an electric field is generated in the microchannel by the electrodes in the electrode channels. The capacitive nature of the barrier between the mixing chambers and the electrode channels generates a nonuniform electric field when an AC signal is applied. In some locations, the electrode channels are separated from the mixing chamber by only a 20  $\mu\text{m}$  thick PDMS barrier, and in other locations they are far from the mixing chambers to prevent their electric effect on the working fluid, thereby creating an electric field similar to that given by the three isolated electrodes in [20].

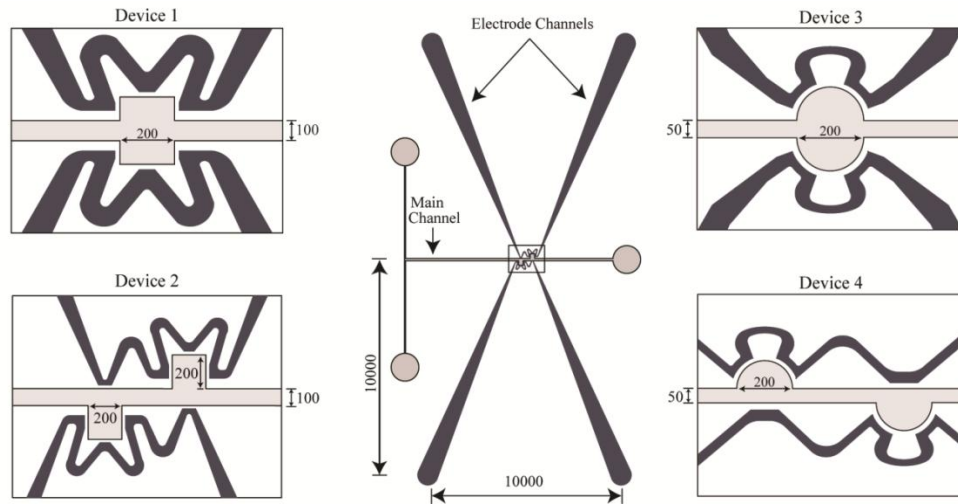


**Fig. 9.1.** 2D top view schematic of the microdevices. All dimensions are in  $\mu\text{m}$  [11].

Once the main channel was primed with fluid from both inlets, the syringe pump was set to the desired (constant) flow rate. Once the required flow rate was maintained for 2 minutes, an AC electric field was created in the microfluidic device using a combination of waveform generation and amplification equipment.

### 9.3 Computational Results

For the computational analysis we non-dimensionalized  $\nabla(\vec{E}_{rms} \cdot \vec{E}_{rms})$  using the applied voltage,  $V_{rms}$ , and the distance between the top and bottom electrode channels in the mixing chamber,  $L$ . The dimensionless form of  $\nabla(\vec{E}_{rms} \cdot \vec{E}_{rms})$  can be written as

$$\gamma = L \nabla(\vec{E}_{rms} \cdot \vec{E}_{rms}) / (V_{rms}/L)^2. \quad (9.1)$$

We solved for  $\gamma$  numerically for the four microdevices in Fig. 9.1 at an applied frequency of 600 kHz and with no imposed fluid flow. Fig. 9.2.a-d show that  $\gamma$  is maximum at the sharp corners inside the main channel. These numerical results also show that spatial variations in  $\nabla(\vec{E}_{rms} \cdot \vec{E}_{rms})$ , and thus the distribution of DEP force, depends strongly on the geometry of the channel and mixing chambers.

Numerical results for  $\gamma$  along the centerline of the main channel at 600 kHz are shown in Fig. 9.2.e. These results also show that the maxima of  $\gamma$  in these four devices occur at sharp corners. For instance, the maximum of  $\gamma$  along the centerline in device 1 occurs at  $x=\pm 100 \mu\text{m}$ , which corresponds directly to the locations of the sharp corners. Fig. 9.2.e also shows that maxima of  $\gamma$  on the centerline of device 2 occur at  $x=\pm 160 \mu\text{m}$  and  $x=\pm 320 \mu\text{m}$ , respectively, which are the locations of the sharp corners of the mixing chamber. In these two locations  $\gamma$  has values 0.167 and 0.261, respectively, which are equivalent to  $\nabla(\vec{E}_{rms} \cdot \vec{E}_{rms})$  values of  $8.7 \times 10^{14}$  and  $5.6 \times 10^{14} \text{ kg}^2 \text{ m C}^{-2} \text{ S}^{-4}$ , respectively.

In terms of the magnitude of  $\nabla(\vec{E}_{rms} \cdot \vec{E}_{rms})$ , the numerical results for devices 3 and 4 are similar to those for device 1 and 2, showing that the magnitude of the DEP force is consistent

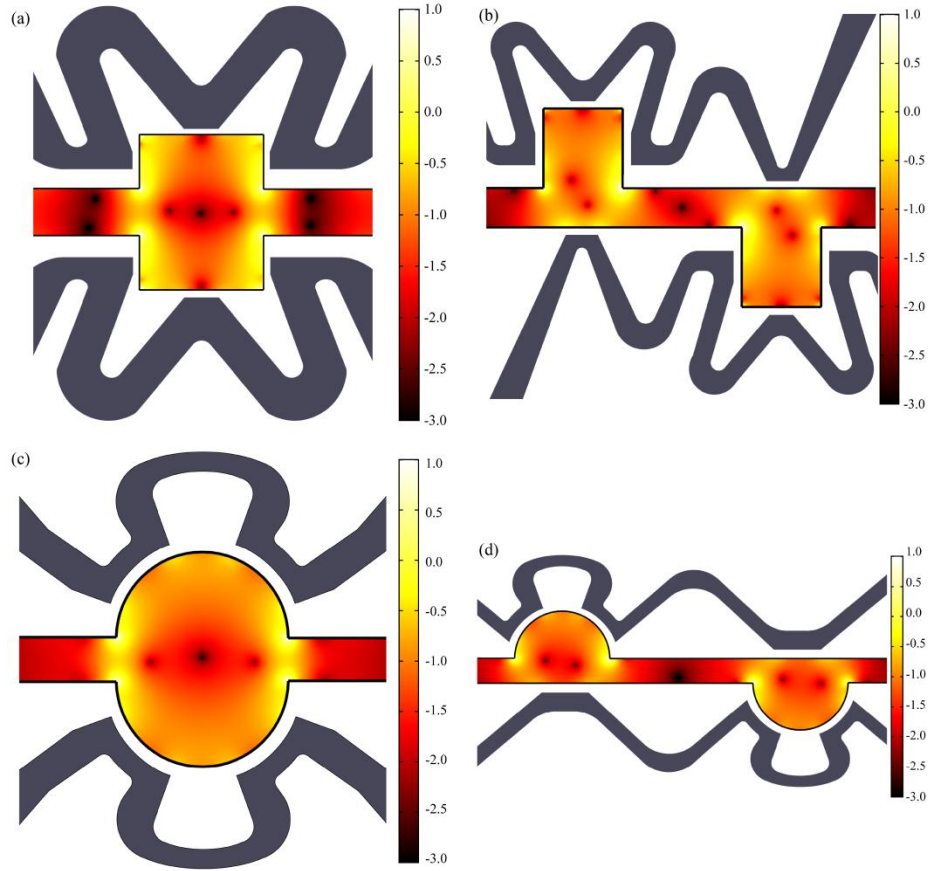
among these devices. However, the distribution of this DEP force does vary among these devices and, as we show below, the shape of the mixing chamber does have a strong effect on mixing.

## 9.4 Experimental Results

We considered the performance of the cDEP micromixer devices in Fig. 9.1. under variations in the applied voltage, actuation frequency, and pressure-driven fluid flow rate. We monitored this performance through optical observation of fluorescent beads and quantified mixing in the devices using the mixing index,  $MI$ , in Eq. (6).

As a control, we first ran experiments in which deionized water was injected through inlet 1 and a mixture of food coloring and deionized water was injected through inlet 2. The working solutions had the same conductivity as in the remainder of the experiments, but no beads were present to experience a DEP force. Experiments were run for voltages from 0 to 300  $V_{\text{rms}}$ , frequencies from 100 to 600 kHz, and flow rates from 0.002 to 0.05 mL/hr. The application of an electric field had no measureable effect on mixing of dye between the two streams, and we conclude that diffusion is the only mixing mechanism in these systems in the absence of beads.

The remaining experiments were run with deionized water injected through inlet 1 and a water-bead mixture injected through inlet 2. In practice, the quantification of mixing has some dependence on the concentration of beads injected through inlet 2. We ran several experiments with different inlet bead concentrations for the same range of parameters as in the control experiment. Too low a bead concentration leads to poorly resolved mixing results. We observed that for bead concentrations greater than approximately  $10^9$  beads/mL, the mixing index results are independent of the bead concentration. For the remainder of the experiments discussed here, we used an initial bead concentration of  $2 \times 10^9$  beads/mL.



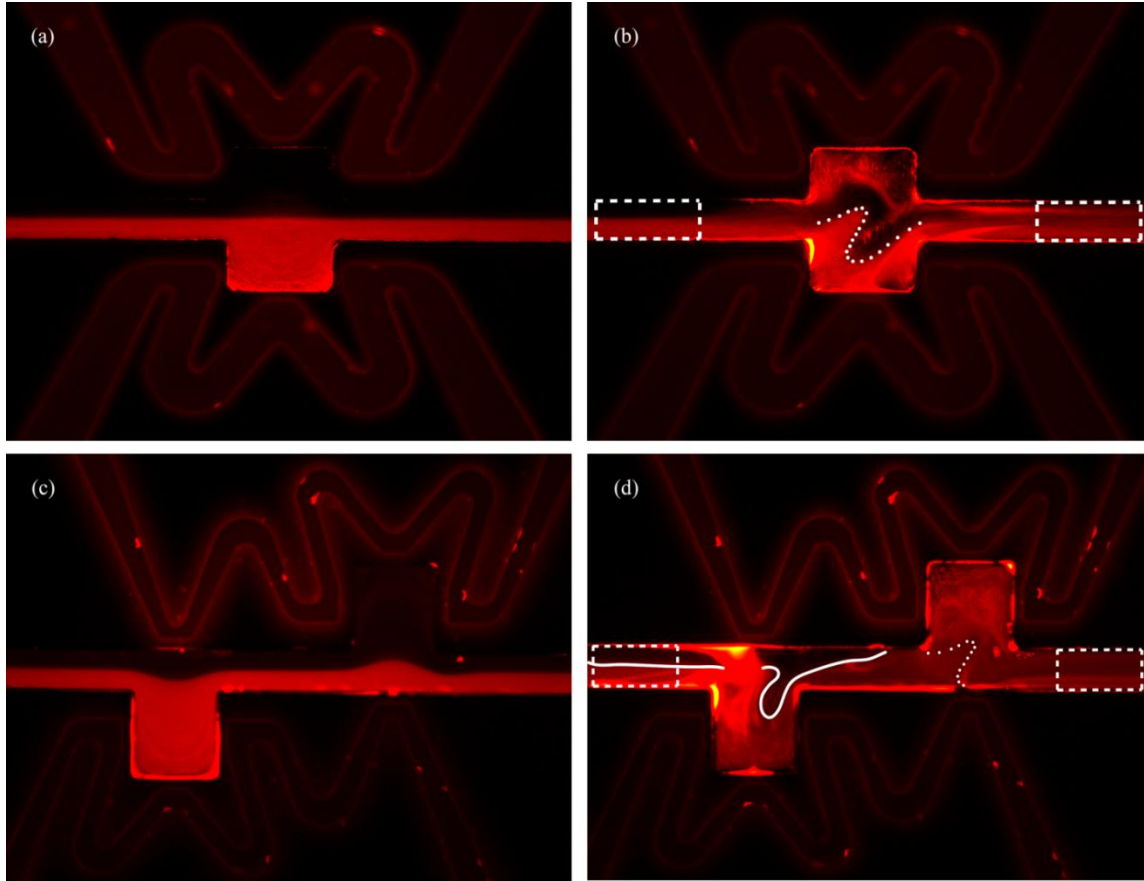
**Fig. 9.2.**  $\log(\gamma)$  surface plot of (a) device 1, (b) device 2, (c) device 3, (d) device 4, at an applied frequency of 600 kHz. (e) Line plot of  $\gamma$  for the four devices at 600 kHz [11].

Fig. 9.3. shows the experimental results for devices 1 and 2 before and after applying an AC electrical signal at  $300 V_{\text{rms}}$  and 600 kHz. Before applying the electric field it is clear that the two inlet streams flow side-by-side through the devices with negligible diffusive mixing (Fig. 9.3.a. and 9.3.c.). After applying the electric field, the beads suspended in the bottom fluid are manipulated by the induced DEP force. The mixing chambers exhibit a resulting secondary flow (Fig. 9.3.b and 9.3.d). This secondary flow is observed to stretch and fold the fluid, which is an important characteristic of rapid mixing. The stretching and folding in device 1 occurs between the symmetrically placed mixing chambers; an estimated interface

is shown by a dotted line in Fig. 9.3.b. In device 2 (see Fig. 9.3.d) the first mixing chamber begins the stretching and folding (with an example interface shown by a continuous line), and then the second chamber amplifies this stretching and folding and enhances mixing. The dotted line in Fig. 9.3.d attempts to show a portion of a stretching and folding pattern, but the bead pattern in this chamber is too convoluted to truly show interfaces. In general, the stretching and folding patterns in devices 1 and 2 are very similar, with the primary difference being that device 2 amplifies the pattern with a second mixing chamber. An occasional intermittency was observed in these patterns, which we suspect is related to the underlying instability that generates the mixing.

We quantify the effectiveness of these devices by evaluating  $MI$  in the target windows shown in Fig. 9.3.b,d and 9.7.b,d, as described in Section 3.4. Since the effect of the DEP force starts before the beads enter into the mixing chamber, the target windows were chosen slightly up and downstream from the mixing chambers. We ran mixing experiments for voltages between 0 and 300  $V_{\text{rms}}$  (0, 50, 100, 150, 200, 250, 300  $V_{\text{rms}}$ ) at a constant frequency of 600 kHz and a flow rate of 0.005 mL/hr in both devices. In these experiments, we first established a steady flow through the device, fixed the frequency at 600 kHz, and then we increased the voltage from zero to the target  $V_{\text{rms}}$ . At that point the flow rate, frequency, and voltage were held constant, and then mixing was evaluated.

Fig. 9.4.a. shows  $MI$  for devices 1 and 2 over the range of tested voltage at 600 kHz and 0.005 mL/hr. Both devices achieve a maximum of  $MI \cong 80\%$ . For voltages less than 250  $V_{\text{rms}}$ , device 1 generates better mixing than device 2, but for voltages greater than 250  $V_{\text{rms}}$  the opposite is true. Both devices show a monotonic increase in mixing with increasing voltage up to 200  $V_{\text{rms}}$ . The mixing index remains almost constant at  $MI \cong 80\%$  for voltages greater than 250  $V_{\text{rms}}$  in device 2. For device 1,  $MI$  decreases after 200  $V_{\text{rms}}$ , so optimal mixing of  $MI \cong 80\%$  occurs at 200  $V_{\text{rms}}$  for this device.



**Fig. 9.3.** Flow in devices 1 (panels a and b) and 2 (panels c and d) before (panels a and c) and after (panels b and d) applying the electric field at  $300 V_{\text{rms}}$  and  $600 \text{ kHz}$  (flow is from left to right). The dotted rectangles ( $100\mu\text{m} \times 200\mu\text{m}$ ) show the areas used for calculating the mixing index before and after the mixing chambers. A small amount of Rhodamine B has been added to the PBS in the electrode channels to make them visible [11].

In order to better understand the variation in mixing index, we compare the characteristic time needed for the DEP force to have an influence on the position of a bead with a characteristic residence time for that bead. The magnitudes of  $\nabla(\vec{E}_{\text{rms}} \cdot \vec{E}_{\text{rms}})$  that are generated near the inlet corners of a mixing chamber have an influence on a passing bead over approximately the first half of the mixing chamber, so we base the residence time on this

characteristic transport length. In device 2, for instance, the half-width of the mixing chamber is  $L_{flow} = 100 \mu\text{m}$ , so if we take the characteristic bead velocity due to the flow to be  $u_{flow} = 280 \mu\text{m/s}$  (which is roughly equivalent to a flow rate of 0.005 mL/hr in the channel), the relevant residence time for a bead is  $\tau_{flow} \cong 100/280 \cong 0.4 \text{ s}$ . Over this distance, the electric field exerts a DEP force that is roughly perpendicular to the flow direction. The velocity of the bead due to the DEP force is given by Eq. (4). Consider in particular the case 300  $V_{\text{rms}}$  with 600 kHz, which corresponds to the transition between poor mixing and good mixing in device 2. Based on the COMSOL calculations, we assume that the average of  $\nabla(\vec{E}_{\text{rms}} \cdot \vec{E}_{\text{rms}})$  is on the order of  $10^{15} \text{ kg}^2\text{m}/\text{C}^2\text{S}^4$ . Since we have observed positive DEP forces in these experiments, we also assume  $f_{CM} \cong 0.5$ . With these assumptions, the bead velocity due to the DEP force is  $u_p \cong 10 \mu\text{m/s}$ . We further assume that the influence of the DEP force is significant when it causes a bead to move 10 bead diameters, or  $L_p = 5 \mu\text{m}$ , perpendicular to the flow-induced path. Under these assumptions, the characteristic time for the DEP influence is  $\tau_{DEP} \cong L_p/u_p \cong 0.5 \text{ s}$ . As  $V_{\text{rms}}$  decreases,  $\tau_{DEP}$  increases. Thus, it appears that good mixing occurs in these devices when the time scales of the DEP force and the fluid flow are on the same order of magnitude.

At higher voltages, the DEP time scale,  $\tau_{DEP}$ , becomes higher than the fluid flow time scale,  $\tau_{flow}$ , the DEP force overcomes the drag force from the flow, and beads can get trapped in high  $\nabla(\vec{E}_{\text{rms}} \cdot \vec{E}_{\text{rms}})$  areas. This trapping can lead to less secondary flow and a reduction in mixing, as observed in device 1 for applied voltages above 200  $V_{\text{rms}}$ .

The dependence of mixing on the frequency of the AC field is shown in Fig. 9.4.b. for device 2 at an applied voltage magnitude of 250  $V_{\text{rms}}$  and a flow rate of 0.005 mL/hr. In order to achieve  $MI \geq 70\%$ , the frequency should be 200 kHz or higher, and at these higher frequencies the mixing index is independent of the frequency.

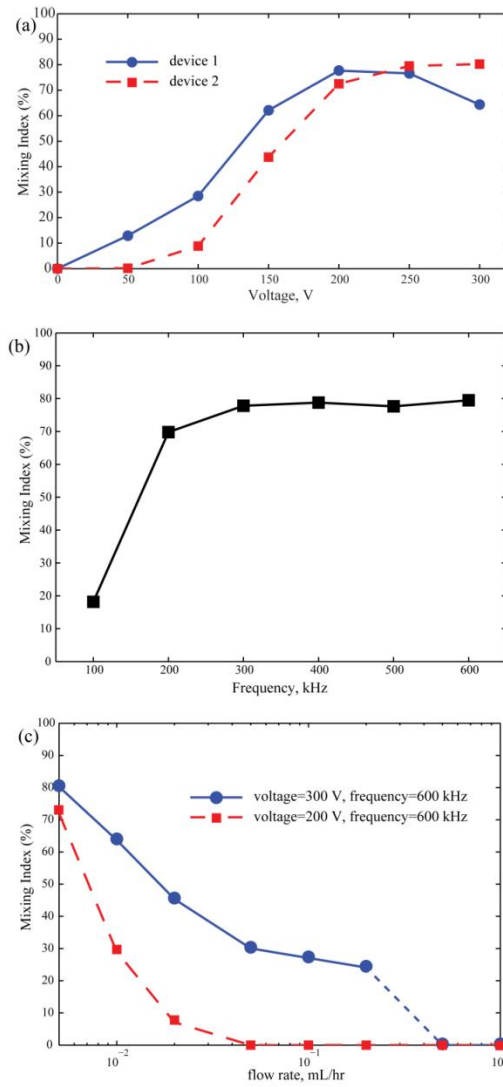


**Fig. 9.4.** (a) Variation of mixing index with respect to the applied voltage at a frequency of 600 kHz and a flow rate of 0.005 mL/hr for device 1 and 2, (b) variation of mixing index for device 2 versus the applied frequency at 250 V<sub>rms</sub> and a flow rate of 0.005 mL/hr, and (c) variation of mixing index for device 2 versus flow rate at a frequency of 600 kHz with two different voltages: 200 V<sub>rms</sub> and 300 V<sub>rms</sub> [11].

We have also considered the dependence of mixing on the flow rate in device 2 for a fixed

voltage and frequency. Fig. 9.4.c. shows that the proposed cDEP mixing is a strong function of the flow rate of the samples: the mixing efficiency decreases by increasing the flow rate, which is equivalent to decreasing the flow time scale. According to the scaling arguments discussed above, decreasing the time scale of the flow,  $\tau_{flow}$ , decreases the time available for the DEP force to move beads a significant distance from their regular flow paths. These results show that the mixing index is negligible for flow rates greater than or equal to 0.05 mL/hr at 200 V<sub>rms</sub> and 600 kHz and for flow rates greater than or equal to 0.5 mL/hr at 300 V<sub>rms</sub> and 600 kHz. We cannot yet explain the rapid decrease in mixing observed between flow rates of 0.2 mL/hr and 0.5 mL/hr for the 300 V<sub>rms</sub>, 600 kHz case. The results in Fig. 9.4.c. again show that in device 2 a higher mixing index can be obtained at higher voltages for a given flow rate.

Fig. 9.5, in combination with Fig. 9.3.d., further illustrates the relationship between the flow rate and mixing in device 2 for 300 V<sub>rms</sub> and 600 kHz. As the flow rate increases, the pattern of the secondary flow in the mixing chamber changes. At low flow rates,  $\tau_{DEP}$  is on the same order of magnitude as  $\tau_{flow}$ , and stretching and folding of the flow is observed in both mixing chambers (Fig. 9.3.d.). By increasing the flow rate, the stretching and folding decreases, and at flow rates higher than 0.02 mL/hr, Fig. 9.5.a shows that the dominant pattern of stretching and folding that was observed in Fig. 9.3.d disappears. When the flow rate increases to 0.2 mL/hr, the fluid flow time scale decreases to  $\tau_{flow} \cong 0.01$  s, which is much smaller than the DEP time scale ( $\tau_{DEP} = 0.7$  s as was discussed above), and the mixing index decreases significantly (Fig. 9.5.b).

In addition to mixing beads with a fluid, these microdevices can also be used for mixing two fluids when one of those fluids contains beads. To prove this claim, we suspended beads in a water-based blue dye solution and pumped this sample through inlet 2 of device 1. Deionized water was pumped through inlet 1. Fig. 9.6. shows device 1 under bright field illumination after applying an AC signal of 300 V<sub>rms</sub> and 600 kHz. This result clearly shows that the dye

solution is mixed with the deionized water due to the secondary flow generated by the DEP force on the beads.

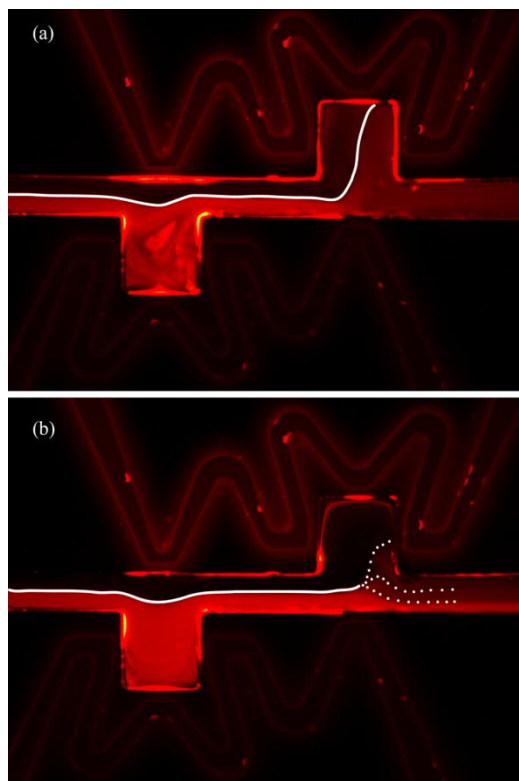


**Fig. 9.5.** Device 2 at frequency of 600 kHz and voltage of 300 V<sub>rms</sub> and flow rates of (a) 0.02 mL/hr, and (b) 0.2 mL/hr. Flow is from left to right [11].

Finally, we considered the effect of chamber geometry on mixing enhancement by comparing the performance of devices 3 and 4 with that of devices 1 and 2 at a single applied voltage and frequency. Fig. 9.7. shows the flow in devices 3 and 4 both before and after applying the electric field. According to the numerical results (see Fig. 9.2.), the DEP forces in devices 3 and 4 should be as strong as that in devices 1 and 2. However, the circular shape of the mixing chamber in device 3 clearly decreases the overall mixing. The maximum mixing index obtained in device 3 was 57%, which is low compared to that observed in devices 1

and 2 (see Fig. 9.4.). The rectangular shape of devices 1 and 2 increases the residence time of particle inside the mixing chamber relative to device 3, which allows more time for the DEP force to influence the particles and generate better mixing in devices 1 and 2.

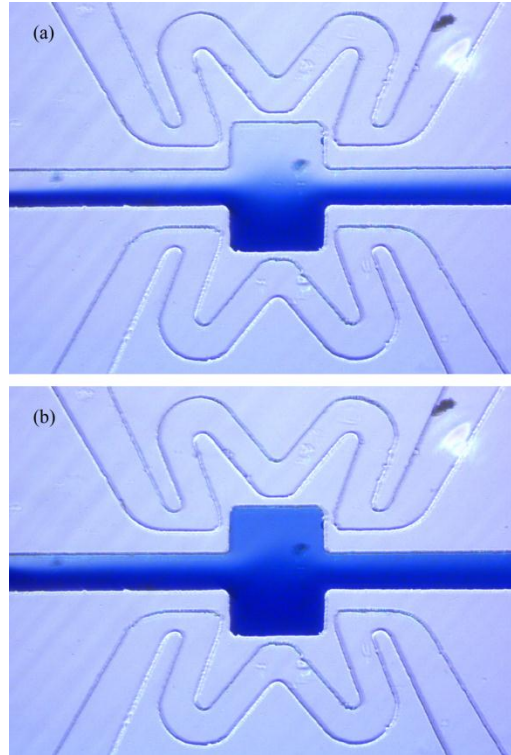


**Fig. 9.6.** Mixing of two inlet streams using DEP at a frequency of 600 kHz and voltage of 300 V<sub>rms</sub>. The two streams are pure DI water and DI water containing blue dye and beads. Flow is from left to right [11].

Device 4 appears to work differently than the other devices. In device 4, the first mixing chamber works relatively efficiently and generates relatively high mixing, which can be seen in Fig. 9.7.d by comparing the first and second target windows (marked by dotted rectangles). After the first mixing chamber,  $MI \cong 73\%$  for 300 V<sub>rms</sub> and 600 kHz. However, the second mixing chamber attracts the beads toward the bottom of the chamber, which

attenuates the previously generated mixing and cancels the effect of the first mixing chamber (compare the second and third target windows). After the second mixing chamber,  $MI \cong 52\%$  for 300  $V_{\text{rms}}$  and 600 kHz. Thus, for device 4 it appears that one mixing chamber works more effectively than two sequential mixing chambers. Further investigation is needed to explain this behavior.

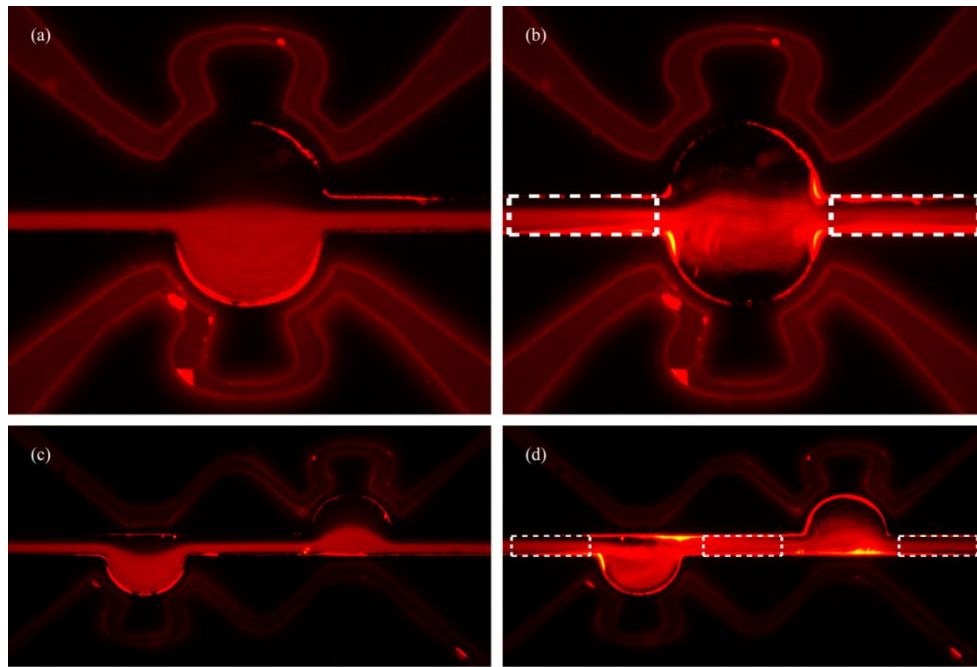


**Fig. 9.7.** Flow in devices 3 (panels a and b) and 4 (panels c and d) before (panels a and c) and after (panels b and d) applying the electric field at 300  $V_{\text{rms}}$  and 600 kHz (flow is from left to right). A small amount of Rhodamine B has been added to the PBS in the electrode channels to make them visible [11].

## 9.5 Conclusions

In this study, four micromixers were designed and fabricated based on cDEP technology. If we only relied on molecular diffusion for mixing 0.5  $\mu\text{m}$  beads with deionized water,

assuming flow with an average velocity,  $U$ , of 280  $\mu\text{m/s}$  at room temperature ( $\sim 300\text{ K}$ ) in a microchannel that is  $w=100\ \mu\text{m}$  wide, we would need a 3.2 m long channel ( $\sim Pe \times w$ ) and more than 3 hours ( $\sim w^2/D$ ) to achieve high mixing. In these calculations, the diffusion constant was calculated from  $D = kT/6\eta r\pi = 8.8 \times 10^{-13}$ , where  $k=1.381 \times 10^{-23}\ \text{m}^2\ \text{kg}\ \text{s}^{-2}\ \text{K}^{-1}$  is the Boltzmann constant and  $T$  is the absolute temperature. The Reynolds number ( $Re = \rho d_H U/\eta$ , where  $d_H$  is the hydraulic diameter of the channel) and Peclet number ( $Pe = Uw/D$ ) in this flow rate are about 0.025 and  $3.2 \times 10^4$ , respectively. Even for a small protein (with radius of 5 nm and diffusion constant of  $40\ \mu\text{m}^2/\text{s}$ ) a 7cm long channel and 250 seconds time are required. By using the cDEP mixing chambers, good mixing results are generated in a distance of 200  $\mu\text{m}$  in less than a second. These results depend on mixing chamber geometry, flow rate, applied voltage, and the frequency of the AC field. For a flow rate of 0.005 mL/hr, our best mixing results were observed in device 2 for an applied voltage of 250  $V_{\text{rms}}$  or greater and a frequency of 200 kHz or greater. For devices of this size with essentially two-dimensional geometries, it is typically necessary to introduce an externally imposed time-dependence in order to induce efficient mixing [253]. In contrast to the previous analysis of mixing with DEP [260], we achieved these results without any time-periodic modulation of the frequency. We also demonstrated that two fluids can be mixed due to the secondary flows generated by beads that are subjected to a DEP force. It is important to be mentioned that the effect of AC-electroosmosis (see Chapter Ten) was not considered in this study. AC-electroosmosis in the presented microdevices will be investigated further in our future study.

# Chapter Ten

## Investigating AC-electroosmotic flow in cDEP microdevices using particle tracking velocimetry

### 10.1 Introduction

In this study, we applied AC field in a microfluidic device to manipulate particles and to study different AC electrokinetic phenomena. Micro-particle tracking velocimetry ( $\mu$ PTV) was used to measure the velocity of particles and their trajectories. We studied experimentally and computationally the effects of AC-electroosmosis, dielectrophoresis, and electrothermal and their relative importance. We showed that dielectrophoresis and electrothermal effects are negligible in our study while AC-EO is the dominant phenomena. Lack of contact between the electrodes and sample in our technique can be considered as the main reason of preventing thermal effects which is essential in working with bioparticles. The study presented in this chapter has been done in collaboration and equal contribution of Jaime Raben, PhD candidate in Dr. Vlachos' lab at Virginia Tech [273].

### 10.2 Particle Tracking Velocimetry

Particle tracking velocimetry (PTV) is an experimental technique used to identify the velocity of a fluid or particles within a region of interest by tracking the movement of particles residing in the fluid. Particle tracking is a favorable method for several microfluidic applications as the

method is non-invasive, has high spatial resolution, performs well in unpredictable flows and high velocity gradients, and favors low seeding densities in comparison to particle image velocimetry (PIV). PTV can be used to identify fluid velocities where particles reproducibly follow the flow and in cases where external forces are acting on the particle such as dielectrophoresis.

### 10.3 Microdevice layout

The microdevice consists of two electrode channels located around a microchamber, see Fig. 10.1. The microchamber has almost a circular shape with radius of  $200\ \mu\text{m}$ . The edges of connection of the microchamber to the inlet and outlet channel, which are  $50\ \mu\text{m}$  wide, are designed rounded, not sharp, to prevent a very high gradient of electric field on corners. The electrode channels are separated from sample channel by  $20\ \mu\text{m}$  PDMS barriers. The schematic of the microdevice is shown in Fig. 10.1. The depth of electrode and sample channels is  $50\ \mu\text{m}$ .

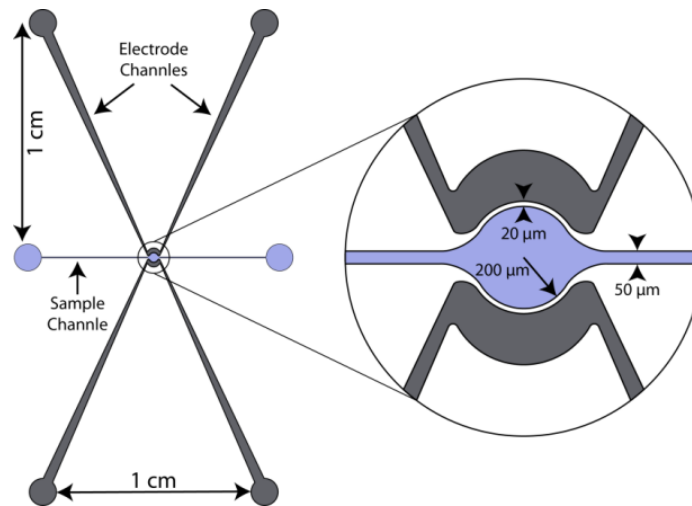


**Fig. 10.1.** schematic of the device.

Two upside-down 5 mL syringes were connected to the inlet and outlet of the sample channels with 15 gauge blunt needles (Howard Electronic Instruments, USA). These syringes were used as reservoirs to keep the pressure the same in both sides of the sample channels to prevent particles movement in the microchamber and to provide a quiescent fluid.

1  $\mu\text{m}$  diameter red fluorescent polymer microspheres (Fluoro-Max, Thermo Scientific, CA, USA) were suspended in deionized water. The electrical conductivity of the sample was determined using a conductivity meter (Horiba B-173 Twin Conductivity/Salinity Pocket Testers, Cole-Parmer) prior to each experiment, which was 7  $\mu\text{S}/\text{cm}$ .

## 10.4 Computational Results

The fluid dynamics and the electric field within the sample channel were computationally modeled using COMSOL 4.3. Microfluidics module was used to model fluid dynamics and the electroosmotic boundary condition was applied to the channels walls. Zeta potential and permittivity were defined on walls. The inlet velocity was set to zero and the outlet was set to no viscous stress (the Dirichlet condition for pressure). Then, the Navier-Stokes equation was solved for an incompressible laminar flow. Electric field was also modeled using AC/DC module to find electric field inside the sample channel and, consequently, to find DEP force on particles.

## 10.5 Dimensionless number

A dimensionless number is defined to study the ratio of DEP and ACEO effects. This dimensionless number can help us to predict which of DEP or ACEO phenomena is dominant. We defined this number,  $\beta$ , as the ratio of DEP time scale to ACEO time scale

$$\beta = \frac{\text{ACEO time scale}}{\text{DEP time scale}}$$

Since the DEP force length scale,  $l$ , the distance between the electrode channels, and ACEO length scale,  $R$ , the radius of the chamber which is approximately half of the distance between electrode channels, are the in the same order of magnitude in our microdevice,  $\beta$  can be written as

$$\beta = \frac{\frac{DEP \text{ length scale}}{DEP \text{ velocity}}}{\frac{ACEO \text{ length scale}}{ACEO \text{ velocity}}} = \frac{\frac{l}{\vec{u}_{DEP}}}{\frac{R}{\vec{u}_{EO}}} \propto \frac{\vec{u}_{EO}}{\vec{u}_{DEP}} = \frac{\frac{\varepsilon\zeta}{\eta} \vec{E}}{\frac{\varepsilon_m r^2 f_{CM}}{6\eta} \nabla(\vec{E} \cdot \vec{E})} \propto \frac{\zeta}{r^2} \frac{\vec{E}}{\nabla(\vec{E} \cdot \vec{E})} \quad (10.1)$$

$\frac{\vec{E}}{\nabla(\vec{E} \cdot \vec{E})}$  is a field quantity which can be written as the characteristic length and applied voltage

$$\frac{\vec{E}}{\nabla(\vec{E} \cdot \vec{E})} \propto \frac{\frac{V}{l}}{\left(\frac{V}{l}\right)^2} = \frac{Rl}{V} \quad (10.2)$$

This enables us to define another dimensionless number which does not depend on field quantities

$$\gamma \propto \frac{Rl \zeta}{r^2 V} \quad (10.3)$$

$R$  is approximately equivalent to half of the distance between electrode channels,  $l$ . Fig. 10.2. shows  $\gamma$  for the flow inside the microchamber at different zeta potentials, applied voltages, and particle with different sizes. This figure shows that when  $\gamma < 1$ , DEP force is dominant and when  $\gamma > 1$  ACEO is dominant and four counter-rotating cells appear.

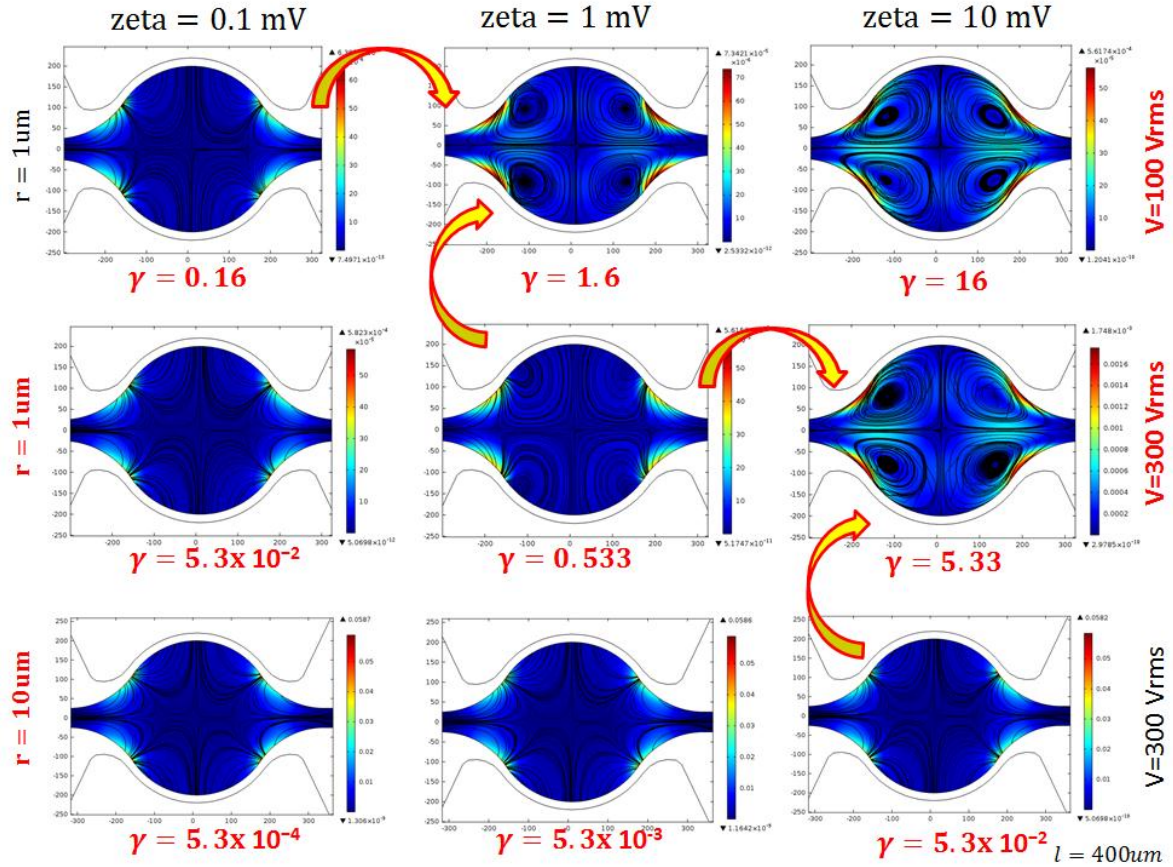


**Fig. 10.2.** Dimensionless number,  $\gamma$ , for the flow inside the microchamber at different zeta potentials, 0.1, 1, and 10 mV, for applied voltages of 100 and 300  $V_{\text{rms}}$ , and for 1 and 10  $\mu\text{m}$  particles.

## 10.6 Experimental Methodology for PTV

Images were acquired at 50 frames per second using an IDT Xs-5i intensified camera and a continuous widefield bulb. A Leica microscope with 40x objective was used to view the microchannel providing a resolution of 0.32 microns/pixel. An in-house PTV algorithm was applied to all particle images to acquire velocity information. This open source code is available

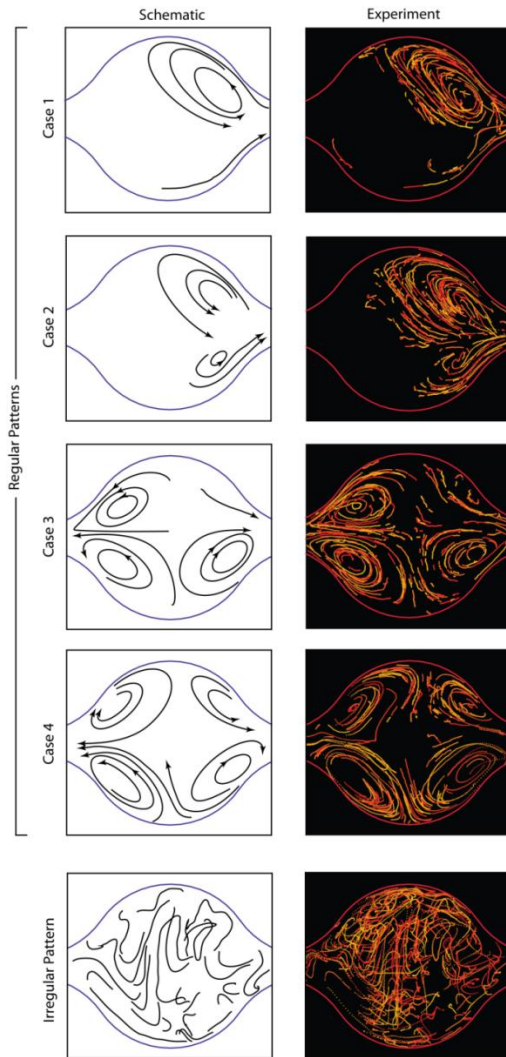


**Fig. 10.3.** Examples of regular and irregular trajectory patterns. Several examples of regular trajectory patterns were observed with varying numbers of swirling regions.

at <http://sourceforge.net/projects/qi-tools/> and has been tested by several publications. For this work, in-focus particles were identified after intensity-based thresholding to remove out-of-focus particles. Sizing was performed using an intensity-weighted centroid algorithm and tracking was

performed using a nearest neighbor approach with no velocity information used from previous time instances. Although available, advanced tracking algorithms such as utilizing velocity information from previous time steps and PIV-PTV hybrid schemes performed inferiorly in comparison with the nearest neighbor algorithm, likely due to the unpredictable flow.

## 10.7 PTV Results

Fig. 10.3. presents examples of trajectory patterns found by using PTV. Several examples of regular trajectory patterns were observed with varying numbers of swirling regions. Also, in some cases irregular movement of particles was observed. It is not still clear why particles show different behavior. One hypothesize is that these differences are due to the uneven distribution of particles in the chamber. Counter-rotating cells can only be observed when there is enough number of particles to track. When there is not enough number of particles, no counter-rotating cell is observable.

The asymmetry in the counter-rotating cells can be due to the fact that the chamber walls are not perfectly smooth. Also the geometrical dimensions after the fabrication process are not perfectly symmetrical. This asymmetry in the fabrication can happen whether in the fabrication of the silicon master or during peeling off PDMS from the silicon master. There is another possibility that the zeta potential is not exactly equal on top and bottom walls of the chamber.

## 10.8 Temperature Measurement

Additional experiments were conducted to rule out contributions from electrothermal sources. Temperature measurement was conducted using laser induced fluorescent thermometry with Rhodamine B as outlined by Ross et al. [274]. In the current work, the system was calibrated in a 0.5 mm square glass channel which was suspended in a water bath. Rhodamine B at a concentration of 0.1 mmol and conductivity of 26  $\mu\text{S}/\text{cm}$  was used for calibrations and

experiments. Calibrations were conducted over the range of 22-80°C and the reference (room) temperature was 22°C for each microchannel experiment.

Images were acquired at 10 Hz using an IDT Xs-5i intensified camera with constant gain. A pulsing LED provided illumination to limit photobleaching. Control cases were performed without the application of an electric field to confirm the absence of photobleaching up to approximately 10 minutes. Images were normalized by the reference image at room temperature. No decrease in the median normalized intensity was detected over the duration of our initial experiments (30 seconds) suggesting no increase in temperature occurred in the microchannel. Furthermore, the variance of the median normalized intensity was approximately  $5 \times 10^{-4}$  for all cases.

## 10.9 Temperature dependence

Efforts were taken to quantify temperature changes inside the channel through methods outlined by Ross et al. [274]. Calibrations were performed in a 0.5mm square glass channel, which was suspended in a temperature bath. Rhodamine B at a concentration of 0.1 mmol Rhodamine B was placed inside the channel and the water bath system was imaged using a 25x oil immersion objective (NA=0.8). Pulsing LEDs were used for illumination to eliminate photobleaching effects and were synchronized with an IDT XS-5i camera, both sampling at 10Hz. Control experiments showed no photobleaching effects over a duration of several minutes.

Calibration images of the glass channel were acquired as the bath temperature was varied over a 20°-80° range with 22° being used as a reference in the calibration curve. Calibration curves were computed as the ratio of intensity to reference intensity versus temperature ( $I/I_{\text{ref}}$  vs. T). Next, 0.1 mmol Rhodamine B was placed in the PDMS microchannel and experiments were conducted with voltage and frequency values corresponding to 300 V<sub>RMS</sub> and 600 kHz, respectively. Five trials were conducted with identical illumination and camera settings. Each

case resulted in no changes in illumination over the duration of our previous experiments (~22 seconds).

As expected, the experimental results showed no temperature changes coinciding with computational results obtained through COMSOL modeling (not shown). Furthermore, these results follow intuition in that the sample is not in direct contact with electrodes, thus reducing the chance of high temperature gradients.

## **10.10 Conclusions**

In this chapter, we used AC field in a microfluidic device to manipulate particles. We also investigated different AC electrokinetic phenomena including DEP and AC-EO utilizing micro-particle tracking velocimetry ( $\mu$ PTV). We studied experimentally and computationally the effects of AC-electroosmosis, dielectrophoresis, and electrothermal and their relative importance. We showed that DEP and electrothermal effects are negligible in our study while AC-EO is the dominant phenomena.

# Chapter Eleven

## Continuous Cell Sorting using Multilayer cDEP Microdevices

### 11.1 Introduction

DEP-based particle separation can be classified as continuous or discontinuous (batch) separation. Through batch separation [6, 10, 35, 36, 102, 128, 202, 275-285] target particles are trapped due to positive DEP force while the background particles pass through the microdevice without trapping. In discontinuous (batch) separation, particles mixture is injected to the microdevice. The electric field turns on and the target particles become trapped by positive DEP force. Unwanted particles are washed out from the microdevice by a pressure gradient flow. Then the buffer is injected into the microchannel and the electric field turns off and the target particles can be collected in a reservoir [9, 285]. This method has some disadvantages, such as complicated process of manipulating particles due to discontinuous operating procedure. Also taking cells off the chip is usually challenging. Moreover, because of irreversible adsorption, target cells stick to electrodes even after turning off the electric field. The cells also may be affected due to being exposed to electric field for a long time. The most common DEP batch sorting method is using interdigitated electrodes, which has applications not only for particle sorting through conventional DEP and travelling electric fields (twDEP) [286, 287], but also in other AC electrokinetic application such as micropumping [288].

Continuous separation [81, 289-294] can solve some of the batch sorting drawbacks. Instead of trapping the target particles, the particles can be sorted gradually by passing the sample over electrode channels. Different particles experience different dielectrophoretic forces due to their

intrinsic electrical properties and/or differences in their sizes. In continuous sorting, different particles deflect to various directions and finally particles will be sorted and can be collected in the outlet of the device. Different continuous DEP-based particles sorting methods have been reported including 3D electrodes [287, 295], serpentine microchannel [296], and sheath flow [297]. In conventional DEP techniques, metallic microelectrodes with various geometries, such as interdigitated [36, 102, 128, 277, 279-282], castellated [202, 275, 278, 298], oblique [289], spiral [276], circular [6, 35], ring shape [284], and wedge shape [283] are patterned on a microfluidic device using conventional lithography techniques.

We designed a multilayer contactless dielectrophoresis (cDEP) to sort particles continuously. We investigated this microdevice analytically in 2D and computationally in 2D and 3D. In cDEP multilayer devices, the electrode channels are located on top of the sample channel and are separated from the sample channel by a thin ( $\sim 20 \mu\text{m}$ ) membrane. This means that in contrast to previous cDEP microdevices [9, 158, 299], the width of the channel is not limited to the distance between electrode channels in this device, thus, the width of the channel and consequently the throughput can be increased.

We predicted DEP force analytically for an interdigitated infinite array of electrodes with periodic boundary conditions. DEP force is modeled as a cosine function which decreases exponentially through the channel height. Here, we presented two analytical models. The first one is based on the Fourier series, in which the first and the second terms were considered. We showed that considering the second term changes the results less than 1.2 % for distances larger than the average width and the gap between the electrode channels. The second analytical model is a cosine function multiplied by an exponential function in z-direction which is suggested based on the computational observations.

Then, multilayer cDEP devices with periodic boundary conditions were modeled computationally in 2D. Different geometrical parameters, such as the distance between electrode

channels, membrane thickness, number of crossing electrode channels, the angle between electrode channels and the sample channel, were studied to improve the performance of the device. The comparison between the analytical results of conventional interdigitated infinite array of electrodes and cDEP computational results revealed agreement between these two models. The advantage of multilayer cDEP device is that it is more predictable than pillar-based devices, due to the simplicity of the sample channel and fluidic electrode channels geometry. Thus, the analytical models in addition to computational models can be used to predict its behavior. Moreover, since the cross-section of the sample channel is a rectangular shape, analytical relations for velocity profile can be used with high accuracy to predict the fluid flow which saves computation time and memory.

## 11.2 Dominant forces

Particles suspended in a fluid moving over an interdigitated array of electrodes experiences several forces, including drag, DEP, buoyancy, and gravity. The net effects of these forces determine the location of the particle such as its height. Particles with different intrinsic DEP properties will locate at different heights (in z-direction) and will deflect at different rates (in x-y plane), thus an interdigitated array of electrodes enables us to sort particles. Moreover, due to the parabolic profile of the velocity field, particles experience different drag forces at different heights which is considered in this study too.

As was presented in the Chapter Two, DEP and drag force can be written as

$$\vec{F}_{DEP} = 2\pi\epsilon_m r^3 \text{Re}\{f_{CM}(\omega)\} \nabla(\vec{E}_{rms} \cdot \vec{E}_{rms}), \quad (11.1)$$

$$\vec{F}_{Drag} = 6\eta r \pi u, \quad (11.2)$$

As shown in Fig. 11.1., DEP force is perpendicular to the electrode direction and drag force is in the direction of the fluid flow. To be able to force the particles to move towards the fluidic electrode direction, DEP force should be larger than the vertical component of the drag force

$$F_{DEP} \geq F_{Drag} \sin\theta \quad (11.3)$$

Thus, the maximum fluid flow velocity is limited to

$$u \leq \frac{\epsilon_m r^2 Re\{f_{CM}\} \nabla(\vec{E}_{RMS} \cdot \vec{E}_{RMS})}{3\eta \sin\theta} \quad (11.4)$$

This means that by decreasing the angle between the fluidic electrode channels and the fluid flow, flow rate can be increased. However, decreasing this angle decreases the number of fluidic electrode channels a particle can pass through in the per device length, which is proportional to  $\cos\theta$ . If DEP force becomes much stronger than the drag force due to the too small angle, then cells may become trapped and make long pearl chains and decrease the efficiency of sorting. This behavior has been observed in previous studies [300]. Thus, there is a trade-off between these two parameters which are proportional to  $\sin\theta$  and  $\cos\theta$ , respectively. Consequently we chose 45 degree as the optimum angle in this trade-off.

The size of the particle to be sorted at a specific voltage and flow rate can be found from Equations (11.1), (11.2), and (11.3):

$$r \geq \left( \frac{3\eta u \sin\theta}{\epsilon_m Re\{f_{CM}\} \nabla(\vec{E}_{RMS} \cdot \vec{E}_{RMS})} \right)^{0.5} \quad (11.5)$$

This relation shows that by decreasing the angle between the fluidic electrode channels and the fluid flow, smaller particles can be deflected. The maximum angle to sort particles with a certain size at a specific flow rate can be found from Equations (11.1), (11.2), and (11.3):

$$\theta \leq \sin^{-1} \left[ \frac{\epsilon_m r^2 Re\{f_{CM}\} \nabla(\vec{E}_{RMS} \cdot \vec{E}_{RMS})}{3\eta u} \right] \quad (11.6)$$

For instance, for the application of separating cancer cells from blood cells, the minimum size of cells is equal to the size of red blood cells. Assuming constant voltage and frequency,  $u \cdot \sin\theta$  will be equal to a certain value. Then, the fluid velocity can be increased and  $\theta$  decreased to reach the highest possible flow rate. We should make sure our design parameters can separate cancer cells ( $\sim 15 \mu\text{m}$  in diameter) from WBCs ( $\sim 10 \mu\text{m}$ ) and RBCs ( $\sim 3 \mu\text{m}$ ). Thus if we have

electrode channels with two different angles designed to separate cancer cells and then WBCs, we will have enriched RBCs in the outlet. We can have two other outlets to collect cancer cells and WBCs.

### 11.3 Theoretical consideration of traditional DEP interdigitated electrode array in 2D

For a homogeneous linear dielectric the Maxwell's equations can be written as [301]

$$\sigma \nabla^2 \varphi + \varepsilon \nabla^2 \varphi = 0 \quad (11.7)$$

where  $\sigma$  is the conductivity and  $\varepsilon$  the permittivity of the dielectric. Then for a harmonic AC signal, the general stationary solution can be written as

$$\varphi = \varphi_1 \cos \omega t + \varphi_2 \sin \omega t \quad (11.8)$$

where  $\omega$  is the frequency. In this equation it is assumed that the frequency is high enough to ignore the double-layer. The power dissipation is also ignored.

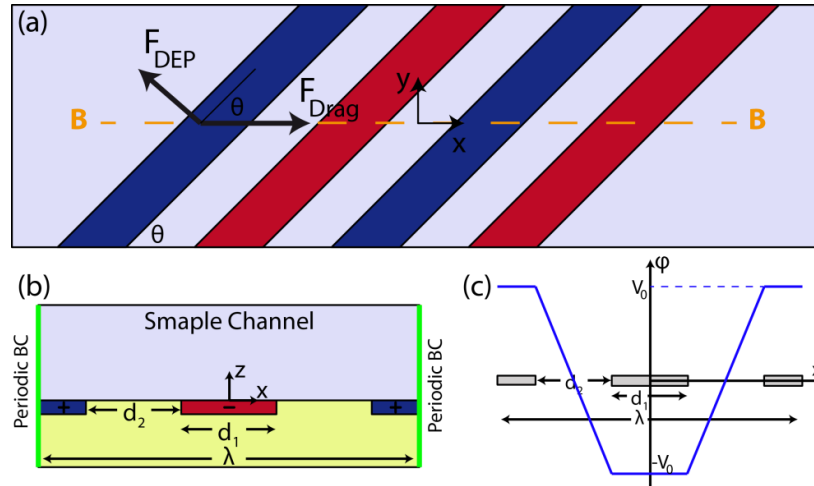


**Fig. 11.1.** (a) Schematic of the top view of the device. (b) Schematic of a periodic conventional interdigitated electrode array on a cross-section B-B. (c) Boundary condition at  $z=0$

For an infinite array of interdigitated electrodes, a 180 phase exists between the alternative electrodes which causes  $\varphi_2 = 0$ . Boundary conditions for this system, shown in Fig. 11.1.c, are

- $\varphi$  goes to zero when  $y$  goes to infinity
- The boundary condition at  $z=0$  is shown in Fig. 11.1.b.
- Current across the interface between substrate and liquid is continuous

Electrodes are assumed to be very thin thus the electrodes thickness is negligible. Then the electric potential as the solution of the Laplace equation can be written as a Fourier series

$$\varphi(x, 0) = \sum_{n=1}^{\infty} A_n \cos(k_n x) \quad z > 0 \quad (11.9)$$

where  $A_n$  is the Fourier coefficient,  $k_n = 2\pi n/\lambda$ ,  $\lambda = 2(d_1 + d_2)$  is the period length in  $x$ -direction, and  $n$  is an integer. Since  $x=0$  is chosen at the center of the electrode,  $\varphi$  becomes an even function of  $x$  and  $\varphi(x, z)$  can be written as

$$\varphi(x, z) = \sum_{n=1}^{\infty} A_n \cos(k_n x) e^{-k_n z} \quad z > 0 \quad (11.10)$$

Since there is an odd symmetry at  $x = \lambda/4$ , then  $\varphi(\lambda/4, z) = 0$ , and  $\cos\left(\frac{k_n \lambda}{4}\right) = 0$ . Thus,  $n$  should be an odd number,  $n = 2m + 1$ , where  $m$  is an integer.  $A_n$  can be written as

$$\begin{aligned} A_n &= \frac{2}{\lambda} \int_0^{\lambda/2} \varphi(x, 0) \cos(k_n x) dx & (11.11) \\ &= \frac{4}{\lambda} \left[ \int_0^{\frac{d_1}{2}} (-V_0) \cos(k_n x) dx + \int_{\frac{d_1}{2}}^{\frac{d_1+d_2}{2}=\frac{\lambda}{4}} \left(\frac{2V_0}{d_2}\right) \left(x - \frac{(d_1 + d_2)}{2}\right) \cos(k_n x) dx \right] \\ &= \frac{4}{\lambda} \frac{2}{k_n^2} \left[ \cos\left(\frac{d_1 k_n}{2}\right) + \cos\left(\frac{(d_1 + d_2)}{2} k_n\right) \right] \end{aligned}$$

Based on the definition of  $k_n$

$$\frac{(d_1 + d_2)}{2} k_n = \frac{\lambda}{4} k_n = (2m + 1) \frac{\pi}{2} \quad (11.12)$$

and knowing that

$$\cos\left(\frac{\lambda}{4} k_n\right) = \cos(2m + 1) \frac{\pi}{2} = 0 \quad (11.13)$$

then,

$$A_n = \frac{16V_0 d}{\pi^2 d_2 (2m + 1)^2} \cos\left((2m + 1) \frac{\pi d_1}{4d}\right) \quad (11.14)$$

where  $d = (d_1 + d_2)/2$ ,  $d_1$  is the electrode width, and  $d_2$  is the distance between electrodes.

Then,  $E = -\nabla\phi_1(x, z) = \sum_{n=1}^{\infty} E_n \cos(k_n x)$  and from above relation, we can write:

$$E_{m,x}(x, z) = \sum_{n=1}^{\infty} A_{2m+1} k_{2m+1} \cos(k_{2m+1} x) e^{-k_{2m+1} z} \quad (11.15)$$

$$E_{m,z}(x, z) = \sum_{n=1}^{\infty} A_{2m+1} k_{2m+1} \sin(k_{2m+1} x) e^{-k_{2m+1} z}$$

The first and the second terms of  $E^2$  will be  $E_0^2$  and  $E_0 E_1$  which have exponential terms of  $e^{-\pi z/d}$  and  $e^{-2\pi z/d}$ , respectively. For the heights greater than  $z \sim d$

$$10 = e^{\pi z/d}$$

$$\frac{z}{d} = \frac{\ln(10)}{\pi} = 0.733 \approx 1,$$

Fourier series can be simplified and the higher order terms can be neglected; thus only the first term will be considered here

$$A_1 = \frac{16V_0d}{\pi^2d_2} \cos\left(\frac{\pi d_1}{4d}\right) \quad (11.16)$$

$$k_1 = \frac{2\pi}{\lambda} \quad (11.17)$$

$$E_{0,x}(x, z) = A_1 k_1 \sin(k_1 x) e^{-k_1 z} \quad (11.18)$$

$$E_{0,z}(x, z) = A_1 k_1 \cos(k_1 x) e^{-k_1 z}$$

$$E^2 = E_{0,x}^2 + E_{0,z}^2 = A_1^2 k_1^2 e^{-2k_1 z} = \frac{64V_0^2}{\pi^2 d_2^2} \cos^2\left(\frac{\pi d_1}{4d}\right) e^{-\pi z/d} \quad (11.19)$$

$$\nabla E^2 = -\frac{64V_0^2}{\pi d_2^2 d} \cos^2\left(\frac{\pi d_1}{4d}\right) e^{-\pi z/d} \quad (11.20)$$

Then the time averaged DEP force can be written as:

$$F_{DEP} = \pi \varepsilon_m r^3 \text{Re}\{f_{CM}\} \nabla E^2 = -\varepsilon_m r^3 \text{Re}\{f_{CM}\} \frac{64V_0^2}{d_2^2 d} \cos^2\left(\frac{\pi d_1}{4d}\right) e^{-\pi z/d} \quad (11.21)$$

This relation is valid for  $z > d$  and shows that DEP force decreases logarithmically far from the electrodes.

The levitation height of particles can be find assuming particles experiencing positive DEP force

$$F_{Buoyancy} = F_{DEP} \quad (11.22)$$

$$\Delta \rho_m \frac{4\pi r^3}{3} g = -\varepsilon_m r^3 \text{Re}\{f_{CM}\} \frac{64V_0^2}{d_2^2 d} \cos^2\left(\frac{\pi d_1}{4d}\right) e^{-\pi h/d} \quad (11.23)$$

$$h = \frac{d}{\pi} \ln \left[ \frac{48V_0^2 \varepsilon_m}{\pi d_2^2 d \Delta \rho_m g} \cos^2\left(\frac{\pi d_1}{4d}\right) \text{Re}\{f_{CM}\} \right] \quad (11.24)$$

Considering drag, DEP, and buoyancy forces at the same time:

Now, if we also consider the second terms of  $E_{m,x}$  and  $E_{m,z}$

$$A_3 = \frac{16V_0 d}{9\pi^2 d_2} \cos\left(\frac{3\pi d_1}{4d}\right) \quad (11.25)$$

$$k_3 = \frac{6\pi}{\lambda} \quad (11.26)$$

$$E_{1,x}(x, z) = A_3 k_3 \sin(k_3 x) e^{-k_3 z} \quad (11.27)$$

$$E_{1,z}(x, z) = A_3 k_3 \cos(k_3 x) e^{-k_3 z} \quad (11.28)$$

Thus

$$\begin{aligned} E^2 &= (E_{0,x} + E_{1,x})^2 + (E_{0,z} + E_{1,z})^2 \\ &= E_{0,x}^2 + E_{1,x}^2 + E_{0,z}^2 + E_{1,z}^2 + 2(E_{0,x}E_{1,x} + E_{0,z}E_{1,z}) \\ &= A_1^2 k_1^2 e^{-2k_1 z} + A_3^2 k_3^2 e^{-2k_3 z} + 2A_1 A_3 k_1 k_3 (\sin(k_1 x) \sin(k_3 x) \\ &\quad + \cos(k_1 x) \cos(k_3 x)) e^{-(k_1 + k_3)z} \end{aligned} \quad (11.29)$$

Knowing that  $\sin(A) \sin(B) + \cos(A) \cos(B) = \cos(A + B)$ , then

$$E^2 = A_1^2 k_1^2 e^{-2k_1 z} + A_3^2 k_3^2 e^{-2k_3 z} + 2A_1 A_3 k_1 k_3 \cos((k_1 + k_3)x) e^{-(k_1 + k_3)z} \quad (11.30)$$

Sorting based on the order

$$E^2 = A_1^2 k_1^2 e^{-\pi z/d} + 2A_1 A_3 k_1 k_3 \cos\left(\frac{2\pi}{d} x\right) e^{-2\pi z/d} + A_3^2 k_3^2 e^{-3\pi z/d} \quad (11.31)$$

The last term can be ignored comparing to first two terms.

$$E^2 = \frac{64V_0^2}{\pi^2 d_2^2} \cos^2\left(\frac{\pi d_1}{4d}\right) e^{-\frac{\pi z}{d}} + \frac{132V_0^2}{3\pi^2 d_2^2} \cos\left(\frac{\pi d_1}{4d}\right) \cos\left(\frac{3\pi d_1}{4d}\right) \cos\left(\frac{2\pi}{d} x\right) e^{-2\pi z/d} \quad (11.32)$$

Defining  $\alpha$  and  $\beta$  as

$$\alpha = \frac{64V_0^2}{\pi^2 d_2^2} \cos^2\left(\frac{\pi d_1}{4d}\right) \quad (11.33)$$

$$\beta = \frac{128V_0^2}{3\pi^2 d_2^2} \cos\left(\frac{\pi d_1}{4d}\right) \cos\left(\frac{3\pi d_1}{4d}\right) \quad (11.34)$$

$$E^2 = \alpha e^{-\frac{\pi z}{d}} + \beta \cos\left(\frac{2\pi}{d}x\right) e^{-\frac{2\pi z}{d}} = e^{-\frac{\pi z}{d}} \left( \alpha + \beta \cos\left(\frac{2\pi}{d}x\right) e^{-\frac{\pi z}{d}} \right) \quad (11.35)$$

This means that the average value of  $E^2$  in x-direction decreases exponentially in z-direction and the maximum and minimum values of DEP force decrease faster (twice exponentially faster than the average value).

$$F_{DEP,x} = -\frac{2\pi^2}{d} r^3 \varepsilon_m R\{f_{CM}\} \beta \sin\left(\frac{2\pi}{d}x\right) e^{-\frac{2\pi z}{d}} \quad (11.36)$$

$$F_{DEP,z} = -\frac{\pi^2}{d} r^3 \varepsilon_m R\{f_{CM}\} \left( \alpha + 2\beta \cos\left(\frac{2\pi}{d}x\right) e^{-\frac{\pi z}{d}} \right) e^{-\frac{\pi z}{d}} \quad (11.37)$$

To find the velocity of the particle

$$F_{Drag} = F_{DEP} \quad (11.38)$$

$$6\pi r \eta \frac{dx}{dt} = -\frac{2\pi^2}{d} r^3 \varepsilon_m R\{f_{CM}\} \beta \sin\left(\frac{2\pi}{d}x\right) e^{-\frac{2\pi z}{d}} \quad (11.39)$$

$$6\pi r \eta \frac{dz}{dt} = -\frac{\pi^2}{d} r^3 \varepsilon_m R\{f_{CM}\} \left( \alpha + 2\beta \cos\left(\frac{2\pi}{d}x\right) e^{-\frac{\pi z}{d}} \right) e^{-\frac{\pi z}{d}} \quad (11.40)$$

By solving these 2 equations,  $x(t)$  and  $z(t)$  can be calculated.

To consider the accuracy of adding the second term in the Fourier series, the different between considering and not considering the second term relative to the first term is studied here:

$$\epsilon = \frac{(E_2)_2 - (E_2)_1}{(E_2)_1} = \frac{\beta \cos\left(\frac{2\pi}{d}x\right) e^{-\frac{\pi z}{d}}}{\alpha} = \frac{2 \cos\left(\frac{3\pi d_1}{4d}\right)}{3 \cos\left(\frac{\pi d_1}{4d}\right)} \cos\left(\frac{2\pi}{d}x\right) e^{-\frac{\pi z}{d}} \quad (11.41)$$

Knowing that

$$\frac{\cos(3A)}{\cos(A)} = -1 + 2\cos(A) \quad (11.42)$$

Then,

$$\epsilon = \frac{2}{3} \left( -1 + 2 \cos \left( \frac{\pi d_1}{4d} \right) \right) \cos \left( \frac{2\pi}{d} x \right) e^{-\frac{\pi z}{d}} \quad (11.43)$$

This relation shows that  $\epsilon$  decreases exponentially by increasing the distance from the electrodes. Also, far from electrodes  $\epsilon$  does not depend on  $x$  anymore, but close to electrodes it does. This is in agreement with our assumption that the discussed Fourier series is valid at  $z > d$ . Table below shows percentage of error for a few  $z/d$  values assuming that  $d_1 \approx d$  and knowing that  $\max \left| \cos \left( \frac{2\pi}{d} x \right) \right| = 1$ . Thus, at  $z=d$  we only add 1.2% error to  $E^2$  by ignoring the second term in Fourier series.

$$\max[\epsilon] \approx \frac{2}{3} (-1 + \sqrt{2}) e^{-\frac{\pi z}{d}} \quad (11.44)$$

$z/d$	0.001	0.01	0.1	1	2	5	10	100
$\epsilon$	27.5 %	26.7 %	20.2 %	1.2 %	0.52 %	0.0004 %	$6 \times 10^{-13}$ %	$6 \times 10^{-135}$ %

## 11.4 Computational parametric study of 2D model with periodic BCs

To do a parametric study, first we considered a 2D reference geometry (shown in Fig. 11. 2). Then, different geometric parameters, such as electrode channels width and height, the distance between electrode channels with the same potential or opposite potential, sample channel height, and membrane thickness, as well as electrical parameters were investigated one by one and were compared to the reference case. The distance between similar,  $d_{pp/nn}$ , and opposite,  $d_{pn}$ , electrode channels is 50  $\mu\text{m}$ , electrode channels widths,  $w_E$ , and heights,  $h_E$ , are 50  $\mu\text{m}$ , the membrane thickness,  $t_{mem}$ , is 20  $\mu\text{m}$ , and sample channels depth,  $h_S$ , is 5 mm in the reference geometry. The reference applied frequency is 500 kHz and applied voltage 100  $V_{RMS}$ .

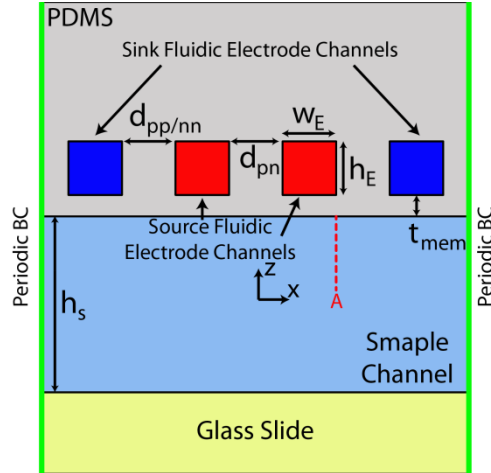


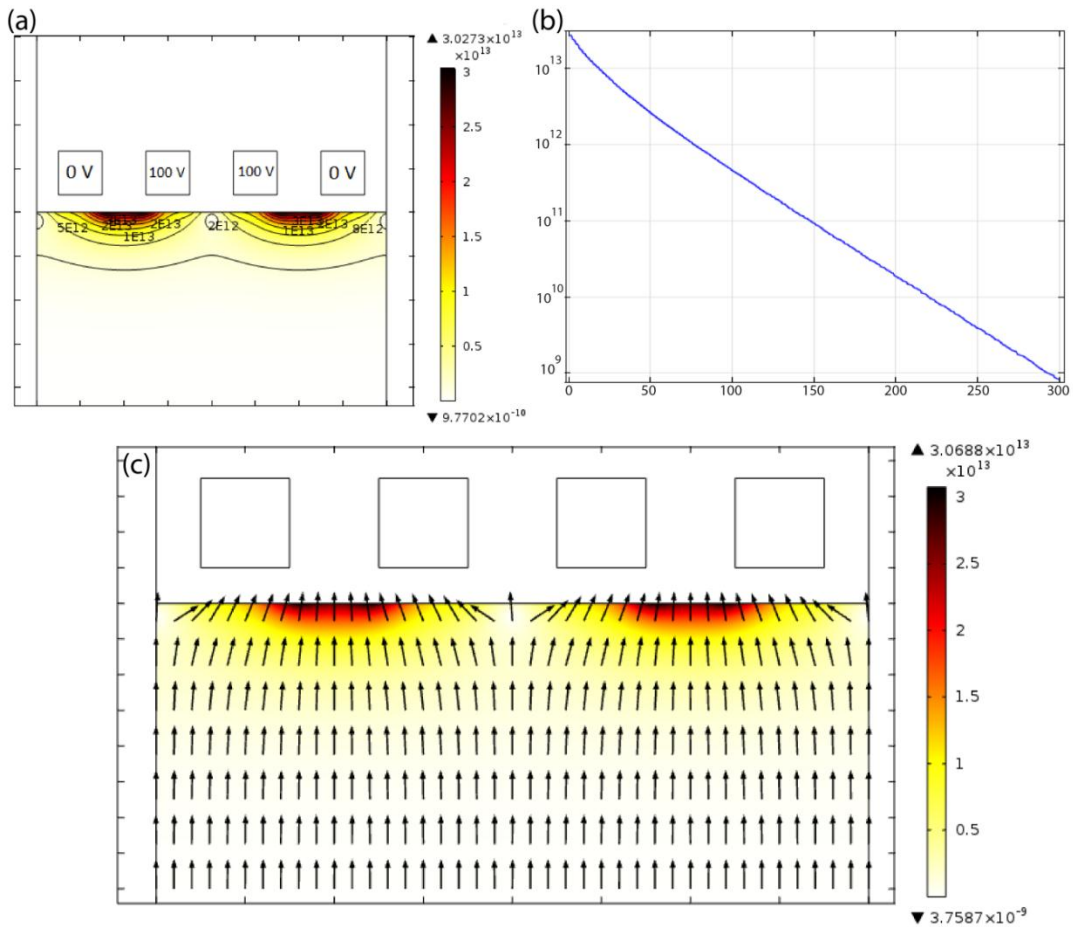
**Fig. 11.2.** Schematic of the 2D model with periodic boundary conditions.

We tried to find the optimum geometrical conditions and electrical signature that increase  $\nabla(\vec{E}_{RMS} \cdot \vec{E}_{RMS})$ , because it will allow to apply less voltage and frequency (which is better for cells viability) and have deeper sample channels (which increases the throughput of the system). Moreover,  $\nabla(\vec{E}_{RMS} \cdot \vec{E}_{RMS})$  is particle independent, only geometry dependent, and can be considered as a direct measure of cDEP microdevices ability to create DEP force. Studying  $\nabla(\vec{E}_{RMS} \cdot \vec{E}_{RMS})$  instead of DEP force facilitates our investigation and discussion of the geometry. Further in this study, the device is investigated on x-y plane separately to increase the deflection of the particles. On x-y plane, other parameters such as the angle between electrode channels and the sample channel become important which cannot be considered in 2D modeling.

Fig. 11.3. demonstrates  $\nabla(\vec{E}_{RMS} \cdot \vec{E}_{RMS})$  and its contours for the geometry shown in Fig. 11.2.  $\nabla(\vec{E}_{RMS} \cdot \vec{E}_{RMS})$  reaches its highest value close to sharp corners of electrode channels with opposite charge. Since we are interested to increase the maximum value of  $\nabla(\vec{E}_{RMS} \cdot \vec{E}_{RMS})$ , it was investigated on a line located directly under this sharp corner (shown in Fig. 11.2 as a red dashed line, line "A").  $\nabla(\vec{E}_{RMS} \cdot \vec{E}_{RMS})$  on line "A" is shown in Fig. 11.3.b. in logarithmic scale.  $\nabla(\vec{E}_{RMS} \cdot \vec{E}_{RMS})$  decreases exponentially on line "A" except for the area close to the electrode

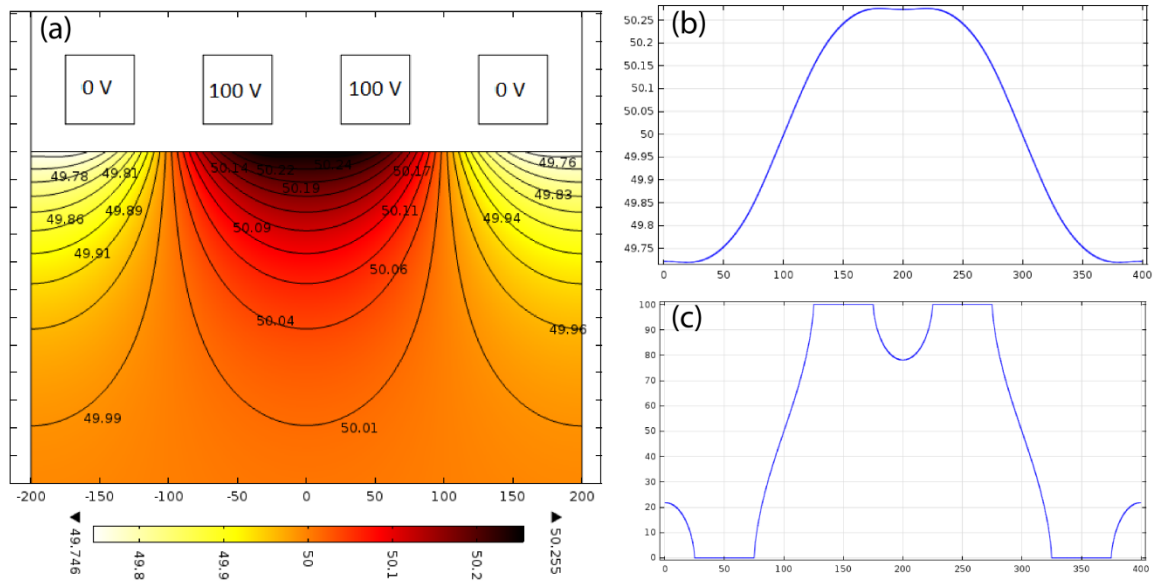
surface. This is in agreement with our analytical studies on the conventional interdigitated DEP techniques. Those analyses are also valid for areas  $z > d$ , where  $d$  is the average of the width of the electrodes and electrodes distances.

Fig. 11.3.c shows the vector plot of the direction of DEP force under the electrode channels. It shows that far from the electrode channels ( $z > d$ ) DEP force can be assumed to be vertical. However, close to electrode channels the direction of the force is towards the sharp corners of electrode channels.



**Fig. 11.3.** (a)  $\nabla(\vec{E}_{RMS} \cdot \vec{E}_{RMS})$  and its contours for the geometry shown in Fig. 11.2 inside the sample channel with 5mm depth. (b)  $\nabla(\vec{E}_{RMS} \cdot \vec{E}_{RMS})$  on line “A” in logarithmic scale (c) the vector plot of the direction of DEP force under the electrode channels

Fig. 11.4 demonstrated the contour of potential inside the sample channel after applying 100 V in source fluidic electrode channels (see Fig. 11.2). This contour is similar qualitatively with the contour of voltage for conventional interdigitated electrodes. Also, the voltage on the surface of the membrane is shown in Fig 11.4.b which is qualitatively similar to Fig. 11.1.b. The averaged voltage in Fig. 11.4.b is 50 V.



**Fig. 11.4.** (a) Voltage for the basic case. (b) Voltage at the surface of PDMS, (c) voltage under the electrode channels inside the PDMS.

Fig. 11.4.c shows the voltage on a line exactly under the electrode channels inside the PDMS. This figure can be compared to Fig. 11.5.b which shows the voltage on the PDMS surface when the membrane thickness is zero. Fig. 11.5.a shows the simulation of a conventional interdigitated electrode array with periodic boundary conditions.

Fig. 11.5.a and 11.5.b present two different cases in which whether electrodes change sign one by one (Fig. 11.5.a) or two by two (Fig. 11.5.b). Voltage on the line right under the electrodes (in the interface between the PDMS and the sample channel) is drawn for both cases in Fig. 11.5.c and (d). We modeled electric potential inside the sample channel for both cases. Fig. 11.5.a is

similar to conventional DEP case studied earlier (Fig. 11.1). Fig. 11.5.d is simplified in two ways shown in Fig. 11.5.e and f and Fourier expansion for both cases can be find.

For Fig. 11.5.e, the equation of the center line is  $V(x) = \frac{2x}{d_2}(V_0 - V_1) + V_1$ . The symmetry line has the equation of  $V(x) = V_0 - \frac{2xV_0}{d_3} + \frac{2(d_1+d_2/2)V_0}{d_3}$ .

$$k_n = 2\pi n/\lambda, \lambda = 2(2d_1 + d_2 + d_3)$$

$$k_n = 2\pi n/\lambda, \lambda = 2(2d_1 + d_2 + d_3) \quad (11.45)$$

$$A_n = \frac{2}{\lambda} \int_0^{\lambda/2} \varphi(x, 0) \cos(k_n x) dx \quad (11.46)$$

$$= \frac{4}{\lambda} \left[ \int_0^{\frac{d_2}{2}} \left( \frac{2x}{d_2}(V_0 - V_1) + V_1 \right) \cos(k_n x) dx + \int_{\frac{d_2}{2}}^{d_1 + \frac{d_2}{2}} \left( \frac{2V_0}{d_2} \right) (V_0) \cos(k_n x) dx \right. \\ \left. + \int_{d_1 + \frac{d_2}{2}}^{d_1 + \frac{d_2}{2} + \frac{d_3}{2}} \left( V_0 - \frac{2xV_0}{d_3} + \frac{2(d_1 + d_2/2)V_0}{d_3} \right) \cos(k_n x) dx \right] \quad (11.47)$$

$$= \frac{4}{\lambda} \frac{\lambda}{2} \left[ \frac{V_0}{d_3 \pi^2 n^2} \left[ \lambda \cos \left( (d_1 + d_2/2) \frac{2n\pi}{\lambda} \right) - d_3 n \pi \sin \left( (d_1 + d_2/2) \frac{2n\pi}{\lambda} \right) \right] \right. \\ \left. + \frac{V_0}{n\pi} \left( \sin \left( (d_1 + d_2/2) \frac{2n\pi}{\lambda} \right) - \sin \left( \frac{d_2 n \pi}{\lambda} \right) \right) \right. \\ \left. + \frac{1}{\pi^2 n^2} \left( -\frac{2\lambda(V_0 - V_1)}{d_2} \sin^2 \left( \frac{d_2 n \pi}{\lambda} \right) + n\pi V_0 \sin \left( \frac{d_2 n \pi}{\lambda} \right) \right) \right] \quad (11.48)$$

$$\begin{aligned}
&= \frac{2\lambda}{d_2 d_3 \pi^2 n^2} \left( -d_3(V_0 - V_1) + d_3(V_0 - V_1) \cos\left(\frac{d_2 n \pi}{\lambda}\right) \right. \\
&\quad \left. + d_2 V_0 \cos\left((d_1 + d_2/2) \frac{2n\pi}{\lambda}\right) \right)
\end{aligned} \tag{11.49}$$

By choosing the slope of center lines in Fig. 11.5.e the same as the symmetric line, the equation of the center line becomes  $V(x) = \frac{2V_0}{d_3} \left(x - \frac{d_2}{2}\right)$ , then we will have

$$A_n = \frac{2\lambda V_0}{d_3 \pi^2 n^2} \left( -1 + \cos\left(\frac{d_2 n \pi}{\lambda}\right) + \cos\left((d_1 + d_2/2) \frac{2n\pi}{\lambda}\right) \right) \tag{11.50}$$

In the case that  $d_2 = 0$  and  $V_1 = V_0$ , both above equations reduce to Equation (11.14).

We can also model Fig. 11.5.d as shown in Fig. 11.5.f. Then, the slope of the center line becomes  $V(x) = \frac{2V_0}{d_3} (x - d_2/2) + V_0$

$$\begin{aligned}
A_n = \frac{2}{d_3 \pi^2 n^2} &\left( \lambda \left( \cos\left(\frac{d_2 n \pi}{\lambda}\right) + \cos\left((d_1 + d_2/2) \frac{2n\pi}{\lambda}\right) + \cos\left(\frac{d_4 n \pi}{\lambda}\right) \right) \right. \\
&\left. + V_1 d_3 n \pi \sin\left(\frac{d_4 n \pi}{\lambda}\right) + n \pi (d_2 - d_3 - d_4) \sin\left(\frac{d_4 n \pi}{\lambda}\right) \right)
\end{aligned} \tag{11.51}$$

When  $d_2$  goes to zero,  $A_n$  goes to the Equation (11.14).

$\nabla(\vec{E}_{RMS} \cdot \vec{E}_{RMS})$  is simulated for a system with circular electrode channels, with a radius equal to the rectangular electrode channel height and width (= 50  $\mu\text{m}$ ), shown in Fig. 11.6.a.  $\nabla(\vec{E}_{RMS} \cdot \vec{E}_{RMS})$  is demonstrated in Fig. 11.6.b on a line in the same location as line ‘‘A’’ in Fig. 11.2.  $\nabla(\vec{E}_{RMS} \cdot \vec{E}_{RMS})$  is approximately half of the value of the system with rectangular electrode channels. This shows that the high gradient areas are not necessarily due to the sharp corners of the rectangular electrode channels. It can be due to the change in the electrode channel shape,

whether this change is more gradual, like a circle, or sudden, like a rectangle. Fig. 11.6.b also shows that  $\nabla(\vec{E}_{RMS} \cdot \vec{E}_{RMS})$  changes logarithmically in the sample channel, except close to the surface similar to rectangular electrode channels.

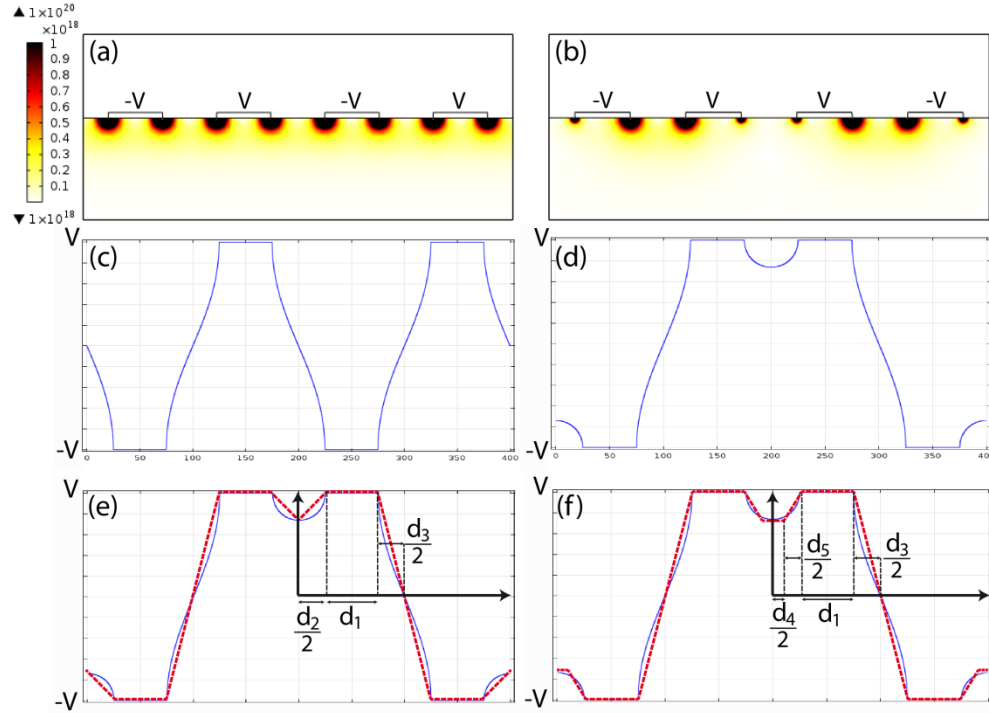


**Fig. 11.5.**  $\nabla(\vec{E}_{RMS} \cdot \vec{E}_{RMS})$  for conventional interdigitated electrode array (membrane thickness = 0) when electrodes change sign (a) one by one or (b) two by two. Voltage at the surface of the electrodes (c) for case (a), and (d) for case (b). (e) and (f) show two approximation of (d).

The effect of frequency at a constant applied voltage of 100 V is shown in Fig. 11.7.a.  $\nabla(\vec{E}_{RMS} \cdot \vec{E}_{RMS})$  was drawn on line “A” at 1, 10, 100, 200, and 500 kHz. As was expected, by increasing the frequency,  $\nabla(\vec{E}_{RMS} \cdot \vec{E}_{RMS})$  and consequently DEP force increase. Membrane thickness was also studied while the other geometrical parameters were kept constant (Fig. 11.7.b). Membrane thickness of 0, 10, 20, 50, and 100  $\mu\text{m}$  were modeled and it was found that by increasing the membrane thickness,  $\nabla(\vec{E}_{RMS} \cdot \vec{E}_{RMS})$  and DEP force decrease. This was

expected based on the relations for resistance,  $R = \rho d/A$ , and capacitance,  $C = \epsilon A/d$  as a function of the membrane area,  $A$ , and thickness,  $d = t_{mem}$ , where  $\rho$  and  $\epsilon$  are resistivity and permittivity of the barrier. By increasing the membrane thickness, the resistance increases and the capacitance decreases, thus  $\nabla(\vec{E}_{RMS} \cdot \vec{E}_{RMS})$  decreases. One limitation for the membrane thickness is the breakdown voltage of the PDMS membrane which for a 20  $\mu\text{m}$  PDMS membrane is about 300  $V_{RMS}$ .

$\nabla(\vec{E}_{RMS} \cdot \vec{E}_{RMS})$  as a function of the distance between positive and negative electrode channels (0, 10, 20, 50, 100, and 200  $\mu\text{m}$ ) and the distance between positive-positive and negative-negative electrode channels (10, 50, 100, 500, and 1000  $\mu\text{m}$ ) are also demonstrated in Fig. 11.7.c and d, respectively.  $\nabla(\vec{E}_{RMS} \cdot \vec{E}_{RMS})$  decreases by increasing the distance between any two of electrode channels, which is in agreement with our analytical model. Although larger  $\nabla(\vec{E}_{RMS} \cdot \vec{E}_{RMS})$  is desirable, increasing the distance between positive and negative electrode channels generates more uniform  $\nabla(\vec{E}_{RMS} \cdot \vec{E}_{RMS})$  which is preferable. Thus, there is a trade-off between  $\nabla(\vec{E}_{RMS} \cdot \vec{E}_{RMS})$  magnitude and its uniformity.

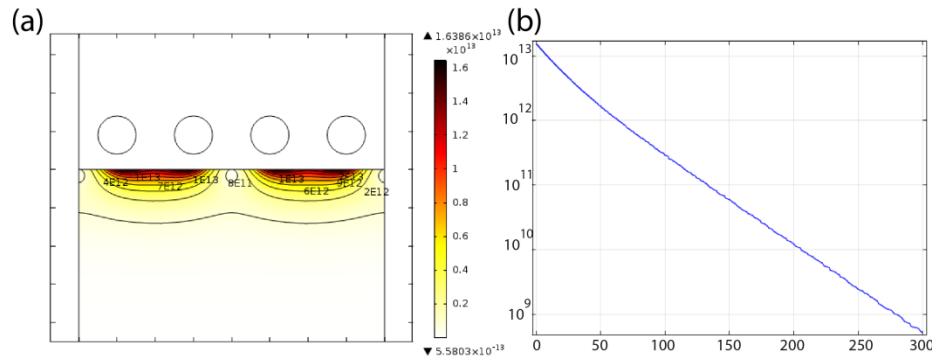


**Fig. 11.6.** (a)  $\nabla(\vec{E}_{RMS} \cdot \vec{E}_{RMS})$  for circular electrode channels. (b)  $\nabla(\vec{E}_{RMS} \cdot \vec{E}_{RMS})$  on a line in the same location as line “A” in Fig. 11.2.

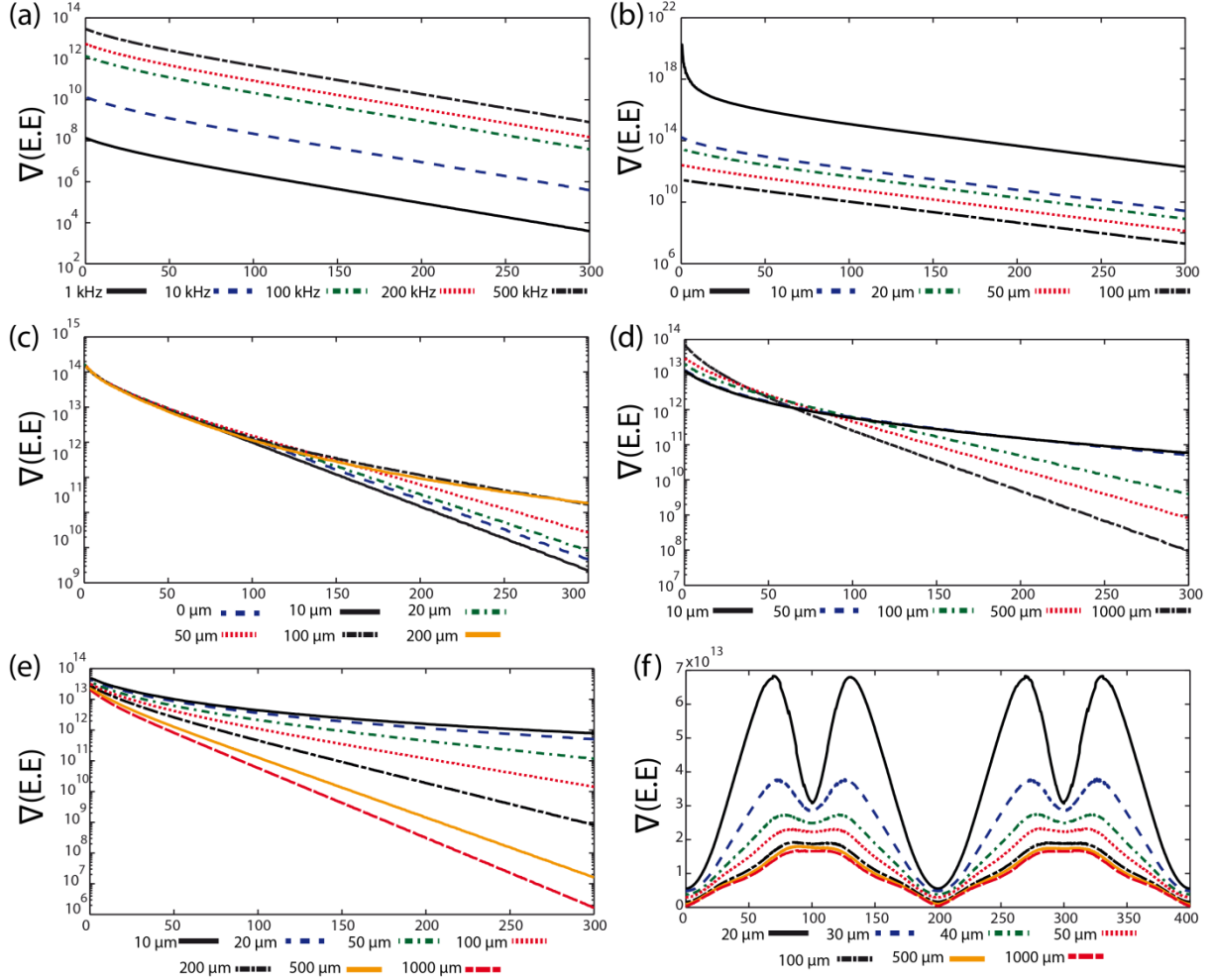


**Fig. 11.7.**  $\nabla(\vec{E}_{RMS} \cdot \vec{E}_{RMS})$  as a function of (a) applied frequency (1, 10, 100, 200, and 500 kHz) at a constant applied voltage of 100 V, (b) membrane thickness (0, 10, 20, 50, and 100  $\mu\text{m}$ ) (c) the distance between positive and negative electrode channels (0, 10, 20, 50, 100, and 200  $\mu\text{m}$ ), (d) the distance between positive-positive and negative-negative electrode channels (10, 50, 100, 500, and 1000  $\mu\text{m}$ ), (e) electrode channel width (10, 20, 50, 100, 200, 500, and 1000  $\mu\text{m}$ ), and (f) sample channel heights (20, 30, 40, 50, 100, 500, and 1000  $\mu\text{m}$ ).

$\nabla(\vec{E}_{RMS} \cdot \vec{E}_{RMS})$  as a function of electrode channels depth (50, 100, 200, 500, and 1000  $\mu\text{m}$ ) was studied (not shown). It was found that electrode channels height does not affect  $\nabla(\vec{E}_{RMS} \cdot \vec{E}_{RMS})$ .

Fig. 11.7.e presents  $\nabla(\vec{E}_{RMS} \cdot \vec{E}_{RMS})$  as a function of electrode channel width (10, 20, 50, 100,

200, 500, and 1000  $\mu\text{m}$ ) which shows that  $\nabla(\vec{E}_{RMS} \cdot \vec{E}_{RMS})$  decreases by increasing the electrode channels width which was predictable by the analytical model. Fig. 11.7.d and e also show that lower distance between positive-positive and negative-negative electrode channels and lower electrode channel width are favorable since they increase the uniformity of DEP force through channel depth. Fig 11.7.f demonstrated  $\nabla(\vec{E}_{RMS} \cdot \vec{E}_{RMS})$  on a line 10  $\mu\text{m}$  under the PDMS surface for devices with different sample channel heights (20, 30, 40, 50, 100, 500, and 1000  $\mu\text{m}$ ). By increasing the sample channels height,  $\nabla(\vec{E}_{RMS} \cdot \vec{E}_{RMS})$  decreases, however the change is negligible for channel heights higher than 100  $\mu\text{m}$ .

The pattern of the fluctuation of  $\nabla(\vec{E}_{RMS} \cdot \vec{E}_{RMS})$  at different heights in the sample channel inspired us to investigate further  $\vec{E}_{RMS} \cdot \vec{E}_{RMS}$  in the sample channel.  $\vec{E}_{RMS} \cdot \vec{E}_{RMS}$  is shown at different heights (10, 20, 30, 40, 50, 100, and 200  $\mu\text{m}$ ) inside the sample channel in Fig. 11.8. It is important to be mentioned that grid resolution study was performed on all the computational results presented to ensure the convergence of results.

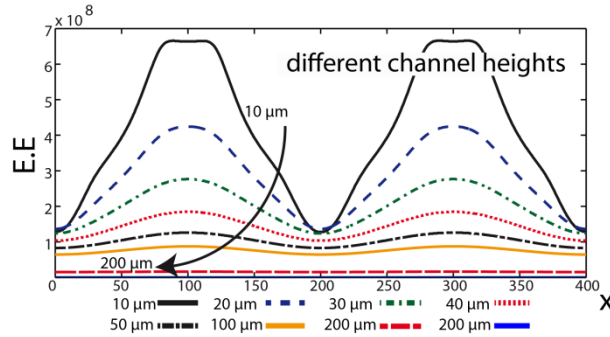


**Fig. 11.8.**  $\vec{E}_{RMS} \cdot \vec{E}_{RMS}$  at heights of 10, 20, 30, 40, 50, 100, and 200  $\mu\text{m}$  under the PDMS surface.

Fig. 11.8 demonstrates that  $\vec{E}_{RMS} \cdot \vec{E}_{RMS}$  can be estimated as a sine/cosine function which is in agreement with our theoretical model and also shows that the presented multilayer cDEP follows roughly the theoretical predictions of conventional interdigitated electrode array. Thus,

$\vec{E}_{RMS} \cdot \vec{E}_{RMS}$  can be modeled as a sine wave with a period equal to the geometrical period of the device shown in Fig. 11.2. Since  $\vec{E}_{RMS} \cdot \vec{E}_{RMS}$  also changes exponentially with the height of the sample channel, we suggested estimating  $\vec{E}_{RMS} \cdot \vec{E}_{RMS}$  as

$$\vec{E}_{RMS} \cdot \vec{E}_{RMS}(x, z) = \left( A \sin\left(\frac{2\pi x}{\lambda}\right) + B \right) e^{-\alpha z} \quad (11.52)$$

where  $\lambda$  is the period of the domain,  $A$ ,  $B$ , and  $\alpha$  are constants. Then the components of  $\nabla(\vec{E}_{RMS} \cdot \vec{E}_{RMS})$  can be find as

$$\frac{\partial(\vec{E}_{RMS} \cdot \vec{E}_{RMS})}{\partial x} = A \frac{2\pi}{\lambda} \cos\left(\frac{2\pi x}{\lambda}\right) e^{-\alpha z} \quad (11.53)$$

$$\frac{\partial(\vec{E}_{RMS} \cdot \vec{E}_{RMS})}{\partial z} = -\alpha \left( A \sin\left(\frac{2\pi x}{\lambda}\right) + B \right) e^{-\alpha z} \quad (11.54)$$

Then, by knowing that the DEP and drag forces components in x- and z-directions should be equal, we can write

$$6\pi\eta R \frac{dx}{dt} = 2\pi R^3 \varepsilon_m \text{Re}\{f_{CM}\} A \frac{2\pi}{\lambda} \cos\left(\frac{2\pi x}{\lambda}\right) e^{-\alpha z} \quad (11.55)$$

$$6\pi\eta R \frac{dz}{dt} = 2\pi R^3 \varepsilon_m \text{Re}\{f_{CM}\} (-\alpha) \left( A \sin\left(\frac{2\pi x}{\lambda}\right) + B \right) e^{-\alpha z} \quad (11.56)$$

By dividing the two expressions

$$\frac{dx}{dz} = \frac{A \frac{2\pi}{\lambda} \cos\left(\frac{2\pi x}{\lambda}\right)}{(-\alpha) \left( A \sin\left(\frac{2\pi x}{\lambda}\right) + B \right)} \quad (11.57)$$

Right side of the relation is only a function of  $x$ , thus

$$dz = \frac{(-\alpha) \left( A \sin \left( \frac{2\pi x}{\lambda} \right) + B \right)}{A \frac{2\pi}{\lambda} \cos \left( \frac{2\pi x}{\lambda} \right)} dx \quad (11.58)$$

$$z(t) = z(0) + \frac{-\alpha}{A \left( \frac{2\pi}{\lambda} \right)^2} \left[ -A \ln \left[ \cos \left( \frac{2\pi x}{\lambda} \right) \right] + B \ln \left[ \frac{\cos \left( \frac{\pi x}{\lambda} \right) + \sin \left( \frac{\pi x}{\lambda} \right)}{\cos \left( \frac{\pi x}{\lambda} \right) - \sin \left( \frac{\pi x}{\lambda} \right)} \right] \right] \quad (11.59)$$

$$z(t) = z(0) + \frac{\alpha}{A \left( \frac{2\pi}{\lambda} \right)^2} \left[ A \ln \left[ \cos \left( \frac{2\pi x}{\lambda} \right) \right] - B \ln \left[ \tan \left( \frac{\pi}{4} + \frac{\pi x}{\lambda} \right) \right] \right] \quad (11.60)$$

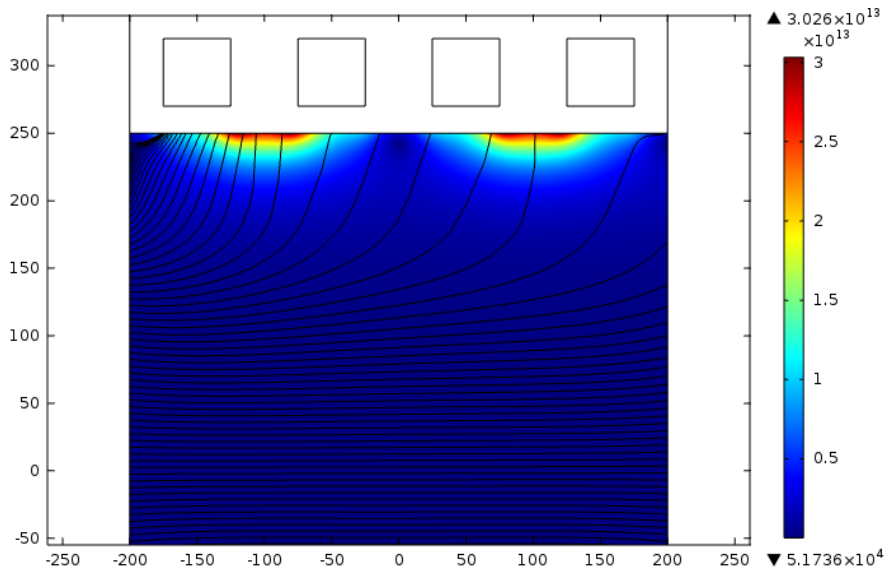
This relation enables us to predict the trajectories of the particles on x-z lane.

Fig. 11.9 demonstrated the trajectory of particles from the computational results with initial velocity of 55.56  $\mu\text{m/s}$  (equivalent to flow rate of 0.2 mL/hr in our previous cDEP studies [9]). Particles enter the sample channel from the left boundary and move towards the right one. This figure shows that particles on heights larger than approximately 140  $\mu\text{m}$  can be attracted towards the higher  $\nabla(\vec{E}_{RMS} \cdot \vec{E}_{RMS})$  area. However, the trajectories of particles under approximately 140  $\mu\text{m}$  do not change direction toward electrode channels and they exit the channel with approximately the same height as they entered from the left boundary. Thus, in our experimental devices we should make sample channel maximum 140  $\mu\text{m}$  deep to make sure all particle will experience DEP forces and will be deflected and manipulated. This result is approximately in agreement with the theoretical results discussed previously. If we assume  $\nabla(\vec{E}_{RMS} \cdot \vec{E}_{RMS}) \geq 10^{12}$  is required to manipulate particle (assuming  $f_{CM} = 0.5$  and  $V_0 = 50 \text{ V}$ ) based on our previous cDEP studies [9], a sample channel with depth of maximum 200  $\mu\text{m}$  is required based on the Equation (11.20):

$$10^{12} = - \frac{64 \times 50^2}{\pi \times (50 \times 10^{-6})^3} e^{-\frac{\pi z}{50 \times 10^{-6}}}$$

This estimation is close enough to what the computational model predicts considering that equation (11.20) is for conventional DEP not cDEP. What the analytical model suggested is larger from what computational model predict because the thin membrane layer (which reduces the voltage in the sample channel comparing to the applied voltage) has not been considered in equation (11.20) but it is considered in the computational model.

Fig. 11.10 shows a five layer PDMS microdevice which has electrode channels both on top and bottom of the sample channel. The sink and source fluidic electrode channel can be arranged in two forms shown in Fig. 11.10.a and b. If the sink and source electrode channels are identical in both sides of the electrode channel, higher  $\nabla(\vec{E}_{RMS} \cdot \vec{E}_{RMS})$  can be generated, although it is not significantly larger than its counterpart. The 3D model of this device is discussed later (see Fig. 11.15).



**Fig. 11.9.** Trajectories of particles and  $\nabla(\vec{E}_{RMS} \cdot \vec{E}_{RMS})$  at a sample channel 500  $\mu\text{m}$  in depth.

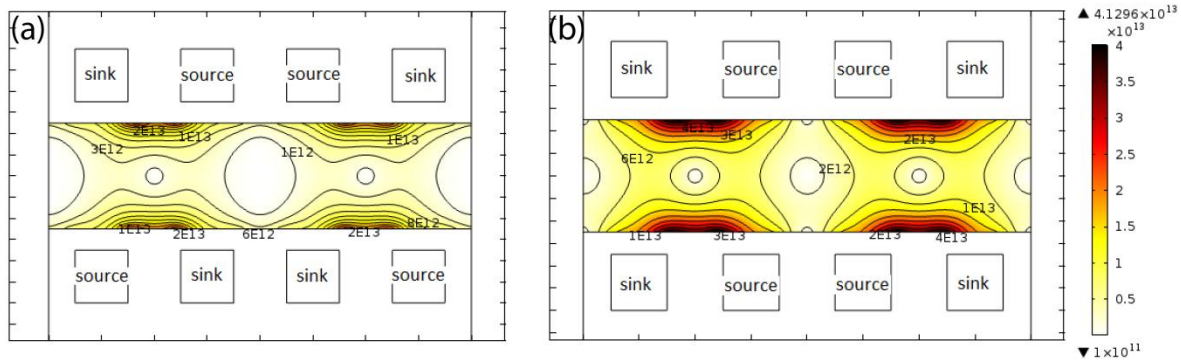


**Fig. 11.10.**  $\nabla(\vec{E}_{RMS} \cdot \vec{E}_{RMS})$  in sample channel for (a) electrode channel with opposite charge (b) with the same charge as electrode channels on the other side.

Fig. 11.11.a shows the top view of a conventional interdigitated electrode array. Fig. 11.11.b shows the equivalent multilayer cDEP device; in this device the distance between similar fluidic electrode channels is smaller than the distance between dissimilar ones to make it more similar geometrically and electrically to Fig. 11.11.a. Since we use fluidic electrode channels instead of metallic electrodes, the electrode channels cannot be located as sink-source pattern; instead they are located as sink-sink-source-source pattern (compare Fig. 11.1 and 11.2 too).

To study the similarities between devices shown in Fig. 11.11.a and b, two devices with cross-sections shown in Fig. 11.11.c and d are modeled computationally. The width of the electrode channels in Fig. 11.11.c is equal to the width of two electrode channels and the gap between the similar charge electrode channels in Fig. 11.11.d  $\nabla(\vec{E}_{RMS} \cdot \vec{E}_{RMS})$  on lines 10, 20, 30, 40, 50, and 100  $\mu\text{m}$  under the membrane for these two cases are shown Fig. 11.11.e.  $\nabla(\vec{E}_{RMS} \cdot \vec{E}_{RMS})$  for these two devices are in the same range (Fig. 11.11.e), except for a small areas between similar electrode channels in the case of Fig. 11.11.d. Since the presented computational model is 2D, the 3D effects, specifically the angle between the fluid flow and electrode channels, are not considered in computations shown in Fig. 11.11.

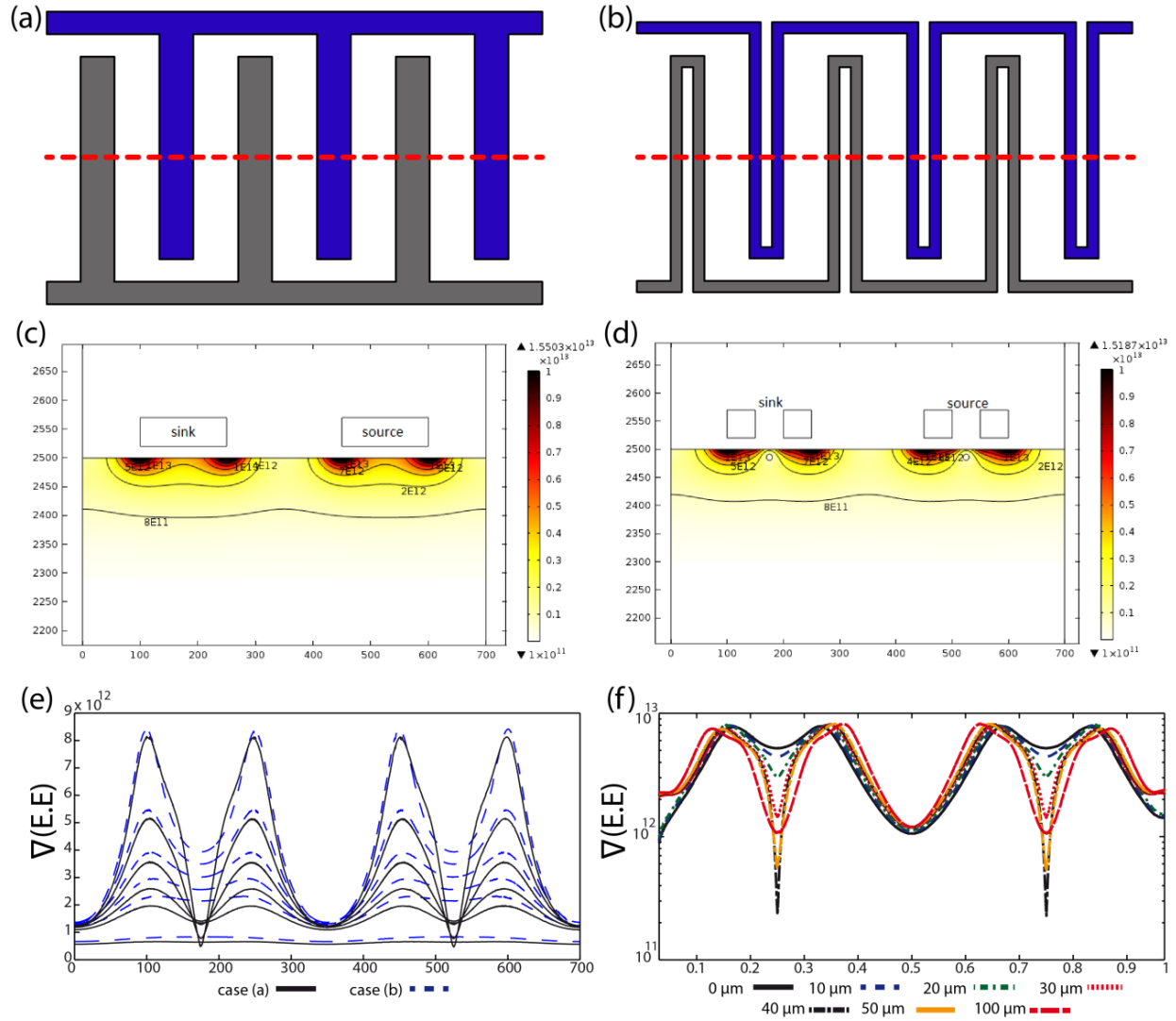


**Fig. 11.11.** (a) The top view of a conventional interdigitated electrode array (sink-source pattern). (b) The equivalent multilayer cDEP device (sink-sink-source-source pattern). (c) and (d) show  $\nabla(\vec{E}_{RMS} \cdot \vec{E}_{RMS})$  for two cases presented in (a) and (b), respectively. (e)  $\nabla(\vec{E}_{RMS} \cdot \vec{E}_{RMS})$  on lines 10, 20, 30, 40, 50, and 100  $\mu\text{m}$  under the membrane for two cases shown in (c) and (d). Blue dashed line represents sink-source pattern (case (a)) and black solid line represents sink-sink-source-source pattern (case (b)). (f)  $\nabla(\vec{E}_{RMS} \cdot \vec{E}_{RMS})$  on a line parallel to the membrane, 10  $\mu\text{m}$  under the membrane, when the gap between similar charge electrode channels changes as 0, 10, 20, 30, 40, 50, and 100  $\mu\text{m}$ . The sample channel width is normalized since it changes by changing the gap between electrode channels.

Fig. 11.11.f demonstrates  $\nabla(\vec{E}_{RMS} \cdot \vec{E}_{RMS})$  on a line parallel to the membrane, 10  $\mu\text{m}$  under the membrane. In this figure the gap between similar charge electrode channels changes as 0, 10, 20, 30, 40, 50, and 100  $\mu\text{m}$ . By decreasing the gap between the electrode channels, the minimum value of  $\nabla(\vec{E}_{RMS} \cdot \vec{E}_{RMS})$  decreases and the system becomes more similar to the device shown in Fig. 11.11.c. Since the width of the channel changes by changing the gap between electrodes, the width is normalized in Fig. 11.11.f.

## 11.5 3D computational modeling

The computing time and memory is limited when modeling in 3D. To address this issue, we used the analytical solutions for the velocity profile and replaced it with the computational results for fluid flow. We considered that the velocity in x-direction is a function of both y and z. Then we used a more simple case where velocity is only a function of z assuming that it is infinitely long in y direction.

The Navier-Stokes equations can be written as

$$\frac{\partial^2 u}{\partial y^2} + \frac{\partial^2 u}{\partial z^2} = \frac{1}{\mu} \frac{dP}{dx} \quad \text{for } -\frac{b}{2} < y < \frac{b}{2} \text{ and } -\frac{h}{2} < z < \frac{h}{2} \quad (11.61)$$

With the boundary conditions, shown in Fig. 11.12, as

$$u(y, z) = 0 \quad \text{for } y = \pm \frac{b}{2} \text{ and } z = \pm \frac{h}{2} \quad (11.62)$$

assuming that  $b > w$ . To satisfy  $z = \pm \frac{h}{2}$  boundary conditions, we should only use sine term in the Fourier series expansion in z-direction. The Fourier expansion for  $\frac{1}{\mu} \frac{dP}{dx}$  can be written as

$$\frac{1}{\mu} \frac{dP}{dx} = \frac{1}{\mu} \frac{dP}{dx} \frac{4}{\pi} \sum_{n, \text{odd}}^{\infty} \frac{1}{n} \sin\left(\frac{2n\pi z}{h}\right) \quad (11.63)$$

where  $n$  is an odd positive integer. Then  $u(y, z)$  can be expanded as

$$u(y, z) = \sum_{n=1}^{\infty} f_n(y) \sin\left(\frac{2n\pi z}{h}\right) \quad (11.64)$$

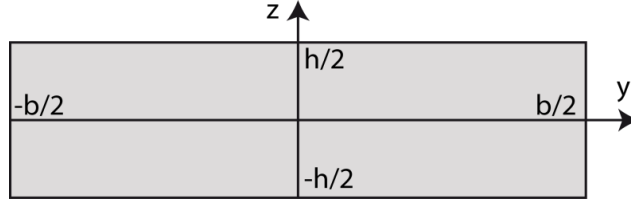


**Fig. 11.12.** (a) the schematic of the cross-section of the sample channel. The velocity profiles on a center line on.

where  $f_n(y)$  are the coefficients of the Fourier expansion in  $z$ -direction and are constant in  $z$ -direction but are function of  $y$ . Then

$$\frac{\partial^2 u}{\partial y^2} + \frac{\partial^2 u}{\partial z^2} = \sum_{n=1}^{\infty} \left[ f_n''(y) - \frac{4n^2\pi^2}{h^2} f_n(y) \right] \sin\left(\frac{2n\pi z}{h}\right) \quad (11.65)$$

The coefficients of both side of Equation (11.61) should be equal, thus

$$f_n''(y) - \frac{4n^2\pi^2}{h^2} f_n(y) = \frac{1}{\mu} \frac{dP}{dx} \frac{4}{\pi n} \quad \text{for } n \text{ odd} \quad (11.66)$$

$$f_n(y) = 0 \quad \text{for } n \text{ even} \quad (11.67)$$

The inhomogeneous solution of this equation is

$$f_n(y) = \frac{h^2}{\pi^3 \mu} \frac{dP}{dx} \frac{1}{n^3} \quad \text{for } n \text{ odd} \quad (11.68)$$

And the homogenous solution is

$$f_n(y) = A \cosh\left(\frac{2n\pi y}{h}\right) + B \sinh\left(\frac{2n\pi y}{h}\right) \quad (11.69)$$

Applying the boundary condition of  $f_n\left(\pm \frac{b}{2}\right) = 0$

$$f_n(y) = \frac{h^2}{\pi^3 \mu} \frac{dP}{dx} \frac{1}{n^3} \left[ 1 - \frac{\cosh\left(\frac{2n\pi y}{h}\right)}{\cosh\left(\frac{n\pi b}{h}\right)} \right] \quad \text{for } n \text{ odd} \quad (11.70)$$

And the velocity field for a rectangular channel can be written as

$$u(y, z) = \frac{h^2}{\pi^3 \mu} \frac{dP}{dx} \sum_{n, \text{odd}}^{\infty} \frac{1}{n^3} \left[ 1 - \frac{\cosh\left(\frac{2n\pi y}{h}\right)}{\cosh\left(\frac{n\pi b}{h}\right)} \right] \sin\left(\frac{2n\pi z}{h}\right) \quad (11.71)$$

Then the flow rate can be calculated as

$$Q = 4 \int_0^{h/2} \int_0^{b/2} u(y, z) dy dz \quad (11.72)$$

$$Q \approx \frac{h^3 w}{12\mu} \frac{dP}{dx} \left( 1 - 0.63 \frac{h}{w} \right) \quad (11.73)$$

In a general form, the relation between pressure drop and a constant flow rate for a pressure-driven, steady-state flow for a non-Newtonian incompressible fluid inside a straight channel can be written as

$$dP = R_{hyd} Q \quad (11.74)$$

where  $R_{hyd}$  is the hydraulic resistance and the above relation is known as Hagen- Poiseuille. For a rectangular cross-section, as we derives,  $R_{hyd}$  can be written as

$$\frac{12\mu}{h^3 w} \frac{dx}{\left( 1 - 0.63 \frac{h}{w} \right)} \quad (11.75)$$

Since in our case the channel height is approximately one order of magnitude smaller than the channel width (channel depth is limited to 150-200  $\mu\text{m}$  as was stated before, but the channel width can be in the order of millimeters), the flow on x-z plane can be assumed as a Couette flow with applied pressure. Thus, the Navier-Stokes questions can be simplified as

$$\begin{aligned} \frac{\partial^2 u}{\partial z^2} &= \frac{1}{\mu} \frac{dP}{dx} & (11.76) \\ \frac{\partial u}{\partial z} &= \frac{1}{\mu} \frac{dP}{dx} z + C_1 \\ u(z) &= \frac{1}{2\mu} \frac{dP}{dx} z^2 + C_1 z + C_2 \end{aligned}$$

The boundary conditions are

$$u\left(\pm \frac{h}{2}\right) = 0$$

Thus,

$$C_1 = 0$$

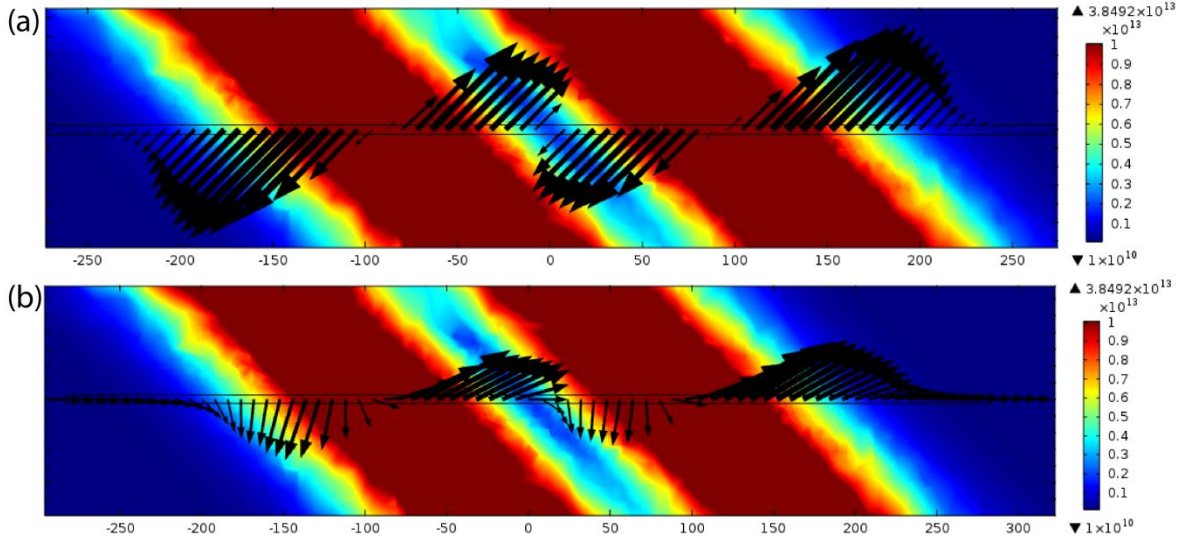


**Fig. 11.13.** (a) DEP force on a 15  $\mu\text{m}$  diameter particle with  $Re\{f_{CM}\} = 0.5$  on line “B”. (b) The net force (DEP and drag forces) in devices with  $\theta = 45$  degree. The surface plots of DEP are shown on a plane 5  $\mu\text{m}$  under the PDMS surface and force vectors are shown on the center line of the plane in x-direction.

$$C_2 = -\frac{1}{2\mu} \frac{dP}{dx} \frac{h^2}{4} \quad (11.77)$$

$$u(z) = \frac{1}{2\mu} \frac{dP}{dx} \left(z^2 - \frac{h^2}{4}\right) \quad (11.78)$$

Thus the flow velocity in x direction can be modeled as a parabolic profile.  $\frac{dP}{dx}$  can be predicted analytically or computationally. The pressure loss for a fully developed internal flow is

$$\frac{dP}{dx} = f \frac{\rho V_{ave}^2}{2D_H} \quad (11.79)$$

where  $f$  is the friction factor and  $D_H$  is the hydrodynamic diameter of the channel.  $D_H$  can be find from

$$D_H = \frac{2bh}{b+h} \quad (11.80)$$

where  $b$  and  $h$  are the channel width and depth, respectively. Assuming  $b$  and  $h$  to be approximately 1 mm and 100  $\mu\text{m}$ ,  $D_H = 1.82 \times 10^{-4}$  m. Also  $f$  for a rectangular channel with the width to depth ratio of 0.1 is

$$f = 84.68/Re_H \quad (11.81)$$

$Re_H$  is 0.01 based on the calculated  $D_H$ . Then for the average velocity of 55.56  $\mu\text{m/s}$ ,  $\frac{dP}{dx} = -71.8 \text{ Pa/m}$ .

The force on the particle at each point can be estimated as

$$F_x = F_{DEP,x} + F_{Drag} \quad (11.82)$$

$$F_y = F_{DEP,y}$$

Thus, DEP force can be calculated using COMSOL simulations and the drag force using the presented equations.

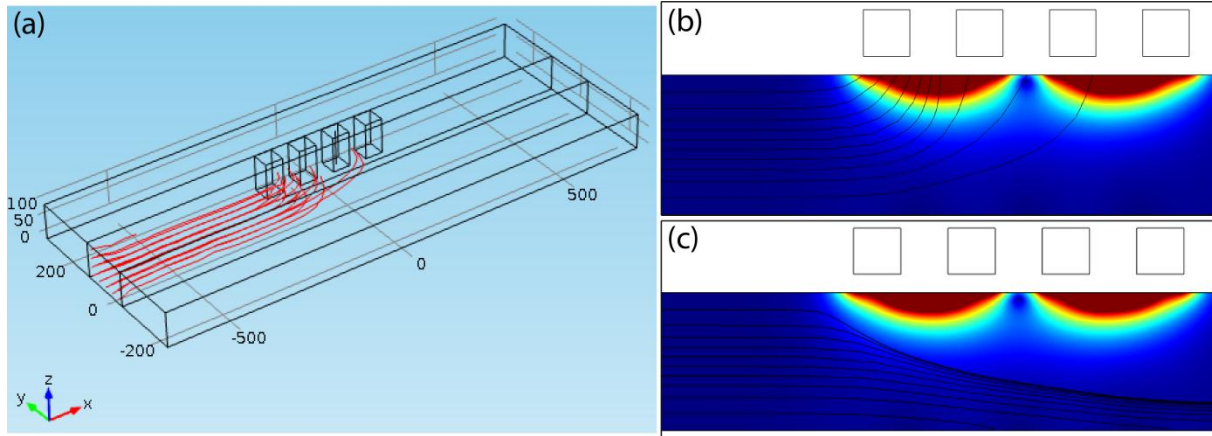


**Fig. 11.14.** (a) 3D view of the device with fluidic electrode channel on one side. 2D model of  $\nabla(\vec{E}_{RMS} \cdot \vec{E}_{RMS})$  and particle trajectory at 100 V and 500 kHz for a 15  $\mu\text{m}$  diameter particle when particles experience (b) positive (c) negative DEP.

Fig. 11.13.a demonstrates the DEP force on a 15  $\mu\text{m}$  diameter particle with  $Re\{f_{CM}\} = 0.5$  on line “B” in Fig. 11.1.a (in the same direction as fluid flow (x-direction) and 5  $\mu\text{m}$  under the

PDMS surface). The angle between the electrode channels and the fluid flow,  $\theta$ , is 45 degree in this device. As can be seen in this figure, DEP force is perpendicular to the electrode channels.

Fig. 11.13.b shows the net force (DEP and drag forces) in devices with  $\theta = 45$  degree. Drag force is the dominant force far from high  $\nabla(\vec{E}_{RMS} \cdot \vec{E}_{RMS})$  areas and it is in x-direction. By approaching the high  $\nabla(\vec{E}_{RMS} \cdot \vec{E}_{RMS})$  areas, DEP force dominates, thus particle moves downward or upward in y-direction. The net effect of movements in y-direction is not necessarily zero and particle may have a net lateral movement.

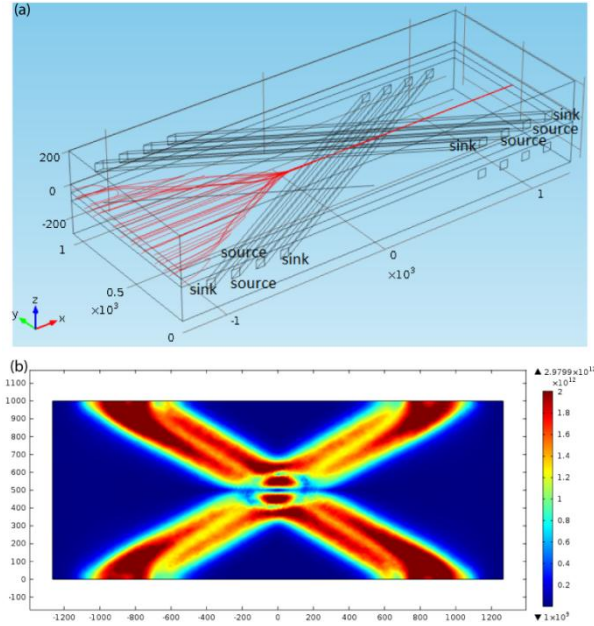
We can also use the previously discussed analytical and computational models for a device in which electrode channels are only located on one side of the device (Fig. 11.14.a). This device can be considered as a 90 degree-rotated of multilayer devices. Since the angle between the fluid flow and the electrode channels is 90 degree, there is not net force on particles in z-direction. However, particles can be attracted or repelled from the electrode channels in y-direction, shown in Fig. 11.14.b and c, respectively. The advantage of this device is that it can be as deep as we can fabricate the sample channel; however, the width is limited to 140-200, as was discussed before.

Fig. 11.15 demonstrated five layer cDEP devices where a sample channel is sandwiched between two sets of fluidic electrode channels on top and bottom. Fig. 11.15.a shows the trajectories of particles when the top and bottom electrode channels have similar charge to their counterparts. In this case particles are focused at the center of channel. Fig. 11.15.b demonstrate  $\nabla(\vec{E}_{RMS} \cdot \vec{E}_{RMS})$  on x-y plane at  $z=0$ .

## 11.6 Experimental results

A mixture of white blood cells (WBCs) and breast cancer cells (MDA-MB-231) were used to test to device. In these proof-of-concept experiments we tried to isolate cancer cells from WBCs. To visualize cells better, cancer cells were stained in green and WBCs were stained in red. Fig. 11.16 shows an image from one of the experiments. The fluid flow is from left to right. After

applying electric field ( $300V_{RMS}$  and  $500\text{ kHz}$ ) we observed that cancer cell start moving towards the fluid electrode channels direction while WBCs were still following the fluid flow direction. Pearl chaining was observed when cancer cells were close to electrode channel where they experience the highest DEP force. These results show that we can selectively separate cancer cells from WBCs continuously using multilayer cDEP microdevices.



**Fig. 11.15.** (a) Schematic of the device at  $\theta=30$ ,  $V=100$ , and frequency= $500\text{ kHz}$ . The particles trajectory are shown in red. (b)  $\nabla(\vec{E}_{RMS} \cdot \vec{E}_{RMS})$  on x-y plane at  $z=0$ .

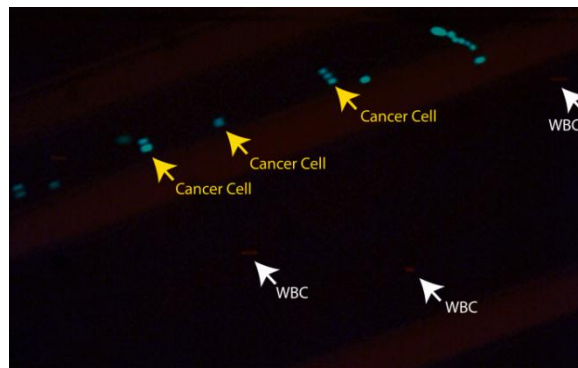


**Fig. 11.16.** Experimental results. Cancer cells are shown in green and WBCs are shown in red. The fluid flow is from left to right.

## 11.7 Conclusion

In this Chapter a multilayer contactless dielectrophoresis (cDEP) was presented to sort particles continuously. In cDEP multilayer devices, the electrode channels are located on top of the sample channel and are separated from the sample channel by a thin membrane. This means that in contrast to previous cDEP microdevices, the width of the channel is not limited to the distance between electrode channels in this device, thus, the width of the channel and consequently the throughput can be increased. We investigated this microdevice analytically in 2D using Fourier series. We also modeled the microdevice computationally in 2D and 3D. Different geometrical parameters were studied to improve the performance of the device. The comparison between the analytical results of conventional interdigitated infinite array of electrodes and cDEP computational results revealed agreement between these two models. Proof-of-concept experiments showed that multilayer cDEP devices are able to separate cancer cells from WBCs.

# Chapter Twelve

## Future Work

Future work will be mostly towards three main objectives which will be done in parallel and simultaneously. First objective is Advancing our understanding of the biophysical properties of cells. Our strategy for manipulating cells, specifically isolating rare cells for early cancer diagnoses, relies upon the cells' biophysical properties, which are closely aligned with stage of differentiation, transformation, and tumorigenicity of cells. We will assess whether theories and models explained previously in Chapter Two, such as the multi-shell model, can be used to investigate cells biophysical properties. We will also connect this biophysical information to the mechanical properties and cytoskeleton structure of the cells. From fluid mechanics point of view, we will study the drag force cells with different shapes (such as red blood cells) and surface roughness (such as metastatic cancer cells) experience moving in microfluidic devices.

The second and third objectives are improving the selectivity and increasing the throughput of cDEP microdevices, respectively. Limitations in the throughput and selectivity of our current devices are the main barriers to use cDEP technique in more significant applications and in a more efficient way. For instance, in CTC isolation application, it is required to isolate a few cancer cells from billions of red blood cells and millions of white blood cells, making high throughput a necessity. Also the high selectivity between white blood cells and cancer cells which have more similar size is very critical. Isolating TICs from normal cancer cells is another example. By increasing the throughput of our devices we will be able to isolate more than 100,000 TICs which will enable us to do animal study. This will also enable us to assess whether cDEP can isolate possible TIC subpopulations based on their dielectrophoretic properties at a gradient of frequencies at different voltages. Shifting towards continuous sorting can be considered as one of the important changes in designing cDEP-based microdevices. Designing

multilayer devices will enable us to enhance both selectivity and throughput as well as to sort cells continuously, which are explained further in this chapter.

## **12.1 Advancing our understanding of the biophysical properties of cells**

Challenges of cancer diagnoses and treatment indicate a need for further characterization of target cells by their biophysical properties independent of their heterogeneous genotype that will lead to finding more efficient cell manipulation techniques. Our strategy for cells isolation and characterization, specifically isolating TICs, CTCs, and ovarian cancer cells, relies upon the cells' biophysical properties and the differences between cells. Future work will be towards using multi-shell model, explained in Chapter Two, to investigate cells biophysical properties. This model will enable us to study the effects of different biophysical parameters such as the nucleus/cytoplasm ratio, membrane protrusions, and cytoplasm permittivity and conductivity, on cells electrical properties.

It is also important to study the drag force (and other potential electrical or mechanical forces) cells with different shapes (such as red blood cells) and surface roughness (such as metastatic cancer cells) experience while moving in microfluidic devices. Studying of biophysical properties of cells will be used 1) to deepen our understanding of the differences between TICs and normal cancer cells to isolate TICs more efficiently, and 2) to characterize ovarian cancer biophysics under both treated and un-treated conditions, and to use these insights in cancer detection and treatment techniques.

The electrical fingerprint of cells has not previously been used to achieve isolation of TICs from non-TICs and ovarian cancer cells from peritoneal fluid, or to compare the morphological effects of lower-toxicity dosages of anti-cancer drugs to biophysical properties of progressive stages of ovarian cancer. From fluid mechanics point of view, we will investigate how cells with different shapes, such as red blood cells comparing to white blood cells and cancer cells, and with

different membrane surface roughness, such as benign comparing to malignant metastatic cancer cells, experience different force, specifically drag force, while moving in a microfluidic device. This profounder understanding will give us another tool to manipulate cells and use their physical differences to sort them. Deepening our understanding about the biophysical and mechanical properties of cells will help us to design more efficient devices with higher selectivity for sorting these cells based on the difference in cells biophysical properties. This study will provide a new focus for cancer detection efforts by shifting from genotypic and biomarker-focused approaches to sorting based on biophysical properties of cells. This approach may lead to future clinical diagnostic assays for early cancer diagnosis and drug screening.

## **12.2 Enhancing selectivity**

Improving the selectivity of separation while maintaining the high throughput is one of the challenges in current cDEP devices. Most procedures suffer a tradeoff between throughput versus selectivity. Several strategies are suggested to improve selectivity:

- 1- Improving the geometry and arrangement of cDEP pillar-based devices.
- 2- Designing devices operating at crossover frequency of cells.
- 3- Designing devices with more uniform DEP force.

**Improving the geometry and arrangement of cDEP pillar-based devices:** The insulating structures inside the main channel are essential tools to enhance the dielectrophoretic force by increasing the electrical resistance of the main channel as well as increasing the nonuniformity of the squared electric field gradient. Without these structures, the gradient of the electric field is limited to areas close to the side walls of the main channel and most of the cells far from the side walls do not experience strong enough dielectrophoretic force. Adding the insulating structures facilitates wider channels with more uniform DEP force, which consequently, will increase the throughput and selectivity of the cDEP devices.

The selectivity of the pillar-based cDEP devices can be enhanced by further improving the size of the pillars, the gap between them, and their arrangement. So far these parameters have been improved mostly to increase DEP force and to reduce physical trapping. Further study is required to improve them to generate more uniform gradient of electric field squared.

**Designing devices operating at crossover frequency of cells:** Our high throughput devices operate in frequencies in the range of 100-600 kHz which is much higher than mammalian cells crossover frequencies (10-30 kHz) in a sample with conductivity of 100  $\mu\text{S}/\text{cm}$ . This relatively high range of frequency is required to generate sufficient electric field in the sample channel to manipulate cells; however, it decreases the selectivity of isolation. The other option is finding a buffer with a lower conductivity than 100  $\mu\text{S}/\text{cm}$ . This buffer should have osmolality equal to our current buffer, about 300 mOsmol, to keep cells alive. Decreasing the conductivity of the buffer enables us to reduce the applied frequency closer to the crossover frequency of mammalian cells. The future cDEP-based microdevices should be able to generate high electric fields to manipulate the cells, but at the same time to be able to operate at frequencies as low as cells crossover frequency. Operating in the range of cells crossover frequency will enable us to enhance the selectivity of separation.

**Designing devices with uniform DEP force:** Designing devices with more uniform DEP force is another option which is mostly possible through using multilayer cDEP devices (explained in chapter 11).

### **12.3 Increasing the throughput of cDEP microdevices**

Increasing the throughput is the main challenge for almost all cell sorting techniques. Current efforts in separation of rare cells such as CTCs and TICs are hampered by the lack of suitable high throughput and rapid methods to isolate these cells. For instance, there are only about 10 CTCs in 1 mL of blood, thus several mLs of blood should be analyzed to capture a few CTCs.

Most of current methods rely on time-consuming labeling of surface marker expression followed by cell sorting via flow cytometry. Recently, microfluidic techniques have been shown as an alternative for biomarker-based methods. However, microfluidic techniques also suffer from low throughput. Microelectrode-based devices are not suitable for high-throughput applications since the electric field gradient rapidly dissipates above the surface of the electrode array. Typical sample volumes that are processed within these devices are on the order of nano- to microliters, far below that of typical clinical diagnostic sample volumes (mL).

Although cDEP have solved some of the issues of conventional DEP techniques, it still suffers from low throughput mainly due to the fact that the sample channels width is limited by the distance between the electrode channels. Previous cDEP techniques were using flow rates in the range of 0.005-0.02 mL/hour [158, 159]. In our recent cDEP-based microdevices (shown in Fig. 10.1.), we succeed to increase the flow rate to 1 mL/hour which is equivalent to yielding approximately  $10^6$  sorted cells per hour when processing samples with a concentration of  $10^6$  cells/mL. In the next generation of cDEP microdevice, we will increase the flow rate further to 5 mL/hour or higher which will enable us to sort five million of cells in an hour. To do so, we should use other fabrication techniques, such as hot embossing and injection molding, rather than soft lithography to fabricate deeper cDEP devices to increase the cross sectional area and consequently the throughput. The other option is using a multilayer device which is explained below.

The other parameters playing important roles in increasing the throughput, as well as enhancing the selectivity as was mentioned before, are the number and arrangement of pillars inside the sample channel. Through this study the number of pillars increased from 8 in previous cDEP devices [158] to about 100,000 pillars in recent cDEP device (shown in Fig. 12.1.). If in average each pillar could trap 5 cells, this device will enable us to trap 500,000 cells, making animal study feasible.

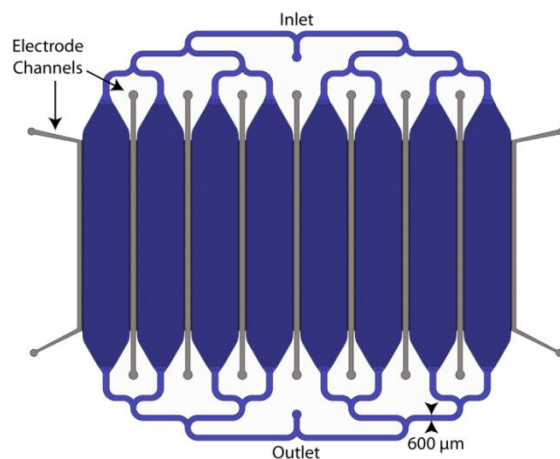


**Fig. 12.1.** A high-throughput cDEP microdevice with parallel sample channels in blue and fluid electrode channels in gray. The throughput of this device is 1 mL/hr.

After enhancing the throughput and improving the selectivity of cDEP technique, new devices will be used for sorting TICs and non-TICs and validate them by *in vivo* tumor formation. High throughput devices are essential for sorting about 100,000 cells required for animal study. Putative TICs and non-TICs will be enriched using markers for TICs such as ALDH, CD133, CD44, and  $\beta$ 1-integrin in prostate cancer cell lines and primary human prostate cells. Sorted cells will be used to establish the dielectrophoretic responses in prototype cDEP devices.

Then, we will isolate cells based entirely on cDEP parameters without preconceived notions of the TIC populations to determine if multiple fractions of TIC populations exist. We will assess whether cDEP can isolate possible TIC subpopulations based on their dielectrophoretic properties at a gradient of frequencies at different voltages. Subpopulations will be characterized *in vitro* and *in vivo*. Quantitative success of this research will be the discovery of a subpopulation which exhibits a 5 fold increase tumor growth rate versus the least tumorigenic subpopulation. If successful, this approach will impact the methods used for TIC isolation and characterization and may lead to future clinical diagnostic assays to monitor tumor aggressiveness.

## References

1. Pethig, R., et al., *Dielectrophoresis: a review of applications for stem cell research*. J Biomed Biotechnol, 2010. **2010**: p. 182581.
2. Salmanzadeh, A., et al., *Investigating dielectric properties of different stages of syngeneic murine ovarian cancer cells*. BIOMICROFLUIDICS, 2013. **7**: p. 011809.
3. Marszalek, P., et al., *Determination of electric parameters of cell membranes by a dielectrophoresis method*. Biophysical Journal, 1991. **59**(5): p. 982-7.
4. Pethig, R. and D.B. Kell, *The passive electrical properties of biological systems: their significance in physiology, biophysics and biotechnology*. Physics in Medicine and Biology, 1987. **32**(8): p. 933-70.
5. Pethig, R., *Review Article-Dielectrophoresis: Status of the theory, technology, and applications*. BIOMICROFLUIDICS, 2010. **4**(2).
6. Huang, Y., et al., *Dielectrophoretic cell separation and gene expression profiling on microelectronic chip arrays*. Analytical Chemistry, 2002. **74**(14): p. 3362-3371.
7. Salmanzadeh, A., et al., *Sphingolipid Metabolites Modulate Dielectric Characteristics of Cells in a Mouse Ovarian Cancer Progression Model*. Integrative Biology, 2013. **in press**.
8. Salmanzadeh, A., et al., *Dielectrophoretic differentiation of mouse ovarian surface epithelial cells, macrophages, and fibroblasts using contactless dielectrophoresis*. BIOMICROFLUIDICS, 2012. **6**(2): p. 24104-2410413.
9. Salmanzadeh, A., et al., *Isolation of prostate tumor initiating cells (TICs) through their dielectrophoretic signature*. Lab on a Chip, 2012. **12**(1): p. 182-9.
10. Salmanzadeh, A., et al., *Isolation of Rare Cancer Cells from Blood Cells Using Dielectrophoresis*, in *EMBC 2012*2012: San Diego, CA.
11. Salmanzadeh, A., et al., *Microfluidic mixing using contactless dielectrophoresis*. Electrophoresis, 2011. **32**(18): p. 2569-78.
12. Lostumbo, A., et al., *Flow cytometry: A new approach for the molecular profiling of breast cancer*. Experimental and Molecular Pathology, 2006. **80**(1): p. 46-53.
13. Kato, K. and A. Radbruch, *Isolation and Characterization of CD34 + Hematopoietic Stem Cells From Human Peripheral Blood by High-Gradient Magnetic Cell Sorting*. Cytometry, 1993. **14**(4): p. 384-392.
14. Nagrath, S., et al., *Isolation of rare circulating tumour cells in cancer patients by microchip technology*. Nature, 2007. **450**(7173): p. 1235-1239.
15. Li, C.W., et al., *Identification of pancreatic cancer stem cells*. Cancer Research, 2007. **67**(3): p. 1030-1037.
16. Yu, M., et al., *Circulating tumor cells: approaches to isolation and characterization*. The Journal of cell biology, 2011. **192**(3): p. 373.
17. Hayes, D.F., et al., *Circulating tumor cells at each follow-up time point during therapy of metastatic breast cancer patients predict progression-free and overall survival*. Clin Cancer Res, 2006. **12**(14 Pt 1): p. 4218-24.

18. Wang, X., et al., *Monocyte/macrophage and T-cell infiltrates in peritoneum of patients with ovarian cancer or benign pelvic disease*. J Transl Med, 2006. **4**: p. 30.
19. Gortzak-Uzan, L., et al., *A proteome resource of ovarian cancer ascites: integrated proteomic and bioinformatic analyses to identify putative biomarkers*. J Proteome Res, 2008. **7**(1): p. 339-51.
20. Westermann, A.M., et al., *Malignant effusions contain lysophosphatidic acid (LPA)-like activity*. Ann Oncol, 1998. **9**(4): p. 437-42.
21. Langdon, S.P., *Isolation and culture of ovarian cancer cell lines*. Methods Mol Med, 2004. **88**: p. 133-9.
22. Chan, J.K., et al., *A novel technique for the enrichment of primary ovarian cancer cells*. Am J Obstet Gynecol, 2007. **197**(5): p. 507 e1-5.
23. Nossov, V., et al., *The early detection of ovarian cancer: from traditional methods to proteomics. Can we really do better than serum CA-125?* Am J Obstet Gynecol, 2008. **199**(3): p. 215-23.
24. Reya, T., et al., *Stem cells, cancer, and cancer stem cells*. Nature, 2001. **414**(6859): p. 105-111.
25. Wicha, M.S., S. Liu, and G. Dontu, *Cancer stem cells: an old idea--a paradigm shift*. Cancer Research, 2006. **66**(4): p. 1883-90; discussion 1895-6.
26. Collins, A., et al., *Prospective identification of tumorigenic prostate cancer stem cells*. Cancer Research, 2005. **65**: p. 10946-10951.
27. Patrawala, L., et al., *Side population is enriched in tumorigenic, stem-like cancer cells, whereas ABCG2(+) and ABCG2(-) cancer cells are similarly tumorigenic*. Cancer Research, 2005. **65**(14): p. 6207-6219.
28. Patrawala, L., et al., *Hierarchical organization of prostate cancer cells in xenograft tumors: the CD44+alpha2beta1+ cell population is enriched in tumor-initiating cells*. Cancer Research, 2007. **67**(14): p. 6796-805.
29. Barclay, W.W., et al., *Characterization of adult prostatic progenitor/stem cells exhibiting self-renewal and multilineage differentiation*. Stem Cells, 2008. **26**(3): p. 600-10.
30. Barclay, W.W. and S.D. Cramer, *Culture of mouse prostatic epithelial cells from genetically engineered mice*. Prostate, 2005. **63**(3): p. 291-8.
31. Pohl, H.A., *Dielectrophoresis: The behavior of neutral matter in nonuniform electric fields* 1978, Cambridge: Cambridge University Press.
32. Lambrechts, A., M. Van Troys, and C. Ampe, *The actin cytoskeleton in normal and pathological cell motility*. The International Journal of Biochemistry & Cell Biology, 2004. **36**(10): p. 1890-1909.
33. Becker, F., et al., *The removal of human leukaemia cells from blood using interdigitated microelectrodes*. Journal of Physics D: Applied Physics, 1994. **27**(12): p. 2659-2662.
34. Gascoyne, P.R.C., et al., *Dielectrophoretic separation of cancer cells from blood*. IEEE Transactions on Industry Applications, 1997. **33**(3): p. 670-678.
35. Cheng, J., et al., *Isolation of cultured cervical carcinoma cells mixed with peripheral blood cells on a bioelectronic chip*. Analytical Chemistry, 1998. **70**(11): p. 2321-2326.
36. Stephens, M., et al., *The dielectrophoresis enrichment of CD34(+) cells from peripheral blood stem cell harvests*. Bone Marrow Transplantation, 1996. **18**(4): p. 777-782.

37. Cheng, J., E. Sheldon, L. Wu, A. Uribe, L. Gerrue, J. Carrino, M. Heller, and J. O'Connell, *Preparation and hybridization analysis of DNA/RNA from E. coli on microfabricated bioelectronic chips*. Nat Biotechnol, 1998. **16**: p. 541-546.
38. Altomare, L., et al., *Levitation and movement of human tumor cells using a printed circuit board device based on software-controlled dielectrophoresis*. Biotechnology and Bioengineering, 2003. **82**(4): p. 474-479.
39. Markx, G.H., M.S. Talary, and R. Pethig, *Separation of viable and non-viable yeast using dielectrophoresis*. Journal of Biotechnology, 1994. **32**(1): p. 29-37.
40. Huang, Y., et al., *Introducing dielectrophoresis as a new force field for field-flow fractionation*. Biophysical Journal, 1997. **73**(2): p. 1118-1129.
41. Kim, U., et al., *Selection of mammalian cells based on their cell-cycle phase using dielectrophoresis*. Proceedings of the National Academy of Sciences of the United States of America, 2007. **104**(52): p. 20708-20712.
42. Cummings, E.B. and A.K. Singh, *Dielectrophoresis in Microchips Containing Arrays of Insulating Posts: Theoretical and Experimental Results*. Anal Chem, 2003. **75**: p. 4724-31.
43. Chou, C., et al., *Electrodeless Dielectrophoresis of Single- and Double-Stranded DNA*. Biophys J, 2002. **83**: p. 2170-2179.
44. Melcher, J.R. and G.I. Taylor, *Electrohydrodynamics: A review of the role of interfacial shear stresses*. Annual Review of Fluid Mechanics, 1969. **1**: p. 111-146
45. Toner, M. and D. Irimia, *Blood-on-a-chip*. Annu Rev Biomed Eng, 2005. **7**: p. 77-103.
46. Carlson, R., et al., *Self-Sorting of white blood cells in a lattice*. Molecular Biology of the Cell, 1997. **8**: p. 2407-2407.
47. Ostergaard, S., et al., *A novel approach to the automation of clinical chemistry by controlled manipulation of magnetic particles*. Journal of Magnetism and Magnetic Materials, 1999. **194**(1-3): p. 156-162.
48. Pasqua, L., et al., *Recent Development, Applications, and Perspectives of Mesoporous Silica Particles in Medicine and Biotechnology*. Current Medicinal Chemistry, 2009. **16**(23): p. 3054-3063.
49. Kushchevskaya, N.F., *Use of ferromagnetic particles in medicine*. Powder Metallurgy and Metal Ceramics, 1997. **36**(11-12): p. 668-672.
50. Ding, W.Q., *Micro/nano-particle manipulation and adhesion studies*. Journal of Adhesion Science and Technology, 2008. **22**(5-6): p. 457-480.
51. Anderson, D.G., S. Levenberg, and R. Langer, *Nanoliter-scale synthesis of arrayed biomaterials and application to human embryonic stem cells*. Nature Biotechnology, 2004. **22**(7): p. 863-866.
52. Juncker, D., H. Schmid, and E. Delamarche, *Multipurpose microfluidic probe*. Nature Materials, 2005. **4**(8): p. 622-628.
53. Ramos, A., et al., *Ac electrokinetics: a review of forces in microelectrode structures*. Journal of Physics D-Applied Physics, 1998. **31**(18): p. 2338-2353.
54. Harding, L.J., M. Reading, and D.Q.M. Craig, *The development of thermally assisted particle manipulation and thermal nanointeraction studies as a means of investigating drug-polymer interactions*. Journal of Pharmaceutical Sciences, 2008. **97**(4): p. 1551-1563.

55. Jericho, S.K., et al., *Micro-electro-mechanical systems microtweezers for the manipulation of bacteria and small particles*. Review of Scientific Instruments, 2004. **75**(5): p. 1280-1282.
56. Wiklund, M., et al., *Ultrasonic-trap-enhanced selectivity in capillary electrophoresis*. Ultrasonics, 2003. **41**(4): p. 329-33.
57. Laurell, T., F. Petersson, and A. Nilsson, *Chip integrated strategies for acoustic separation and manipulation of cells and particles*. Chemical Society Reviews, 2007. **36**(3): p. 492-506.
58. Dual, J. and T. Schwarz, *Acoustofluidics 3: Continuum mechanics for ultrasonic particle manipulation*. Lab on a Chip, 2012. **12**(2): p. 244-252.
59. Shao, B., et al., *Manipulation of microspheres and biological cells with multiple agile VCSEL traps*. Sensors and Actuators B-Chemical, 2006. **113**(2): p. 866-874.
60. Jonas, A. and P. Zemanek, *Light at work: The use of optical forces for particle manipulation, sorting, and analysis*. Electrophoresis, 2008. **29**(24): p. 4813-4851.
61. Ashkin, A., *Optical trapping and manipulation of neutral particles using lasers*. Proceedings of the National Academy of Sciences of the United States of America, 1997. **94**(10): p. 4853-4860.
62. Liu, C.X., L. Lagae, and G. Borghs, *Manipulation of magnetic particles on chip by magnetophoretic actuation and dielectrophoretic levitation*. Applied Physics Letters, 2007. **90**(18).
63. Mirowski, E., et al., *Manipulation and sorting of magnetic particles by a magnetic force microscope on a microfluidic magnetic trap platform*. Applied Physics Letters, 2005. **86**(24).
64. Kawamoto, H. and K. Tsuji, *Manipulation of small particles utilizing electrostatic force*. Advanced Powder Technology, 2011. **22**(5): p. 602-607.
65. Takahashi, K., et al., *Voltage required to detach an adhered particle by Coulomb interaction for micromanipulation*. Journal of Applied Physics, 2001. **90**(1): p. 432-437.
66. Saito, S., et al., *Kinetic control of a particle by voltage sequence for a nonimpact electrostatic micromanipulation*. Applied Physics Letters, 2003. **83**(10): p. 2076-2078.
67. Kawamoto, H., *Manipulation of single particles by utilizing electrostatic force*. Journal of Electrostatics, 2009. **67**(6): p. 850-861.
68. Johann, R. and P. Renaud, *A simple mechanism for reliable particle sorting in a microdevice with combined electroosmotic and pressure-driven flow*. Electrophoresis, 2004. **25**(21-22): p. 3720-3729.
69. Fan, S.K., T.H. Hsieh, and D.Y. Lin, *General digital microfluidic platform manipulating dielectric and conductive droplets by dielectrophoresis and electrowetting*. Lab on a Chip, 2009. **9**(9): p. 1236-1242.
70. Fan, S.K., et al., *Cross-scale electric manipulations of cells and droplets by frequency-modulated dielectrophoresis and electrowetting*. Lab on a Chip, 2008. **8**(8): p. 1325-1331.
71. Yasukawa, T., et al., *Electrophoretic cell manipulation and electrochemical gene-function analysis based on a yeast two-hybrid system in a microfluidic device*. Analytical Chemistry, 2008. **80**(10): p. 3722-3727.
72. Harakuwe, A.H. and P.R. Haddad, *Manipulation of separation selectivity in capillary zone electrophoresis of anionic solutes*. Trac-Trends in Analytical Chemistry, 2001. **20**(6-7): p. 375-385.
73. Campbell, L.C., et al., *Electrophoretic manipulation of single DNA molecules in nanofabricated capillaries*. Lab on a Chip, 2004. **4**(3): p. 225-229.

74. Zhang, C., et al., *Dielectrophoresis for manipulation of micro/nano particles in microfluidic systems*. Analytical and Bioanalytical Chemistry, 2010. **396**(1): p. 401-420.
75. Castellanos, A., et al., *Electrohydrodynamics and dielectrophoresis in microsystems: scaling laws*. Journal of Physics D-Applied Physics, 2003. **36**(20): p. 2584-2597.
76. H. Morgan, N.G.G., *AC Electrokinetics: Colloids and Nanoparticles* 2003: Research Studies Press.
77. Castellanos, A., *Electrohydrodynamics*1998: Springer.
78. Du, E. and S. Manoochehri, *Enhanced ac electrothermal fluidic pumping in microgrooved channels*. Journal of Applied Physics, 2008. **104**(6).
79. Lapizco-Encinas, B.H., et al., *Dielectrophoretic concentration and separation of live and dead bacteria in an array of insulators*. Analytical Chemistry, 2004. **76**(6): p. 1571-1579.
80. Markx, G.H., M.S. Talary, and R. Pethig, *Separation of viable and non-viable yeast using dielectrophoresis*. J Biotechnol, 1994. **32**(1): p. 29-37.
81. Kang, K.H., et al., *Continuous separation of microparticles by size with direct current-dielectrophoresis*. Electrophoresis, 2006. **27**(3): p. 694-702.
82. Shafiee, H., J.L. Caldwell, and R.V. Davalos, *A Microfluidic System for Biological Particle Enrichment Using Contactless Dielectrophoresis*. Jala, 2010. **15**(3): p. 224-232.
83. Gagnon, Z. and H.C. Chang, *Aligning fast alternating current electroosmotic flow fields and characteristic frequencies with dielectrophoretic traps to achieve rapid bacteria detection*. Electrophoresis, 2005. **26**(19): p. 3725-37.
84. Hughes, M.P. and H. Morgan, *Dielectrophoretic characterization and separation of antibody coated submicrometer latex spheres*. Analytical Chemistry, 1999. **71**(16): p. 3441-3445.
85. Minerick, A.R., et al., *Manipulation and characterization of red blood cells with alternating current fields in microdevices*. Electrophoresis, 2003. **24**(21): p. 3703-17.
86. Goater, A.D. and R. Pethig, *Electrorotation and dielectrophoresis*. Parasitology, 1998. **117 Suppl**: p. S177-89.
87. Holmes, D., *Electrical Cell Manipulation In Microfluidic Systems*, in *Institut de microélectronique et microsystèmes*2006, ÉCOLE POLYTECHNIQUE FÉDÉRALE DE LAUSANNE (EPFL): Lausanne.
88. Jones, T.B., *Electromechanics of Particles*1995, USA: Cambridge University Press. 265.
89. Irimajiri, A., T. Hanai, and A. Inouye, *A dielectric theory of "multi-stratified shell" model with its application to a lymphoma cell*. J Theor Biol, 1979. **78**(2): p. 251-69.
90. Chan, K.L., et al., *Electrorotation of liposomes: verification of dielectric multi-shell model for cells*. Biochim Biophys Acta, 1997. **1349**(2): p. 182-96.
91. Wang, X.-B., et al., *Theoretical and experimental investigations of the interdependence of the dielectric, dielectrophoretic and electrorotational behaviour of colloidal particles*. Journal of Physics D: Applied Physics, 1993 **26**(2): p. 312-322.
92. Kaler, K. and T.B. Jones, *Dielectrophoretic Spectra of Single Cells Determined by Feedback-Controlled Levitation*. Biophysical Journal, 1990. **57**(2): p. 173-182.
93. Wang, X., F.F. Becker, and P.R. Gascoyne, *The fractal dimension of cell membrane correlates with its capacitance: a new fractal single-shell model*. Chaos, 2010. **20**(4): p. 043133.
94. Wang, X.B., et al., *Changes in Friend murine erythroleukaemia cell membranes during induced differentiation determined by electrorotation*. Biochim Biophys Acta, 1994. **1193**(2): p. 330-44.

95. Pethig, R., *Cell Physiometry Tools based on Dielectrophoresis*, in *BioMEMS and Biomedical Nanotechnology 2007*, SpringerLink. p. 103-126.
96. Miklavčič, D., N. Pavšelj, and F.X. Hart, *Electric Properties of Tissues*, in *Wiley Encyclopedia of Biomedical Engineering 2006*.
97. Huang, Y., et al., *Membrane changes associated with the temperature-sensitive P85(gag-mos)-dependent transformation of rat kidney cells as determined by dielectrophoresis and electrorotation*. *Biochimica Et Biophysica Acta-Biomembranes*, 1996. **1282**(1): p. 76-84.
98. Pethig, R., et al., *Dielectrophoretic studies of the activation of human T lymphocytes using a newly developed cell profiling system*. *Electrophoresis*, 2002. **23**(13): p. 2057-2063.
99. Pethig, R. and M.S. Talary, *Dielectrophoretic detection of membrane morphology changes in Jurkat T-cells undergoing etoposide-induced apoptosis*. *Int Nanobiotechnology*, 2007. **1**(1): p. 2-9.
100. Arnold, W.M. and U. Zimmermann, *Electro-Rotation - Development of a Technique for Dielectric Measurements on Individual Cells and Particles*. *Journal of Electrostatics*, 1988. **21**(2-3): p. 151-191.
101. Pethig, R., et al., *Electrokinetic measurements of membrane capacitance and conductance for pancreatic beta-cells*. *IEE Proc Nanobiotechnol*, 2005. **152**(6): p. 189-93.
102. Gascoyne, P., et al., *Dielectrophoretic detection of changes in erythrocyte membranes following malarial infection*. *Biochim Biophys Acta*, 1997. **1323**(2): p. 240-52.
103. Pethig, R. and D.B. Kell, *The Passive Electrical-Properties of Biological-Systems - Their Significance in Physiology, Biophysics and Biotechnology*. *Physics in Medicine and Biology*, 1987. **32**(8): p. 933-970.
104. Arnold, W.M. and U. Zimmermann, *Rotation of an Isolated Cell in a Rotating Electric-Field*. *Naturwissenschaften*, 1982. **69**(6): p. 297-298.
105. Vykoukal, J., et al., *Enrichment of putative stem cells from adipose tissue using dielectrophoretic field-flow fractionation*. *Lab on a Chip*, 2008. **8**(8): p. 1386-1393.
106. Wang, X., J. Yang, and P.R. Gascoyne, *Role of peroxide in AC electrical field exposure effects on murine erythroleukemia cells during dielectrophoretic manipulations*. *Biochim Biophys Acta*, 1999. **1426**(1): p. 53-68.
107. Ho, C.T., et al., *Rapid heterogeneous liver-cell on-chip patterning via the enhanced field-induced dielectrophoresis trap*. *Lab on a Chip*, 2006. **6**(6): p. 724-34.
108. Borgatti, M., et al., *New trends in non-invasive prenatal diagnosis: applications of dielectrophoresis-based Lab-on-a-chip platforms to the identification and manipulation of rare cells*. *Int J Mol Med*, 2008. **21**(1): p. 3-12.
109. Flanagan, L.A., et al., *Unique dielectric properties distinguish stem cells and their differentiated progeny*. *Stem Cells*, 2008. **26**(3): p. 656-665.
110. Broche, L.M., et al., *Early detection of oral cancer - Is dielectrophoresis the answer?* *Oral Oncol*, 2007. **43**(2): p. 199-203.
111. Yang, L., et al., *Real-time electrical impedance-based measurement to distinguish oral cancer cells and non-cancer oral epithelial cells*. *Analytical and Bioanalytical Chemistry*, 2011. **399**(5): p. 1823-33.

112. Huang, Y., et al., *Membrane changes associated with the temperature-sensitive P85gag-mos-dependent transformation of rat kidney cells as determined by dielectrophoresis and electrorotation*. *Biochim Biophys Acta*, 1996. **1282**(1): p. 76-84.
113. An, J., et al., *Separation of malignant human breast cancer epithelial cells from healthy epithelial cells using an advanced dielectrophoresis-activated cell sorter (DACS)*. *Analytical and Bioanalytical Chemistry*, 2009. **394**(3): p. 801-9.
114. Henslee, E.A., et al., *Selective concentration of human cancer cells using contactless dielectrophoresis*. *Electrophoresis*, 2011. **32**(18): p. 2523-2529.
115. Braschler, T., et al., *Continuous separation of cells by balanced dielectrophoretic forces at multiple frequencies*. *Lab on a Chip*, 2008. **8**(2): p. 280-6.
116. Mulhall, H.J., et al., *Cancer, pre-cancer and normal oral cells distinguished by dielectrophoresis*. *Analytical and Bioanalytical Chemistry*, 2011. **401**(8): p. 2455-63.
117. Gascoyne, P.R., et al., *Membrane changes accompanying the induced differentiation of Friend murine erythroleukemia cells studied by dielectrophoresis*. *Biochim Biophys Acta*, 1993. **1149**(1): p. 119-26.
118. Burt, J.P.H., et al., *Dielectrophoretic Characterization of Friend Murine Erythroleukaemic Cells as a Measure of Induced-Differentiation*. *Biochim Biophys Acta*, 1990. **1034**(1): p. 93-101.
119. Wang, X.B., et al., *Changes in Friend Murine Erythroleukemia Cell-Membranes during Induced-Differentiation Determined by Electrorotation*. *Biochimica Et Biophysica Acta-Biomembranes*, 1994. **1193**(2): p. 330-344.
120. Gascoyne, P.R.C., et al., *Membrane-Changes Accompanying the Induced-Differentiation of Friend Murine Erythroleukemia-Cells Studied by Dielectrophoresis*. *Biochim Biophys Acta*, 1993. **1149**(1): p. 119-126.
121. Gascoyne, P.R.C., et al., *Use of Dielectrophoretic Collection Spectra for Characterizing Differences between Normal and Cancerous Cells*. *IEEE Trans Ind Appl*, 1994. **30**(4): p. 829-834.
122. Gimsa, J., et al., *Dielectrophoresis and Electrorotation of Neurospora Slime and Murine Myeloma Cells*. *Biophysical Journal*, 1991. **60**(4): p. 749-760.
123. Huang, Y., et al., *Membrane dielectric responses of human T-lymphocytes following mitogenic stimulation*. *Biochimica Et Biophysica Acta-Biomembranes*, 1999. **1417**(1): p. 51-62.
124. Wang, X.J., et al., *Changes in membrane dielectric properties of HL-60 cells during genistein-induced apoptosis - Significance indiscrimination of apoptotic, necrotic and normal cells*. *Blood*, 1998. **92**(10): p. 167b-167b.
125. Yang, J., et al., *Dielectric properties of human leukocyte subpopulations determined by electrorotation as a cell separation criterion*. *Biophysical Journal*, 1999. **76**(6): p. 3307-3314.
126. Labeed, F.H., H.M. Coley, and M.P. Hughes, *Differences in the biophysical properties of membrane and cytoplasm of apoptotic cells revealed using dielectrophoresis*. *Biochimica Et Biophysica Acta-General Subjects*, 2006. **1760**(6): p. 922-929.
127. Wang, X.J., F.F. Becker, and P.R.C. Gascoyne, *Membrane dielectric changes indicate induced apoptosis in HL-60 cells more sensitively than surface phosphatidylserine expression or DNA fragmentation*. *Biochimica Et Biophysica Acta-Biomembranes*, 2002. **1564**(2): p. 412-420.
128. Huang, Y., et al., *The removal of human breast cancer cells from hematopoietic CD34+ stem cells by dielectrophoretic field-flow-fractionation*. *J Hematother Stem Cell Res*, 1999. **8**(5): p. 481-90.

129. Ye, X.Q., et al., *Heterogeneity of mitochondrial membrane potential: a novel tool to isolate and identify cancer stem cells from a tumor mass?* Stem Cell Rev, 2011. **7**(1): p. 153-60.
130. Chen, L.B., *Mitochondrial membrane potential in living cells.* Annu Rev Cell Biol, 1988. **4**: p. 155-81.
131. Kroemer, G. and J. Pouyssegur, *Tumor cell metabolism: cancer's Achilles' heel.* Cancer Cell, 2008. **13**(6): p. 472-82.
132. Hockenbery, D.M., *A mitochondrial Achilles' heel in cancer?* Cancer Cell, 2002. **2**(1): p. 1-2.
133. Schieke, S.M., et al., *Mitochondrial metabolism modulates differentiation and teratoma formation capacity in mouse embryonic stem cells.* J Biol Chem, 2008. **283**(42): p. 28506-12.
134. Hassanein, M.K., et al., *Stem-like and non-stem human pancreatic cancer cells distinguished by morphology and metastatic behavior.* J Cell Biochem, 2011. **112**(12): p. 3549-54.
135. Kabashima, A., et al., *Side population of pancreatic cancer cells predominates in TGF-beta-mediated epithelial to mesenchymal transition and invasion.* Int J Cancer, 2009. **124**(12): p. 2771-9.
136. Keysar, S.B. and A. Jimeno, *More than markers: biological significance of cancer stem cell-defining molecules.* Mol Cancer Ther, 2010. **9**(9): p. 2450-7.
137. Turgeon, M.L., *Clinical Hematology: Theory and Procedures* 2004: Lippincott Williams and Wilkins.
138. Arpitha, P., et al., *High expression of p63 combined with a large N/C ratio defines a subset of human limbal epithelial cells: implications on epithelial stem cells.* Invest Ophthalmol Vis Sci, 2005. **46**(10): p. 3631-6.
139. de Vet, H.C., et al., *Sources of interobserver variation in histopathological grading of cervical dysplasia.* J Clin Epidemiol, 1992. **45**(7): p. 785-90.
140. Rusch, V., et al., *Aberrant expression of p53 or the epidermal growth factor receptor is frequent in early bronchial neoplasia and coexpression precedes squamous cell carcinoma development.* Cancer Research, 1995. **55**(6): p. 1365-72.
141. Heng, B.C., H. Liu, and T. Cao, *Can the high nuclear to cytoplasmic ratio of human embryonic stem cells make them more vulnerable to physical stress encountered with bulk-passage protocols?* Med Hypotheses, 2005. **64**(6): p. 1242-3.
142. Pethig, R., *Review Article-Dielectrophoresis: Status of the theory, technology, and applications* BIOMICROFLUIDICS, 2010. **4**(2).
143. Khoshmanesh, K., et al., *Dielectrophoretic platforms for bio-microfluidic systems* BIOSENS BIOELECTRON, 2011 **26**(5): p. 1800-1814.
144. Cummings, E.B. and A.K. Singh, *Dielectrophoresis in Microchips Containing Arrays of Insulating Posts: Theoretical and Experimental Results.* Analytical Chemistry, 2003. **75**: p. 4724-31.
145. Chou, C., et al., *Electrodeless Dielectrophoresis of Single- and Double-Stranded DNA.* Biophysical Journal, 2002. **83**: p. 2170-2179.
146. Gonzalez, C.F. and V.T. Remcho, *Harnessing dielectric forces for separations of cells, fine particles and macromolecules.* Journal of Chromatography A, 2005. **1079**(1-2): p. 59-68.
147. Li, H.B. and R. Bashir, *Dielectrophoretic separation and manipulation of live and heat-treated cells of Listeria on microfabricated devices with interdigitated electrodes.* Sensors and Actuators B-Chemical, 2002. **86**(2-3): p. 215-221.

148. Markx, G.H., et al., *Dielectrophoretic Characterization and Separation of Microorganisms*. Microbiology-Uk, 1994. **140**: p. 585-591.
149. Lapizco-Encinas, B.H., S. Ozuna-Chacón, and M. Rito-Palomares, *Protein manipulation with insulator-based dielectrophoresis and direct current electric fields*. Journal of Chromatography A, 2008. **1206**: p. 45-51.
150. Simmons, B.A., et al., *The Development of Polymeric Devices as Dielectrophoretic Concentrators*. MRS Bull, 2006. **31**: p. 120-124.
151. Barrett, L.M., et al., *Dielectrophoretic manipulation of particles and cells using insulating ridges in faceted prism microchannels*. Analytical Chemistry, 2005. **77**: p. 6798-804.
152. Sabounchi, P., et al., *Sample concentration and impedance detection on a microfluidic polymer chip*. Biomed Microdevices, 2008. **10**: p. 661-70.
153. Chou, C.F., et al., *Electrodeless dielectrophoresis of single- and double-stranded DNA*. Biophysical Journal, 2002. **83**(4): p. 2170-2179.
154. Gallo-Villanueva, R.C., et al., *DNA manipulation by means of insulator-based dielectrophoresis employing direct current electric fields*. Electrophoresis, 2009. **30**(24): p. 4195-4205.
155. Pysker, M.D. and M.A. Hayes, *Electrophoretic and dielectrophoretic field gradient technique for separating bioparticles*. Analytical Chemistry, 2007. **79**(12): p. 4552-4557.
156. Moncada-Hernandez, H. and B.H. Lapizco-Encinas, *Simultaneous concentration and separation of microorganisms: insulator-based dielectrophoretic approach*. Analytical and Bioanalytical Chemistry, 2010. **396**(5): p. 1805-1816.
157. Gallo-Villanueva, R.C., et al., *Assessment of microalgae viability employing insulator-based dielectrophoresis*. Microfluidics and Nanofluidics, 2011. **10**(6): p. 1305-1315.
158. Shafiee, H., et al., *Selective isolation of live/dead cells using contactless dielectrophoresis (cDEP)*. Lab on a Chip, 2010. **10**(4): p. 438-445.
159. Sano, M.B., et al., *Contactless dielectrophoretic spectroscopy: examination of the dielectric properties of cells found in blood*. Electrophoresis, 2011. **32**.
160. Henslee, E., et al., *Selective Concentration of Human Cancer Cells using Contactless Dielectrophoresis (cDEP)*. Electrophoresis, 2011.
161. Arnold, W.M.K.J.G.m.b.H., Juelich (Germany, F.R.). Inst. fuer Medizin); Zimmermann, U., *Rotating-field-induced rotation and measurement of the membrane capacitance of single mesophyll cells of Avena sativa* Plant physiology and biochemistry, 1982. **v. 37**(10): p. 908-915.
162. Hutt, L.D., et al., *Microfabricated capillary electrophoresis amino acid chirality analyzer for extraterrestrial exploration*. Analytical Chemistry, 1999. **71**(18): p. 4000-6.
163. Beard, N.P., J.B. Edel, and A.J. deMello, *Integrated on-chip derivatization and electrophoresis for the rapid analysis of biogenic amines*. Electrophoresis, 2004. **25**(14): p. 2363-73.
164. Lagally, E.T., P.C. Simpson, and R.A. Mathies, *Monolithic integrated microfluidic DNA amplification and capillary electrophoresis analysis system*. Sensors and Actuators B-Chemical, 2000. **63**(3): p. 138-146.
165. Wainright, A., et al., *Preconcentration and separation of double-stranded DNA fragments by electrophoresis in plastic microfluidic devices*. Electrophoresis, 2003. **24**(21): p. 3784-3792.

166. Vieillard, J., et al., *Application of microfluidic chip with integrated optics for electrophoretic separations of proteins*. Journal of Chromatography B-Analytical Technologies in the Biomedical and Life Sciences, 2007. **845**(2): p. 218-225.
167. Wu, D.P., J.H. Qin, and B.C. Lin, *Electrophoretic separations on microfluidic chips*. Journal of Chromatography A, 2008. **1184**(1-2): p. 542-559.
168. Kenyon, S.M., M.M. Meighan, and M.A. Hayes, *Recent developments in electrophoretic separations on microfluidic devices*. Electrophoresis, 2011. **32**(5): p. 482-493.
169. Culbertson, C.T., R.S. Ramsey, and J.M. Ramsey, *Electroosmotically induced hydraulic pumping on microchips: Differential ion transport*. Analytical Chemistry, 2000. **72**(10): p. 2285-2291.
170. Lazar, I.M. and B.L. Karger, *Multiple open-channel electroosmotic pumping system for microfluidic sample handling*. Analytical Chemistry, 2002. **74**(24): p. 6259-6268.
171. Ng, W.Y., et al., *DC-biased AC-electroosmotic and AC-electrothermal flow mixing in microchannels*. Lab on a Chip, 2009. **9**(6): p. 802-809.
172. Glasgow, I., J. Batton, and N. Aubry, *Electroosmotic mixing in microchannels*. Lab on a Chip, 2004. **4**(6): p. 558-562.
173. Landau, L.D. and E.M. Lifshitz, *Fluid Mechanics* 1959 Oxford: Pergamon.
174. Sasaki, N., *Recent Applications of AC Electrokinetics in Biomolecular Analysis on Microfluidic Devices*. Analytical Sciences, 2012. **28**(1): p. 3-8.
175. Ramos, A., et al., *Pumping of liquids with traveling-wave electroosmosis*. Journal of Applied Physics, 2005. **97**(8).
176. Perch-Nielsen, I.R., N.G. Green, and A. Wolff, *Numerical simulation of travelling wave induced electrothermal fluid flow*. Journal of Physics D-Applied Physics, 2004. **37**(16): p. 2323-2330.
177. Bennett, D.J., et al., *Combined field-induced dielectrophoresis and phase separation for manipulating particles in microfluidics*. Applied Physics Letters, 2003. **83**(23): p. 4866-4868.
178. Cahill, B.P., et al., *Electro-osmotic pumping on application of phase-shifted signals to interdigitated electrodes*. Sensors and Actuators B-Chemical, 2005. **110**(1): p. 157-163.
179. Lastochkin, D., et al., *Electrokinetic micropump and micromixer design based on ac faradaic polarization*. Journal of Applied Physics, 2004. **96**(3): p. 1730-1733.
180. Wu, J., M. Lian, and K. Yang, *Micropumping of biofluids by alternating current electrothermal effects*. Applied Physics Letters, 2007. **90**(23).
181. Studer, V., et al., *An integrated AC electrokinetic pump in a microfluidic loop for fast and tunable flow control*. Analyst, 2004. **129**(10): p. 944-949.
182. Brown, A.B.D., C.G. Smith, and A.R. Rennie, *Pumping of water with ac electric fields applied to asymmetric pairs of microelectrodes*. Physical Review E, 2001. **63**(1).
183. Clift, R., J.R. Grace, and M.E. Weber, *Bubbles, Drops and Particles* 1978 New York: Academic.
184. Beebe, D.J., G.A. Mensing, and G.M. Walker, *Physics and applications of microfluidics in biology*. Annu Rev Biomed Eng, 2002. **4**: p. 261-86.
185. Madou, M.J., *Fundamentals of Microfabrication* 2002: CRC Press.
186. Stremmer, M.A., *Mixing measures*, in *Encyclopedia of Micro- and Nanofluidics*, D. Li, Editor 2008, Springer. p. 1376-1382.
187. McDonald JC and W. GM, *Poly(dimethylsiloxane) as a Material for Fabricating Microfluidic Devices*. ACCOUNTS OF CHEMICAL RESEARCH, 2002. **35**(7): p. 491-499.

188. Creekmore, A.L., et al., *Changes in gene expression and cellular architecture in an ovarian cancer progression model*. PLoS One, 2011. **6**(3): p. e17676.
189. Roberts, P.C., et al., *Sequential molecular and cellular events during neoplastic progression: a mouse syngeneic ovarian cancer model*. Neoplasia, 2005. **7**(10): p. 944-56.
190. Visintin, I., et al., *Diagnostic markers for early detection of ovarian cancer*. Clin Cancer Res, 2008. **14**(4): p. 1065-72.
191. Jacobs, I.J. and U. Menon, *Progress and challenges in screening for early detection of ovarian cancer*. Mol Cell Proteomics, 2004. **3**(4): p. 355-66.
192. Jemal, A., et al., *Cancer statistics, 2010*. CA Cancer J Clin, 2010. **60**(5): p. 277-300.
193. Auersperg, N., T. Ota, and G.W. Mitchell, *Early events in ovarian epithelial carcinogenesis: progress and problems in experimental approaches*. Int J Gynecol Cancer, 2002. **12**(6): p. 691-703.
194. Sundfeldt, K., *Cell-cell adhesion in the normal ovary and ovarian tumors of epithelial origin; an exception to the rule*. Mol Cell Endocrinol, 2003. **202**(1-2): p. 89-96.
195. Hanahan, D. and R.A. Weinberg, *Hallmarks of cancer: the next generation*. Cell, 2011. **144**(5): p. 646-74.
196. Sano, M.B., et al., *Contactless dielectrophoretic spectroscopy: examination of the dielectric properties of cells found in blood*. Electrophoresis, 2011. **32**(22): p. 3164-71.
197. Skalak, R.C., S. , *Handbook of Bioengineering*1987, New York: McGraw-Hill.
198. Fung, Y.C.P., N.; Anliker, M. , *Biomechanics, Its Foundations and Objectives*1972, Englewood Cliffs, NJ: Prentice Hall.
199. Han, A., L. Yang, and A.B. Frazier, *Quantification of the heterogeneity in breast cancer cell lines using whole-cell impedance spectroscopy*. Clin Cancer Res, 2007. **13**(1): p. 139-43.
200. Gascoyne, P.R.C., et al., *Use of dielectrophoretic collection spectra for characterizing differences between normal and cancerous cells* Industry Applications, IEEE Transactions on, 1994 **30**(4): p. 829 - 834
201. Becker, F.F., et al., *The removal of human leukaemia cells from blood using interdigitated microelectrodes* J. Phys. D: Appl. Phys., 1994 **27** p. 2659 -2662.
202. Becker, F.F., et al., *Separation of human breast cancer cells from blood by differential dielectric affinity*. Proc Natl Acad Sci U S A, 1995. **92**(3): p. 860-4.
203. Jiang, W.G., *Membrane ruffling of cancer cells: a parameter of tumour cell motility and invasion*. Eur J Surg Oncol, 1995. **21**(3): p. 307-9.
204. Creekmore, A.L., et al., *Changes in gene expression and cellular architecture in an ovarian cancer progression model*. PLoS One, 2011. **6**(3).
205. Ketene, A.N., et al., *Actin filaments play a primary role for structural integrity and viscoelastic response in cells*. Integrative Biology, 2012. **4**(5): p. 540-549.
206. Schmelz, E.M., et al., *Modulation of intracellular beta-catenin localization and intestinal tumorigenesis in vivo and in vitro by sphingolipids*. Cancer Research, 2001. **61**(18): p. 6723-9.
207. Schmelz, E.M., et al., *Colonic cell proliferation and aberrant crypt foci formation are inhibited by dairy glycosphingolipids in 1, 2-dimethylhydrazine-treated CF1 mice*. J Nutr, 2000. **130**(3): p. 522-7.

208. Lemonnier, L.A., et al., *Sphingomyelin in the suppression of colon tumors: prevention versus intervention*. Arch Biochem Biophys, 2003. **419**(2): p. 129-38.
209. Simon, K.W., et al., *Suppression of breast xenograft growth and progression in nude mice: implications for the use of orally administered sphingolipids as chemopreventive agents against breast cancer*. Food Funct, 2010. **1**(1): p. 90-8.
210. Mazzei, J.C., et al., *Suppression of intestinal inflammation and inflammation-driven colon cancer in mice by dietary sphingomyelin: importance of peroxisome proliferator-activated receptor gamma expression*. J Nutr Biochem, 2011.
211. Gault, C.R., L.M. Obeid, and Y.A. Hannun, *An Overview of Sphingolipid Metabolism: From Synthesis to Breakdown*. Sphingolipids as Signaling and Regulatory Molecules, 2010. **688**: p. 1-23.
212. Gangoiti, P., et al., *Control of metabolism and signaling of simple bioactive sphingolipids: Implications in disease*. Progress in Lipid Research, 2010. **49**(4): p. 316-334.
213. Kolesnick, R. and D.W. Golde, *The Sphingomyelin Pathway in Tumor-Necrosis-Factor and Interleukin-1 Signaling*. Cell, 1994. **77**(3): p. 325-328.
214. Kolesnick, R.N. and M.R. Hemer, *Characterization of a Ceramide Kinase-Activity from Human Leukemia (HL-60) Cells - Separation from Diacylglycerol Kinase-Activity*. Journal of Biological Chemistry, 1990. **265**(31): p. 18803-18808.
215. Spiegel, S. and S. Milstien, *Sphingosine-1-phosphate: An enigmatic signalling lipid*. Nature Reviews Molecular Cell Biology, 2003. **4**(5): p. 397-407.
216. Maceyka, M., et al., *Sphingosine kinase, sphingosine-1-phosphate, and apoptosis*. Biochimica Et Biophysica Acta-Molecular and Cell Biology of Lipids, 2002. **1585**(2-3): p. 193-201.
217. Teichgraber, V., et al., *Ceramide accumulation mediates inflammation, cell death and infection susceptibility in cystic fibrosis*. Nat Med, 2008. **14**(4): p. 382-91.
218. Wang, D., et al., *S1P differentially regulates migration of human ovarian cancer and human ovarian surface epithelial cells*. Mol Cancer Ther, 2008. **7**(7): p. 1993-2002.
219. Visentin, B., et al., *Validation of an anti-sphingosine-1-phosphate antibody as a potential therapeutic in reducing growth, invasion, and angiogenesis in multiple tumor lineages*. Cancer Cell, 2006. **9**(3): p. 225-238.
220. Becker, F.F., et al., *The Removal of Human Leukemia-Cells from Blood Using Interdigitated Microelectrodes*. Journal of Physics D-Applied Physics, 1994. **27**(12): p. 2659-2662.
221. Becker, F.F., et al., *Separation of Human Breast-Cancer Cells from Blood by Differential Dielectric Affinity*. Proceedings of the National Academy of Sciences of the United States of America, 1995. **92**(3): p. 860-864.
222. Huang, Y., et al., *Membrane changes associated with the temperature-sensitive P85(gag-mos)-dependent transformation of rat kidney cells as determined by dielectrophoresis and electrorotation*. Biochimica et Biophysica Acta, 1996. **1282**(1): p. 76-84.
223. Mulhall, H.J., et al., *Cancer, pre-cancer and normal oral cells distinguished by dielectrophoresis*. Anal Bioanal Chem, 2011. **401**(8): p. 2455-63.
224. Gascoyne, P.R., et al., *Correlations between the dielectric properties and exterior morphology of cells revealed by dielectrophoretic field-flow fractionation*. Electrophoresis, 2012.

225. Gascoyne, P.R., et al., *Correlations between the dielectric properties and exterior morphology of cells revealed by dielectrophoretic field-flow fractionation*. Electrophoresis, 2013.
226. Strub, G.M., et al., *Extracellular and Intracellular Actions of Sphingosine-1-Phosphate*. Sphingolipids as Signaling and Regulatory Molecules, 2010. **688**: p. 141-155.
227. Hanna, A.N., et al., *Tumor necrosis factor-alpha induces stress fiber formation through ceramide production: Role of sphingosine kinase*. Molecular Biology of the Cell, 2001. **12**(11): p. 3618-3630.
228. Jemal, A., et al., *Global cancer statistics*. CA Cancer J Clin, 2011. **61**(2): p. 69-90.
229. Leonard, K.M. and A.R. Minerick, *Explorations of ABO-Rh antigen expressions on erythrocyte dielectrophoresis: changes in cross-over frequency*. Electrophoresis, 2011. **32**(18): p. 2512-22.
230. Nagrath, S., et al., *Isolation of rare circulating tumour cells in cancer patients by microchip technology*. Nature, 2007. **450**(7173): p. 1235-9.
231. Skalak, R. and S. Chien, *Handbook of bioengineering*1987, New York: McGraw-Hill.
232. Fung, Y.C., et al., *Biomechanics, its foundations and objectives*1972, Englewood Cliffs, N.J.,: Prentice-Hall. xiii, 641 p.
233. Sukhorukov, V.L., W.M. Arnold, and U. Zimmermann, *Hypotonically induced changes in the plasma membrane of cultured mammalian cells*. J Membr Biol, 1993. **132**(1): p. 27-40.
234. Gascoyne, P.R. and J. Vykoukal, *Particle separation by dielectrophoresis*. Electrophoresis, 2002. **23**(13): p. 1973-83.
235. Martinez-Duarte, R., et al., *The integration of 3D carbon-electrode dielectrophoresis on a CD-like centrifugal microfluidic platform*. Lab on a Chip, 2010. **10**(8): p. 1030-43.
236. Gascoyne, P.R.C., et al., *Use of Dielectrophoretic Collection Spectra for Characterizing Differences between Normal and Cancerous Cells*. Ieee Transactions on Industry Applications, 1994. **30**(4): p. 829-834.
237. Ketene, A.N., et al., *The effects of cancer progression on the viscoelasticity of ovarian cell cytoskeleton structures*. Nanomedicine, 2011.
238. Ikeda, I., S. Tsukahara, and H. Watarai, *Effects of viability and lectin protein binding on dielectrophoretic behavior of single yeast cells*. Analytical Sciences, 2003. **19**(1): p. 27-31.
239. Cohen, C.A., et al. *Early immune modulatory events during ovarian cancer outgrowth in the omental fat band*. in *Proceedings: AACR 103rd Annual Meeting 2012*. 2012. Chicago, IL.
240. Pohl, H.A., *Dielectrophoresis*1978: Cambridge University Press.
241. DeMello, A.J., *Control and detection of chemical reactions in microfluidic systems*. Nature, 2006. **442**: p. 394-402.
242. Hinsmann, P., et al., *Design, simulation and application of a new micromixing device for time resolved infrared spectroscopy of chemical reactions in solution*. Lab on a Chip, 2001. **1**: p. 16-21.
243. Sasaki, N., T. Kitamori, and H.B. Kim, *AC electroosmotic micromixer for chemical processing in a microchannel*. Lab on a Chip, 2006. **6**: p. 550-4.
244. Nguyen, N.T. and Z. Wu, *Micromixers-a review*. J Micromech Microeng, 2005. **15**: p. R1-R16.
245. Hessel, V., H. Lowe, and F. Schonfeld, *Micromixers? a review on passive and active mixing principles*. Chem Eng Sci, 2005. **60**: p. 2479-2501.
246. Burke, B.J. and F.E. Regnier, *Stopped-flow enzyme assays on a chip using a microfabricated mixer*. Analytical Chemistry, 2003. **75**: p. 1786-91.

247. Cherepanov, A.V. and S.d. Vries, *Microsecond freeze-hyperquenching: development of a new ultrafast micro-mixing and sampling technology and application to enzyme catalysis*. *Biochim Biophys Acta*, 2004. **1656**(1): p. 31.
248. Sotowa, K.I., et al., *Mixing and Enzyme Reactions in a Microchannel Packed with Glass Beads*. *Korean J Chem Eng*, 2005. **22**(4): p. 4.
249. Lee, N.Y., M. Yamada, and M. Seki, *Development of a passive micromixer based on repeated fluid twisting and flattening, and its application to DNA purification*. *Analytical and Bioanalytical Chemistry*, 2005. **383**: p. 776-82.
250. Lee, C.Y., et al., *Integrated microfluidic systems for cell lysis, mixing/pumping and DNA amplification*. *J Micromech Microeng*, 2005. **15**: p. 1215-1223.
251. Hui, W., et al., *Microfluidic systems for extracting nucleic acids for DNA and RNA analysis*. *Sensors Actuat A-Phys*, 2007. **133**: p. 335-339.
252. Pollack, L., et al., *Time resolved collapse of a folding protein observed with small angle x-ray scattering.*, in *Phys Rev Lett* 2001. p. 4962-5.
253. Stremmer, M.A., F.R. Haselton, and H. Aref, *Designing for chaos: applications of chaotic advection at the microscale*. *Philos T R Soc A*, 2004. **362**: p. 1019-36.
254. Chang, C.C. and R.J. Yang, *Electrokinetic mixing in microfluidic systems*. *Microfluidics and Nanofluidics*, 2007. **3**: p. 501-525.
255. El Moctar, A.O., N. Aubry, and J. Batton, *Electro-hydrodynamic micro-fluidic mixer*. *Lab on a Chip*, 2003. **3**: p. 273-80.
256. Glasgow, I., J. Batton, and N. Aubry, *Electroosmotic mixing in microchannels*. *Lab Chip*, 2004. **4**: p. 558-62.
257. Johnson, T.J., D. Ross, and L.E. Locascio, *Rapid microfluidic mixing*. *Analytical Chemistry*, 2002. **74**: p. 45-51.
258. Paik, P., et al., *Electrowetting-based droplet mixers for microfluidic systems*. *Lab on a Chip*, 2003. **3**: p. 28-33.
259. Paik, P., V.K. Pamula, and R.B. Fair, *Rapid droplet mixers for digital microfluidic systems*. *Lab on a Chip*, 2003. **3**: p. 253-9.
260. Deval, J. and P. Tabeling, *Chaotic mixing in electrokinetically and pressure driven micro flows*. *Technical Digest. MEMS 2001. 14th IEEE International Conference on Micro Electro Mechanical Systems (Cat. No.01CH37090)*, 2001. **00**: p. 483-486.
261. Deval, J. and P. Tabeling, *A dielectrophoretic chaotic mixer*. *Technical Digest. MEMS 2002. 15th IEEE International Conference on Micro Electro Mechanical Systems (Cat. No.02CH37266)*, 2002: p. 36-39.
262. Lin, H., et al., *Instability of electrokinetic microchannel flows with conductivity gradients*. *Phys Fluids*, 2004. **16**: p. 1922.
263. Oddy, M.H., J.G. Santiago, and J.C. Mikkelsen, *Electrokinetic instability micromixing*. *Analytical Chemistry*, 2001. **73**: p. 5822-32.
264. Lapizco-Encinas, B.H., et al., *Dielectrophoretic Concentration and Separation of Live and Dead Bacteria in an Array of Insulators voltages across a microchannel containing an array of*. *Analytical Chemistry*, 2004. **76**: p. 1571-1579.

265. Pethig, R. and G.H. Markx, *Applications of dielectrophoresis in biotechnology*. Trends Biotechnol, 1997. **15**: p. 426-32.
266. Markx, G.H., M.S. Talary, and R. Pethig, *Separation of viable and non-viable yeast using dielectrophoresis*. J Biotech, 1994. **32**: p. 29-37.
267. Kang, K.H., et al., *Continuous separation of microparticles by size with direct current-dielectrophoresis*. Electrophoresis, 2006. **27**: p. 694-702.
268. Morgan, H., *Separation of Submicron Bioparticles by Dielectrophoresis*. Biophysical Journal, 1999. **77**: p. 516-525.
269. Gagnon, Z. and H.C. Chang, *Aligning fast alternating current electroosmotic flow fields and characteristic frequencies with dielectrophoretic traps to achieve rapid bacteria detection*. Electrophoresis, 2005. **26**: p. 3725-37.
270. Regtmeier, J., et al., *Dielectrophoretic Manipulation of DNA : Separation and Polarizability able to perform efficient and fast DNA separation accord-*. Analytical Chemistry, 2007. **79**: p. 3925-3932.
271. Minerick, A.R., et al., *Manipulation and characterization of red blood cells with alternating current fields in microdevices*. Electrophoresis, 2003. **24**: p. 3703-17.
272. Wang, M.W., *Combined Microfluidic–Electric Diffused Mixing of Living Cells in Continuous Flow*. JPN J Appl Phys, 2010. **49**: p. 024205.
273. Salmanzadeh, A., et al., *Investigating the AC-electroosmotic flow in contactless dielectrophoresis (cDEP)-based microdevices*. under-preparation.
274. Ross, D., M. Gaitan, and L.E. Locascio, *Temperature measurement in microfluidic systems using a temperature-dependent fluorescent dye*. Analytical Chemistry, 2001. **73**(17): p. 4117-4123.
275. Becker, F., et al., *The removal of human leukaemia cells from blood using interdigitated microelectrodes*. J Phys D: Appl Phys, 1994. **27**(12): p. 2659-2662.
276. Gascoyne, P., et al., *Microsample preparation by dielectrophoresis: isolation of malaria*. Lab on a Chip, 2002. **2**: p. 70–75.
277. Vykoukal, J., et al., *Enrichment of putative stem cells from adipose tissue using dielectrophoretic field-flow fractionation*. Lab on a Chip, 2008. **8**: p. 1386–1393.
278. Talary, M.S., et al., *Dielectrophoretic separation and enrichment of CD34+ cell subpopulation from bone marrow and peripheral blood stem cells*. Med Biol Eng Comput, 1995. **33**(2): p. 235-7.
279. Yang, J., et al., *Cell separation on microfabricated electrodes using dielectrophoretic/gravitational field-flow fractionation*. Analytical Chemistry, 1999. **71**(5): p. 911-8.
280. Gascoyne, P.R.C., et al., *Isolation of rare cells from cell mixtures by dielectrophoresis*. Electrophoresis, 2009. **30**(8): p. 1388-1398.
281. Huang, Y., et al., *Introducing dielectrophoresis as a new force field for field-flow fractionation*. Biophysical Journal, 1997. **73**(2): p. 1118-29.
282. Wang, X.B., et al., *Cell separation by dielectrophoretic field-flow-fractionation*. Analytical Chemistry, 2000. **72**(4): p. 832-9.
283. Yang, F., et al., *Dielectrophoretic separation of colorectal cancer cells*. BIOMICROFLUIDICS, 2010. **4**(1): p. 13204.

284. Thomas, R.S., et al., *Trapping single human osteoblast-like cells from a heterogeneous population using a dielectrophoretic microfluidic device*. BIOMICROFLUIDICS, 2010. **4**(2).
285. Gadish, N. and J. Voldman, *High-throughput positive-dielectrophoretic bioparticle microconcentrator*. Analytical Chemistry, 2006. **78**(22): p. 7870-7876.
286. Cen, E.G., et al., *A combined dielectrophoresis, traveling wave dielectrophoresis and electrorotation microchip for the manipulation and characterization of human malignant cells*. J Microbiol Methods, 2004. **58**(3): p. 387-401.
287. Cheng, I.F., et al., *A continuous high-throughput bioparticle sorter based on 3D traveling-wave dielectrophoresis*. Lab on a Chip, 2009. **9**(22): p. 3193-201.
288. Ramos, A., et al., *Pumping of liquids with ac voltages applied to asymmetric pairs of microelectrodes*. Phys Rev E Stat Nonlin Soft Matter Phys, 2003. **67**(5 Pt 2): p. 056302.
289. Moon, H.-S., et al., *Continuous separation of breast cancer cells from blood samples using multi-orifice flow fractionation (MOFF) and dielectrophoresis (DEP)* Lab on a Chip, 2011. **11**: p. 1118–1125.
290. Kang, K.H., et al., *Effects of dc-dielectrophoretic force on particle trajectories in microchannels*. Journal of Applied Physics, 2006. **99**: p. 064702.
291. Barrett, L.M., et al., *Dielectrophoretic manipulation of particles and cells using insulating ridges in faceted prism microchannels*. Analytical Chemistry, 2005. **77**(21): p. 6798-804.
292. Kralj, J.G., et al., *Continuous dielectrophoretic size-based particle sorting*. Analytical Chemistry, 2006. **78**(14): p. 5019-25.
293. Kim, U. and H.T. Soh, *Simultaneous sorting of multiple bacterial targets using integrated dielectrophoretic-magnetic activated cell sorter*. Lab on a Chip, 2009. **9**(16): p. 2313-8.
294. Hawkins, B.G., et al., *Continuous-flow particle separation by 3D Insulative dielectrophoresis using coherently shaped, dc-biased, ac electric fields*. Analytical Chemistry, 2007. **79**(19): p. 7291-300.
295. Iliescu, C., et al., *Bidirectional field-flow particle separation method in a dielectrophoretic chip with 3D electrodes*. Sensors and Actuators B, 2008. **129**: p. 491–496.
296. Church, C., J. Zhu, and X. Xuan, *Negative dielectrophoresis-based particle separation by size in a serpentine microchannel*. Electrophoresis, 2011. **32**(5): p. 527-31.
297. Li, Y., et al., *Continuous dielectrophoretic cell separation microfluidic device*. Lab on a Chip, 2007. **7**(2): p. 239-48.
298. Sabuncu, A.C., et al., *Dielectrophoretic separation of mouse melanoma clones*. BIOMICROFLUIDICS, 2010. **4**(2).
299. Shafiee, H., et al., *Contactless dielectrophoresis: a new technique for cell manipulation*. Biomed Microdevices, 2009. **11**(5): p. 997-1006.
300. Moschalski, M., et al., *MicroPrep: chip-based dielectrophoretic purification of mitochondria*. Electrophoresis, 2010. **31**(15): p. 2655-63.
301. Morgan, H., et al., *The dielectrophoretic and travelling wave forces generated by interdigitated electrode arrays: analytical solution using Fourier series*. Journal of Physics D: Applied Physics, 2001. **34**: p. 1553–1561.